DOE/MC/30086 -- 5077
(DE96000608)

Naturally Fractured Tight Gas Reservoir Detection Optimization

Annual Report
September 1993 - September 1994

October 1994

Work Performed Under Contract No.: DE-AC21-93MC30086

For
U.S. Department of Energy
Office of Fossil Energy
Morgantown Energy Technology Center
Morgantown, West Virginia

By
Advanced Resources International
Denver, Colorado

DISCLAIMER

DOE/MC/30086 -- 5077
(DE96000608)
Distribution Category UC-132

Naturally Fractured Tight Gas Reservoir Detection Optimization

Annual Report
September 1993 - September 1994

Work Performed Under Contract No.: DE-AC21-93MC30086

For
U.S. Department of Energy
Office of Fossil Energy
Morgantown Energy Technology Center
P.O. Box 880
Morgantown, West Virginia 26507-0880

By
Advanced Resources International
165 S. Union Boulevard
Denver, Colorado 80228

October 1994

U.S. DEPARTMENT OF ENERGY
MORGANTOWN ENERGY TECHNOLOGY CENTER
ANNUAL STATUS REPORT
DATE OF SUBMISSION: 10/31/94

CONTRACT NUMBER:
DE-AC21-93MC30086

CONTRACT PERIOD:
September 30, 1993-March 31, 1997

Project Overview:

The project entitled *Naturally Fractured Tight Gas Reservoir Detection Optimization* is a multi-year project designed to predict the intensity and geometry of natural fracture systems in the subsurface. The presence of naturally fractured reservoirs is a requirement for commercial production from the vast storehouse of natural gas held in tight gas reservoirs. In the past, numerous techniques have been used to identify fractured zones. One of the most promising techniques involves the use of shear wave birefringence to delineate fractured reservoir geometries. Unfortunately, the expense of the technique precludes its use as an exploration tool over large areas. These surface seismic fracture detection technologies, however, may be cost-effective if they are applied to regions where fractures are already known to exist. Current methods to locate fractures in a large tight gas basin are too imprecise to justify the commitment of using advanced seismic methods to verify their location and characteristics.

The central premise of the model is that an integrated approach using geological, geophysical, and numerical basin modeling can be used in a cost-effective manner to locate fractured areas where advanced seismic methods can be utilized. By linking geologic investigations and remote imagery analysis with a unique reaction-transport-mechanical (RTM) numerical basin model we will be able to produce a predictive fracture mapping model to document fracture genesis throughout the basin evolution. The fracture detection numerical simulator will be calibrated at the MWX site in Rulison Field, located in the Piceance Basin of Western Colorado. Research at the MWX site has resulted in a wealth of data critical to the RTM model output calibration. Because of the forward nature of the RTM model, final

KEY ELEMENTS OF INTEGRATED DOE-METC FRACTURE DETECTION TECHNICAL APPROACH

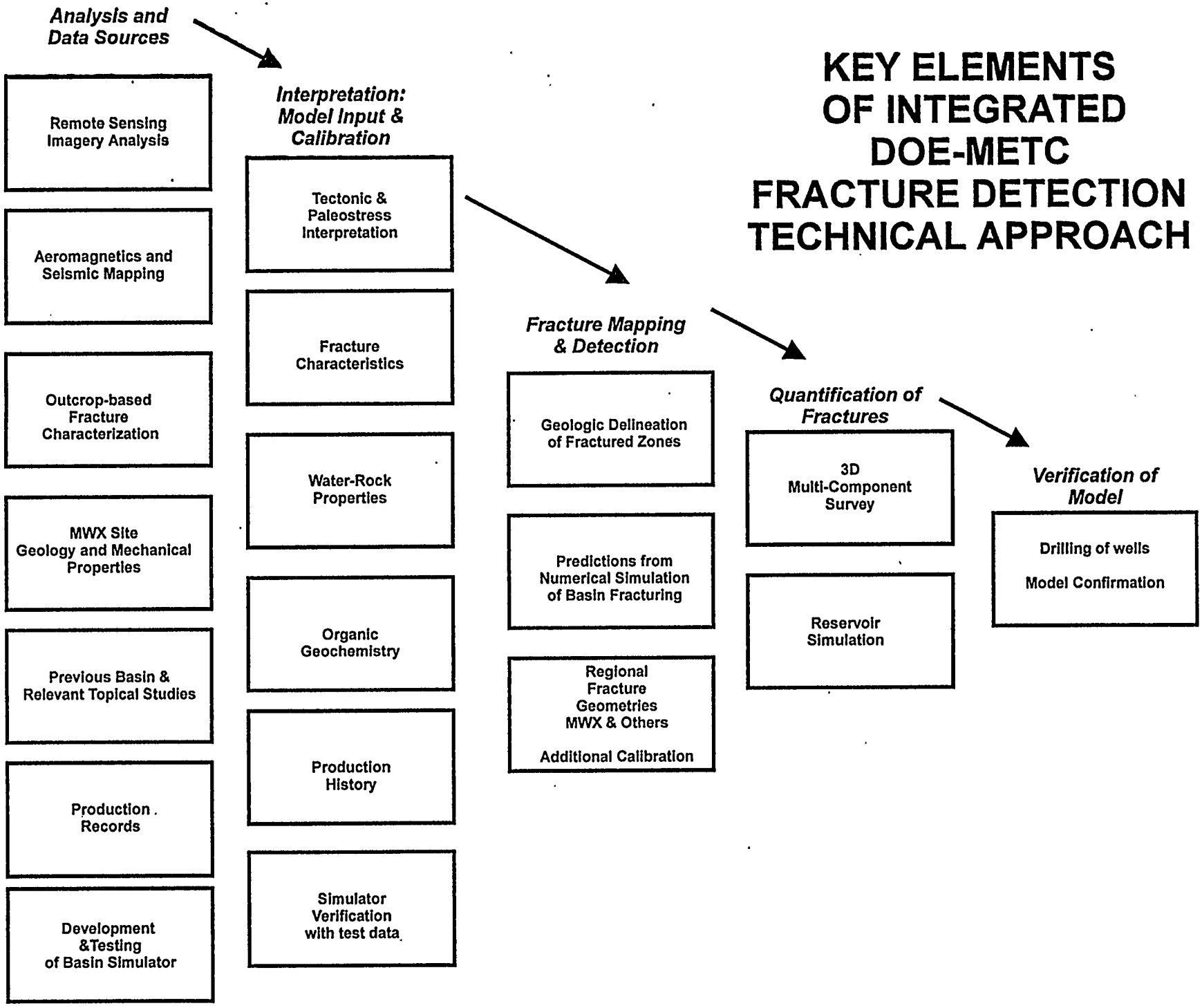

modeling results should match the present-day characteristics observed at the MWX site. The model's capability to map subsurface lateral and vertical fracture geometries will be compared: 1) **locally**, with in-situ fracture data from the MWX site; and 2) **regionally**, to structural and basement fault blocks and related fractured zones derived from integrated remote sensing imagery analysis, aeromagnetics, 2-D seismic and regional structural geologic interpretations.

Field application of ARI's proposed natural fracture detection and optimization methodology will be demonstrated at Barrett Resources Parachute Field, located to the west of the Rulison Field and the MWX site. The basin simulator model will identify those areas of the field possessing the most favorable subsurface fracture characteristics. High resolution airborne and spaceborne imagery will be used to verify the RTM model map by comparing surficial fractures. An area identified as being fractured in both data sets will be further investigated using a 3D multicomponent seismic survey and reservoir simulation. The final verification will be performed by drilling of new wells or recompletions of existing wells in the fractured interval.

The following flow chart summarizes the activities involved in our integrated approach to fracture detection in the Piceance Basin. It is important to emphasize that many of these different tasks are occuring in parallel and will be integrated into the final interpretation in the near future. ARI is conducting all phases of the geologic and geophysical characterization of the basin. This work involves a high-resolution aeromagnetic flyover of the basin to delineate the geometry of basement structures. This data will be integrated with 2D seismic and remote sensing imagery analysis to provide internal consistency in the resulting interpretation. Stratigraphic and structural analyses will be integrated with this interpretation to determine the timing of structural deformation throughout the basin. The determination of timing for structural deformation will also place important constraints on the tectonic significance of linear features interpreted from remote sensing imagery. Structural analysis will also provide information about paleostress orientations throughout the tectonic evolution of the basin. Thermal maturity modeling will be used to determine burial depths which in turn can be used to calibrate the magnitude of basinal stresses over time.

The data collected to geologically characterize the basin will be used to both calibrate and to verify the results of the RTM numerical basin simulator. Data from the MWX site have also

been collected to aid in the calibration of the simulation. The integration of the basin-wide data collection and interpretation will provide a highly detailed template on which to model the basin evolution.

The parallel efforts of numerical simulation and geologic evaluation will each generate an interpretation of fractured areas in the basin. As necessary, additonal refinements to the simulations and additional geologic work will be performed until satisfactory agreement exists between the two independent interpretations. At this point, the 3D multicomponent survey and reservoir simulations will be used to further confirm the presence of fractured conditions in the subsurface reservoirs.

At the conclusion of the project, the ultimate reality test of all independent methods will be achieved by drilling activity in the fractured zone. By simultaneously applying three independent fracture detection methods, we will be able to evaluate the efficacy of different fracture detection methods and the cost-effectiveness of the different approachs. In addition, we will be able to realize the strengths and weaknesses of the different techniques. This recognition will permit operators interested in fractured reservoirs to better plan their exploration strategies to minimize the pitfalls associated by reliance on a specific methodology.

TABLE OF CONTENTS

LIST OF TABLES

LIST OF FIGURES

INTRODUCTION

The Piceance Basin, Western Colorado (see Figure 1 for location map) contains a significant natural gas resource base within low permeability reservoirs. The magnitude of this resource has attracted significant exploration and development interest. Economic production of gas in the Piceance Basin requires the presence of natural fractures to permit sufficient flow to the wellbore from tight gas reservoirs. Therefore, the ability to predict fracture geometries, in advanced of drilling or the use of more expensive diagnostic technologies, greatly enhances the ablility to drill successful wells in fractured tight gas regions. The following text represents a summary of the first years geologic assessment and numerical basin modeling tasks of an integrated basin analysis. The report is divided into three primary areas. The first section is a general overview of the entire basin and briefly describes the geology, gas and water-saturated zones, and tectonic evolution of the southern Piceance Basin. The second section describes the analysis of fractured reservoirs in the Parachute and Rulison fields in the east-central basin. The final section is a discussion of a numerical basin modeller being developed for the Piceance Basin.

Basin Overview

The Piceance Basin is an elongate, NNW-trending structurally-downwarped region that formed as a result of Laramide contractional tectonics. The northern boundary of the basin is defined by the Axial Arch. The sinuous eastern margin is formed by the "S"-shaped Grand Hogback lying along the flank of the White River Uplift. The western boundary, formed by the Douglas Creek Arch, separates the Uinta Basin from the Piceance basin. The southwestern boundary is formed by the Uncompaghre Uplift. These uplifts have experienced multiple phases of tectonic deformation ranging from Precambrian tectonism through Pennsylvanian-Permian deformation, culminating in the Laramide thrusting that defines the present-day basin geometry. By understanding the tectonic evolution of the basin we can understand how and where fractures occur.

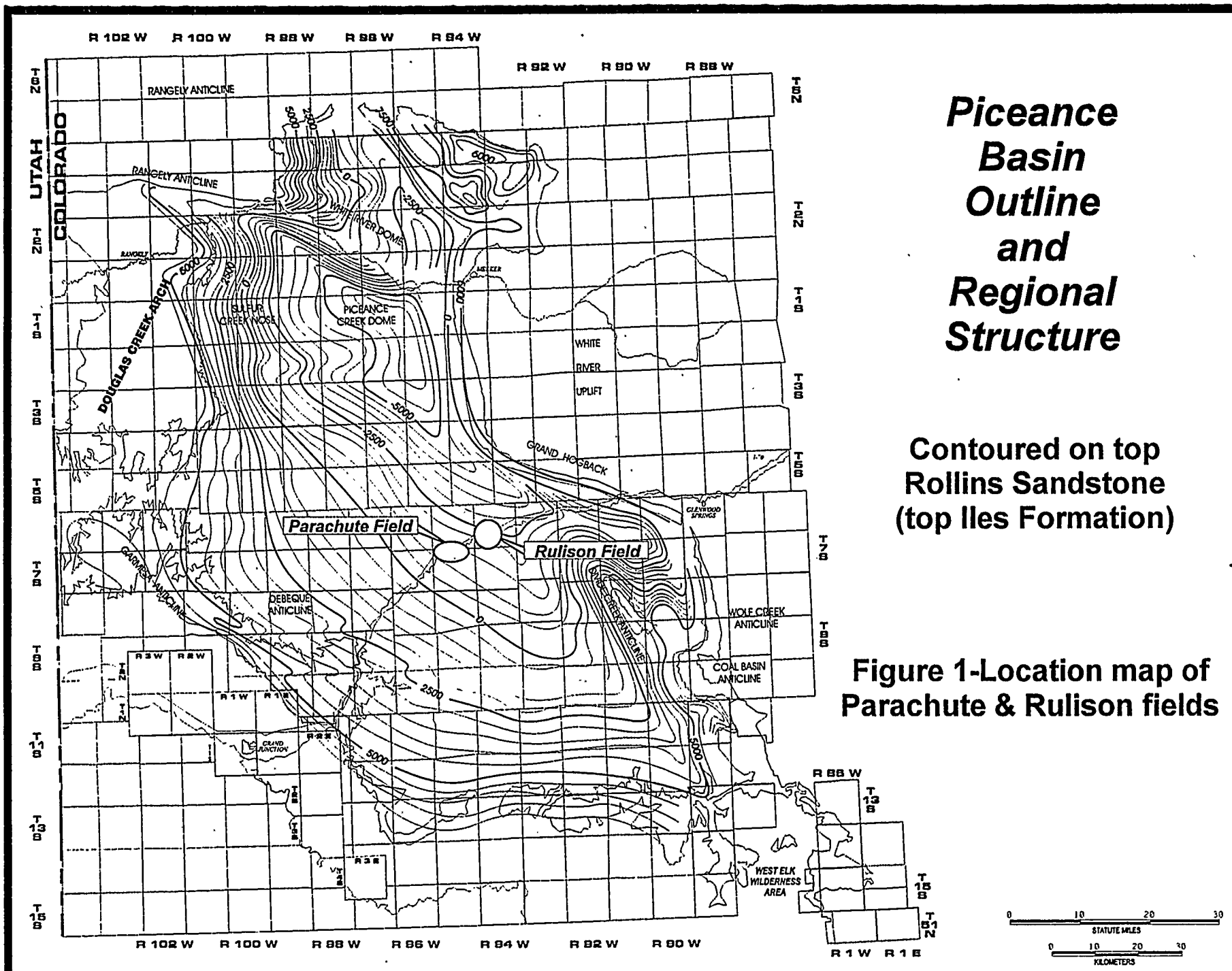

Piceance Basin Outline and Regional Structure

Contoured on top Rollins Sandstone (top Iles Formation)

Figure 1-Location map of Parachute & Rulison fields

Two dominant regional structural trends have been superimposed on the basin. In the eastern basin, the NW-trending Divide Creek, Wolf Creek and Coal Basin anticlines have been formed by WSW-directed thrusting. In the western basin, several broad, low amplitude anticlines have formed with dominant E/W trends. These anticlines include the Debeque, Unnamed (here designated Bull Creek Anticline, located to the south of the Debeque anticline in Plateau Field) and the Douglas Creek Anticline. The latter anticline has an WNW trend. The northern boundary of the basin, the Axial Arch, is a WNW-trending fault-bend fold formed during south-directed Laramide thrusting (Stone, 1986). The timing for the deformation that formed the other folds in the western basin has not been unequivocally determined although some of the folding appears to have occurred during the second phase of Laramide deformation.

The Cretaceous-age Mesaverde Group stratigraphy is pervasively gas-saturated and is overlain by the tremendous oil shale reserves of the Green River Formation. The focus of this report is the gas found within the Cretaceous-age Mesaverde Group (Williams Fork Formation) coals and interbedded sandstones. Additional significant gas resources are found within underlying marine sandstones of the Cretaceous-age Iles Formation, and within overlying fluvial sandstones in both the upper Williams Fork Formation, and the Tertiary-age Wasatch Formation (see Figure 2 for gas fields and producing horizons). The largest hydrocarbon resource (>13 trillion barrels, Taylor, 1987) is found within the lacustrine, Tertiary-age Green River Formation oil shale that overlies the northern half of the basin. Oil shale production from the Green River has gone through several periods of explortation to develop extraction methods that can economically produce oil in an enviromentally acceptable matter. The oil shale deposits coupled with the gas resources hosted by cretaceous-age sediments represents one of the world's largest hydrocarbon accumulations.

GAS- AND WATER-SATURATED CONDITIONS IN THE PICEANCE BASIN

A critical preliminary step during basin partitioning is to locate gas-bearing zones in the subsurface. Further partitioning can then be performed using integrated studies of remote sensing and structural geology to locate fractured reservoirs. To analyze the location of gas-

FIGURE 2

CRETACEOUS GAS FIELDS AND REGIONAL STRUCTURE MAP

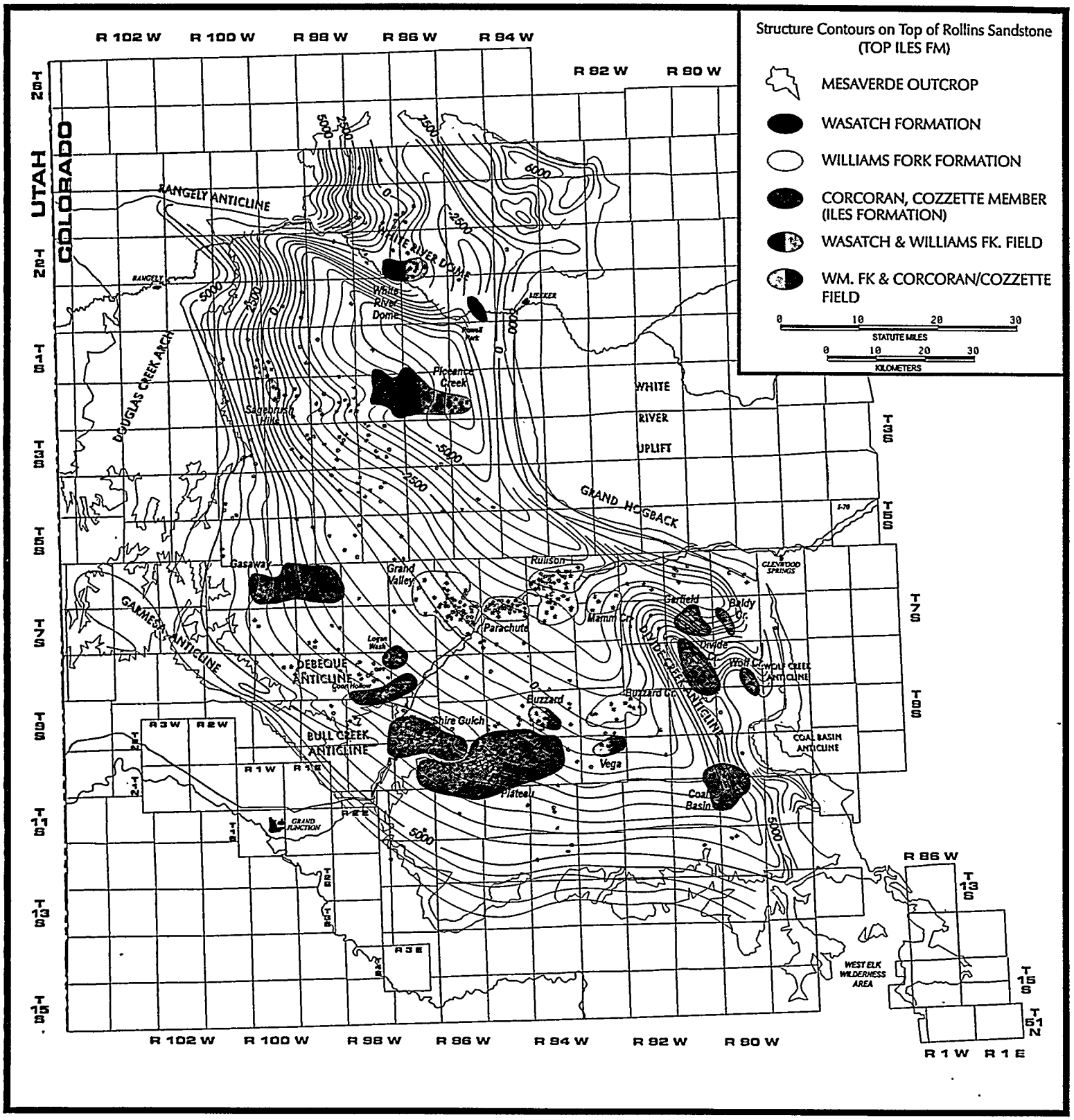

bearing zones, water and gas saturation data were assembled from initial production, and monthly and cumulative production data collected throughout the Piceance Basin. These data were then used to delineate the areal distribution of the gas and water-saturated zones. Gas saturation data were also examined using mud or hydrocarbon logs located throughout the basin. A cross-section was constructed from this information to illustrate the cross-sectional basin hydrodynamics. Recognition of subsurface permeability caused by tectonic structures and related fracturing is a more complex problem. To determine zones or orientations of enhanced subsurface permeability, remote sensing imagery analysis was used to constrain regional macrostructures and related fracture trends.

The following discussion of gas-and-water saturation is organized into three primary sections. The first section outlines the characteristics of typical gas-centered basins and then assesses water and gas-saturated conditions throughout the Piceance Basin. The second section outlines the relationship between subsurface structure and production. The third and final section describes some preliminary remote sensing imagery analysis results.

Basin-Centered Gas Model

Numerous models relating basin subsidence and hydrocarbon generation and retention have been proposed by such authors as Barry (1959), Meissner (1978) and Law and Dickinson (1985). Recently, Law and Dickinson (1985) have further extended this model and described the process by which thermal influences result in abnormal pressure in low-permeability systems. The central idea of this model is the dynamic relationship between thermal maturity, permeability changes and burial depth. In this model, there are four primary phases (Figure 3). It is important to note that the generation and existence of overpressured conditions is an important piece of data to be used in regional fracture studies. By knowing the timing of overpressure generation and the mechanical state of the host rock mass, the geometry of natural fractures that formed during this phase can be much more accurately predicted. Available data from the Piceance and other basins suggests that overpressuring may iniate regional natural fracture development in many tight gas sand reservoirs.

EVOLUTION OF GAS - CENTERED BASIN

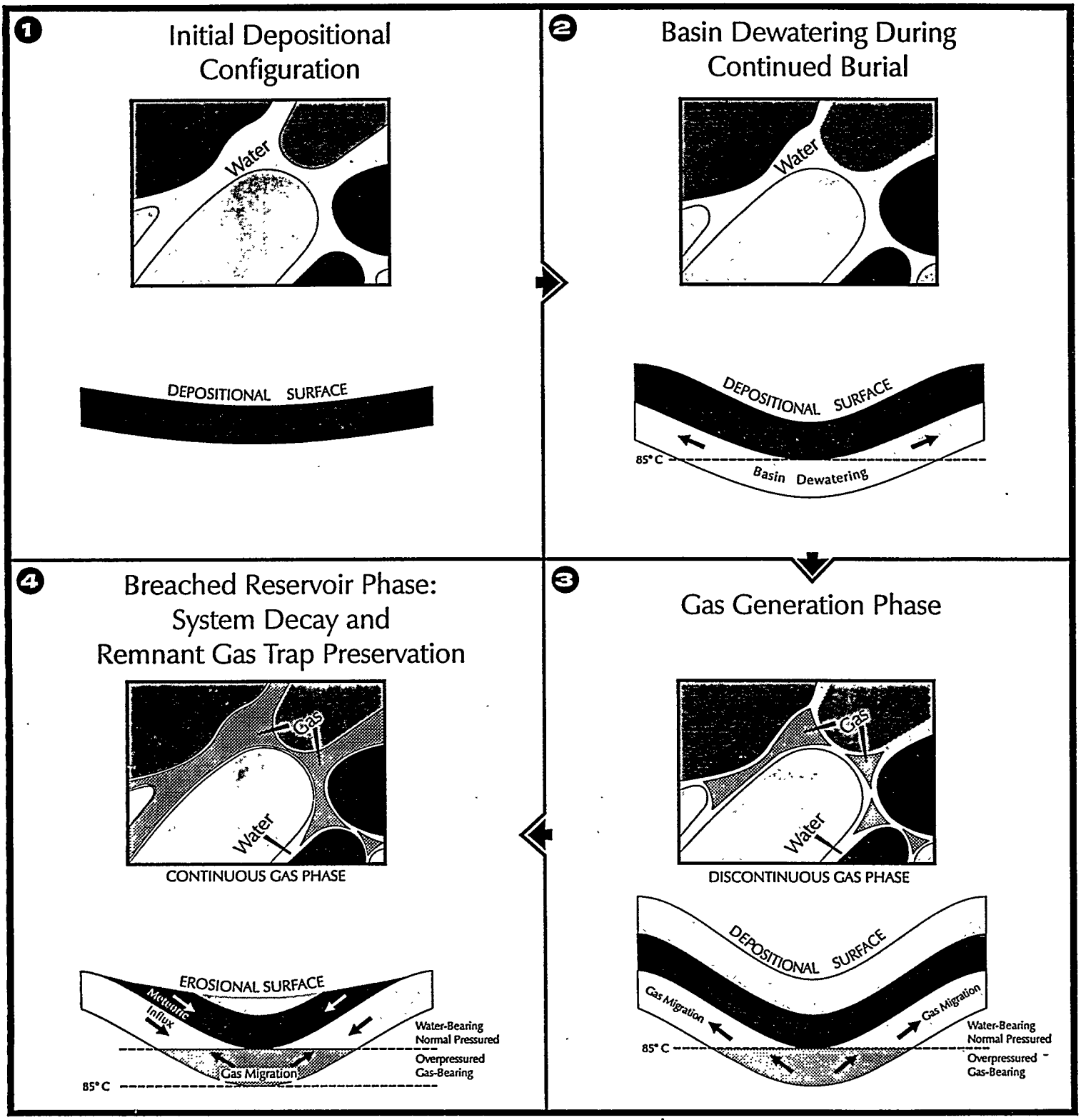

In the gas-centered basin model of Law and Dickinson (1985), the first phase involves sediment deposition and basin dewatering. During this phase, sediments show high porosity (up to 40%) and elevated permeability. Throughout this interval, porosity is being reduced by compaction and precipitation of early pore-filling cements. The sediment mass is experiencing an increase in Young's modulus (a measure of rock stiffness) during this phase.

The second phase is delineated by thermally-induced carbon dioxide generation occurring at a temperature of approximately 120^0 F. The large amount of carbon dioxide produced during this phase reacts with existing water to form carbonic acid. The net effect is a lowering of the pH of the formation fluids. This lower pH dissolves some of the early cement phases and causes the precipitation of other cements. The increase in carbon dioxide also serves to increase the overall fluid or gas pressure in the system.

The third phase occurs when organic materials within the host sediments commence gas generation at a vitrinite reflectance value of approximately 0.76, corresponding to an approximate temperature of 180^0 F for Type III kerogen. During this phase, cementation causes a reduction in permeability and porosity because water mobility and mixing are reduced. Mechanical compaction is considered minimal at this stage. Water is forced up dip and/or up section when gas pressure exceeds the local hydrostatic value and more gas is generated than can be stored in the available pore space. The fluid migration direction is dependent on local pressure gradients. In these dewatered regions, the increased capillary pressure accompanying gas generation further impedes dissolution of both neo-cements and framework grains. This impeded dissolution causes a decrease in permeability and porosity. As capillary pressure increases due to gas generation, water saturation in the system decreases to a minimum level. The solubility of chemical constituents in remaining formation waters approaches chemical equilibrium conditions between fluids and the host rock. This immobility of dissolved chemical constituents inpairs the dissolution processes and further enhances the maintenance of low-permeability conditions.

In theory, provided sufficient quantities of organic materials, gas generation should

continue as long as thermal cracking can occur. However, because of uplift and declining thermal gradients, combined with fracturing and concomitant leakoff, the overpressured zone generally cannot be sustained. As the overpressured zone experiences decay, (a gradual decline in gas pressure due to cessation of gas generation and uplift) meteoric recharge is able to breach the reservoir and flush hydrocarbons from the system. This phase represents the present-day conditions in most gas basins that had a gas-centered origin. Thick, thermally mature coals interbedded within lenticular sand bodies are a common feature in many gas-centered basins. This geometry is also found in the Piceance Basin where the isolated hydrodynamics of lenticular sandstone reservoirs maintain unbreached and overpressured conditions.

In the Piceance Basin, the overpressured zone (as determined by drilling mud weights) has been identified in the lower section of the Williams Fork Formation within the Rulison Field. In this field, the top of the overpressured zone lies just above the Cameo Coal, and appears to have a gradational lower boundary terminating at the top of the laterally continuous marine Rollins sandstone of the Iles Formation. Figure 4 illustrates the gas-centered basin geometry across the Piceance Basin. The geometry of this zone roughly parallels the vitrinite reflectance isotherm of 0.8 along the western boundary and the basin outcrop to the east.

To create this cross-section or basin profile, the total gas curve from hydrocarbon logs, and the gamma log traces from wireline logs from the same well were digitized. The combined gas and gamma log traces for these wells were hung on a structural datum (Top Mesaverde or Cretaceous/Tertiary boundary) to illustrate the basin geometry. Relevant information such as the location of the overpressured zone, stratigraphic correlations, and vitrinite reflectance values (isotherms) were added to the section. From this cross-section, lateral and vertical water/gas transitions are located in the basin. The east/west cross-section defines the overpressured zone as being restricted to Rulison field and approximately one-half township to the east. Parachute field is normally pressured except along the transitional eastern field margin where it grades into Rulison field. From hydrocarbon log traces, the lower Williams Fork Formation appears gas-saturated across the basin interior. The discontinuous, lensoidal geometry of the Williams Fork, combined with its low matrix permeability, requires natural fractures for efficient gas recovery.

HYDROCARBON - GAMMA LOG CROSS SECTION ACROSS THE PICEANCE BASIN ILLUSTRATING GAS - CENTERED BASIN GEOMETRY

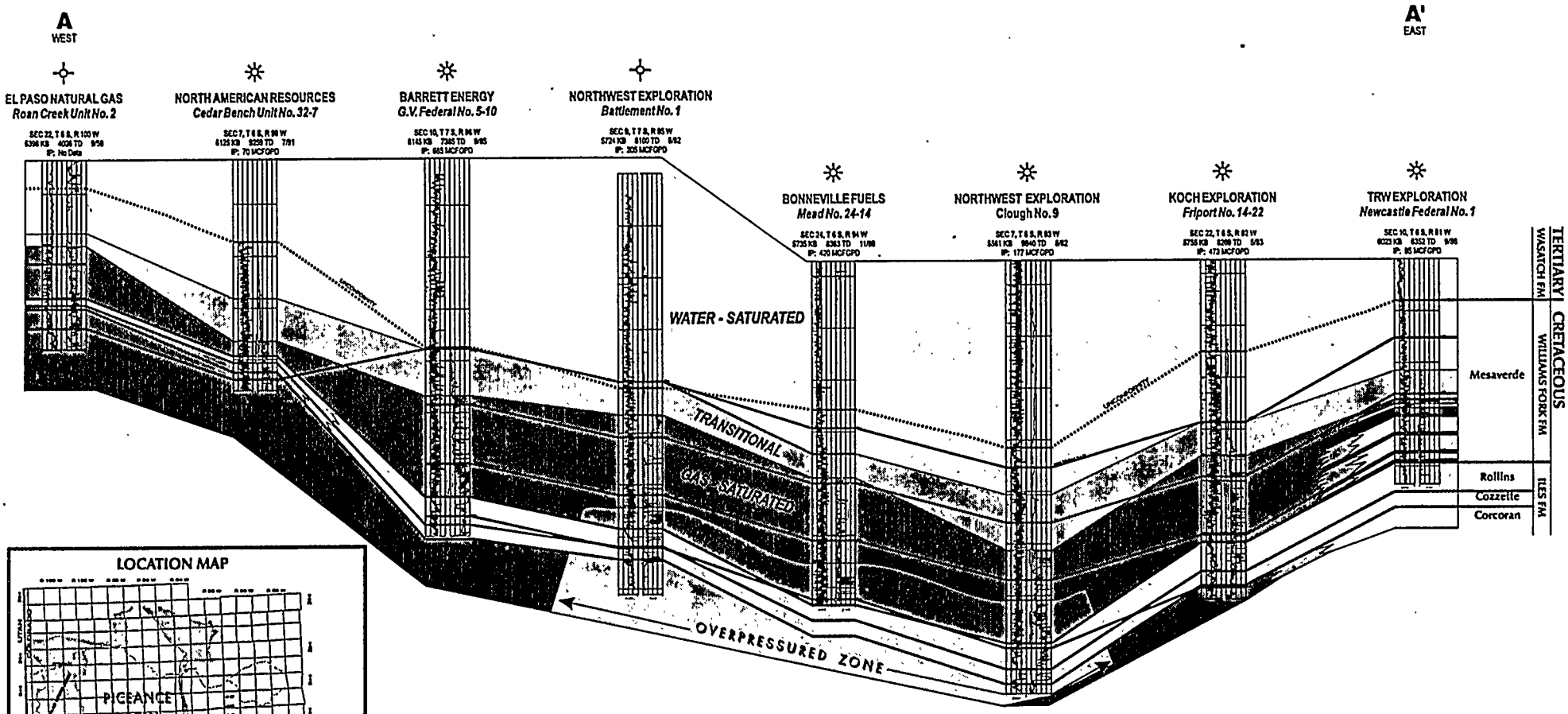

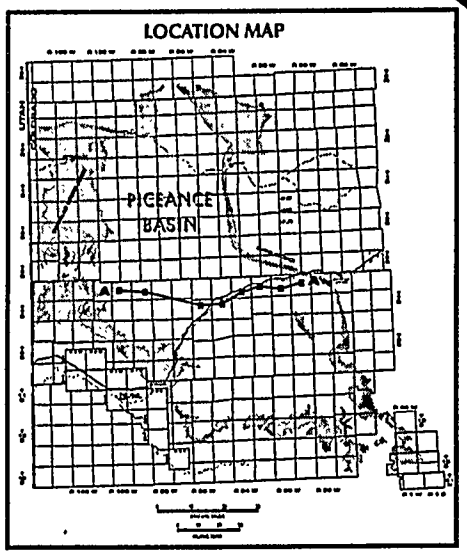

FIGURE 4

The importance of fracture detection is to identify areas capable of economic production from this reservoir horizon. In sharp contrast to the Williams Fork lensoidal stratal geometries, the marine Iles Formation (lying underneath the Williams Fork Formation) sandstones are laterally continuous. However, the low-permeability of these sands also requires fractures to allow economic gas yields.

In cross-section, the Cozzette and Corcoran member sandstones in the Iles Formation appear to be gas-saturated across the basin and were probably once also overpressured in the basin center at one time. The Cozzette member sandstones are water-saturated along the eastern basin margin. The Rollins member sandstone is water-saturated across the basin except for scattered localities along the western basin margin where isolated tests have shown it to be dry and gas-bearing. In the gas-centered basin model, the discontinuous nature of the fluvial sandstones in the Williams Fork has enhanced the preservation of overpressured conditions. In the underlying Rollins sandstone, lateral continuity across the basin may allow this member to serve as a regional aquifer. The Cozzette member has probably behaved in a similar fashion although it appears to have greater internal complexity and may contain flow boundaries that impede ready migration of water through these sands. The Corcoran member has a relatively thin outcrop expanse on the eastern margin so that the area of potential meteoric influx is small compared to the other two Iles Formation sandstones.

A primary control of fluid flow through the basin subsurface is thought to be the approximately two thousand feet of hydraulic head difference between the eastern and western margins of the basin. In this flow regime, artesian flow will occur from east to west (Figure 5). However, the presence of overpressured conditions in the basin center inhibits flow of fluids across the overpressured interface. Lithologic flow barriers are created by the lensoidal geometry of the Williams Fork fluvial channels. Because the Rollins member sandstone is laterally continuous and normally pressured, it is considered the primary conduit for fluid transport across the basin. Similar behavior is expected for Cozzette and Corcoran sandstone members due to their normally pressured state and variable water content across the basin. To verify this hydrodynamic model, zones of meteoric influx and restricted

SCHEMATIC EAST - WEST CROSS SECTION ACROSS PICEANCE BASIN

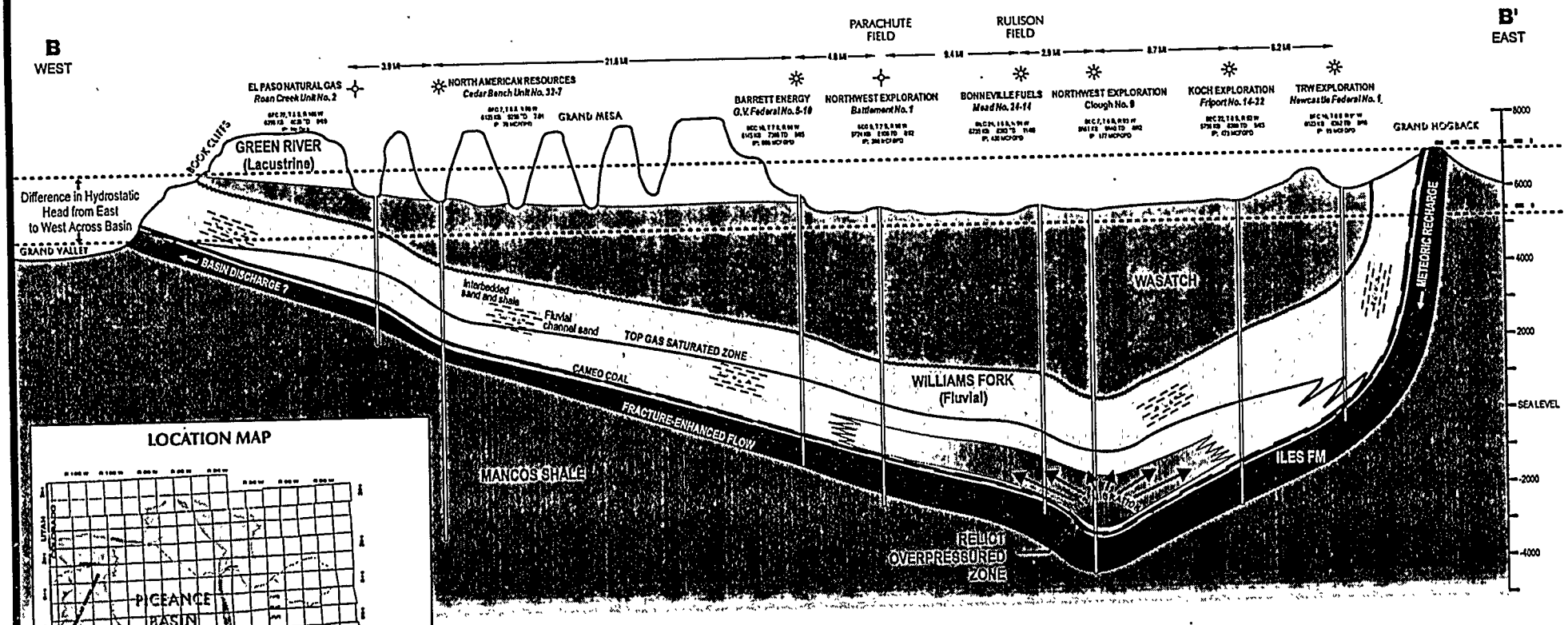

FIGURE 5

inflow are being evaluated using water chemistry data from throughout the basin.

From the basin cross-section, an excellent perspective is gained into the origin and evolution of basin subsurface hydrodynamics. Determination of the areal extent of the water- and gas-saturated zones is the next step.

Water and Gas-Saturated Zones in the Piceance Basin

To assess the areal extent and nature of the gas and water-saturated reservoir horizons throughout the basin, all publically-available hydrocarbon (mud) logs from throughout the basin were collected and the location of the gas-saturated zone was determined on these logs. From a subset of these logs, the cross-section described previously (Figure 4 & schematically in Figure 5) was constructed.

To assess gas and water-saturated conditions, gas-saturated conditions were initially screened by the presence of gas fields producing from that particular reservoir horizon. This was confirmed by verifying the presence and magnitude of gas shows in mud logs from that area. Mud logs are often considered preferable to neutron density logs in the Piceance Basin because the "gas effect" or neutron crossover is commonly suppressed in tight gas sands despite the presence of high gas saturation. Numerous examples are available where significant gas shows are observed on the hydrocarbon log but the neutron density logs do not show any crossover effect. Because of this observation, the cross-over effect is not always a reliable tool for identifying gas-bearing sands. Operators in the region (e.g., Barrett Resources) have found similar relationships in their work. The explanation for the lack of cross-over may have several causes. One possible explanation is the overall shaliness of the section. The effect of the shale is to increase the apparent porosity determined by the neutron porosity tool because of the water bound in the shale structure. In this case, no crossover effect will be observed because the apparent porosity recorded in the neutron porosity tool will always exceed the value measured by the density porosity tool. Other factors that may inhibit the crossover effect include high borehole rugosity that inhibits pad contact with the borehole wall, water-based drilling muds that

further enhance the shale effect, and variable mudcake thickness.

Water-saturation was determined by using initial production data (generally determined by most operators after approximately 6 months of flow to remove load or hydraulic fracture water returns from production information) and flagging all wells in the basin flowing greater than 5 barrels of water per day (BWPD). The production data for these wells were then examined to determine if the wells flowed more than 10 BWPD over time. From this information, the boundaries of the gas and water-saturated zones were delineated. Because many areas show complex water production, those areas with increasing or variable water production over time were labeled as transitional. These complex relationships are particularly true for the Cozzette Member of the Iles Formation. In this reservoir horizon, wells producing no water are often surrounded by wet wells. One possible explanation is that water is sourced from fractures that connect wet zones while gas is trapped in less-connected fractures.

In the Piceance Basin, the vast majority of Williams Fork Formation reservoirs are gas-saturated (Figure 6). Significant breaching of the system is evidenced by water-saturated conditions such as within the Divide Creek Anticline in the southeast area of the basin. Differential amounts of meteoric recharge occur along the basin margins where the Williams Fork Formation or its equivalent crops out. To date, the most productive Williams Fork fields appear to lie in a band along the basin axis. If gas is sourced from the Cameo Coal group within the Williams Fork, this is the most likely zone for gas entrapment in a basin-centered gas model. The majority of gas would be generated at the most thermally mature, deepest part of the basin.

Very limited production and test data are available for the Rollins member sandstone. There are less than a half dozen wells in the south half of the basin that have reported tests in the Rollins. Most operators consider the Rollins to be water-saturated throughout the basin. Only along the western quarter of the basin (where significant facies changes occur in the Rollins and equivalent sands) does the Rollins appear to be gas-saturated, though the test data suggest uneconomic volumes. The source of water produced from the Rollins is unknown.

WILLIAMS FORK FORMATION
GAS-SATURATED ZONE, PICEANCE BASIN

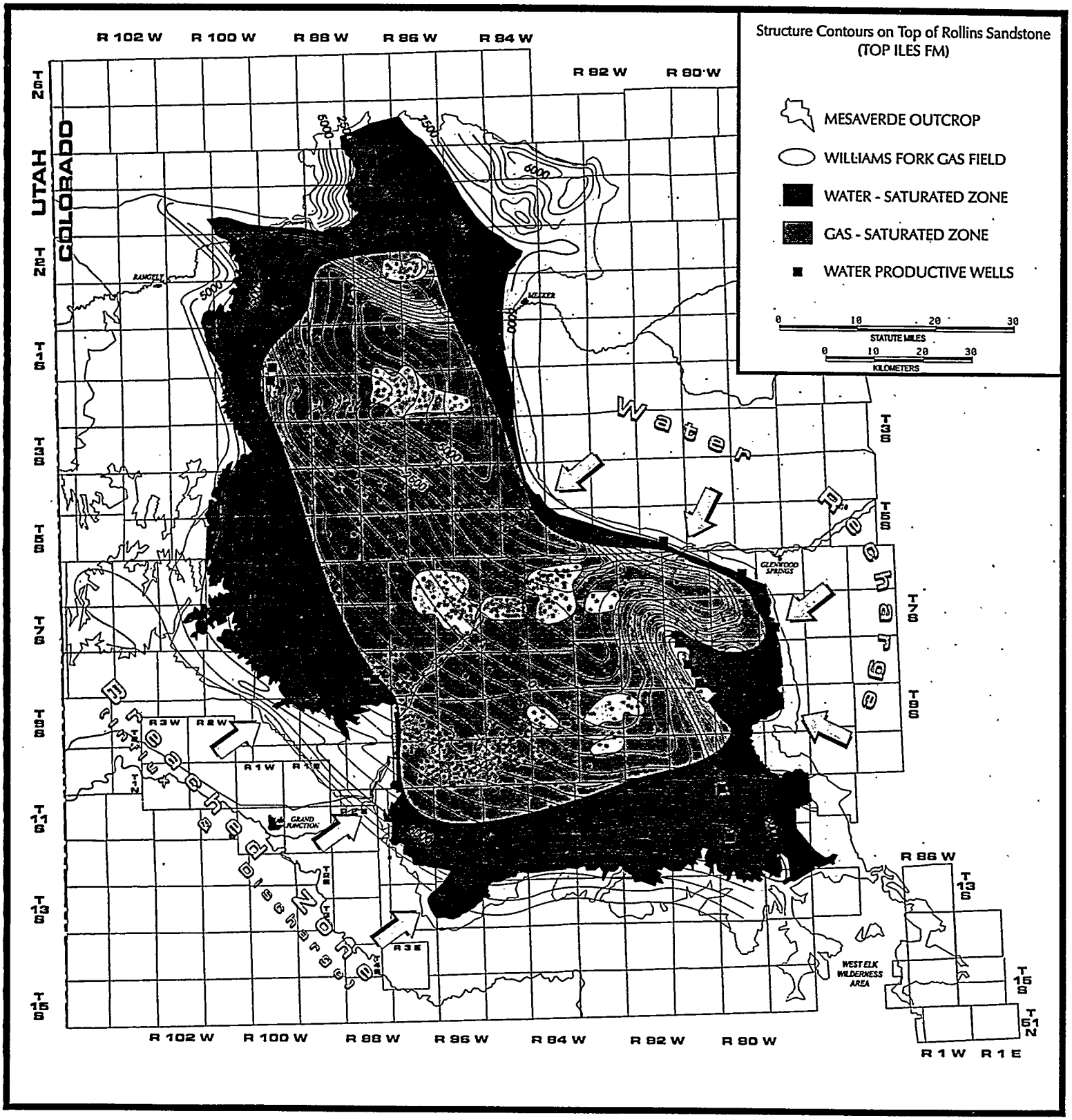

The Cozzette Member of the Iles Formation is a shingled, southeastward-prograding, laterally continuous, marine sandstone (Figure 7). The sandstone was deposited along approximately E/W trending strandlines with depositional limits present along the northern and southern boundaries. Meteoric influx occurs along both eastern and western basin margins. However, influx along the western margin is limited due to the arid conditions that prevail in that region. The source of the Cozzette water is unknown.

Gas and water production from the Corcoran member of the Iles Formation show that most of the Corcoran sandstone is gas-bearing (Figure 8). Only along the basin margins where subsurface depths are relatively shallow does the Corcoran produce water. There are several Corcoran producers that have apparent associated water, however, it is unclear from the reporting of the commingled production data whether the water is sourced from overlying reservoir horizons. Alternatively, some of this water may be fracture flow water sourced from adjacent reservoir horizons. Similar to the Cozzette sandstone, the Corcoran is also breached along the unnamed anticline structure just to the south of Debeque Canyon. The geology of the Corcoran and the Cozzette sandstones are both quite similar and probably represent fining-upwards shoreline sequences. Like the Cozzette, the Corcoran also prograded to the southeast. The source of the Corcoran water is unknown.

A major problem for most gas producers in the southern Piceance Basin is that high permeability zones are commonly water-saturated. Work in progress is attempting to determine if water production is controlled by fracturing. In addition, ongoing efforts are underway to characterize the source of water and geochemical evolution of the basin.

REMOTE SENSING IMAGERY AND FRACTURE ORIENTATIONS

A critical variable in determining producibility of a prospective reservoir lies in the presence of significant subsurface fracture permeability. In this context, basin-wide studies of gas and water-saturated zones identify producible targets in the gas-bearing portion of the basin that require further investigation to find fracture permeability. The nature of the relationship

FIGURE 7

COZZETTE SANDSTONE - ILES FORMATION GAS-SATURATED ZONE, PICEANCE BASIN

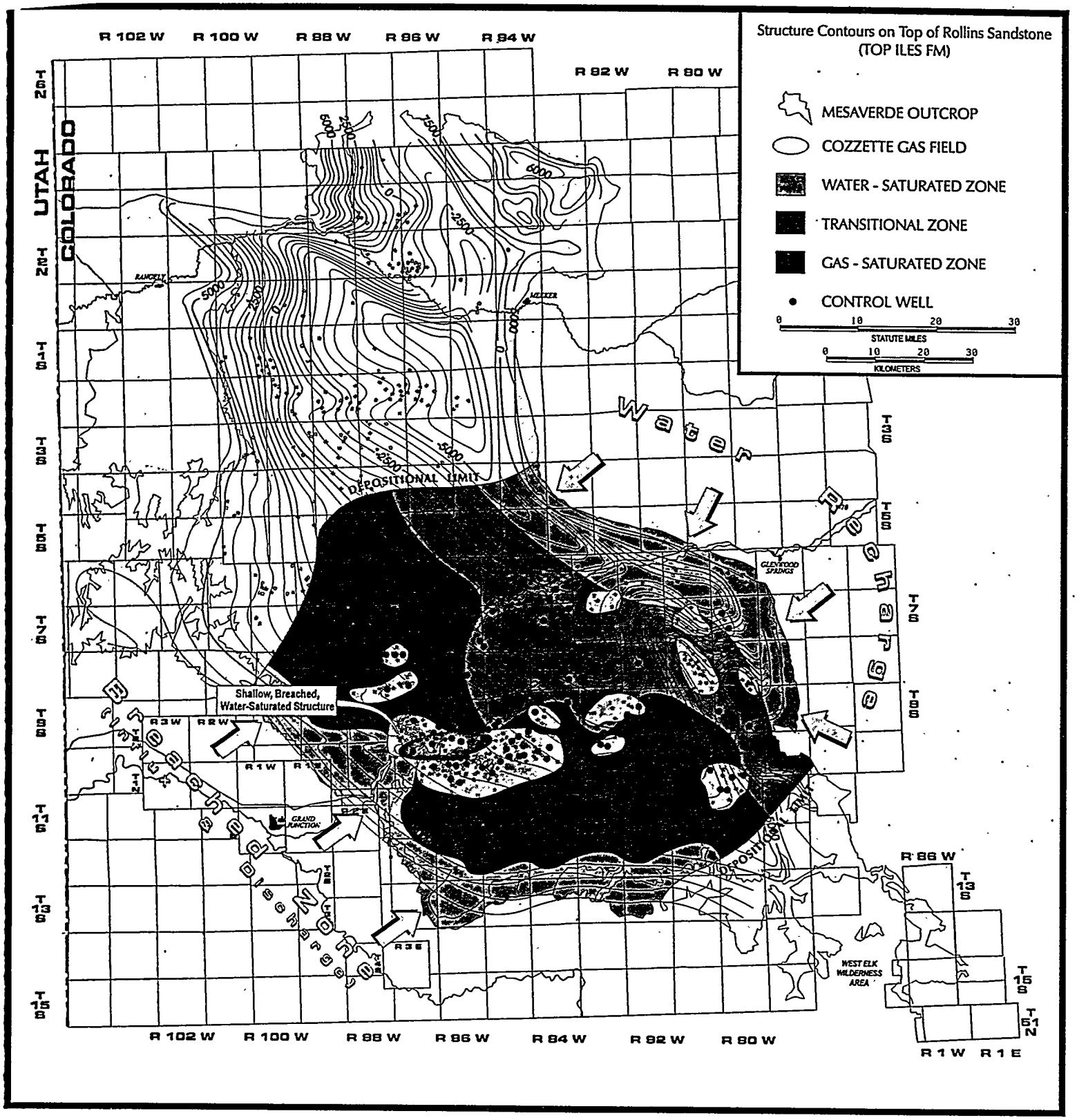

FIGURE 8

CORCORAN SANDSTONE - ILES FORMATION GAS-SATURATED ZONE, PICEANCE BASIN

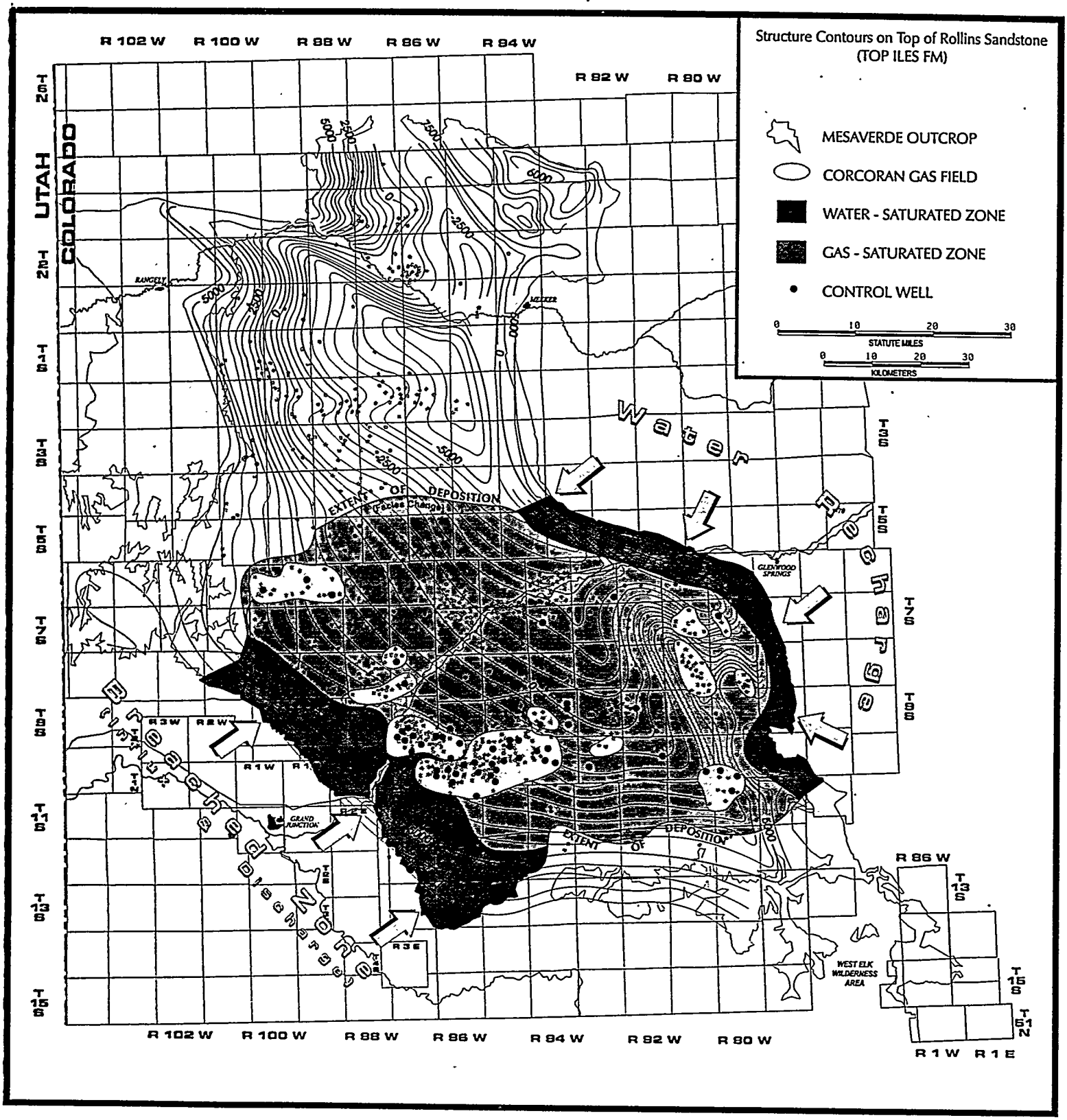

between interpreted linear features and fracture systems must be determined from subsurface mapping, field mapping, and from ancillary geophysical and geologic data to determine if interpreted features do indeed represent fractured zones. Tectonic analysis is necessary to further assess which fracture sets are presently dilatant.

Remote sensing imagery analysis is one tool being used to understand the distribution of subsurface structural trends as manifest by surficial geology. There have been three primary emphases of the remote sensing analysis to date. The first is the creation of a suitable Thematic Mapper (TM) mosaic for the entire Piceance Basin using the optimal band combinations for this region to maximize resolution of surficial features. The image that has been generated is shown in Figure 9. An enlargement of this hard copy image has been used for the TM-based remote sensing image interpretation. Interpretation of this image involved marking non-cultural, tonal anomalies, and linear features on transparent overlays. Upon completion of the image interpretation, the interpreted linear features were digitized and statistics of their orientation and length-weighted orientation analyzed using a proprietary algorithm developed at Advanced Resources International, Inc. From this information, integrated with other data sets, recognition of regionally significant lineaments will be accomplished.

A linear feature interpretation based on synthetic-aperture, side-looking airborne radar imagery (SLAR) has been interpreted for the entire Piceance Basin. This data set is composed of both analog and ARI-reprocessed digital data sets available from U.S. government sources. A typical digital, reprocessed radar image is shown in Figure 10. The image depicts an enlarged view of the Grand Valley-Parachute-Rulison area along the Colorado River in the central and eastern regions of the basin. The interpreted linears for the entire basin are shown in Figure 11. Rose diagrams for this area are shown in Figure 12. The rose diagram shows a dominant set of linear features oriented to the NE. A lesser number of NW-trending linear features are also present. To determine the statistical significance of these linear feature trends, a Monte Carlo simulation was used to determine the statistical significance of the different azimuth data bin sizes (1, 3, 5 degrees of total linear features azimuth range) for a given population of linear features. Applying this level of statistical significance to the radar imagery reveals that there

THEMATIC MAPPER (TM) IMAGE OF PICEANCE BASIN, WESTERN COLORADO

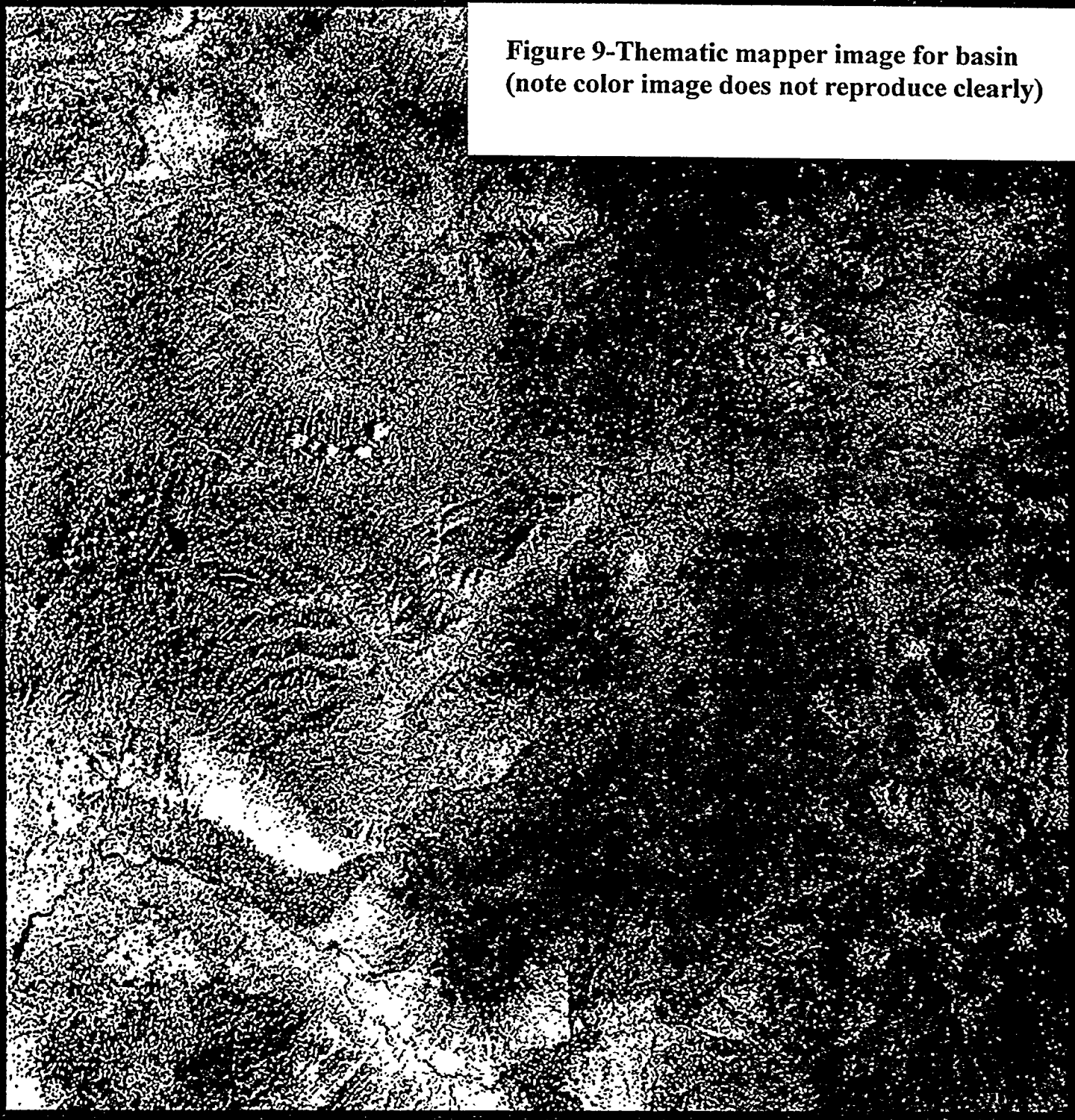

Figure 9-Thematic mapper image for basin (note color image does not reproduce clearly)

TM BANDS 5 7

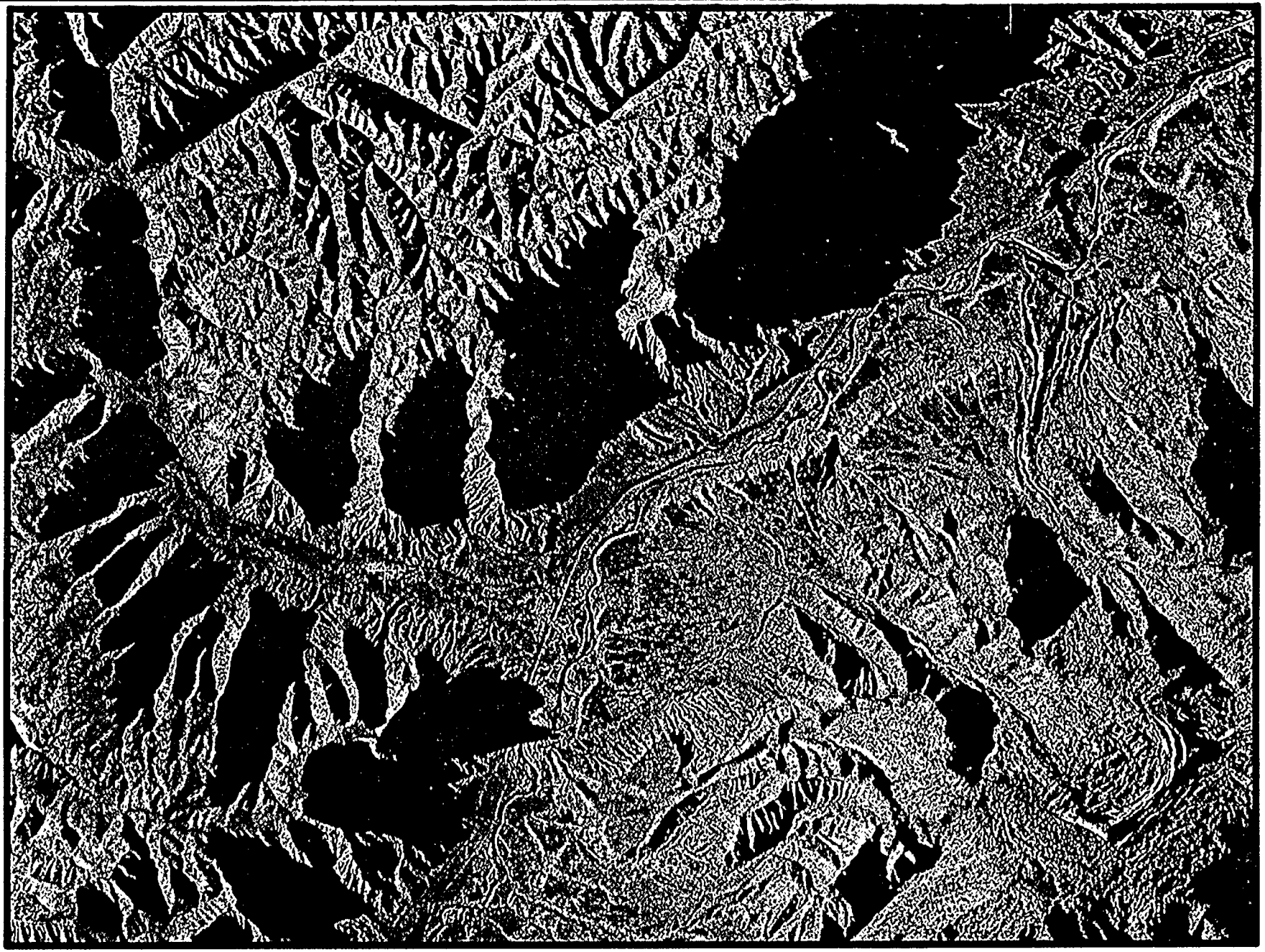

X-BAND SYNTHETIC-APERTURE, SIDE-LOOKING, AIRBORNE RADAR (SLAR) - SE Look Direction

LOCATION OF GRAND VALLEY, PARACHUTE, AND RULISON FIELDS

PICEANCE BASIN, COLORADO

FIGURE 10

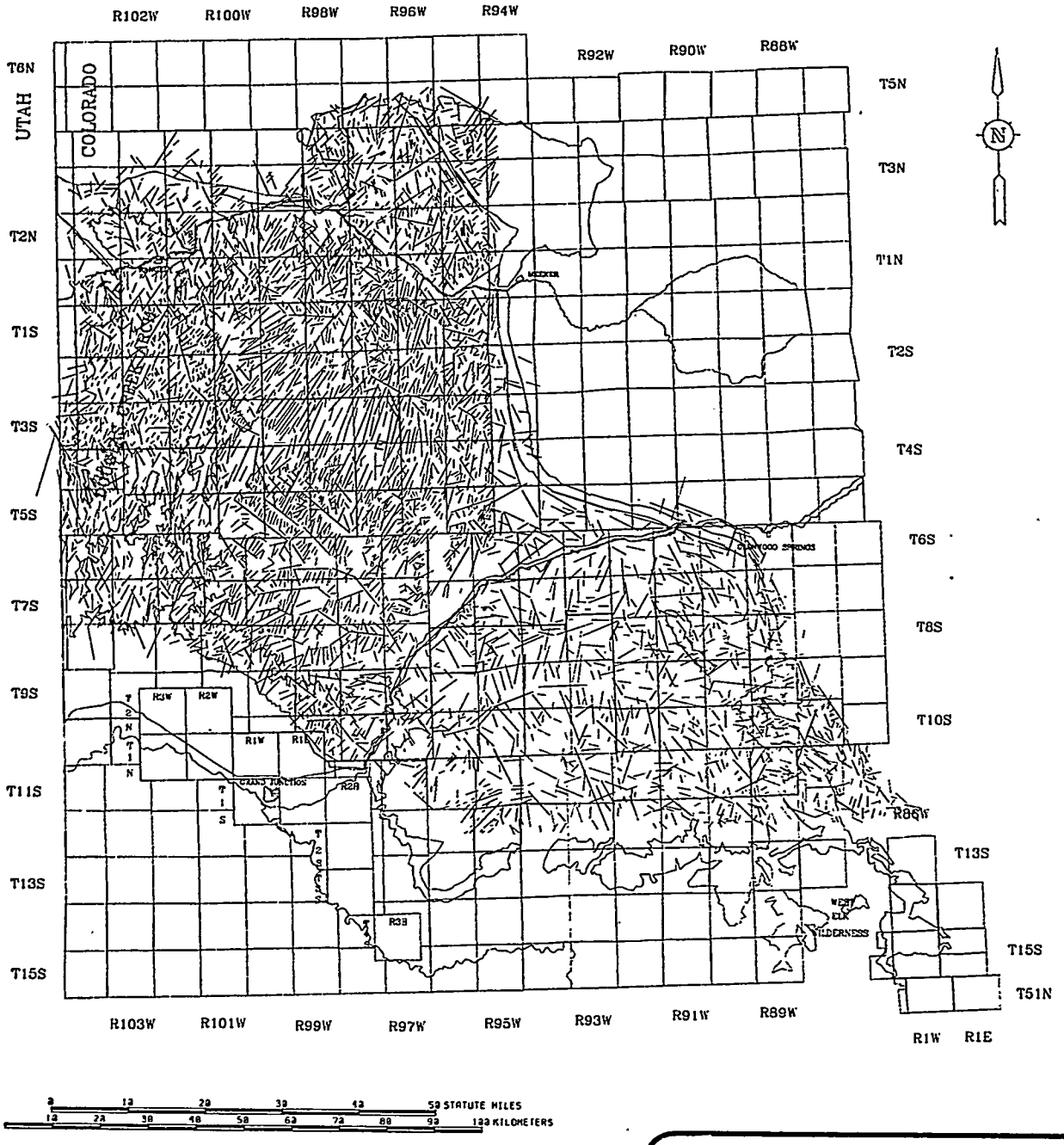

Figure 11

PICEANCE BASIN, NORTHWEST COLORADO

SIDE-LOOKING AIRBORNE RADAR (SLAR) INTERPRETED LINEAR FEATURES

Figure 12

SIDE-LOOKING SYNTHETIC APERTURE RADAR IMAGERY (SLAR)
LINEAR FEATURE ANALYSIS
PICEANCE BASIN, WESTERN COLORADO

SE-LOOK DIRECTION

Population	4,429 linears
Maximum Percentage	5.6 percent
Mean Percentage	2.8 percent
Standard Deviation	1.4 percent
Vector Mean	18.5 degrees
Confidence Interval	3.6 degrees
R-Mag	0.32

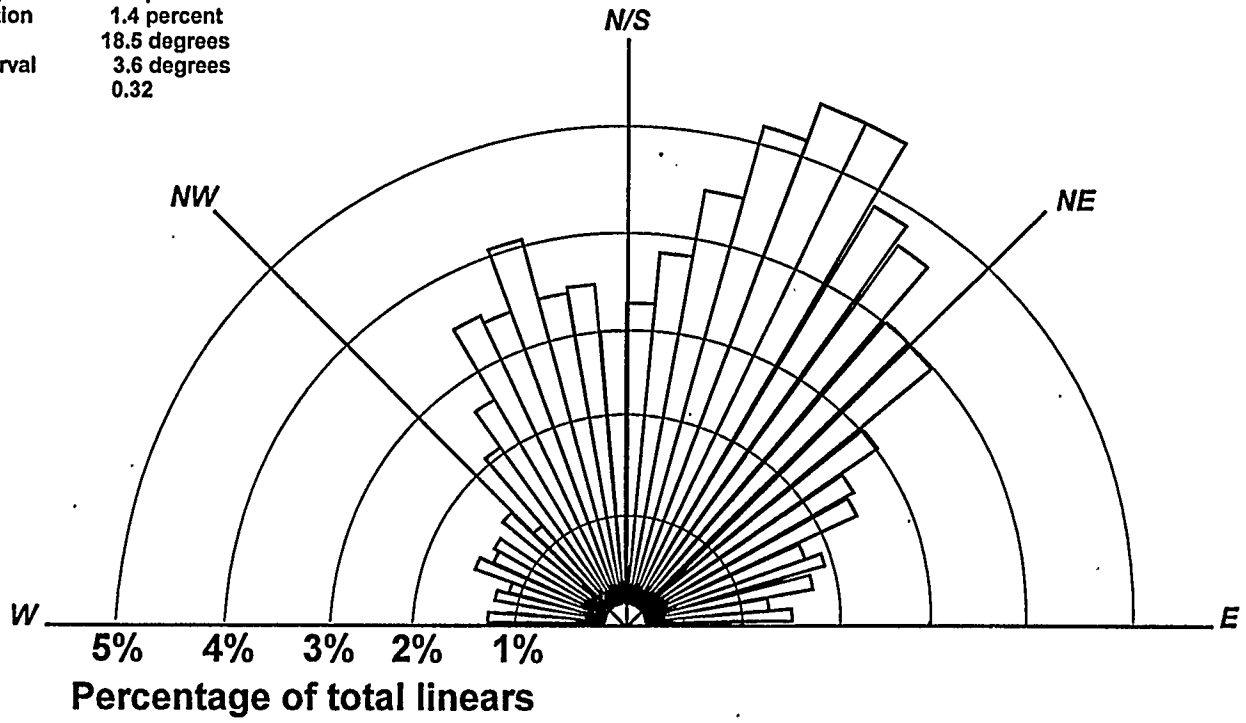

is a statistically significant NE-trend. There is a lesser-developed WNW trend. The statistical analysis of this data set is shown in Figures 13, 14 & 15. These plots illustrate the confidence intervals for 1, 3 and 5 degree bin increments (A bin is defined as an azimuth range within the data, e.g., all linears possessing azimuths 300-305 represent the data in a 5 degree bin). There are a maximum of 180 one degree bins, 60 three degree bins, etc.). The statistically significant linear features fall above the thin horizontal line on each of the three plots. All trends falling below this cutoff are not considered significant at a 95% confidence level.

In interpretation of SLAR (radar) imagery, it is critical to recognize the bias effect of the radar look direction. Linear features oriented perpendicular to the look direction will be enhanced and more prominent than those linear features that trend parallel to the look direction. Because this data set has a SE look direction, we have an amplified perspective of radar reflections along a northeast trend. Also, for the same reason, a northwest-southeast trend is not as prominent. Use of other remote sensing data sets, especially Thematic Mapper (TM) will ameliorate the potential bias introduced by the radar imagery collection methodology. The NE and WNW trends observed in the SLAR imagery are similar to the fracture trends recognized in core during research operations at the MWX site in Rulison Field.

Remote sensing imagery analysis is not intended as a stand-alone technique. It is essential to integrate other data sources into the analysis, especially geophysical data. A major effort on the project has involved the compilation of existing geophysical (in this case, non-seismic) data. One of the more useful geophysical data sets is aeromagnetic data. This data was used to delineate regions within the basin where acquisition of new, higher-resolution data is necessary to resolve complex structures. We have created several magnetic anomaly maps of the basin. The first was a color density slice of magnetic total field residuals (Figure 16). The density slice map represents a horizontal slice through a three-dimensional magnetic total field residual surface. Hotter (e.g., red or orange) possess greater magnetic intensity than cooler colors (e.g., blue and purple). On this image, the area of Mesaverde outcrop is shown as solid black. There is an excellent correlation between positive magnetic areas and regional structures. Note the pronounced E/W trending magnetic feature underlying the Debeque Anticline and the

Piceance Basin Lineament Distribution
1 Degree Bins (SLAR IMAGERY)

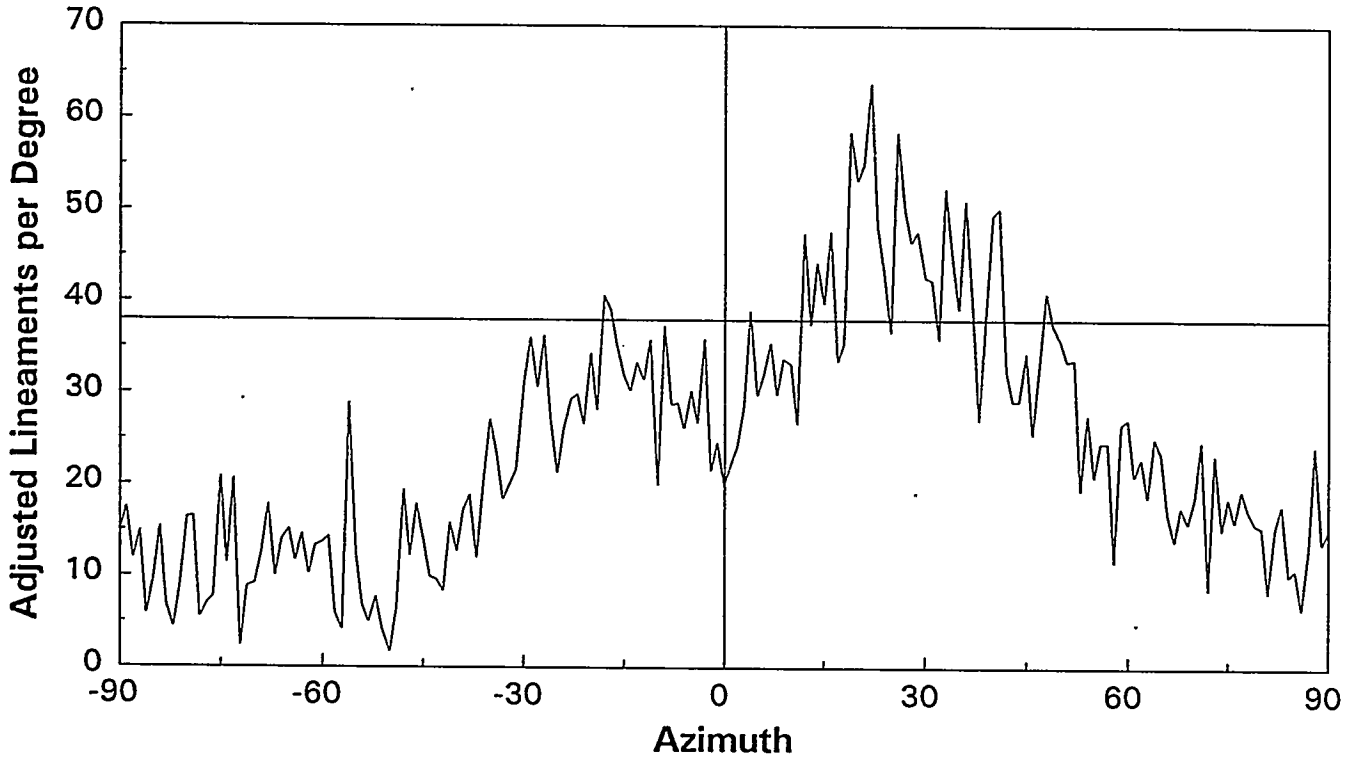

Figure 13

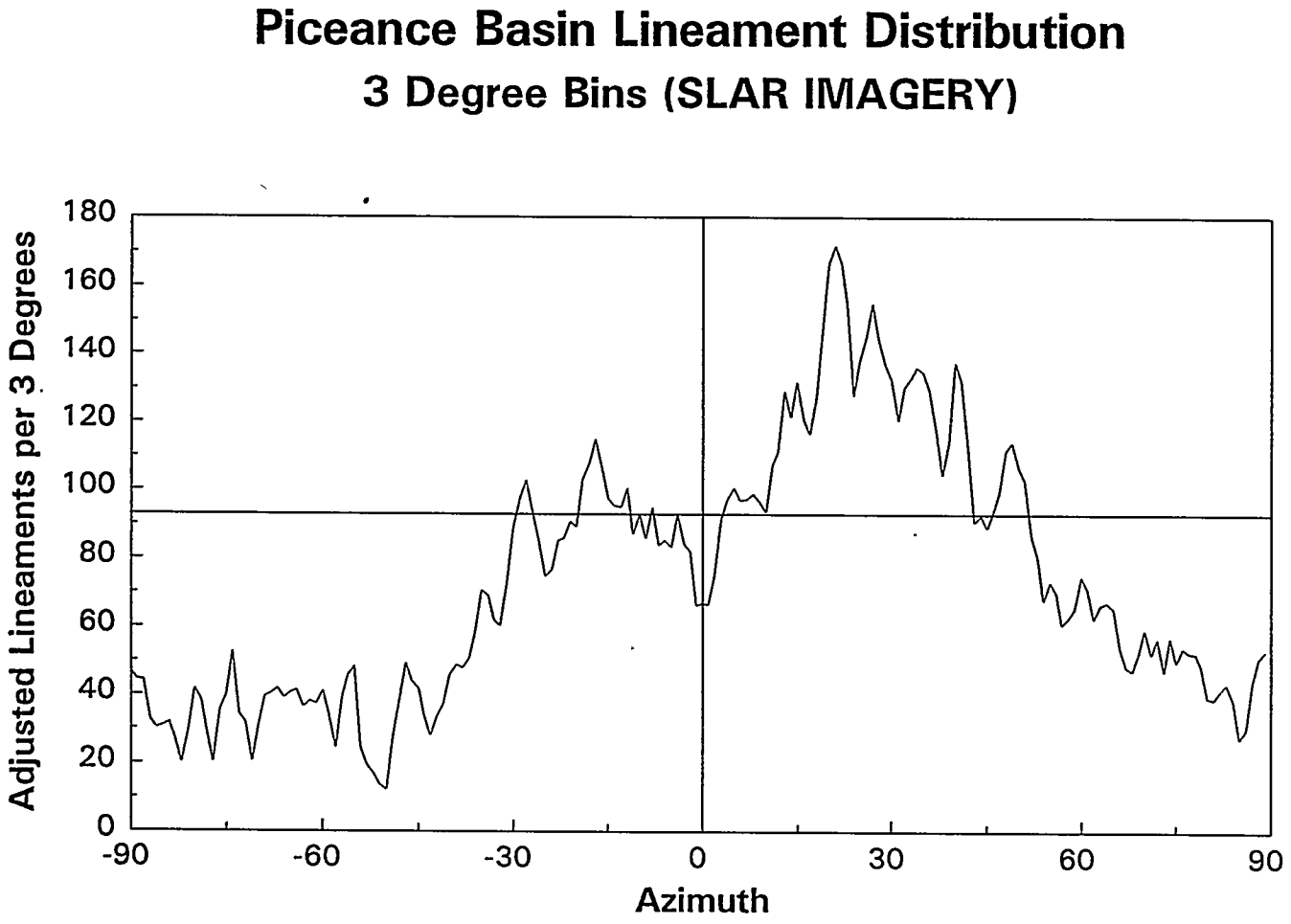
Piceance Basin Lineament Distribution
3 Degree Bins (SLAR IMAGERY)
Adjusted Lineaments per 3 Degrees
180
160
140
120
100
80
60
40
20
0
-90
-60
-30
0
30
60
90
Azimuth

Figure 14

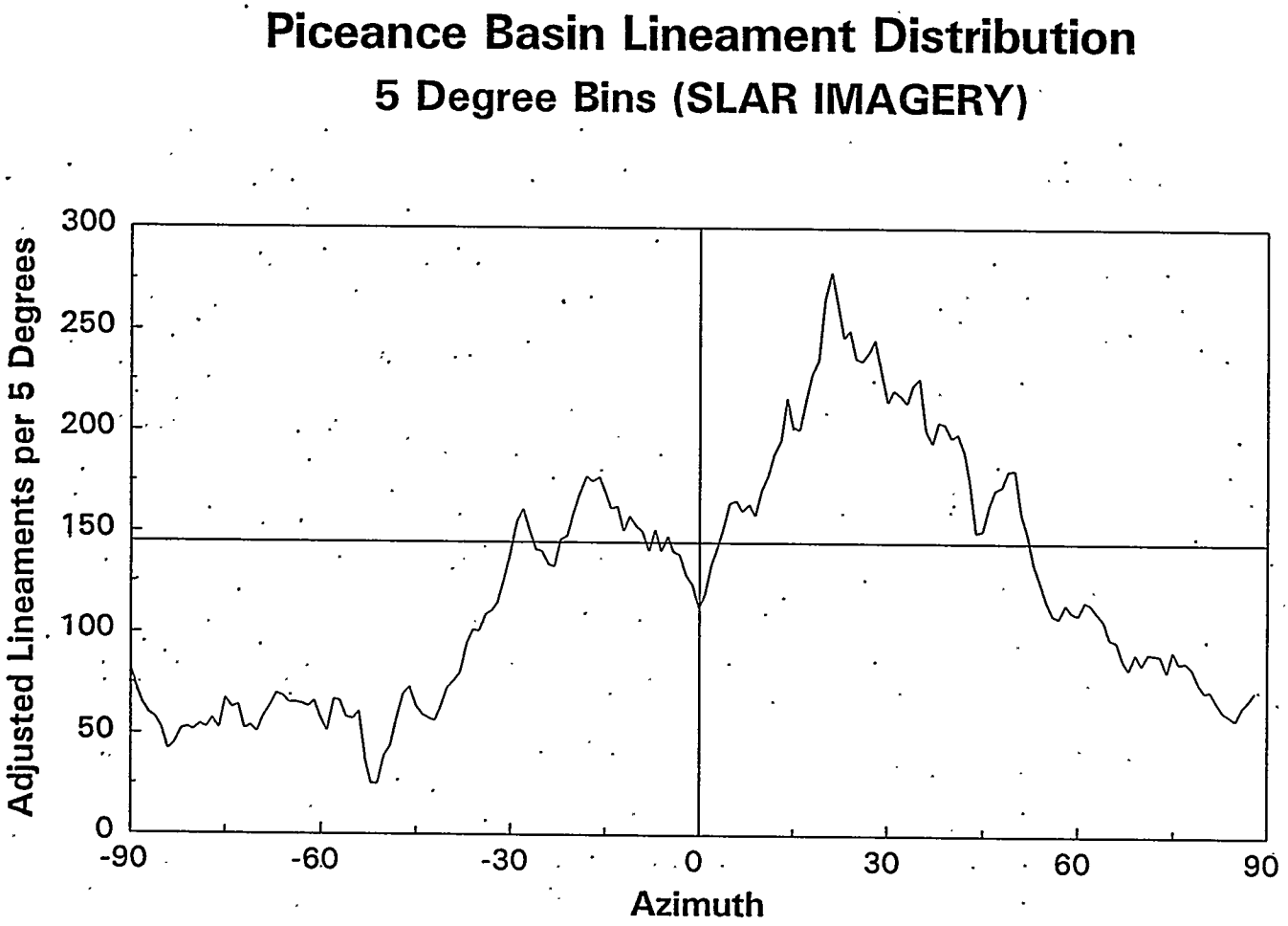
Piceance Basin Lineament Distribution
5 Degree Bins (SLAR IMAGERY)
Adjusted Lineaments per 5 Degrees
300
250
200
150
100
50
0
-90
-60
-30
0
30
60
90
Azimuth

Figure 15

OVERLAY OF ROLLINS STRUCTURE MAP ON RESIDUAL MAGNETICS PICEANCE BASIN

NOTE: COLOR IMAGE DOES NOT REPRODUCE CLEARLY IN BLACK & WHITE

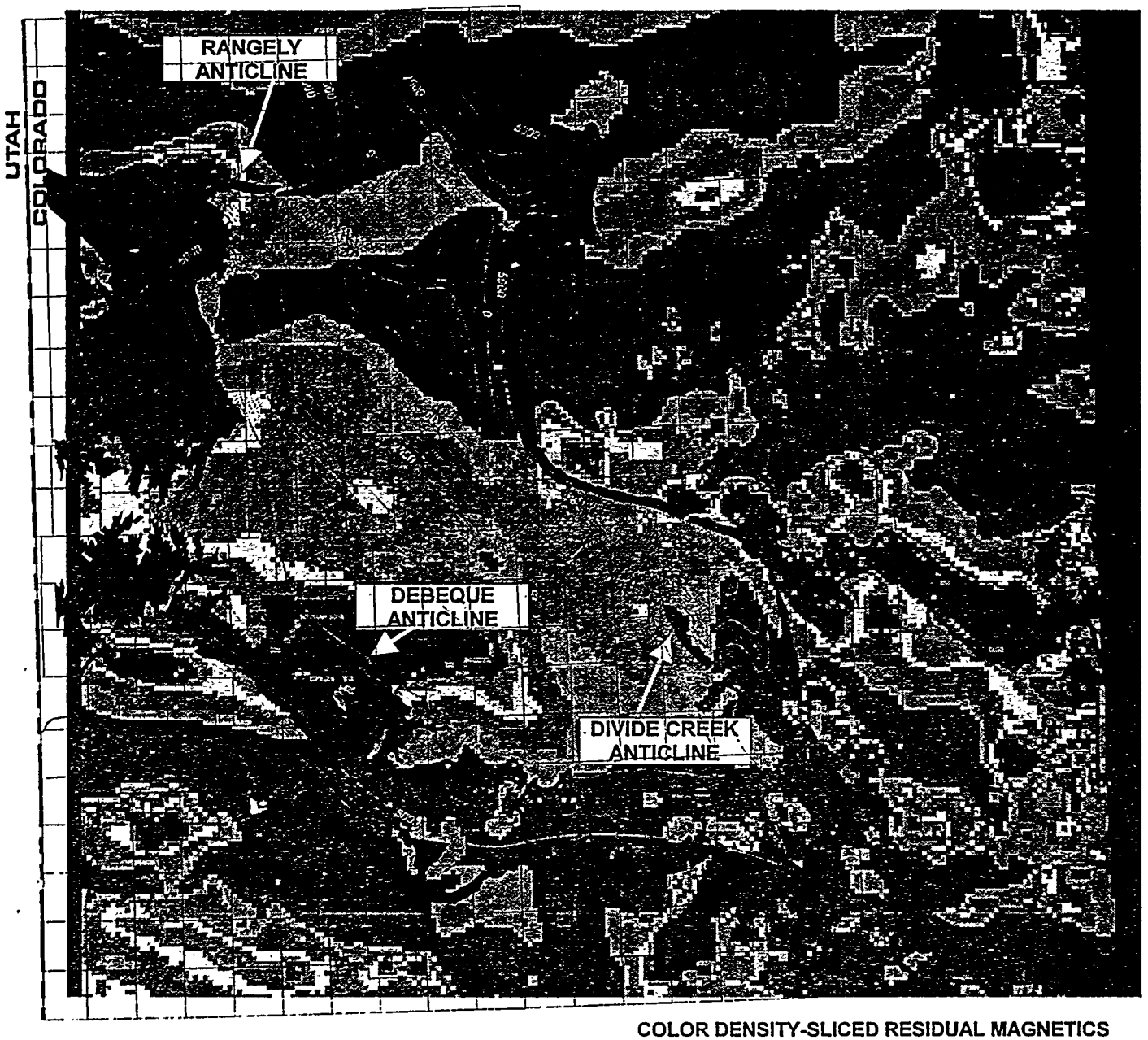

COLOR DENSITY-SLICED RESIDUAL MAGNETICS
COLOR CONTOUR INTERVAL EQUALS 68 GAMMA
DIGITAL DATA FROM GRAUCH & PLESHA, 1989

Figure 16

NW-trending feature along the trend of the Divide Creek Anticline. The Rangely Anticline also possesses a strong E/W magnetic signature parallel to its axis.

The second magnetic data image is a three-dimensional mesh diagram illustrating the three-dimensional aspect of the data (Figure 17). The basin margins are overlain on this image to provide a reference system. This image is a three dimensional image from which the horizontal density slice shown previously was generated. This image presents the three-dimensional variation across the basin in a striking fashion. Large positive total field magnetic potential anomalies are associated with the Debeque, Douglas Creek and Rangely anticlines. It is difficult to completely recognize many of the more subtle structural features on this image because of the coarse sampling grid (3 mile spacing on E/W flightlines with 6 mile N/S ties). This coarseness is also evident on the color depth slice (Figure 18). The aeromagnetic fly-over being flown by World Geoscience (an ARI Subcontractor on this project) in October 1994 will greatly decrease the grid spacing by using 0.4 kilometer N/S flightlines with one kilometer E/W ties. This tightened grid will greatly enhance the resolution of the survey and will permit more detailed interpretation of the regional features.

The third image is a three-dimensional structural image of the top of the Rollins sandstone for the basin (Figure 18). This image best illustrates the subsurface (basement?) control on structures developed in the overlying stratigraphic column. The image clearly depicts the profound structural variation from the outcrop on the eastern basin margin (Grand Hogback) to the basin center. It is clear from this image that the eastern margin of the basin has been much more intensely deformed by tectonic influences. The Debeque, Douglas Creek, and unnamed (hereafter designated Bull Creek Anticline) anticlines that lie along the western margin of the basin are much more subtle using the vertical scale incorporated into the image. Additional future research in remote sensing image analysis will involve detailed lineament analysis of the magnetic, TM, SLAR, and aerial photography from the basin. Statistical analysis of the interpreted linear features will allow much greater information to be gained about subsurface structure. From this information, placed into a tectonic framework, we will be able to better predict subsurface zones of more intense fracturing and its effect on producibility of

THREE-DIMENSIONAL REPRESENTATION OF AEROMAGNETIC TOTAL FIELD RESIDUALS PICEANCE BASIN, WESTERN COLORADO

FIGURE 17

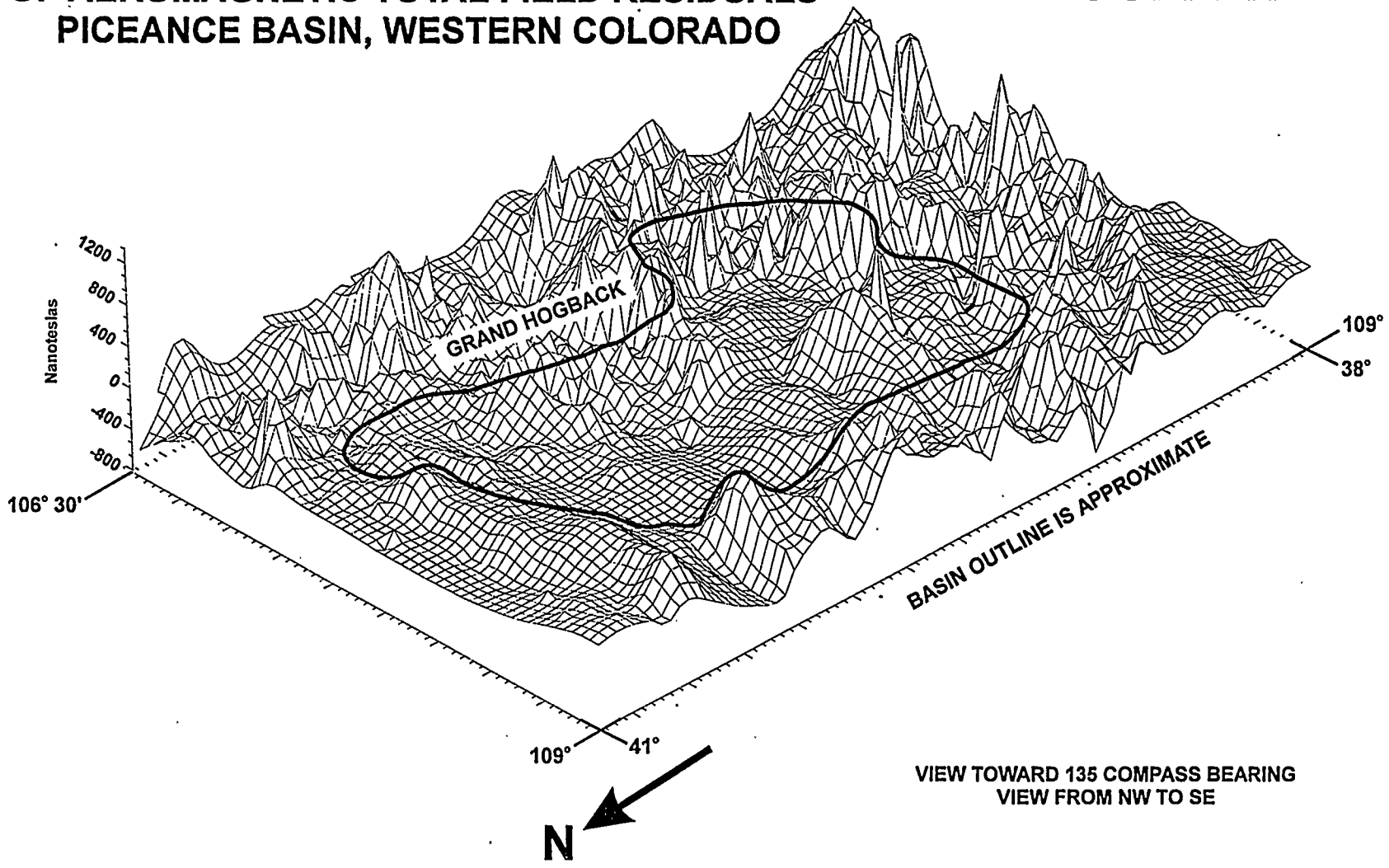

VIEW TOWARD 135 COMPASS BEARING
VIEW FROM NW TO SE

THREE-DIMENSIONAL SURFACE OF TOP ROLLINS SANDSTONE
PICEANCE BASIN, WESTERN COLORADO

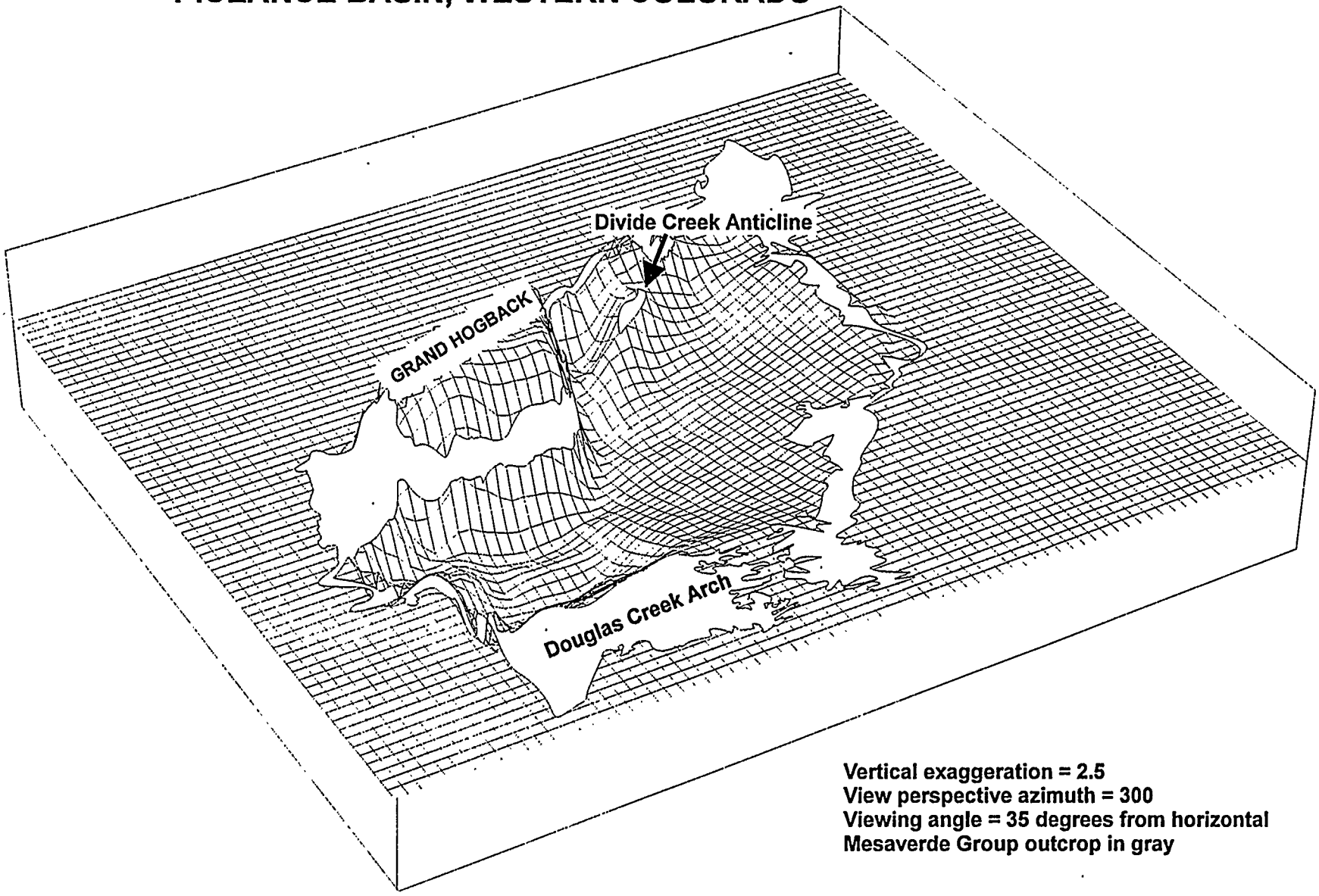

Vertical exaggeration = 2.5
View perspective azimuth = 300
Viewing angle = 35 degrees from horizontal
Mesaverde Group outcrop in gray

FIGURE 18

fractured reservoirs in the Piceance Basin.

FRACTURED RESERVOIR ANALYSIS
PARACHUTE AND RULISON FIELDS: GEOLOGY AND PRODUCTION

Introduction

The framework provided by interpretation of remote sensing imagery requires some means of verification to insure that large-scale linear features do indeed correspond to fractured reservoir conditions. To assess the potential of fractured reservoirs, production trends and detailed regional structure were examined in Parachute and Rulison fields to determine the relationship between production and structure. This section represents an abbreviated geologic and production synthesis of Parachute and Rulison fields (see Figure 19 for field locations). Both fields produce gas from the Tertiary-age Wasatch Formation, the Cretaceous-age Williams Fork, and the underlying Cretaceous-age Iles Formation. In these zones, gas is trapped in structurally enhanced stratigraphic traps. A large percentage of Williams Fork gas is produced from fluvial sand channels, and from thick coals in the Cameo Coal section located below the fluvial interval. Limited production (approximately three wells) also comes from marine sands in the Cozzette-Corcoran sandstones (Iles Formation). Significant production is also sourced from Wasatch wells in Rulison and Parachute fields that typically target the fluvial "G" sand.

The primary objective of this study is to understand the relationship between production trends in the two fields and regional structure, most notably the influence of structural trends on subsurface permeability and reservoir productivity.

Reservoir Stratigraphy

The producing zones in the stratigraphy of the Rulison and Parachute fields can be dissected into three primary reservoir horizons. The youngest and stratigraphically highest reservoirs are Wasatch fluvial sandstones. Most wells producing from the Wasatch have targeted

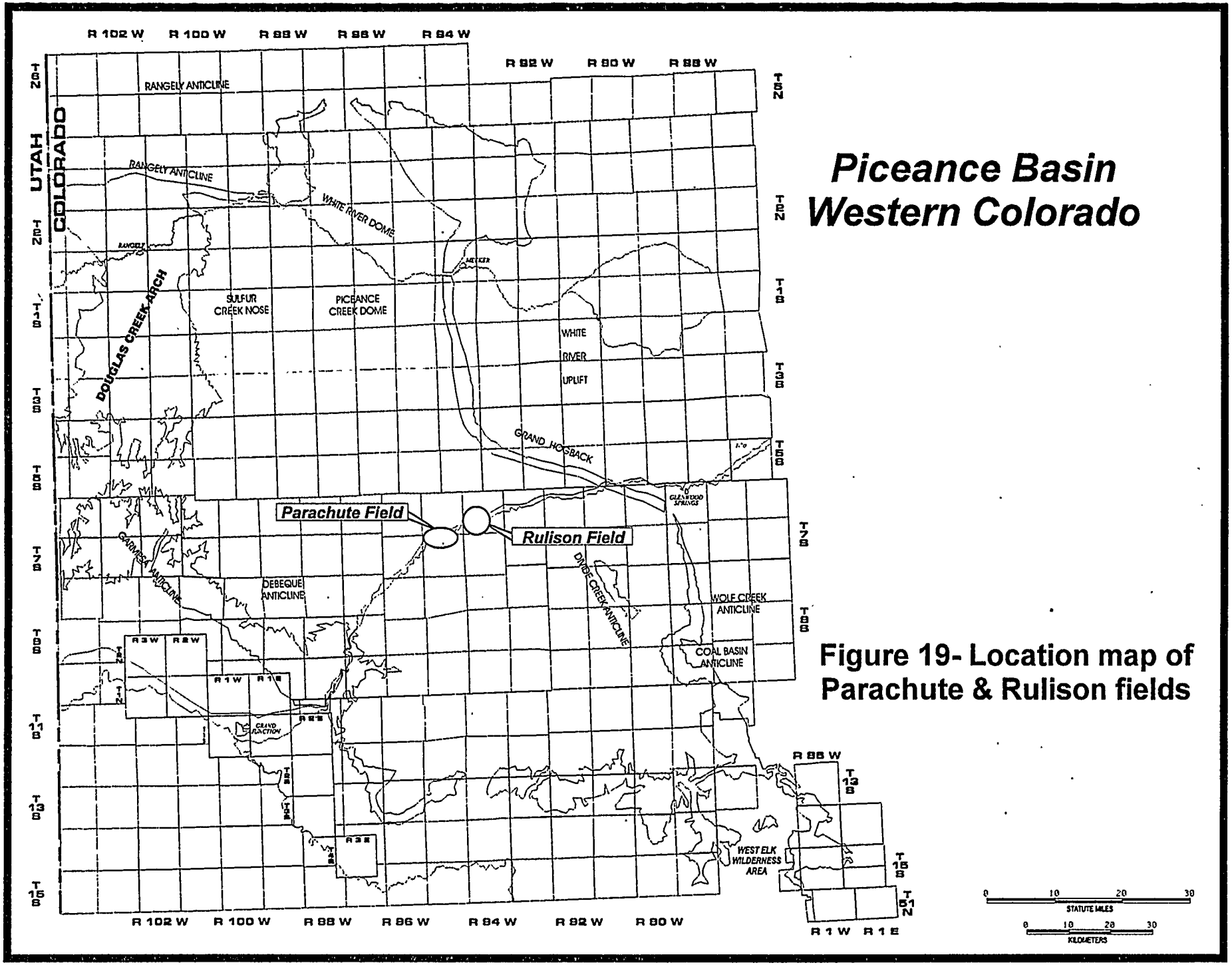

Figure 19- Location map of Parachute & Rulison fields

the "G" sand, a fluvial sand of unknown lateral extent. Underlying the Wasatch are thicker sands of the Cretaceous-age Williams Fork Formation. Most successful Williams Fork wells produce from fluvial sand channels. Extensive research at the MWX site in Rulison field demonstrated that the widths of these sand channels (approximately 300-500' wide, 20-50' thick; Lorenz, 1985) are significantly less than regulated well spacing. Recently, with new field rules (80 acre spacing, 2/94), additional production should be achieved from these lenticular, isolated channel sand reservoirs.

In the Piceance Basin, reservoir characteristics are directly related to depositional environment. In the Iles Formation, shallow marine, shoreline deposits are composed of homogeneous, widespread blanket-type sandstones possessing submicrodarcy permeability. Similar clean sands are found within fluvial channels and in the paludal (coal-bearing) interval of the Williams Fork Formation. These fluvial and paludal sands, especially where fractured, represent the best exploration targets. However, the delta plain, distributary channels, and paludal zones are generally more complex targets because of the anastamosing, discontinuous nature of the reservoir. The complexity is further magnified by the complex internal structure of the reservoir sediments. These latter reservoirs contain abundant laminated zones, shale breaks, and complex diagenetic relationships that make accurate reservoir characterization a difficult task. However, the paludal zones are typically more permeable and contain larger fractures (but more widely spaced) due to the mechanical anisotropy resulting from coal compaction, and from more complex diagenetic effects produced by coalbed-sourced fluids.

Limited production is also sourced from the marine sediments composing the Cozzette-Corcoran lying immediately underneath the Williams Fork Formation. In general, these sediments prograde to the southeast and have an internal shingled geometry typical of a transgressive systems tract. Curiously, very few mapped sequences in the southern Piceance Basin appear to possess highstand systems tracts. The reason for this is presently unclear. To distinguish between limited marine-sourced production in the Cozzette-Corcoran (Iles Formation) and the dominant production derived from the overlying fluvial Williams Fork Formation, Cozzette-Corcoran production has been ascribed to the Iles Formation (top Iles Formation

corresponds to Rollins Sandstone top) while Cameo Coal and upper Mesaverde Group production are ascribed to the Williams Fork Formation. This usage and differentiation differ from reporting conventions used by commercial production databases that place Cozzette-Corcoran production within the Mesaverde Group. The latter usage is confusing because it gives exaggerated importance to Cozzette-Corcoran marine-sourced production because of the large amounts of commingled production from overlying fluvial section of the Mesaverde Group (Williams Fork Formation) produced from the same wellbore. Because of the significant differences in production characteristics and limited commercial success of wells in the Cozzette-Corcoran compared to those well completed in the Williams Fork Formation, these two producing intervals should be kept separate. This separation also better corresponds with existing stratigraphic nomenclature for the Piceance Basin and the provenance and depositional environment of the sediments responsible for reservoir quality.

Regional Structure and Tectonics

Available seismic data integrated with ancillary wellbore data in the southern Piceance Basin clearly image the geometry of subsurface structure and the complex deformation history of the basin. A published E/W seismic line through Parachute and Rulison fields has been interpreted by Waechter and Johnson (1986). Figure 20 is a portion of the seismic line interpreted by Waechter and Johnson. It is important to note that the primary focus of these authors was documentation of Paleozoic structural features. They did not address the geometry of Laramide contractional structures that strongly overprint the older extensional features. Because of this focus, an interpretation of Laramide contractional features has been added to this section. It is essential not to neglect the strong Laramide overprint superimposed on the older extensional horst and graben system.

As shown by Waechter and Johnson (1986), an NW-trending, Pennsylvanian-age horst block is present underneath Rulison field. This block lies parallel to the Pennsylvanian-age tectonic grain, well documented in uplifted blocks flanking the margins of the Piceance Basin. During the deposition of the Eagle Valley Evaporite sequence during the Middle Pennsylvanian,

SEISMIC SECTION ACROSS PICEANCE BASIN

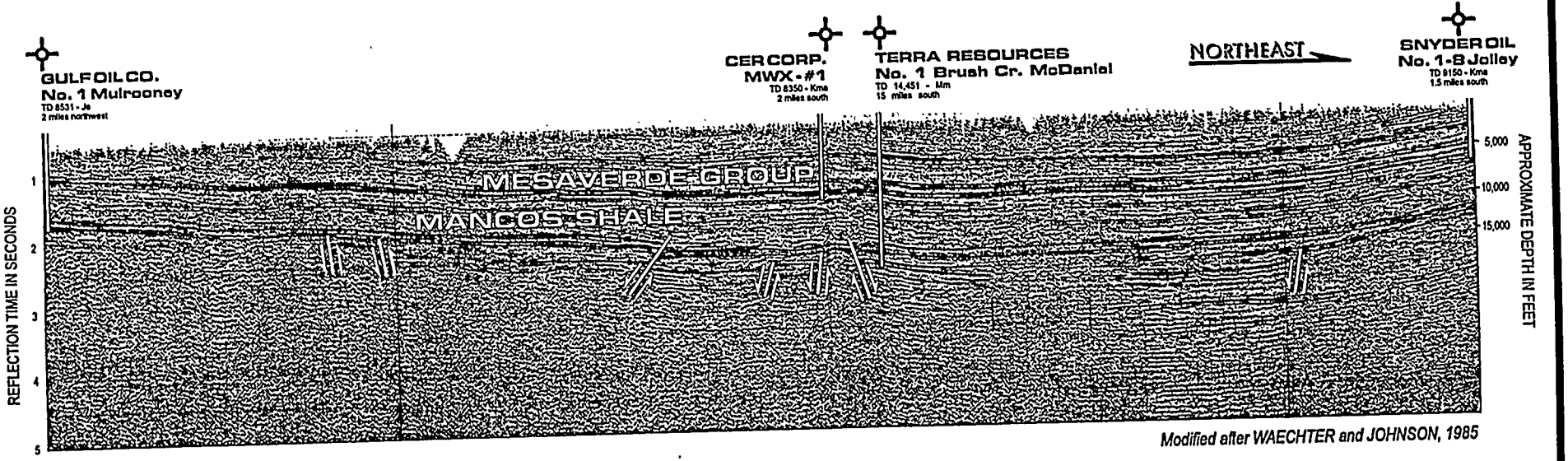

NOTE: *Some Pennsylvanian-Permian normal faults were reactivated during Laramide contraction as thrusts.*

FIGURE 20

it appears that evaporites were deposited in the graben trough located adjacent (to the east) of the horst block. Unfortunately, no drillholes have penetrated the sub-Cretaceous interval on the western margin of the horst block to verify the deep subsurface stratigraphy. It seems likely, given that the Rulison paleograben/horst system is located west of the main salt depocenter, that less voluminous salt was deposited in this area than has been recorded to the east and south of Rulison field.

In a process analogous to that described by Grout et al. (1991) for the Divide Creek and Wolf Creek anticlines, (located southeast of the Rulison area) the small anticline developed below Rulison field probably formed as a result of fault-bend folding as strata were thrust westward. Although the size of the Rulison structure is much smaller than the Wolf Creek and Divide Creek anticlines, the likely presence of an evaporite-hosted decollement, in conjunction with a reactivated fault on the horst block eastern flank suggests a similar process of development. If the evaporite section pinches out against the horst block, the absence of the salt combined with the buttress-like influence of more mechanically rigid Precambrian basement in the horst, would impede lateral thrust propagation and would cause the thrust to ramp up-section. The amount of thrust displacement is small on this structure and work is progress is attempting to quantify the shortening associated with this structure and its subsurface geometry.

Rulison-Parachute Structure Map (Top Rollins Datum)

Because of the fractured reservoir behavior observed in Rulison and Parachute fields and the complex tectonic evolution described above, understanding of subsurface structure is critical to our understanding of production trends and the fracture permeability that creates them. Previous models established for fracturing in Rulison field have suggested a complex fracture model involving overpressuring operating in conjunction with far-field differential stress (Lorenz et al., 1991). A central argument for this interpretation is the apparent absence of subsurface faults and flexures in the vicinity of Rulison field at the MWX site. At that time (early 1980's), little data from infill drilling or non-proprietary seismic data in Rulison field were available to adequately constrain subsurface stratal geometries. Figure 21 is a page-size map of the structure

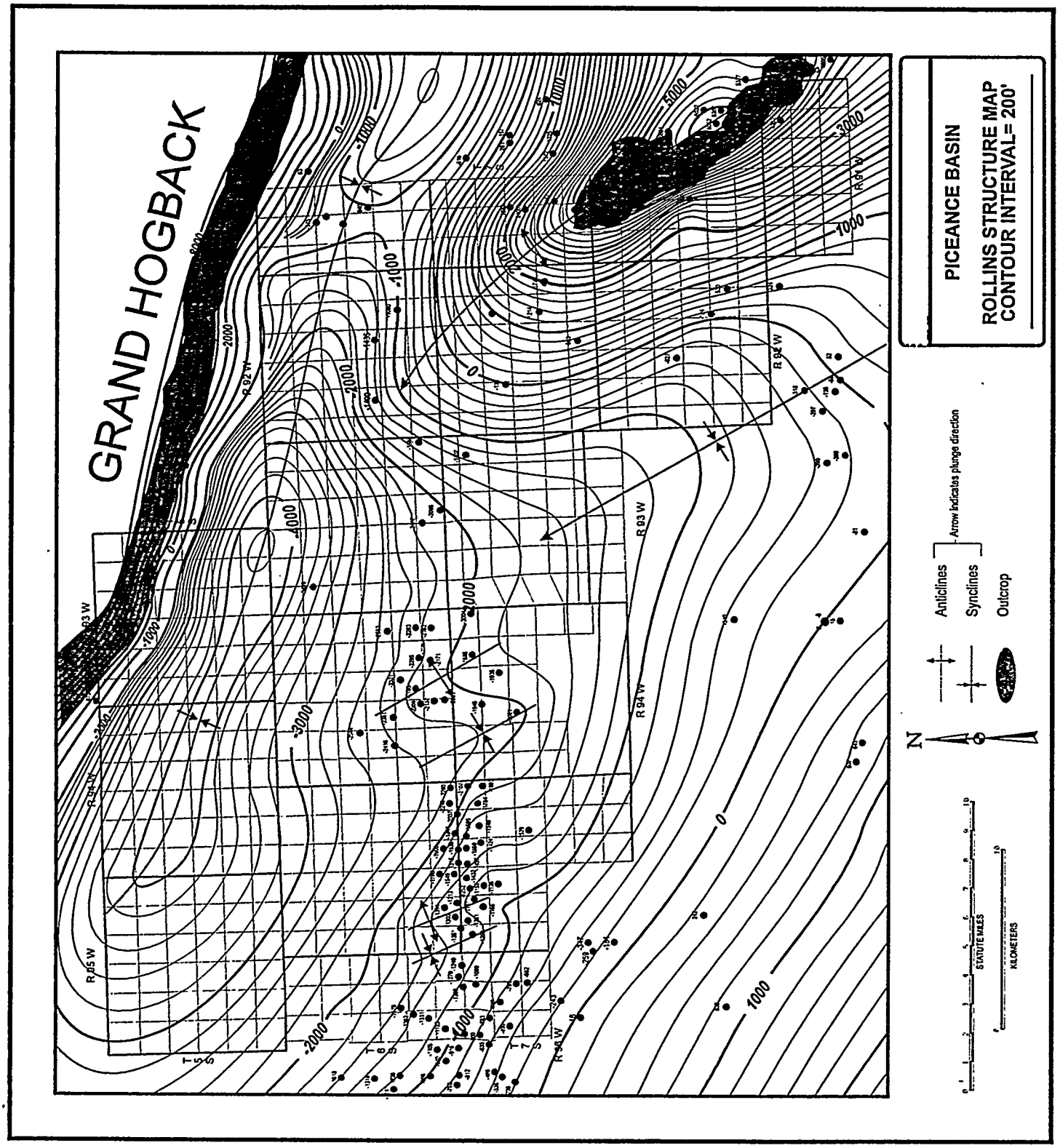

FIGURE 21-ROLLINS STRUCTURE

on the top of the Rollins Sandstone (top Iles Formation, base Williams Fork formation). This map clearly demonstrates that the structure at Parachute and Rulison fields is not a simple homocline. The area to the southeast of the Rulison area is the Divide Creek Anticline, a fault-propagation-fold structure that plunges to the northwest. The explanation for the northwestward plunge and dissipation of the Divide Creek fold is probably related to the termination and/or decreased displacement of a thrust fault in the fold core whose displacement dies out along-strike to the northwest. The termination of the thrust and related fold probably is an analogous geometry to the termination of smaller-scale thrusts into folds common in both the Appalachian and Alberta fold-and-thrust belt. These thrust terminations and related folds represent the source of the fractures common in the Rulison field. The thrust tip termination requires regional strain to be accommodated by internal deformation of the rock (i.e., fractures) because strain cannot be accommodated by additional thrust displacement, or by folding or other ductile processes.

Gas Field Characteristics

To better understand the geology and production history of the two fields, it is necessary to have some understanding of the development history of the field and the completion methods used by operators working in these two areas. Much of the information presented in this section is also applicable to other fields throughout the Piceance Basin.

Rulison Field

Discovery Well

The first well in Rulison field was completed in 1944 but was abandoned as uneconomic. The Williams Fork production that has historically dominated the field was discovered in 1958 with the completion of the Southern Union Juhan Fee #1 (6S, 94W, Sec 26) possessing an initial potential of 1937 Mcfg/day.

The Wasatch discovery well was the Carter & Carter, J.T. Juhan #2 (6S, 94W, Sec 34) that tested an initial potential of 1190 Mcfg/day. Formal field designation apparently did not occur until the early 1970's although historical records are ambiguous.

Logging Analyses

Most log suites contain dual induction logs and neutron density logs. Some Spontaneous Potential, dipmeter, and sonic logs were also run. Most logs are run from casing to total depth. Neutron density logs are preferable for identification of coals because of the low gamma response (clean) and low density of the coal seams. Coal seam thickness can also be evaluated by the size of the breakout observed in the caliper track of a gamma log. Thick coals show a larger breakout or greater rugosity in the well bore compared to thinner seams.

Reservoir Data and Field Rules

Wasatch. Well spacing for Wasatch wells is 160 acres. Average porosity from core is 6%, average permeability is 0.06-.25 md. Initial field pressure is depth-dependent. Water saturation ranges from 25-75%. Estimated productive area is 8000 acres.

Williams Fork. Well spacing in Rulison field is 320 and 640 acres according to the Colorado State Oil and Gas Commission. Recent (2/94) successful petitioning by Barrett Resources has changed the minimum spacing to 80 acres. These well spacings represent the most effective drainage density according to reservoir analyses conducted by Mercer and Frohne (1986) for the Rulison field. The average permeability (*sans* fractures?) is 0.54 md from drawdown tests in the Williams Fork. Average porosity is 8-16% from logs. The initial field pressure was 2400-2900 psi. Water saturation ranges from 30-100% from logs. The estimated productive area is approximately 8000 acres. Estimated primary recovery is approximately 2 Bcf/section.

Drilling and Completion Practices

A significant evolution of drilling practices has occurred in the Rulison field from 1961 until today. Early (1982 and older) techniques involved air drilling through the Wasatch Formation and logging of this interval followed by the setting of casing approximately 100 feet into the underlying Williams Fork Formation where the first gas show is typically encountered. This technique minimized formation damage to the clays common throughout the Wasatch and upper Williams Fork. Wells that were drilled deeper through the Williams Fork used KCl-based mud and were typically completed approximately 200-300 feet into the Williams Fork, immediately prior to penetration of the coal seams. Penetration into the Cameo Coal interval while air drilling frequently caused stuck tools and resulted in hole abandonment. Air drilling through the Williams Fork also attempted to minimize damage to fractured intervals. Prior to 1982, wells were cased, cemented and hydraulically stimulated (fractured) in two or three stages over approximately a 1000 foot interval. Most wells used 25,000 to 35,000 gallons of KCl water and 80,000-100,000 pounds of sand for the fracture treatments. Some success was achieved using nitrogen and carbon dioxide as flushing agents. Completion of thick, multiple-pay intervals increased from 1979 to 1982 with a corresponding decrease in the formation penetration depth of the fracture treatment. Completion intervals increased to greater than 1200 feet with fracture treatments below 150,000 lbs. of sand per well. This strategy has since been abandoned.

Significant gas shows in the overpressured lower Cameo Coal section of the Rulison field preclude air drilling. Because of the gas shows and difficulties in well control, mud-based drilling is preferred. More recently, drilling through the Wasatch uses freshwater (2% KCl) polymer gel-mud that inhibits swelling of the shale. Typically, 1000 gallons of acid are used to clean up perforations. The range of fracture treatments in fluvial sands average 300,000 lbs. of sand and 100,000 gallons of 2% KCl water-gel fluid. Barrett Resources has also performed dual completions in some wells to maximize tax advantages for tight gas sands. After initial coalbed completion, Barrett puts a packer containing a plug at the top of the coal interval and moves uphole to complete the sandstone interval. After the sandstone interval is completed, a

thin tube is lowered downhole to knock out the packer plug. Coalbed gas is produced in the inner tubing and sandstone gas is collected in the wellbore casing. Each flow stream is metered separately for Section 29 tax credits and combined in the final gathering system (Reinecke et al., 1991).

Rulison Field Production Trends

Figures 22 and 23 illustrate the completion target history of Rulison field. Most early wells (1959-1979, Figure 22) were completed in either the Williams Fork or the Wasatch. Most wells were completed in the Williams Fork. More recently, (1979-1993, Figure 23) a greater percentage of Wasatch wells were completed followed by Williams Fork targets. In addition to these reservoirs, the play expanded to include the Cozzette-Corcoran marine sands and the Cameo Coal zones. Upon completion of the MWX test program in 1982 that demonstrated the possibility of producible gas from the Cozzette Sandstone interval of the Iles Formation, new drilling efforts concentrated on delineating production behavior from this zone. Little commercial success in the Cozzette-Corcoran marine sands has yet been realized in Rulison field due to high water production and a decreasing gas flow over time. The majority of gas produced in the Rulison field comes from Williams Fork completions, although the amount produced from the Wasatch Formation is similar in magnitude (see Figure 24). The relative paucity of Cameo Coal production reflects the relatively recent development of the Cameo Coal play in the Rulison field. Plugging of perforations by coal fines has plagued many Cameo Coal completion programs in both Rulison and Parachute fields.

The actual production derived from each reservoir is important to drilling economics. The cumulative amount of gas produced in the Rulison field is more nearly equivalent between the Wasatch and Williams Fork Formation. In Rulison field, slightly fewer Williams Fork wells have produced approximately 2 Bcf more gas than wells completed in the Wasatch.

The longevity of wells completed in the different reservoir horizons over time is an important element in understanding the evolution of the field. Figure 25 shows the number of

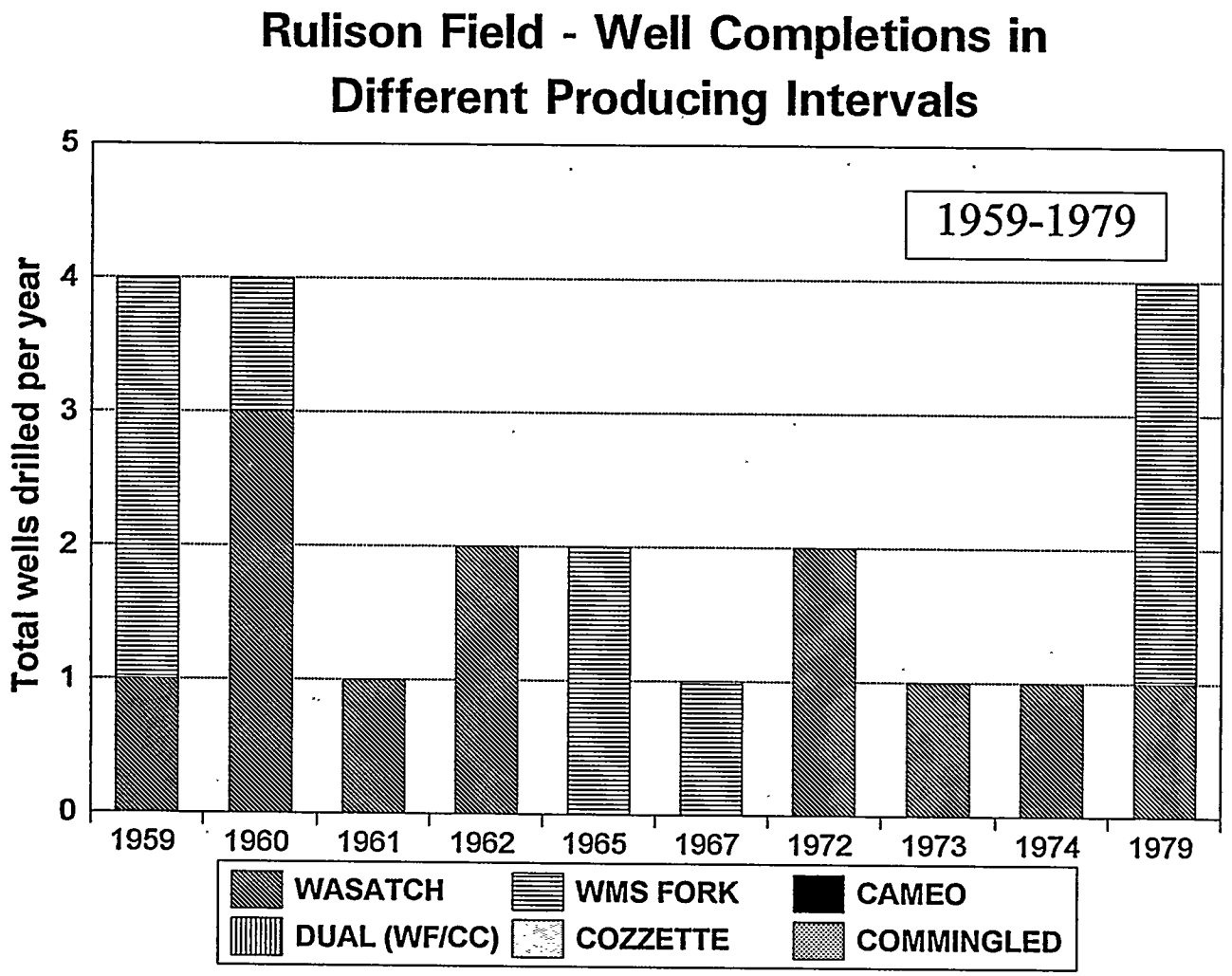

Figure 22 - Rulison Field well completions in different reservoir intervals for the period 1959 - 1979.

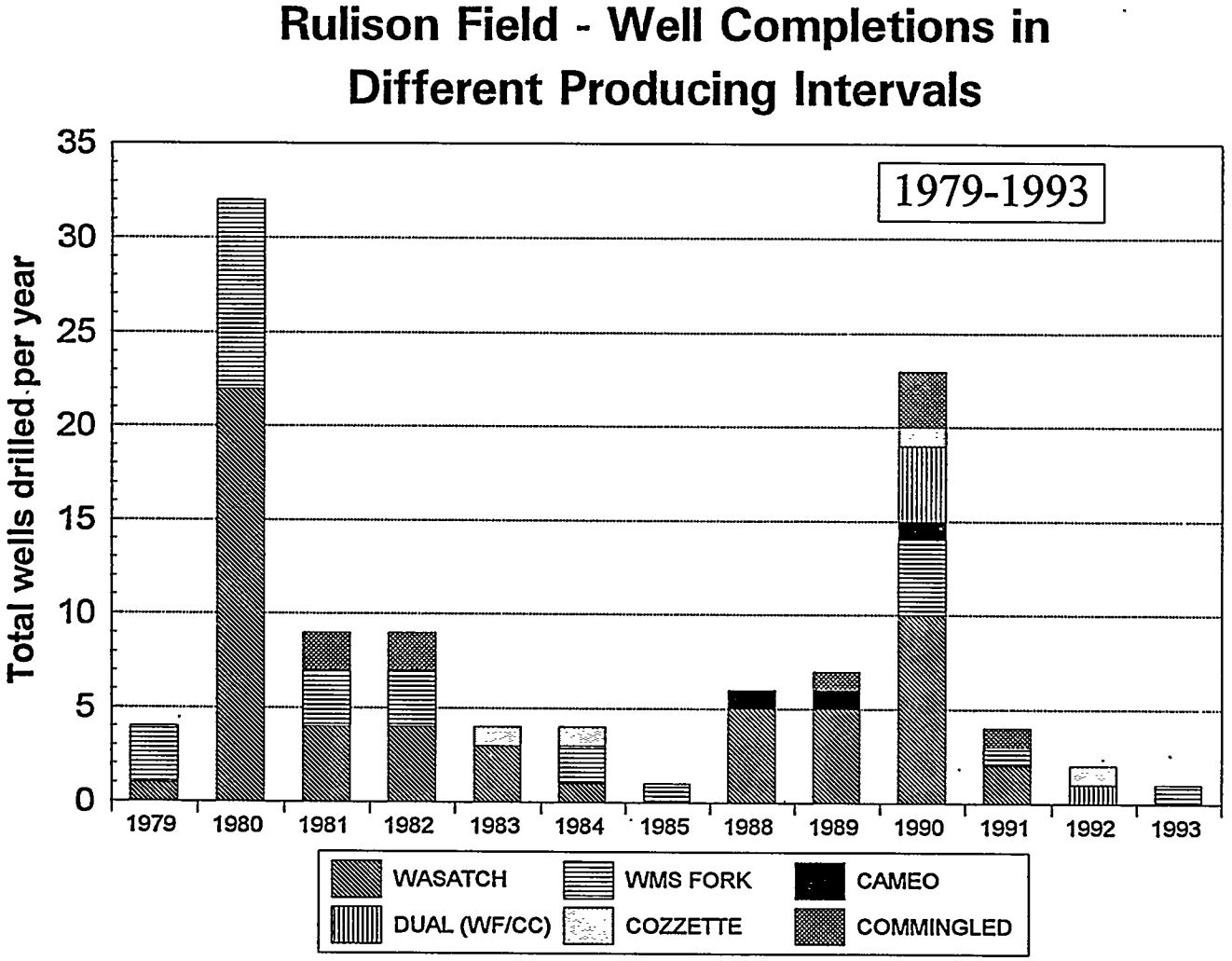

Figure 23 - Rulison Field well completions in different reservoir intervals for the period 1979 - 1993.

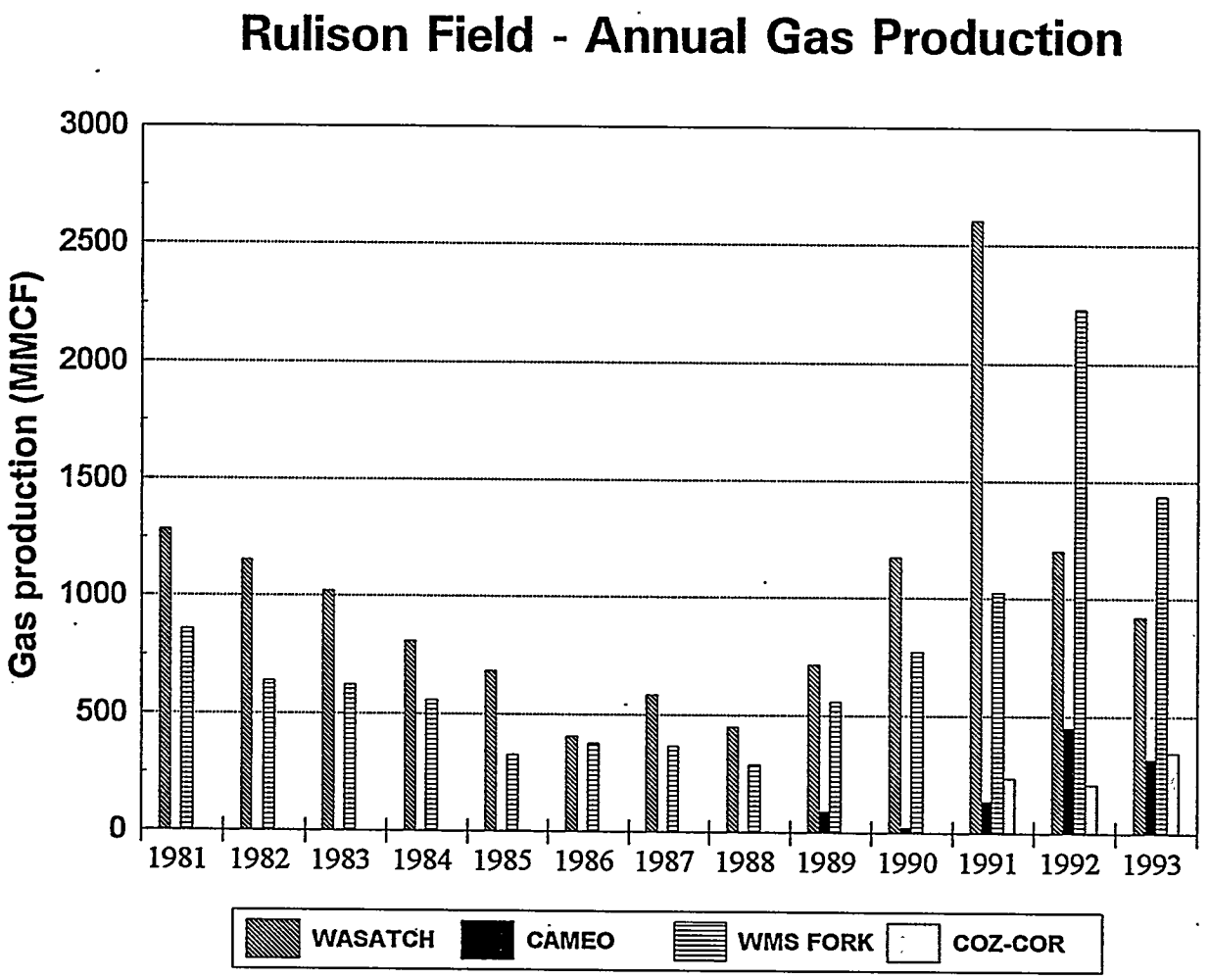

Figure 24 - Rulison Field annual gas production by reservoir

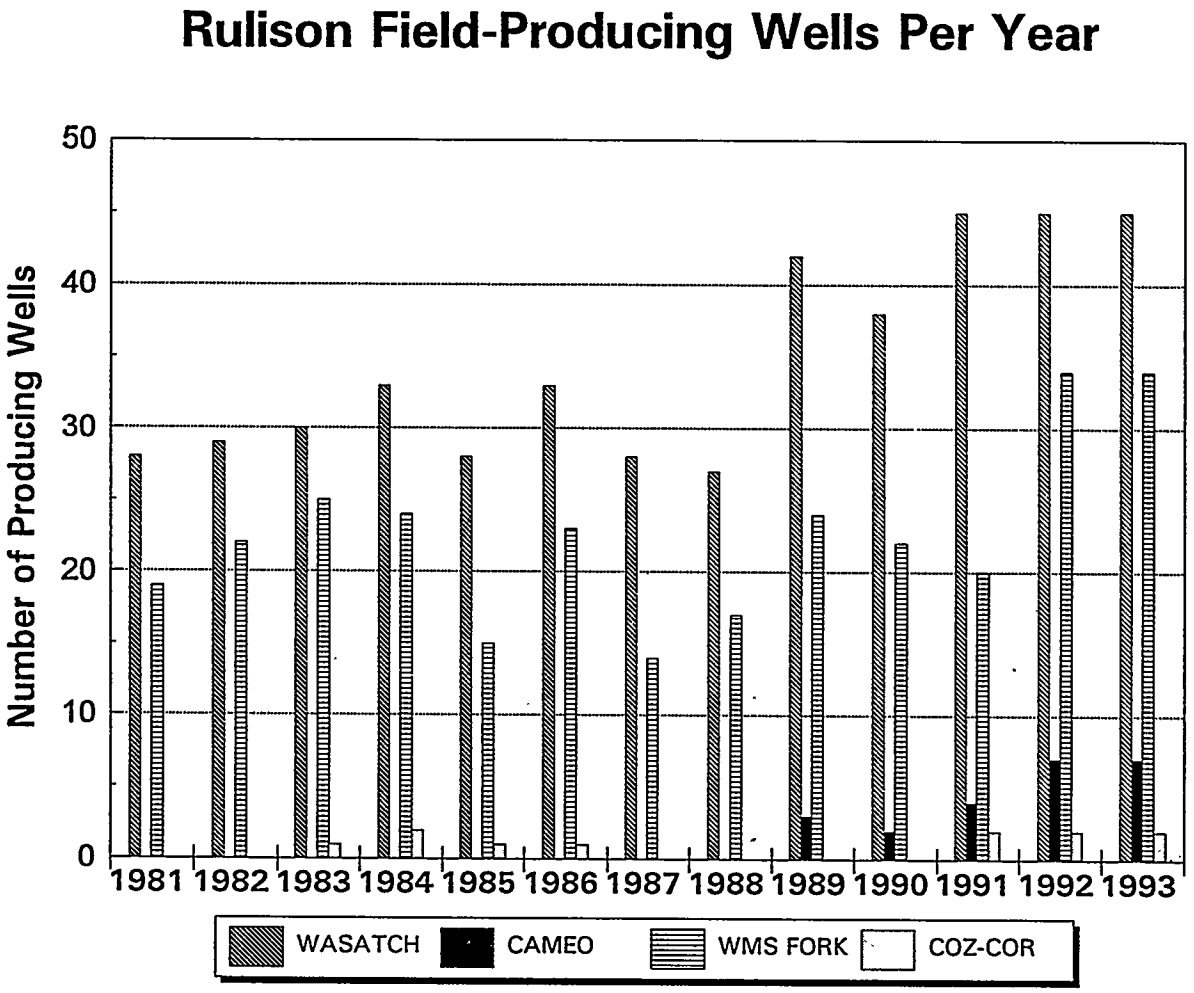

Figure 25 - Number of Rulison Field producing wells over time.

producing wells per year for each reservoir horizon. Note that only Williams Fork and Wasatch completions dominate the early completion history. Only in the late 1980's, drilling interest was shown in the Cameo Coal and deeper plays. Figure 25 demonstrates that Wasatch production dominated the early production in the Rulison field. It is worth noting that the number of Williams Fork and Wasatch wells today is more nearly equal.

Parachute Field

Discovery Well

Parachute field was discovered in 1985 with the drilling of the Barrett Grand Valley W-1 (6S 95W Sec. 33) completed in the Wasatch Formation. This well showed an initial potential of 3200 Mcfgpd and no water. The first Williams Fork production was achieved in the Northwest Exploration Battlement #1 well completed in 1982. This well possessed an initial potential of 205 Mcfgpd and 29 Bwpd. The well was originally assigned to the Rulison field but its location is now encompassed by the Parachute field boundaries for Williams Fork production.

Logging Analyses

Most log suites contain dual induction logs, spontaneous potential logs, and neutron density logs. Some rare sonic logs and dipmeter logs are also run. Most logs are run from casing to total depth.

Reservoir Data and Field Rules

Little published reservoir data is presently available for the Parachute field.

Wasatch. Well spacing for Wasatch wells is 160 acres.

Williams Fork. Well spacing in the Parachute field was initially established at 640 acres by the Colorado Oil and Gas Commission. These field rules were recently changed (2/94) by the Colorado Oil and Gas Commission. The present spacing is 80 acres.

Drilling and Completion Practices

All wells and drilling in the Parachute field are controlled by the sole operator, Barrett Resources. The drilling techniques used in the Parachute field are those adapted from the Grand Valley field located in the adjacent township to the west of the Parachute field. During Wasatch zone drilling operations, Barrett uses freshwater (2% KCl) polymer gel-mud that inhibits swelling of the shale. Significant gas shows in the overpressured lower coal section of the Parachute field precludes air drilling. Because of the overpressured conditions and gas shows, mud-based drilling is preferred. Normally, 1000 gallons of 7.5% acid are used to clean up perforations. Typical ranges of fracture treatments in fluvial sands average 300,000 lbs. of 20/40 sand and 40/70 sand and/or mesh-resin coated sand and 100,000 gallons of 2% KCl water-gel fluid. In general, two-three thousand barrels of gel are used. Limited application of nitrogen for fracture completions has been used. Barrett Resources has also performed dual completions in some wells to maximize tax advantages for tight gas sands. This technology was described earlier for the Rulison field.

Coal seams in the Cameo section are usually perforated at each seam. Preference is given to thin seams adjacent to thicker coal zones. Apparently fracture treatments of the thin coal zones propagate the induced fracture into adjacent sandstones where the proppant is better able to maintain an open fracture and reservoir transmissivity between under-or-overlying thicker, gas-saturated coal seams. Nearly all coal gas producing wells in Parachute field are dual completions using the methodology developed by Barrett Resources that was described previously in the drilling and completion practices section for Rulison field.

The innovative cavity completion that has so dramatically outperformed conventional hydraulic stimulation strategies in the San Juan Basin has not yet been attempted in the Cameo

Coal section in Parachute and Rulison fields.

Parachute Field Production Trends

Figure 26 shows the number of completions by reservoir horizon in the Parachute field over time. Initial completions were restricted to the Wasatch. Later, a large number of dual completions (Williams Fork and Cameo Coal) were performed, probably as a result of successful application of the technology in the Grand Valley field a year earlier.

The actual production derived from each reservoir is important to drilling economics. Figure 27 shows that the majority of gas production in the Parachute field is produced from the Wasatch Formation. This amount is significantly larger than the amount produced from the Williams Fork Most wells in the Parachute field are dual completions and produce from both the Williams Fork sands and the Cameo Coals. It is significant that the Cameo Coal in the Parachute field has produced nearly as much gas as the Williams Fork wells.

Spatial Trends In Production

Production Maps

Cumulative and maximum monthly production data were analyzed using data available from commercial vendors. The best Williams Fork well in Parachute field has produced 414 Mmcf of total production and is located in 6S 95W Section 33 (completed 1990). The best Williams Fork well in Rulison field has produced 1,022 Mmcf of total production and is located in 6S 94W Section 16 (completed 1980). The ten years of production history separating these two wells clearly indicates one of the problems of analyzing production data within Rulison field and comparing it to data from Parachute field and younger wells in the Rulison area.

Initial cumulative production maps were prepared from normalized data to remove potential biases created by differing ages of the wells. Data were normalized by dividing the

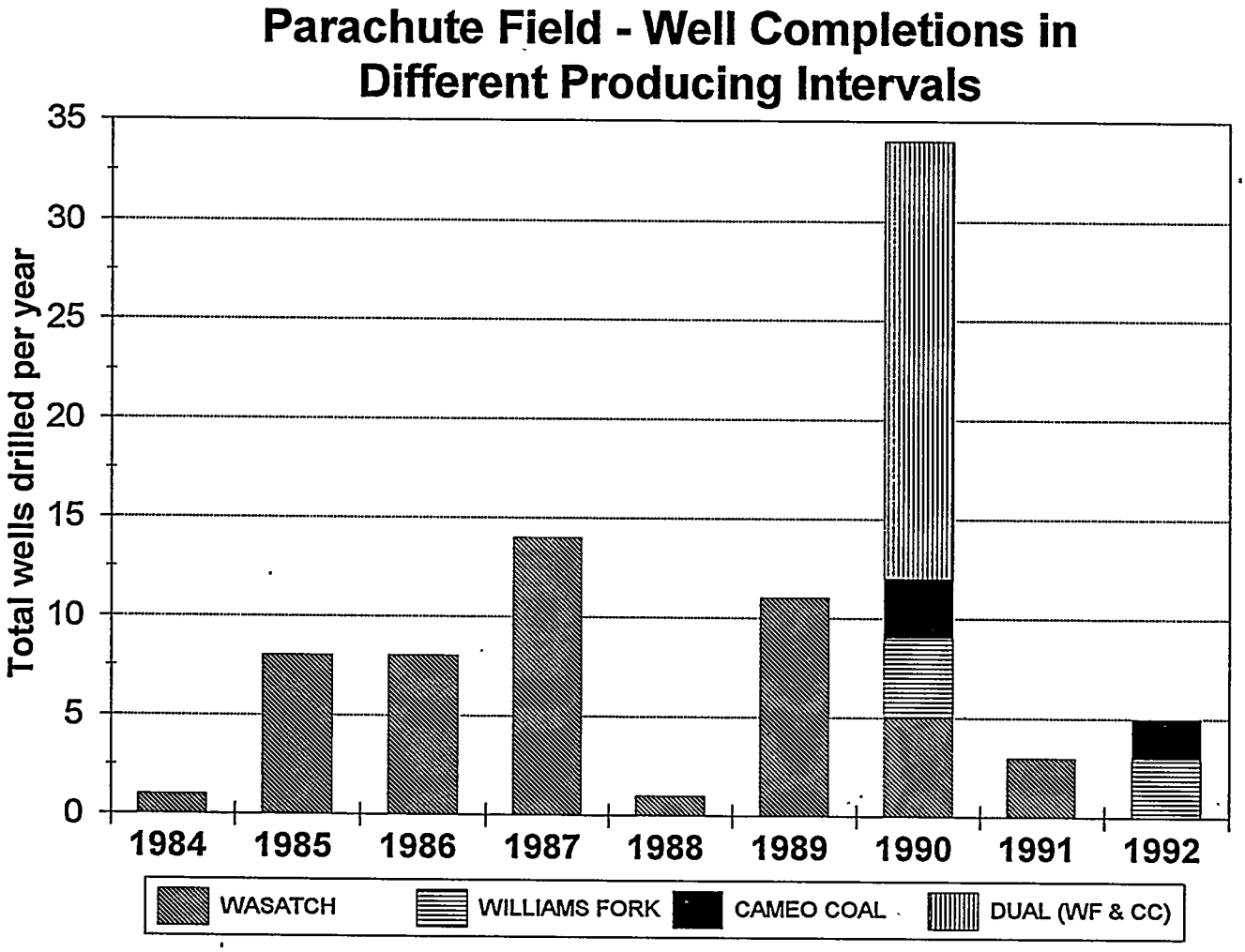

Figure 26 - Parachute Field, total wells drilled in each reservoir horizon over time.

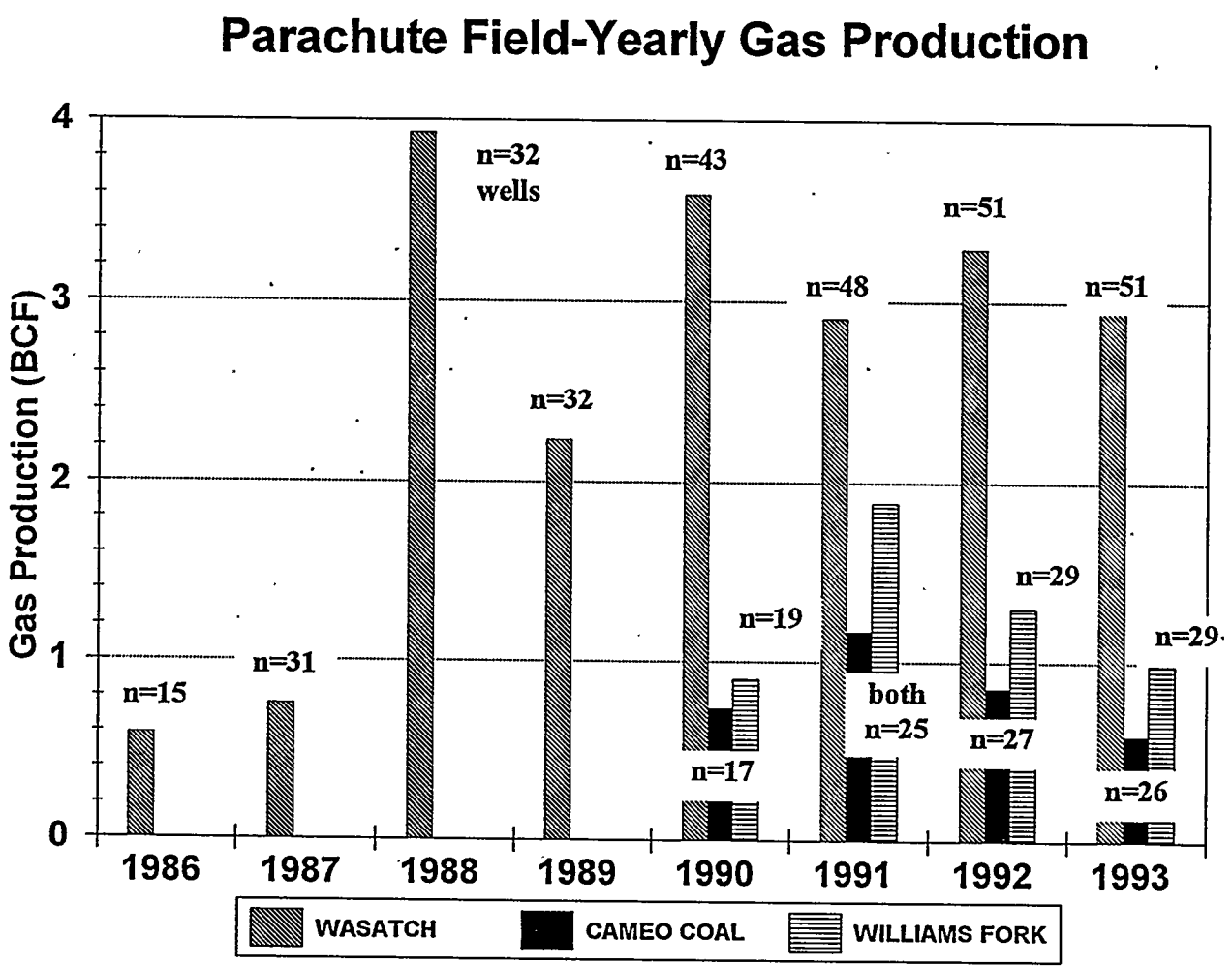
Parachute Field-Yearly Gas Production
Gas Production (BCF)
4
3
2
1
0
n=15
n=31
n=32
wells
n=32
n=43
n=17
n=19
n=48
both
n=25
n=51
n=27
n=29
n=51
n=26
n=29
1986
1987
1988
1989
1990
1991
1992
1993
WASATCH
CAMEO COAL
WILLIAMS FORK

Figure 27

cumulative amount of gas by the number of days of production. Some error in this normalization is introduced by including older wells (i.e. pre-1984) whose number of producing days per year are not available from commercial or public data sources. Because of the bias introduced using the cumulative production values for wells of widely disparate age, another parameter was chosen to represent production trends.

The most suitable parameter is the maximum monthly production reported during the life of the well. The use of this parameter minimizes problems associated with wellbore storage effects, post-completion stimulation fluid loading, and variable reporting histories of the wells. In addition, this number minimizes seasonal and market influences on production and better reflects the success of completion strategies. Most importantly, this number is readily available and easily computed using data available from commercial and regulatory sources. When using this approach, care must be taken to insure that no recompletions have been performed. Successful recompletions are generally easily recognizable by analysis of monthly gas production trends and review of readily available completion data. In general, sudden upward shifts in overall monthly production typically suggest some recompletion activity. Unsuccessful completions will generally not cause a significant shift in monthly production so that the effect of these failures on the maximum monthly production value is minimal. Recompletion failures are also documented by commercial and regulatory completion data.

A map of maximum monthly production for the area encompassing both Rulison and Parachute fields (Figure 28) has been contoured. A map of Parachute field Williams Fork production (see Figure 29 for enlarged map) shows trends approximately parallel to the river with two concentrations of higher production near the west end and center of the field. Cameo Coal production shows similar trends with greatest production lying in the central and eastern areas of the field (see enlarged map, Figure 30).

Rulison field shows a more diffuse concentration of good Williams Fork producers with most good wells concentrated in the northwest area of the field (see enlarged map, Figure 31). Several isolated high production wells are found in the southeast and southwest areas of the

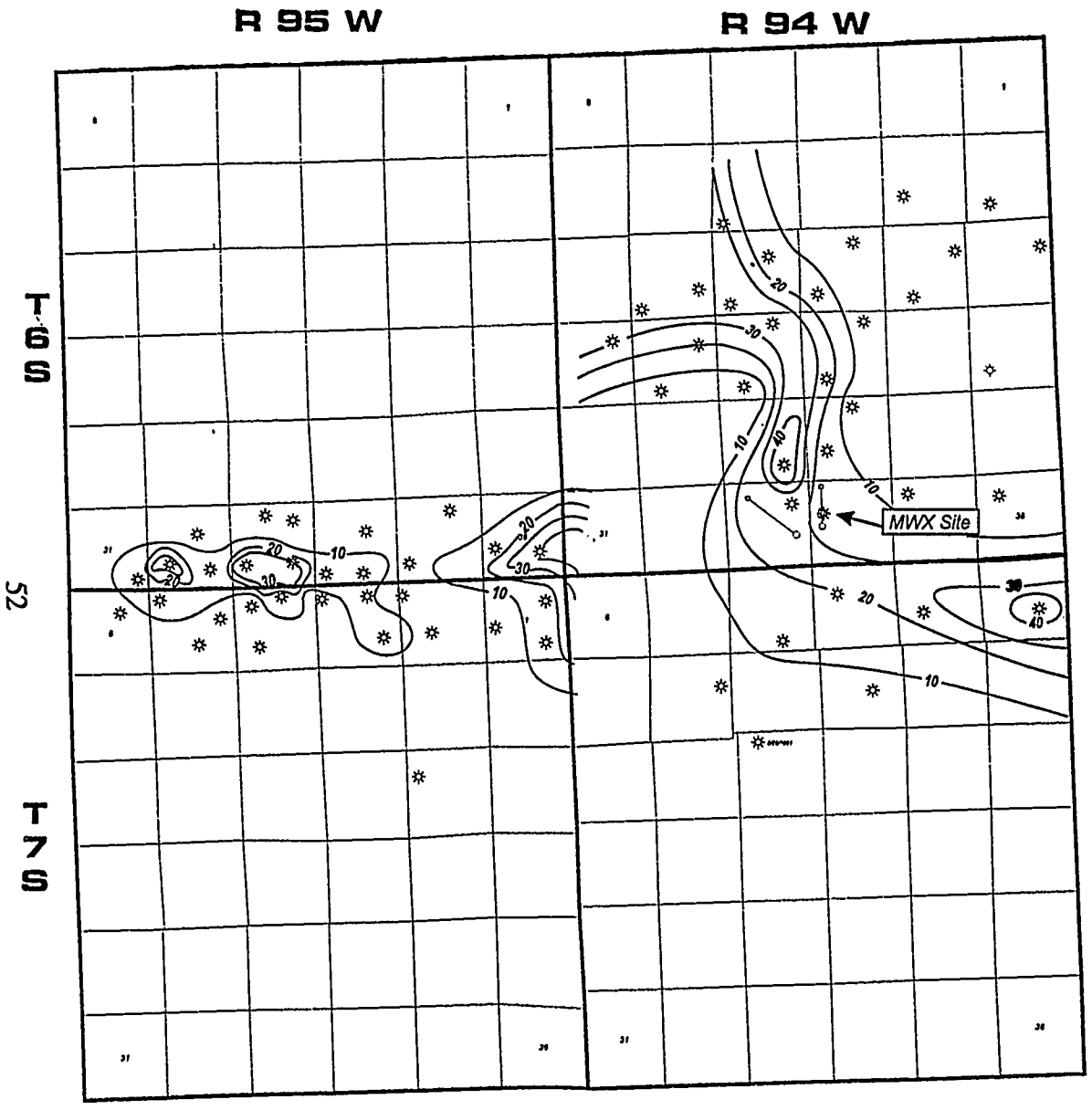

MAXIMUM MONTHLY GAS PRODUCTION
PARACHUTE & RULISON FIELDS

CONTOUR INTERVAL = 10 MMCFG/MONTH
CONTOURED ON WILLIAMS FORK GAS PRODUCTION

Thomas E. Hoak

FIGURE 28

Map Explanation

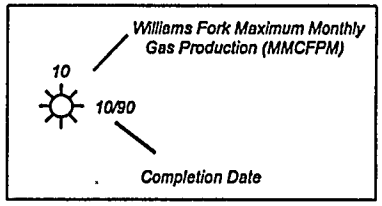

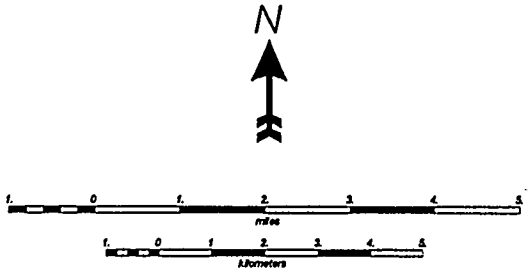

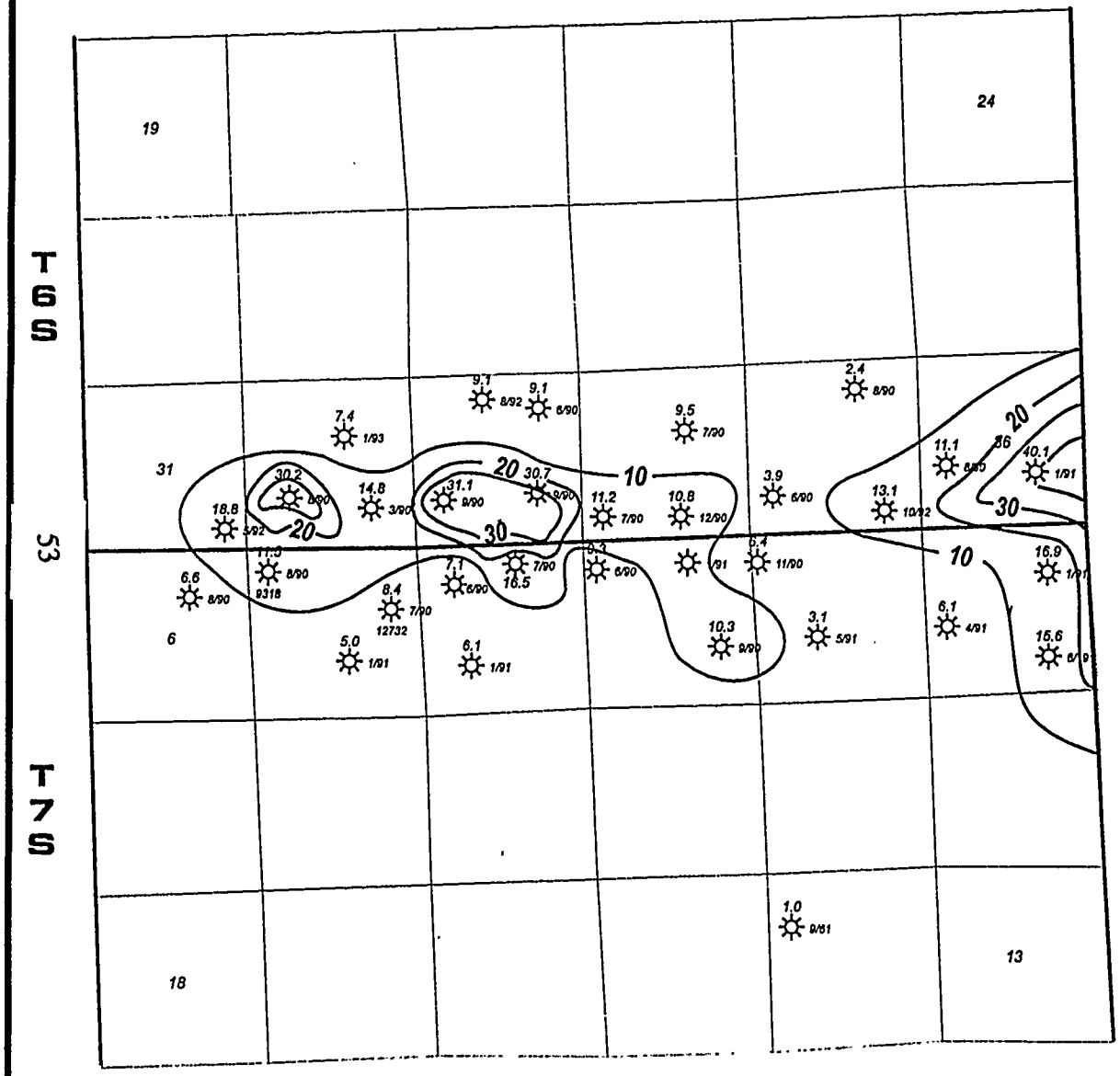

MAXIMUM MONTHLY GAS PRODUCTION
PARACHUTE AREA

CONTOUR INTERVAL =10 MMCFG/MONTH
CONTOURED ON WILLIAMS FORK GAS PRODUCTION

Thomas E. Hoak

FIGURE 29

Map Explanation

Williams Fork Maximum Monthly Gas Production (MCFPM)

1.8 10/90

Completion Date

N

1. 0. 1. 2.

miles

1. 0. 1. 2.

kilometers

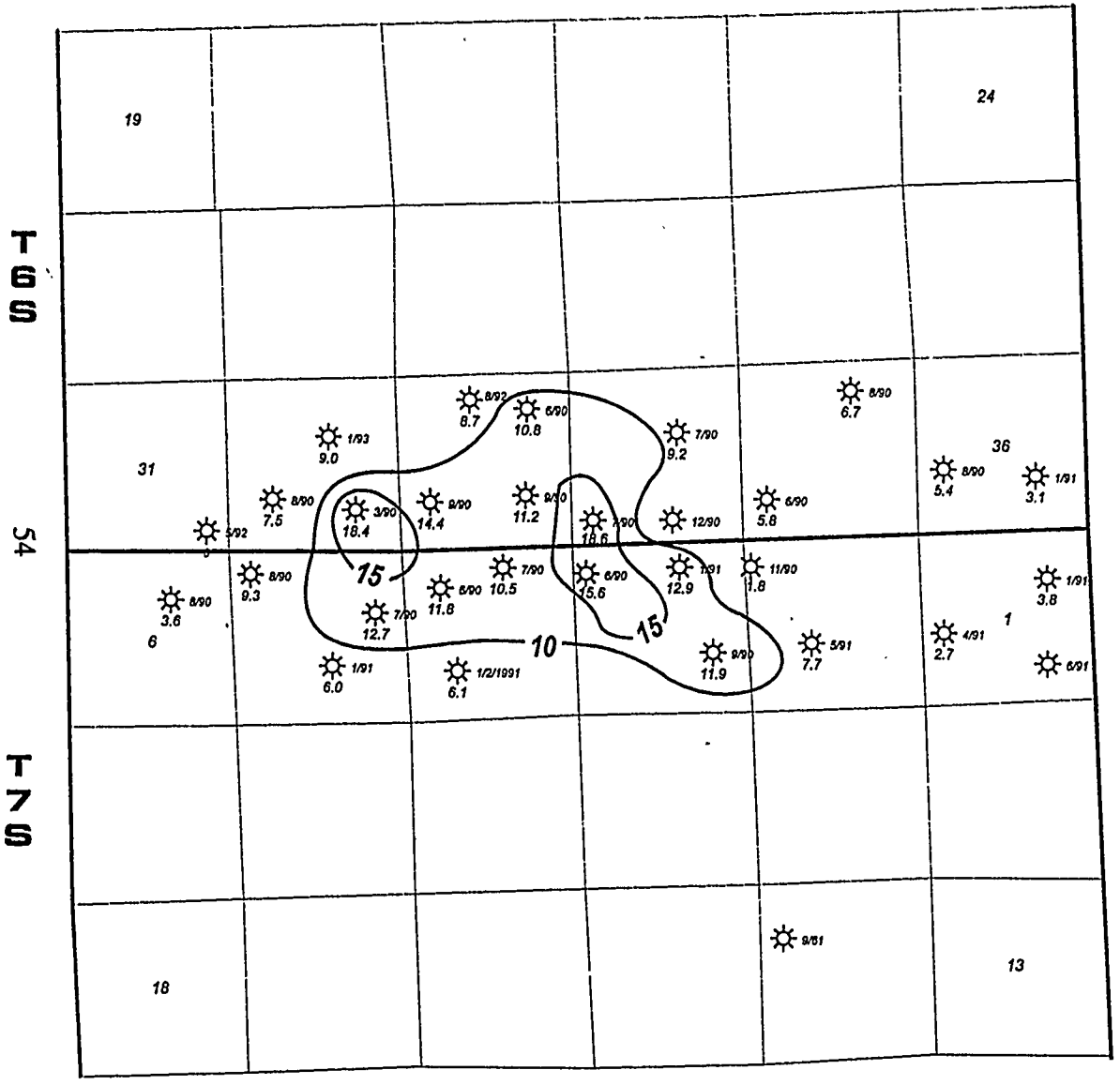

MAXIMUM MONTHLY GAS PRODUCTION
PARACHUTE AREA

CONTOUR INTERVAL =5 MMCFG/MONTH
CONTOURED ON CAMEO COAL GAS PRODUCTION

Thomas E. Hoak

FIGURE 30

Map Explanation

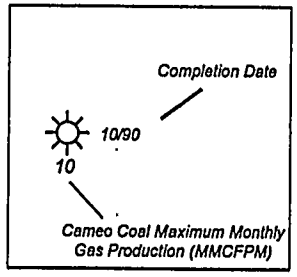

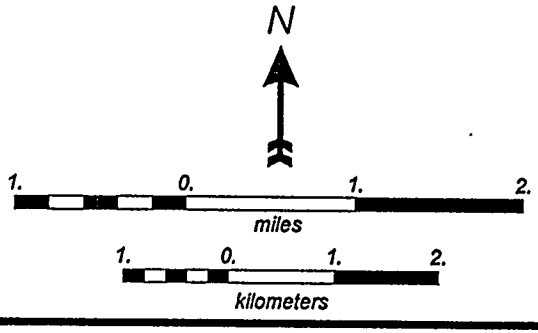

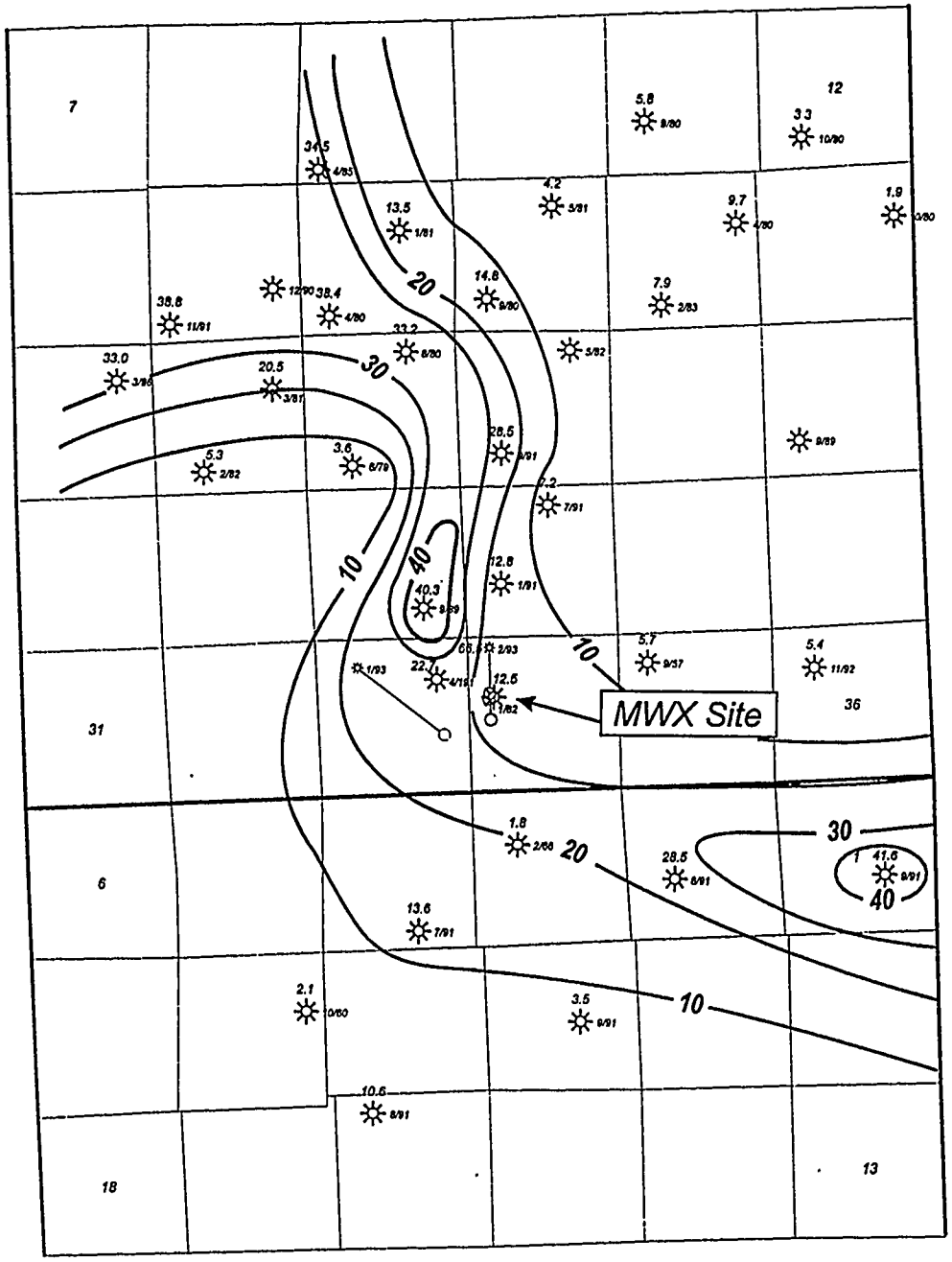

MAXIMUM MONTHLY GAS PRODUCTION
RULISON AREA

CONTOUR INTERVAL = 10 MMCFG/MONTH
CONTOURED ON WILLIAMS FORK GAS PRODUCTION

Thomas E. Hoak

FIGURE 31

Map Explanation

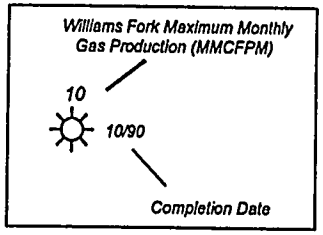

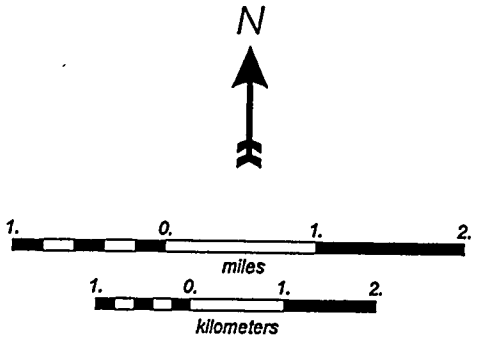

field. Cameo Coal producers in Rulison are too few to contour although they do appear to show slightly greater maximum production rates overall, compared to Parachute field. There appears to be a close relationship between structure and production "sweet spots" in both Parachute and Rulison fields. Work by Peterson (1984) demonstrated that high production in Rulison field does not correspond to sandstone thicknesses (Figure 32). Instead, Peterson shows that maximum production corresponds to the top of an anticlinal structure that divides the field. This structure mapped by Peterson at the top Mesaverde (Top Williams Fork, Cretaceous-Tertiary unconformity) is the same feature as shown earlier in Figure 21 (this text) mapped on the top Rollins Sandstone. The relationship between structure and production trends strongly suggests that production trends are controlled by natural fractures oriented parallel to the regional structure. A contoured map of Williams Fork production is overlaid on the Rollins structure map (Figure 33). Maximum production appears to be localized at points of maximum curvature (i.e. within dip domain reversals) and where trapping closure is maximized in the anticlinal crest. Decline analysis of a dozen wells in both fields using type curve matching has further documented that wells in the most productive zones are more highly fractured than wells located outside these zones. There is an order of magnitude greater permeability in Rulison field than in Parachute. Those wells with more massive hydraulic stimulations (i.e. the "modern" stimulations) show better drainage efficiency and greater flow rates than wells completed with older strategies.

Parachute and Rulison Fields Comparison

Rulison field is significantly older than the Parachute field. Table I and Figure 34 clearly demonstrate that the Parachute field has produced significantly more gas over its shorter production lifetime. The two fields combined have produced approximately 56.8 Bcf of gas. Cumulative production data from the two fields demonstrate that any development program in the Piceance Basin must consider the importance of Wasatch production in drilling economics. The Wasatch in Parachute field is responsible for approximately 19.6 Bcf of gas while it accounts for 12.4 Bcf in the Rulison Field. The Wasatch production for both fields combined accounts for over 56% of the total gas production.

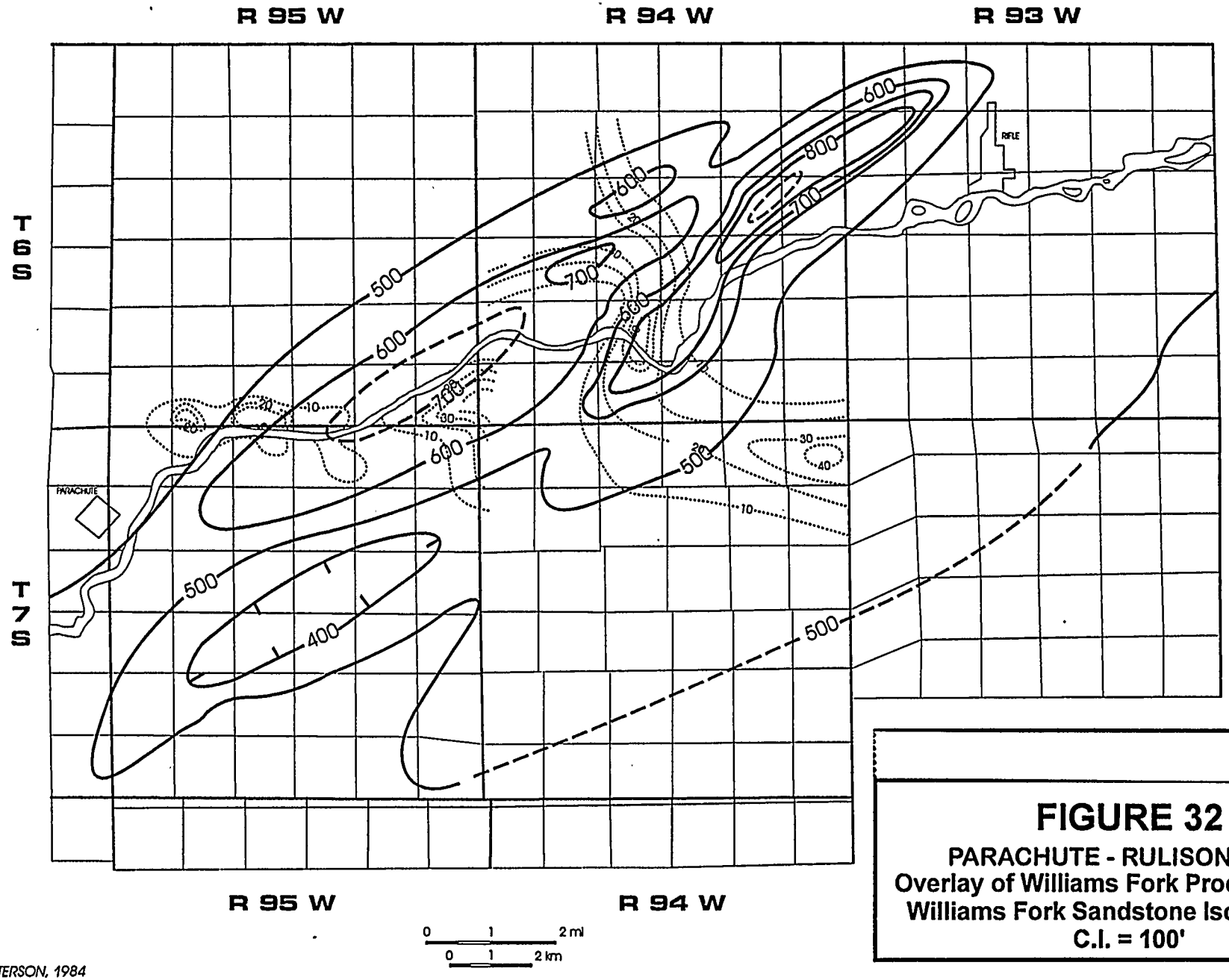

FIGURE 32

PARACHUTE - RULISON FIELD
Overlay of Williams Fork Production and Williams Fork Sandstone Isopach Map
C.I. = 100'

After PETERSON, 1984

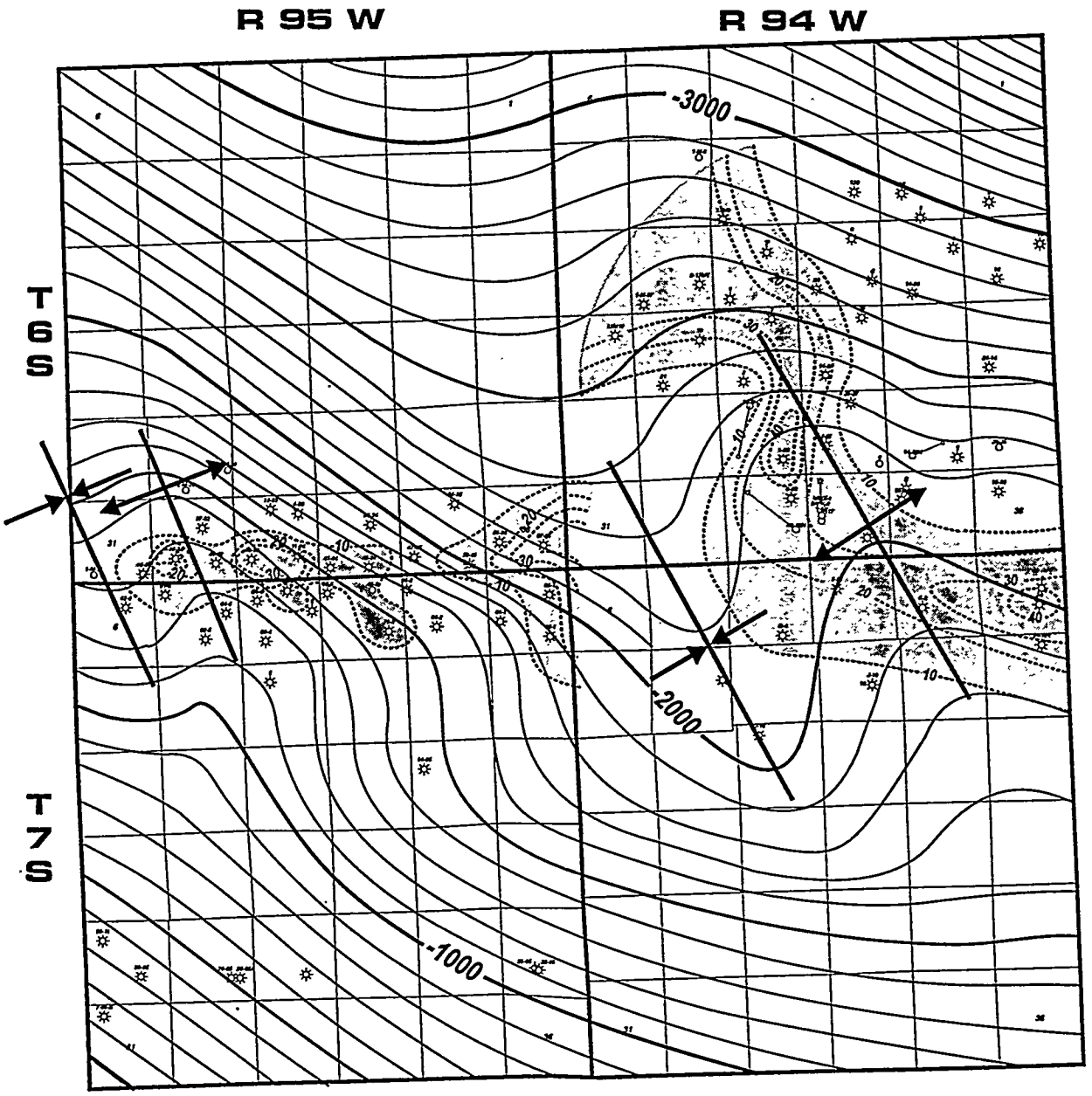

Map Explanation

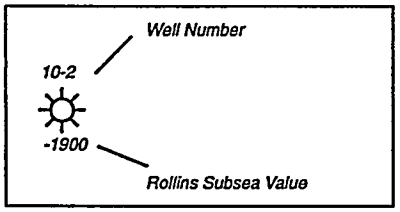

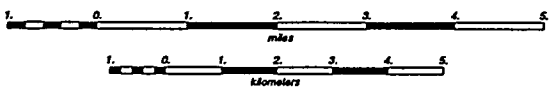

PARACHUTE & RULISON FIELDS

RELATIONSHIP BETWEEN STRUCTURE AND PRODUCTION

OVERLAY OF WILLIAMS FORK GAS PRODUCTION ON ROLLINS STRUCTURE MAP

SUBSURFACE STRUCTURE ON TOP ROLLINS SANDSTONE
(TOP ILES FM)
C.I. = 100'

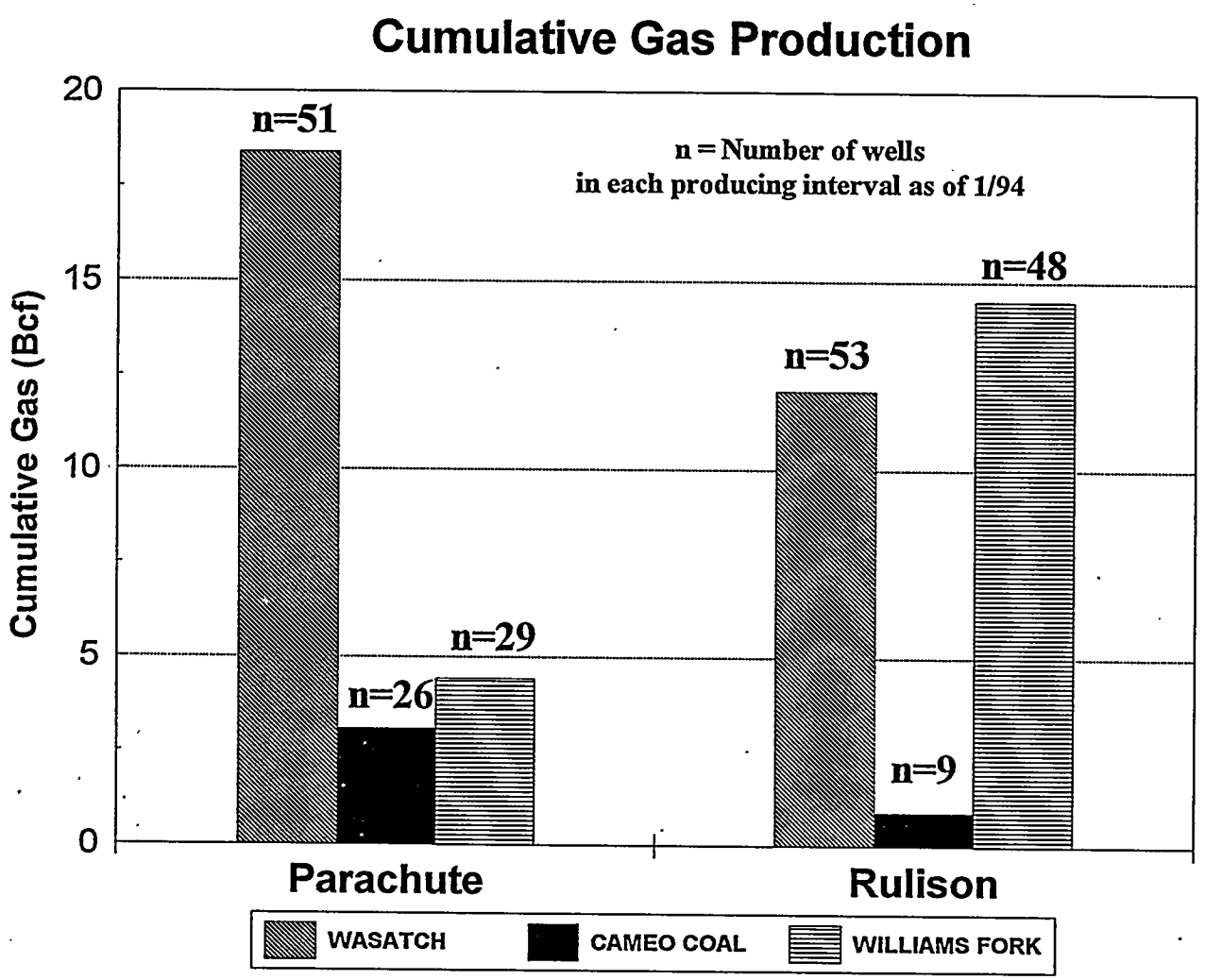
Cumulative Gas Production
Cumulative Gas (Bcf)
20
15
10
5
0
n=51
n=26
n=29
n=53
n=9
n=48
n = Number of wells
in each producing interval as of 1/94
Parachute
Rulison
WASATCH
CAMEO COAL
WILLIAMS FORK

Figure 34

In comparison, the Williams Fork section in the Parachute field has produced 4.4 Bcf of gas and has produced 14.5 Bcf in the Rulison Field. The combined Williams Fork intervals in both fields have produced nearly 33% of the total gas produced. This contrasts with the Cameo Coal in both the Rulison and Parachute fields that have produced 0.9 and 3.1 Bcf, respectively, significantly less gas than any other zones. The total Cameo Coal production accounts for only 7.4 % of the total. Few Cameo Coal completions have been performed in the Rulison field. Similarly, few Cameo Sand completions have also been conducted in the Parachute field although they appear to be more successful compared to other Williams Fork completions. The Cameo Coal section in Rulison field represents a relatively untested interval that may hold significant reserves based on production trends in Cameo Coal intervals elsewhere in the Piceance Basin.

Table I-Cumulative Gas From Rulison and Parachute Field Producing Intervals:

	WASATCH	WILLIAMS FORK	CAMEO COAL	CAMEO SAND	TOTAL GAS (Bcf)
PARACHUTE FIELD (TOTAL GAS IN Bcf)	19.6	4.4	3.3	0.0	27.3
RULISON FIELD (TOTAL GAS IN Bcf)	12.4	14.5	0.9	1.7	29.5
TOTAL GAS (Bcf) =	**32.0**	**18.9**	4.2	1.7	56.8
Percent of total gas from each producing zone =	56.4%	33.3%	7.4%	2.9%	
Total Gas from all Producing Zones = +includes all production, 1/59-6/93	**56.8 Bcf**				

The greater amount of Cameo Coal production in the Parachute field reflects the relatively recent and limited development of the Cameo Coal play in the Rulison field and the early establishment of this play in the Parachute field. It is significant that the Cameo Coal in the Parachute field has produced nearly as much gas as the Williams Fork wells. In contrast with Parachute field, the cumulative amount of gas produced in the Rulison field is more nearly equivalent between the Wasatch and Williams Fork Formation. In Rulison field, slightly fewer Williams Fork wells have produced approximately 2 Bcf more gas than the

Wasatch.

Most wells in Parachute field have used significantly greater amounts of sand in the fracture treatments and have perforated smaller intervals. The major source of this change in completion strategy for the younger Parachute wells is based on poor performance obtained in Rulison field wells used extensive perforation and limited proppant fracture treatments. Rulison and Grand Valley fields, the latter field in particular, have proven to be useful locations to test new completion methods later applied to the Parachute field.

In addition to geologic and engineering constraints on well economics, another important economic consideration is the gas transport infrastructure. New pipeline connections were established in late 1986 in Parachute field and Rulison fields that led to renewed interest in field development. Tight gas sand tax credits combined with shallow drilling depths along the Colorado River valley also played a significant role in determining the economics of drilling success. These infrastructure and regulatory incentives were absent during development of the Rulison field.

Cozzette-Corcoran Completions

After significant gas shows were discovered during initial Cozzette-Corcoran production testing at the MWX site in the early 1980's, some interest was generated in the Cozzette-Corcoran reservoir zone. To date, no Cozzette-Corcoran wells have been economically successful, especially compared to completions in the Williams Fork and Wasatch. Most wells that have tested the Cozzette-Corcoran have perforated the top of the upward-coarsening marine sand interval beneath the Corcoran and the thicker sand interval just below the Cozzette. Four horizontal completions (Meridian Juhan #14-26H; Barrett Bonneville RU-1 #28-SH; Meridian Quarter Circle #43-33H and the CER Superior SHCT #1) have been performed in the Cozzette-Corcoran. Two of these wells (SHCT #1 and Quarter Circle #43-33H) had initial high gas flows combined with high water production. After several months, the gas flow diminished while water rates continued to remain high,

making the well uneconomic. Little information is presently available for the Juhan and Bonneville completions. These wells were drilled fairly recently and completion and initial production data are not yet available. Water saturated conditions within the Cozzette-Corcoran marine sands suggest that these sands maintain hydrodynamic continuity with outcropping recharge areas on the uplifts surrounding the basin. Shale drapes capping each marine sequence probably act as aquitards and prevent fluid migration upward into the overlying fluvial channels and coal section. Additional support for this interpretation is found in the water-prone lower coal lying just above the Rollins. The observation that this coal tends to be wet suggests that the model of outcrop recharge is plausible and that the paludal and fluvial Williams Fork has not been breached due to its lensoidal and laterally discontinuous geometry.

Horizontal completions also permit better access to dominant fracture systems that are the primary source of adequate permeability in Piceance Basin gas reservoirs. Core-based permeability data from Rulison field suggest that fracturing causes a three-orders-of-magnitude increase in permeability (Lorenz et al., 1988). Even calcite-filled closed fractures typically possess an order of magnitude greater permeability than the unfractured host. Abundant subsurface and outcrop fracture data have been collected for the Rulison field as part of the MWX experiment. These data indicate that the dominant set of fractures strike to the west-northwest and possess a vertical orientation. A secondary fracture set possessing an NE-trend is found in outcrops near the MWX site but was not observed in the continuous cores obtained from any of the three MWX wells. The dominant WNW fracture trend lies parallel to the maximum horizontal compressive stress. Most interestingly, the *in situ* stresses in different lithologies possess different orientations. Apparently, the sandstones have retained some element of the paleostress conditions present during diagenesis (Lorenz et al., 1988). Two of the horizontal completions (Barrett Bonneville RU-1 #28-SH; CER Superior SHCT #1) have either a N-or S-striking horizontal component that may be attempting to intersect both the regional NE and WNW fracture trends. One of the other two horizontal wells (Meridian Juhan #14-26H) has a NE/SW-striking horizontal section that probably attempted to intersect the dominant NW-trending fracture system. The other well

(Meridian Quarter Circle #43-33H) has an NW-striking horizontal section that may be trying to intersect thin Cozzette-Corcoran prograding transgressive systems by drilling perpendicular to paleo-shoreline trends. Alternatively, given the water-saturated conditions encountered by all previous horizontal wells in the Cozzette-Corcoran, it is possible that the operators were attempting to avoid intersecting any natural fractures. This drilling strategy suggests that the matrix sands may be gas-charged while the fractures reflect conduits to water-saturated zones. By minimizing contact with fractured zones (i.e. drilling parallel to regional fracture orientations), more of the gas-saturated sand matrix would be drained while water influx would be minimized. Available data are inadequate to fully resolve this problem.

Discussion and Conclusions

Dominant production in Williams Fork fluvial reservoirs appears to be closely related to subsurface fracture trends and unrelated to sand thickness variations. Maximum production is associated with zones of maximum strata flexure (i.e. areas of dip domain change) and in the zones of maximum structural closure. Several zones of enhanced production in the southern area of Rulison field may lie above the margin of the paleohorst/thrust zone and enhanced permeability caused by fracturing in this area may be related to faulting instead of, or in conjunction with, strata flexure.

Clearly the presence of fractures and a clear recognition of basement features and their deformation history are the key to successful drilling programs in the southeastern Piceance Basin. By careful analysis of basement features and their tectonic evolution, the orientation and controlling influence of these relict features on the geometry of natural fractures will be characterized so that their geometries can be accurately predicted. Because of the lack of a clear relationship between stratigraphic variability and production, additional drilling (made possible by new field rules) in Parachute and Rulison fields should focus on areas thought to be more intensely fractured based on an integrated analysis incorporating remote sensing data, seismic, and other subsurface geologic data and geophysical analysis of well logs.

This integrated approach, combined with basin-scale delineation of gas and water saturation represent critical data analysis methods that must be understood to develop and maintain economic production in naturally fractured tight gas sand reservoirs.

NUMERICAL BASIN MODELING FOR FRACTURE GENESIS

Introduction

Advanced Resources International, Inc., in collaboration with Dr. Peter Ortoleva of the Laboratory for Computational Geochemistry (LCG) at Indiana University, is undertaking a parallel effort to characterize the development of fractured reservoirs in the Piceance Basin using computer-based numerical modeling. Significant amounts of data generated during the regional geologic characteriztion of the Piceance Basin conducted by ARI will be integrated into this model.

The overall objective of the modeling effort is to develop a predictive model to determine fracture genesis in the Piceance Basin in the context of a dynamic, self-consistent, forward model. One of the primary advantages of this model is the relatively inexpensive use of modeling for fracture detection compared to the costs of drilling exploration wells, seismic surveying and other technologies. The use of the model allows rapid and quantitative partitioning of the basin into areas where fractured reservoirs are more likely to be present, and where advanced and more costly technologies can be used to confirm fracture geometries and their importance to development programs. The use of self-consistent calculations permits the recognition of internal errors within the program and also permits the analytical significance of different variables to be established. Error checking of the program results is further simplified by the use of a forward model algorithm. In the forward model, the basin commences with an appropriate analog and concludes with the characteristics recognized today in the basin. The use of the forward model allows verification of the model by assessing its correspondence with present-day conditions. Because of the internally consistent calculations and forward model, the potential for successful modeling of basin evolution is

greatly enhanced.

The model uses input data consisting of geochemical data, basin stress history, sediment composition, thickness and flux, thermal generation of hydrocarbon overpressure and other factors to determine the timing and orientation of fracture genesis in the basin. The following parameters are input into the model: 1) basin stress history or the external constraints on basin geometry; 2) sediment composition and thickness; 3) basin thermal flux; 4) sea level changes, solute influx and hydraulic head changes; and 5) initial basin characteristics. The initial basin characteristics are the most difficult to establish because of the wide variability in rock properties in a basin. The use of an appropriate modern analog for the basin prototype greatly simplifies the determination of the initial model characteristics. Once the modeling has commenced, each input parameter generates changes in the existing basin conditions and effects the appropriate changes in internal basin characteristics dependent on the controlling reaction, transport and mechanical equations. The following section briefly outlines the characteristics of the modeling initiative.

Executive Summary

At LCG, we are developing, calibrating, and testing a basin diagenesis simulator for use in the prediction of the distribution and characteristics of natural fracture networks in a sedimentary basin. The physical, chemical model, and computer simulator are to be used to aid in planning and interpreting remote fracture detection-based petroleum exploration. The test site for the study is the Piceance Basin. Progress on simulator testing is approximately on schedule.

The simulator is based on the equations of grain and fluid-phase reactions, pressure solution-mediated, and mechanical compaction, mass and energy transport, incremental stress rock rheology, and fracture kinetics. The coupling of all these processes is fully accounted for so as to yield a fully self-consistent calculation. The simulator comes in both two-(cross-section) and three-dimensional versions for preliminary and complete modeling, respectively.

Data from the MWX site has been analyzed and input into a computer data bank. This data, as well as basin-wide thermal stress and sedimentation history, will be used to test and calibrate the model.

Organic reactions and mutli-phase flow were not a part of the original workplan for this modeling subcontract to the overall ARI project. Because of its potential importance to the project, LCG has developed overpressure and fracturing modules incorporating organic reactions and multiphase flow.

In the course of code improvement, a technology of computational grid adaptation was devised in order to enhance the accuracy in the calculation of fluid pressures and rock stresses needed for fracture prediction. This technology also is providing a key part of our strategy for entering the complexity of sedimentary history for full three dimensional modeling allowing the almost direct input of scanned isopach maps into the simulator. Graphical analysis tools needed to visualize our results are also being developed.

In this first annual report, preliminary results on all aforementioned aspects of the project are presented. The report ends with an estimation of the consistency of progress to date with the originally proposed work schedule and list of personnel participating in the project.

Model Overview

Our approach to prediction of the location and characteristics of fractured tight gas reservoirs is based on a novel basin model and computer simulator. The purpose of the simulator is to provide a platform for integrating all available data into the exploration and field development strategy.

Available information can be divided into geological data and the physico-chemical laws and parameters. The former provides information that makes a basin simulation

tailored to a specific basin while the physico-chemical information gives our model the power to predict reservoir location and characteristics without prior knowledge of the reservoir.

To explain the interplay of these two types of information in making predictions, consider first one time step in our forward modeling as illustrated in Figures 35, 36. The purpose of the incremental evolution step is to advance the state of the basin from a time t in the past to a later time $t + \delta t$ in the past. In our simulator, two distinct operations are taking place simultaneously during this time interval δt. The geological information is used to (a) fix the input/output of energy and mass at the basin boundaries and (b) impose, through the tectonic history, the strain history (i.e., overall basin deformation) at the basin boundary. The physico-chemical processes determine the evolution in time during δt of the spatial distribution of the local state variables. The latter include stress, fluid properties, rock texture, and temperature.

The geological data is divided into four categories as shown in Figure 35. the "tectonic data" determines the change in the lateral extent, shape of the basement-sediment interface and the amount of sediment loading or erosion during δt. As suggested in Figure 35, this data provides the conditions at the basin boundary needed to calculate the change in the spatial distribution of stress and rock deformation within the basin. This latter physico-chemical calculation is carried out by our stress solver module that solves equations based on rock rheology, incremental stress theory and force balance.

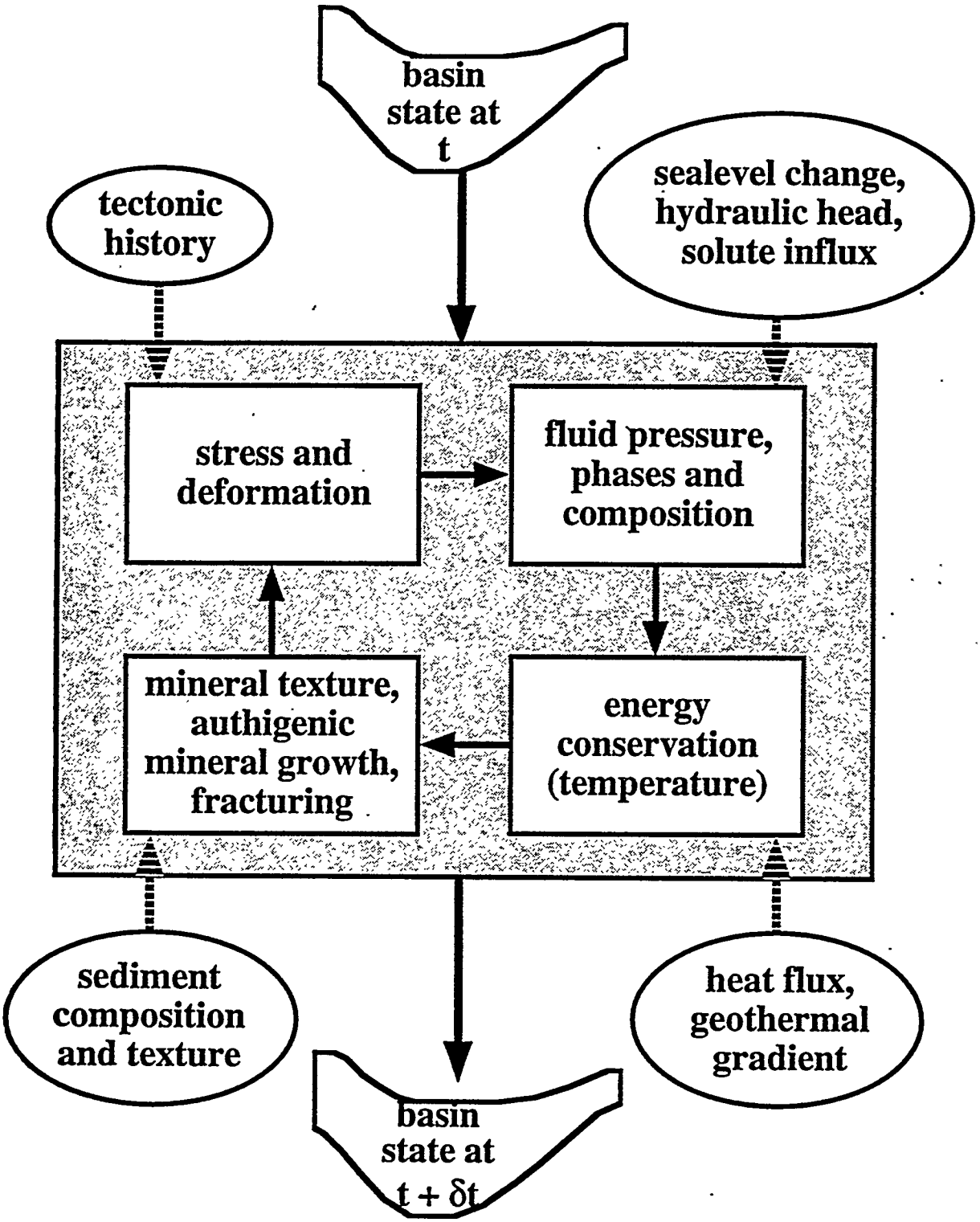

Figure 35-Flow chart showing how interplay of geologic data and physico-chemical (i.e. reaction-transport-mechanical) process modules evolve during a simulation run for a time increment δt.

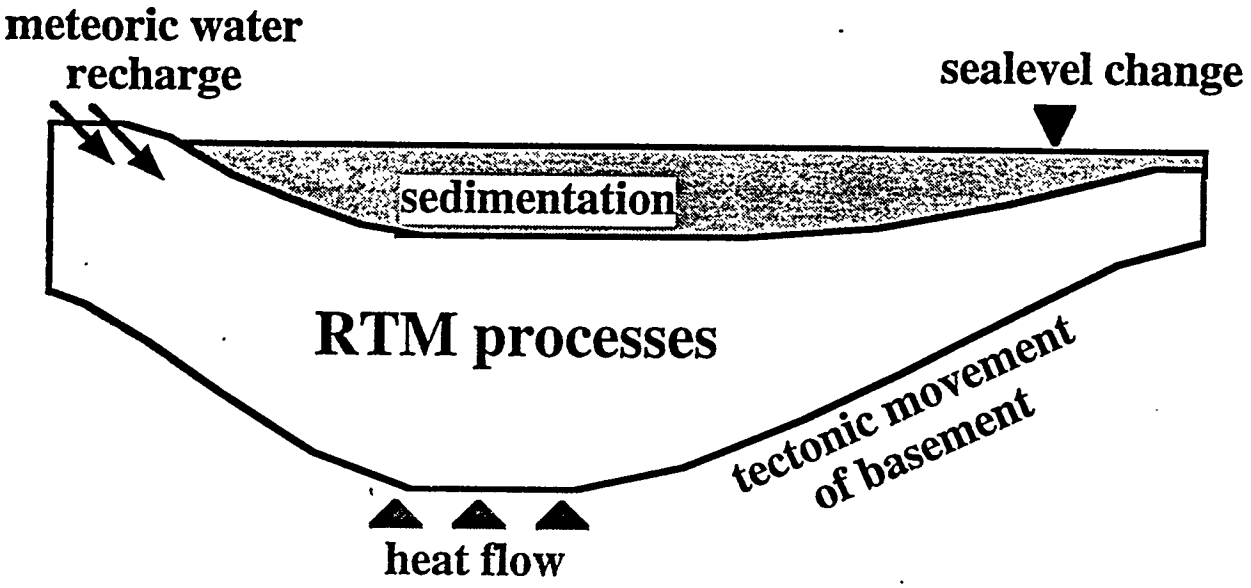

Figure 36- Schematic basin cross-section showing interplay of geologic data and reaction-transport-mechanical simulations modules.

The next type of geological data is that affecting the fluid transport, pressure, and composition. This fluid data includes ocean level changes, recharge conditions, and the composition of fluids injected from the ocean and meteoric sources. This history of boundary input data is then used by the hydrologic and chemical modules to calculate the evolution of the spatial distribution of fluid pressure and composition within the basin. These physico-chemical calculations are based on single or multi-phase flow in a porous medium and fluid phase molecular species conservation of mass (i.e., the reaction-transport equations). The physico-chemical equations draw on look-up tables for permeability-rock texture relations, relative permeability formulae, reaction rate laws, and reaction and phase-equilibrium thermodynamics.

The spatial distribution of heat flux imposed at the bottom of the basin is another geological input/control. This data, as well as the temperature imposed at the top of sediment pile (i.e., climate and ocean bottom temperature), is used to evolve the spatial distribution of temperature within the basin during the time interval δt. This evolution is computed using the equations of conservation of energy, and formulae and data for mineral and rock thermal properties (conductivity and specific heats).

Finally, the geologic data provides the detailed character (grain size, shape, mineralogy, and mode and organic content (i.e., inorganic and organic texture) of the sediment being laid down during δt. The physico-chemical laws and data are used to calculate the change of the spatial distribution of texture within the basin during δt. These physico-chemical calculations involve the rate laws and data for free-face grain chemical kinetics, pressure solution and grain rotation or breakage, grain nucleation and laws of kerogen chemical kinetic transformation. Most notably in the present context are the laws of fracture nucleation, aperture dynamics, and the kinetics of cement infilling.

All geologic input data and physico-chemical calculations are integrated in our basin simulator to uniquely give us the power to predict the present-day internal state of the basin. The physico-chemical laws translate the boundary constraints (geological data) into a

prediction of the changes of internal basin state that took place during δt. The incremental time advancement is repeated until the evolution of the basin internal state, from the inception of the basin to the present, is computed.

The above procedure can only be deemed useful if the required geological data is the same or less than that presently used in exploration and resource development. In fact, all the geologic data noted above is in common usage. It is derived from well log analysis, seismic data, general basin tectonic history, palinspastic restoration studies, vitrinite reflectance, and other temperature indicators, stress and strain indicators, core analysis, and production data. Furthermore, much of the physico-chemical data is available in published literature.

An important perspective is that the physico-chemical computations provide another way of integrating the conventional geological data. In a real sense these calculations put constraints on the interpretation of the geological data. For example, an interpretation of the geological data without the benefit of our model is subject to some assumptions on the relative timing of events which could be made more reliably when the timing of these events is predicted based on the known rates of the underlying physico-chemical processes.

Like any analysis of the geologic data - including that conventionally used - our model-based data integration and predictions are subject to some uncertainties. These are of three types:

- Errors in the geologic data
- Errors in the physico-chemical laws and data
- Numerical errors in the simulation algorithms

All these errors must be addressed in evaluating our predictions. Interestingly, our simulator, itself, provides an important tool for error estimation. By carrying out sensitivity studies, one can determine likely errors and their significance. Parameters to be varied are those given by the geological and the physico-chemical data as well as those parameters controlling the numerical accuracy (time and space step, convergence criteria for iterative algorithms, etc.).

The enormity of the physico-chemical calculation may at first sight make the computations seem impractical. However, the rapid improvements in computer hardware make this a very promising time in this regard. These improvements are in CPU speed, memory, and parallel computation. Furthermore, improvements in modeling tools also allows reductions in the computations. These include homogenization techniques whereby small spatial scale features can be embedded into large (basin) scale simulations. The latter is done such that the particularities of small scale features are not lost in crude averaging. Also, advances in numerical techniques, notably adaptive gridding, higher order discretization schemes, and iterative, sparse linear solvers, also make the computations fast, accurate, and robust.

Previous basin modeling efforts have only focused on a few factors, such as hydrology, stress, or mineral, or organic reactions. While these decoupled models have given insights into specific aspects of the evolving basin, they cannot answer many of the key questions at hand. This is because many of the phenomena of interest involve several processes that are strongly coupled. For example, hydrofracturing depends on stress and fluid pressure. These depend on texture through mechanical and transport (namely permeabilities) parameters and hence on hydrofracturing. Texture evolution is also affected by stress and fluid pressure (through pressure solution) and through fluid flow (by the import of ions affecting grain growth rate laws).

Clearly, there are a variety of such feedback loops that exist in the network of basin reaction-transport-mechanical (RTM) processes. Fracturing is at the heart of many of them as it depends on a number of effects (stress, fluid pressure, mineral infilling reactions) and, in turn, through a number of RTM processes, fracturing affects many other processes. Thus predicting the timing of the development of fractures in the geologic past as well as their present status requires a fully coupled model and simulator. Thus, the solver modules of Figure 35 are not run independently. Rather, the system of fully coupled equations are solved iteratively for each time step increment so that all cross coupling relationships between processes are accounted for. This full self-consistency of our RTM simulator gives it the unique character needed to make the predictions required for the success of the naturally fractured tight gas reservoir project.

In the remainder of this report we outline our progress in tailoring our basin model to the naturally fractured reservoir project. Our work consists of both upgrading and calibrating our code, and re-evaluation and reorganization of geological data for use in our RTM model. The report consists of a main body comprising a summary of all the work of the first year and a number of appendices that give more technical detail.

Two-Dimensional Basin Simulator
CIRF.B2

Our two spatial dimensional (cross-section) basin simulator CIRF.B2 is being upgraded for use in this project. While a basin is three-dimensional, it is important to have a two-dimensional simulator

* to have a relatively low CPU intensive code to gain an understanding of much of the complexity of the coupling of the mechanics, hydrology, and chemistry

* to help in the development of algorithms

* as a backup in case progress on the full three-dimensional code is slower than expected

* as a test/verification for the three-dimensional code

* because much of the chemical aspects of the two-dimensional code are transferable line-for-line to the three-dimensional code.

For these reasons two- and three-dimensional modeling are proceeding simultaneously.

The simulator CIRF.B2 includes the following features:

* generalized chemistry and mineralogic composition;

* kinetically controlled mineral dissolution reaction rates depending on pressure, temperature, stress and, fluid composition;

* pressure solution-mediated compaction using the water film diffusion (WFD) mechanism;

* fluid flow using Darcy's equation for one (the aqueous) phase;

* basin subsidence, sea level curve, and stress history;

* thermal history; and

* the time-course of the rate, texture, and fluid composition of the sediment added.

Detailed descriptions of the model are contained in Appendices A-D.

The WFD mechanism accounts for the effect of stress at grain-grain contacts, the width of the water film layer within the contact, and the diffusion rate along the water film layer, as well as temperature, fluid pressure, and fluid composition. Free face dissolution/overgrowth reactions are also taken into account. The formulation used incorporates temperature, fluid pressure, and ionic strength effects (see Appendices A and B).

In the model as presently developed, porosity reduction and overpressuring in the pore occurs through; 1) pressure solution-induced compaction of pore space, and 2) thermal expansion of the fluid. When a large overpressure accumulates and the fluid pressure approaches lithostatic pressure, the pressure solution rate diminishes, so that no further chemical compaction of sediment takes place. A model accounting for hydrofracturing using a subcritical fracture nucleation and growth theory, augmented with a model of fracture cement infilling, has also been developed (see Appendix C). A grain nucleation module has been implemented and tested. An incremental stress rheology solver that unifies mechanical deformation, pressure solution, and hydrofracturing has also been developed (see Appendix D).

Preliminary Simulation Results

To test the code, simulations have been carried out demonstrating the isolation and overpressuring of a sandstone unit enclosed in shales. Minerals involved were quartz, K-feldspar, kaolinite, and muscovite. The simulated reservoir is seen in Figure 37. In other simulations, overpressured regions were seen to develop (see Figures 38 and 39).

In the case of Figure 37, sandstone overpressuring occurred because of its enclosure in shale. The system, originally 10 km x 0.75 km, was incrementally reduced vertically by compaction. The system was subjected to a subsidence rate of 25 m/my and a geothermal gradient of 25 degrees/km. In this simulation, overpressuring in the sandstone becomes appreciable at 2 km depth. At this point, the sandstone becomes hydrologically sealed by the

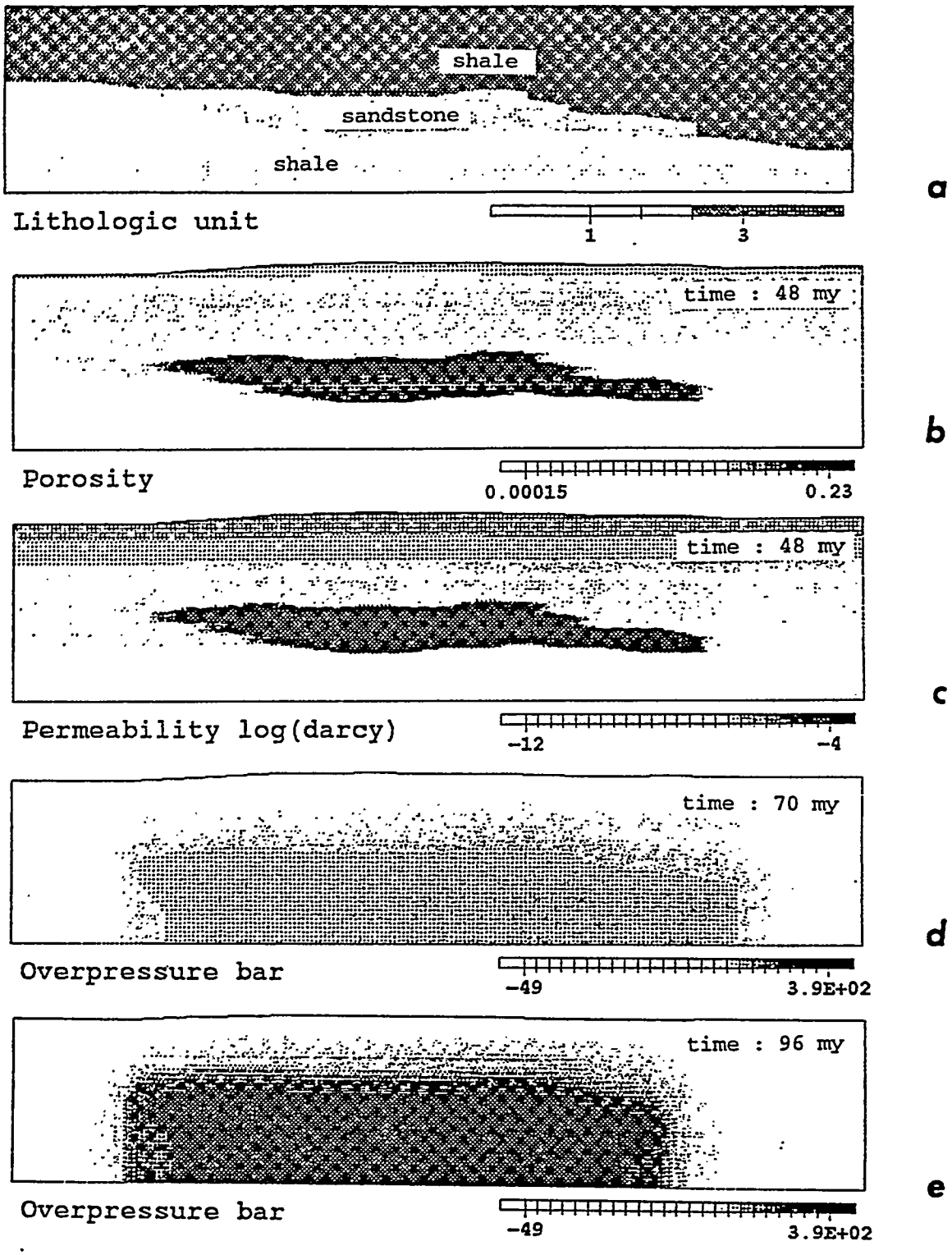

Figure 37 - Development of overpressure in sandstone enclosed in shale; and corresponding alterations of reservoir porosity and permeability. Figure I-1a shows the initial lithology distribution of sandstone enclosed in shaly units. Compaction of sandstone becomes significant around 50 my, when both overlying and underlying shales have compacted and formed hydrologic, permeability barriers (b,c). With continued compaction of sandstone overpressure develops around the sandstone body (d,e). Because of the slow dissipation of the pressure building up within the sandstone the overpressure is shown to invade into the shale units immediately adjacent to the sandstone. The simulation domain is 10 x 0.75 km, with subsidence rate of 30 m/my and geothermal gradient of 40 degrees/km. Minerals used to define the sediments are quartz, K-feldspar, kaolinite, and muscovite.

Fluid Pressure vs. Depth

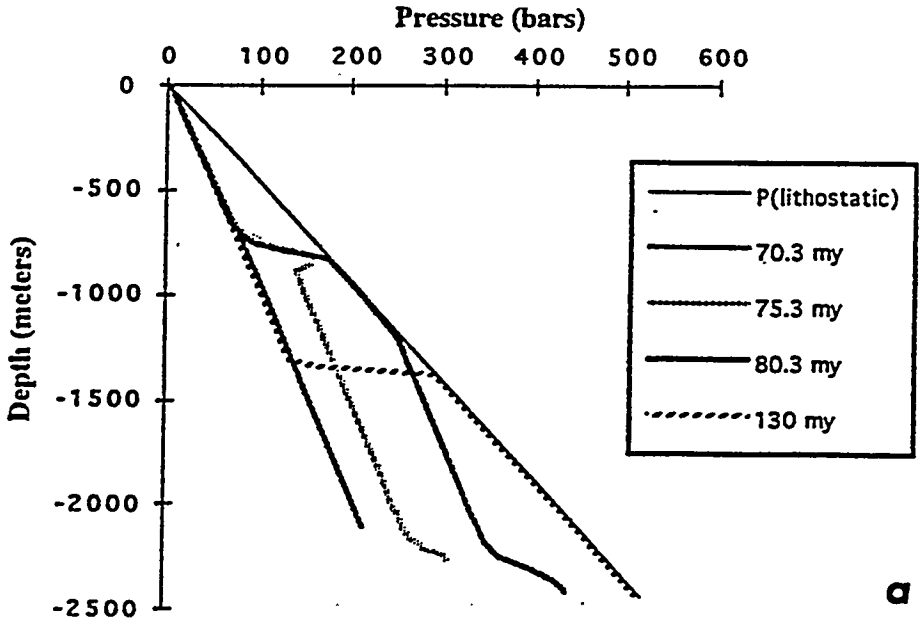

Porosity vs. Depth

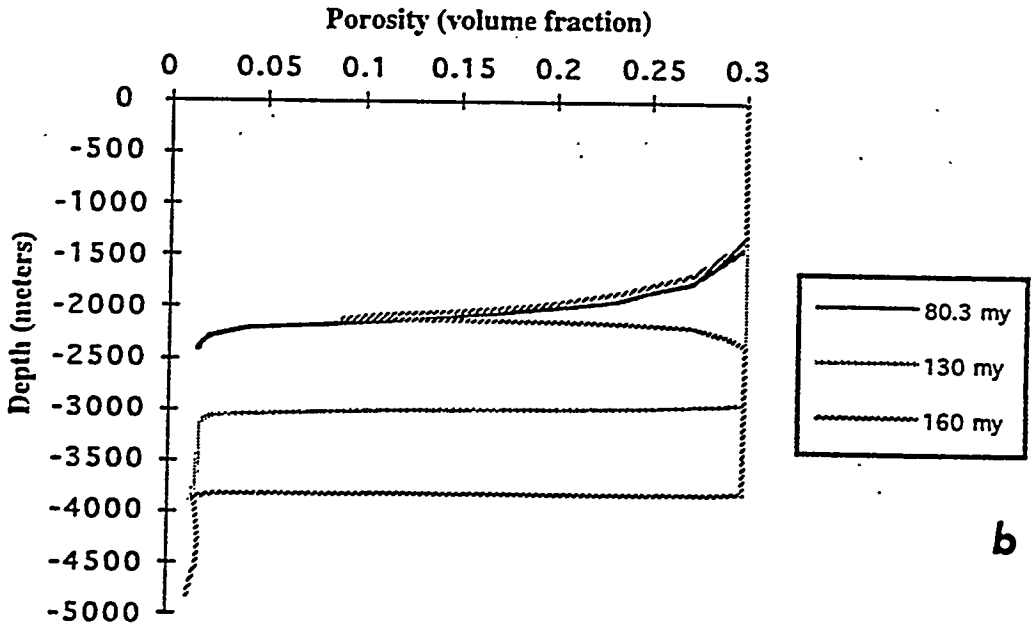

Figure 38- Evolution of fluid pressure (a) and porosity (b) profiles for a simple system defined by constant sedimentation and subsidence rates of 25 m/my and silty sediment input at sediment-water interface at the top. Overpressure is shown to develop around 70my, and reaches lithostatic by 80 my at a depth of 1 km (Fig. I-2a), while chemical compaction of sediment is shown to occur at a depth of 2 km (Fig. I-2b). Between 80 and 130 my the accumulated overpressure retards the pressure solution mechanism, thus the overpressured zone subsides with the sediment. Around 160 my, with sufficient subsidence of the overpressured zone, chemical compaction reduces the porosity of the sediment at 2 km depth once again, thus producing the top seal of the porosity-preserved overpressured compartment between the depths of 2 and 4 km.

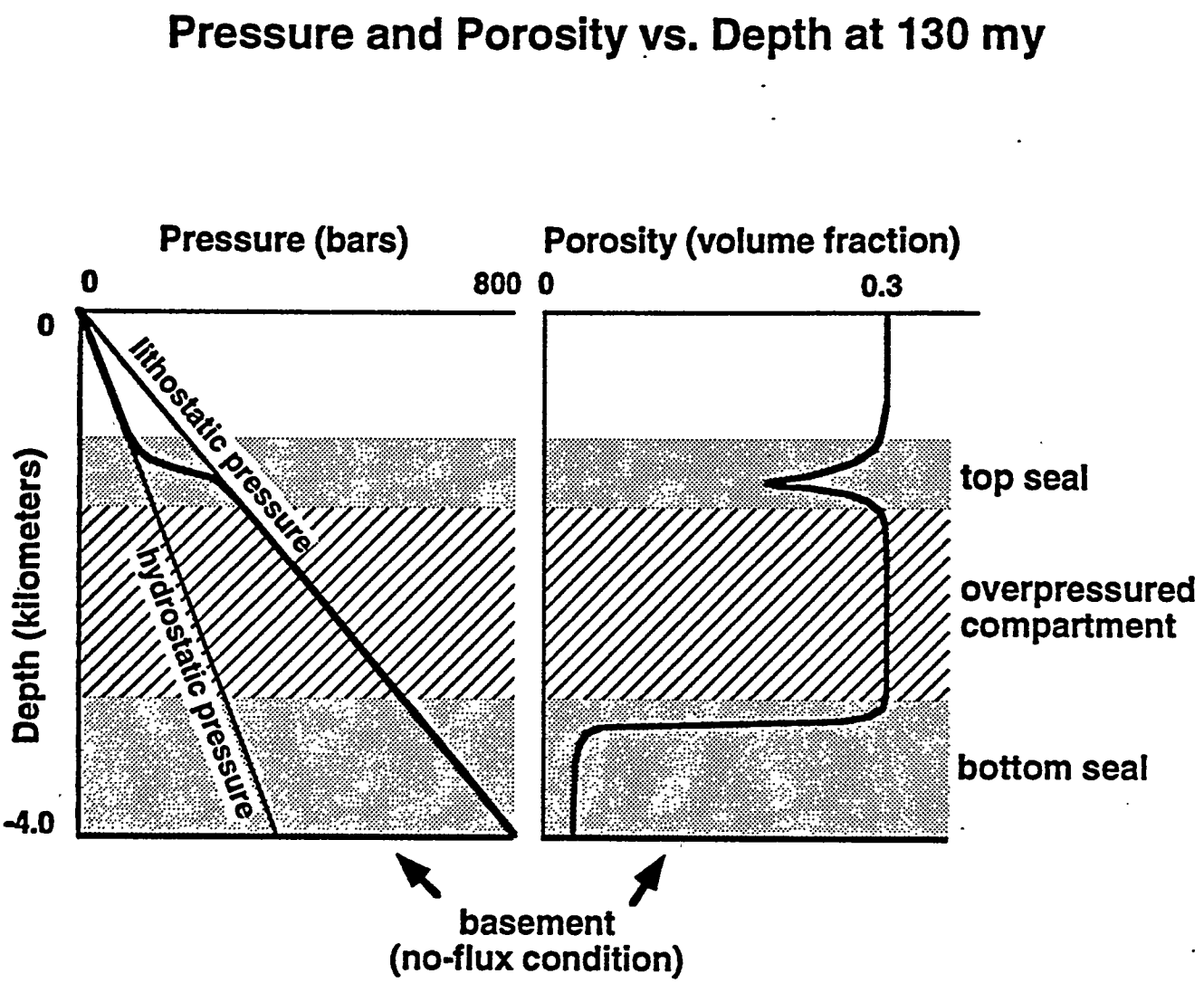

Figure 39- Final time step for simulation of earlier frames (figs. 37 & 38) showing relation of pressure to hydrostatic and lithostatic values. Figure also illustrates the relationship between pressure and low porosity zones (i.e. seals) that formed spontaneously in the absence of sedimentary variations.

surrounding shale. This hydrologic sealing of the sandstone is due to the earlier compaction of the shales at a shallower depth. As a result, fluid that would have been expelled from the sandstone cannot escape, and overpressure accumulates within the sandstone.

The example of Figure 38a, is important for demonstrating the simulator's capacity to capture the coupling between overpressuring and pressure solution. Using constant sedimentation and subsidence rates of 30 m/my, constant geothermal gradient of 40 degrees/km, and a uniform input sediment (porosity 30%, quartz grain radii 0.002 cm), a compartment of preserved porosity autonomously develops above the region of extensive pressure solution. Porosity is preserved due to the diminished rate of pressure solution in the region possessing enhanced fluid pressure (see frame c).

Figures 40-42 demonstrates a basin-scale example of a CIRF.B2 simulation. The basin is 65 kilometers wide, and evolves to the depth of 8.5 km at 250 MY. Spatial and temporal variations in sedimentation and subsidence rates were used to model the basin. Figure 38a, b and c illustrate lithology, porosity and permeability distribution in the basin, as produced by the basin modeling module alone, at 200 MY of simulation time. The function of the basin modeling is to interpret sedimentation, subsidence, thermal, and sea level curves and generate input and boundary conditions for the system being simulated.

Figure 41e and f show overpressure, porosity, and permeability of the basin after 200 MY of RTM evolution, respectively, according to the physico-chemical processes captured by CIRF.B2. The effect of mechano-chemical compaction is demonstrated in the low porosity and permeability values represented on Figure 41e and f compared to those shown on 40b and c. The resulting overpressuring is shown on Figure 41d. Because hydrostatic boundary conditions were used all around the basin the overpressure is zero along the boundaries.

Figure 42g, h, and i are 276 MY analogs of Figure 41d, e and f. Overpressuring is a dynamic phenomena and responds to dissipation, compaction, and thermal expansion effects.

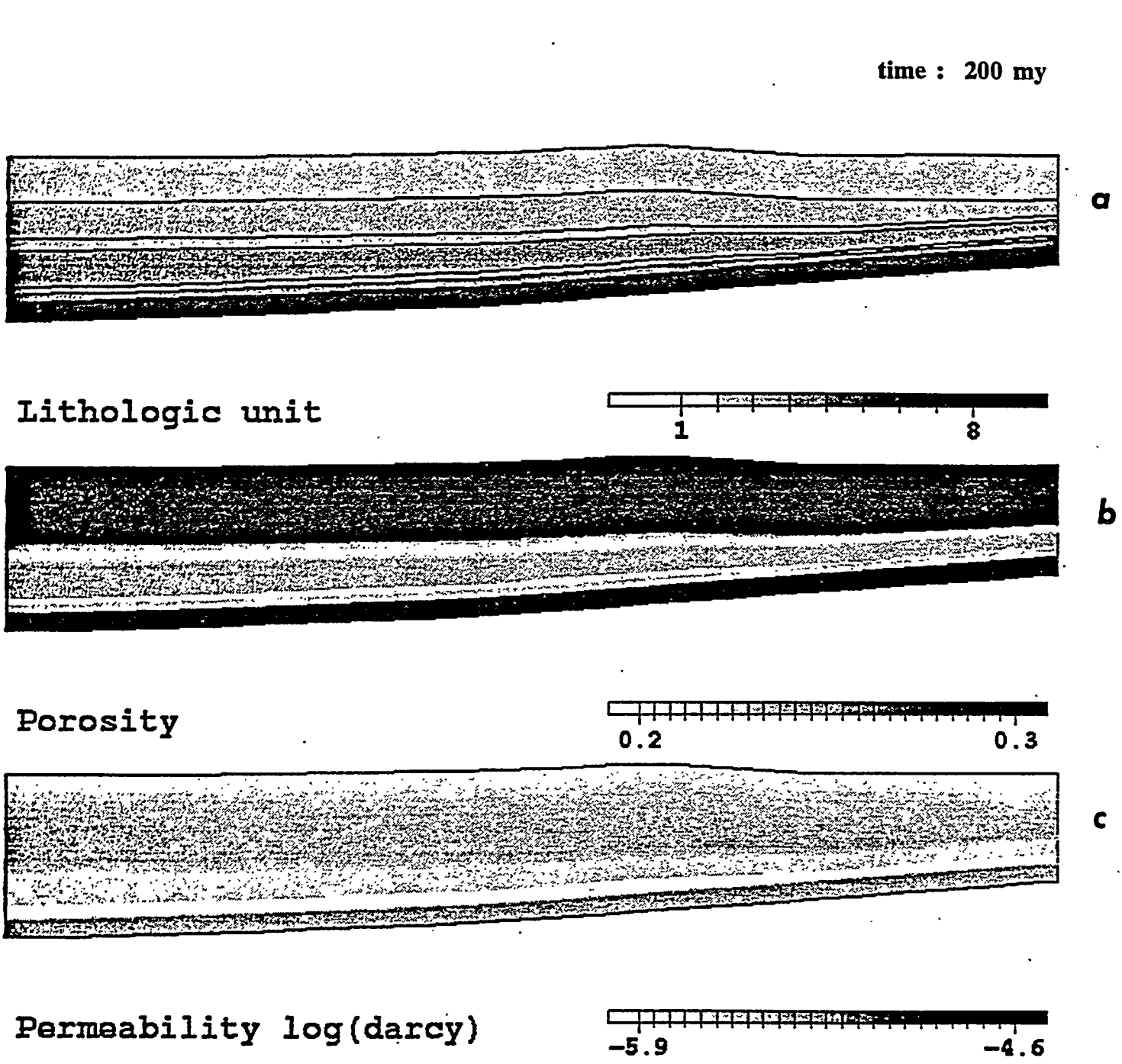

Figure 40-

A two-dimensional simulation of CIRF.B2 using a comprehensive basin evolution history. Temporally and spatially varying sedimentation and subsidence rates were used to simulate a basin evolving from zero to 276 MY, for the deposition of 7 lithostratigraphic sequences using minerald quartz, calcite, and muscovite. Fig. a, b and c represent lithostratigraphic, porosity, and permeability input to the simulator by the history interpretation module, at 200 MY; Fig. d-f are simulation results -- overpressure, porosity and permeability, using the input data of a, b and c. Fig. g, h and i are 276 MY analogues of Fig. d, e, and f, and show the dynamic interplay between compaction and overpressure dissipation. The system is 75 km wide and 8.5 km deep along the left boundary at 276 MY.

time : 200 my

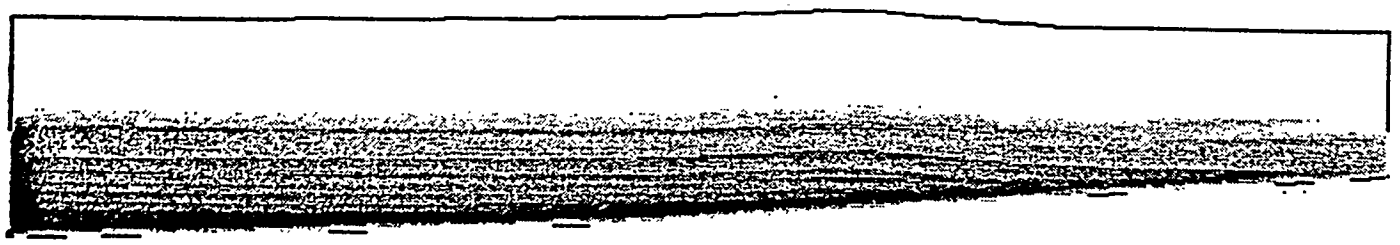

d

Overpressure bar

0 1E+03

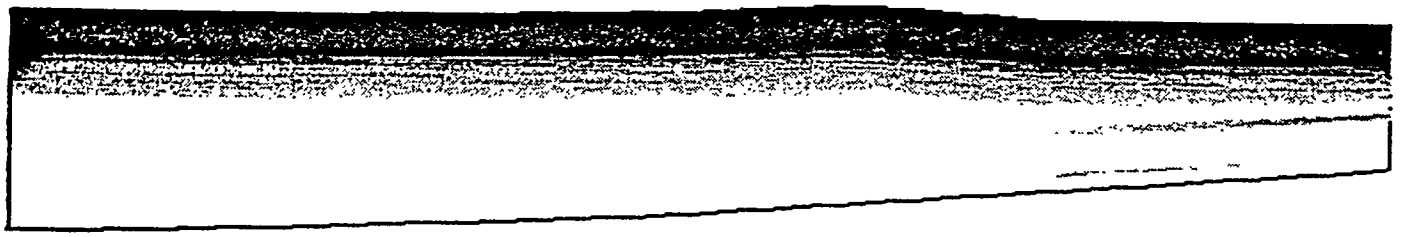

e

Porosity

0.0064 0.3

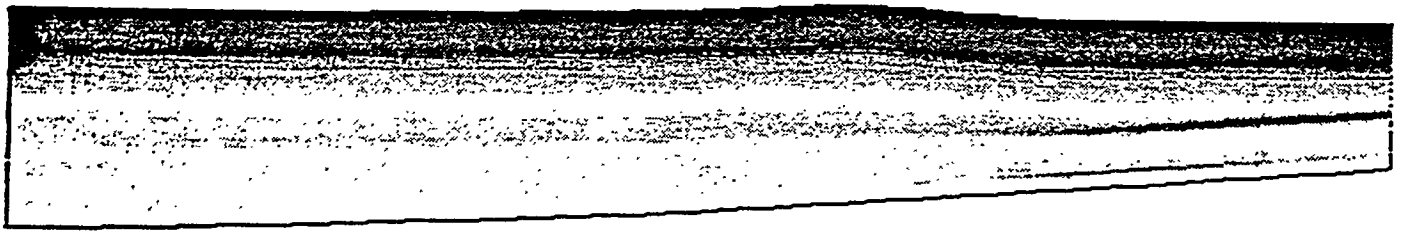

f

Permeability log(darcy)

-12 -4.6

Figure 41-

time : 267 my

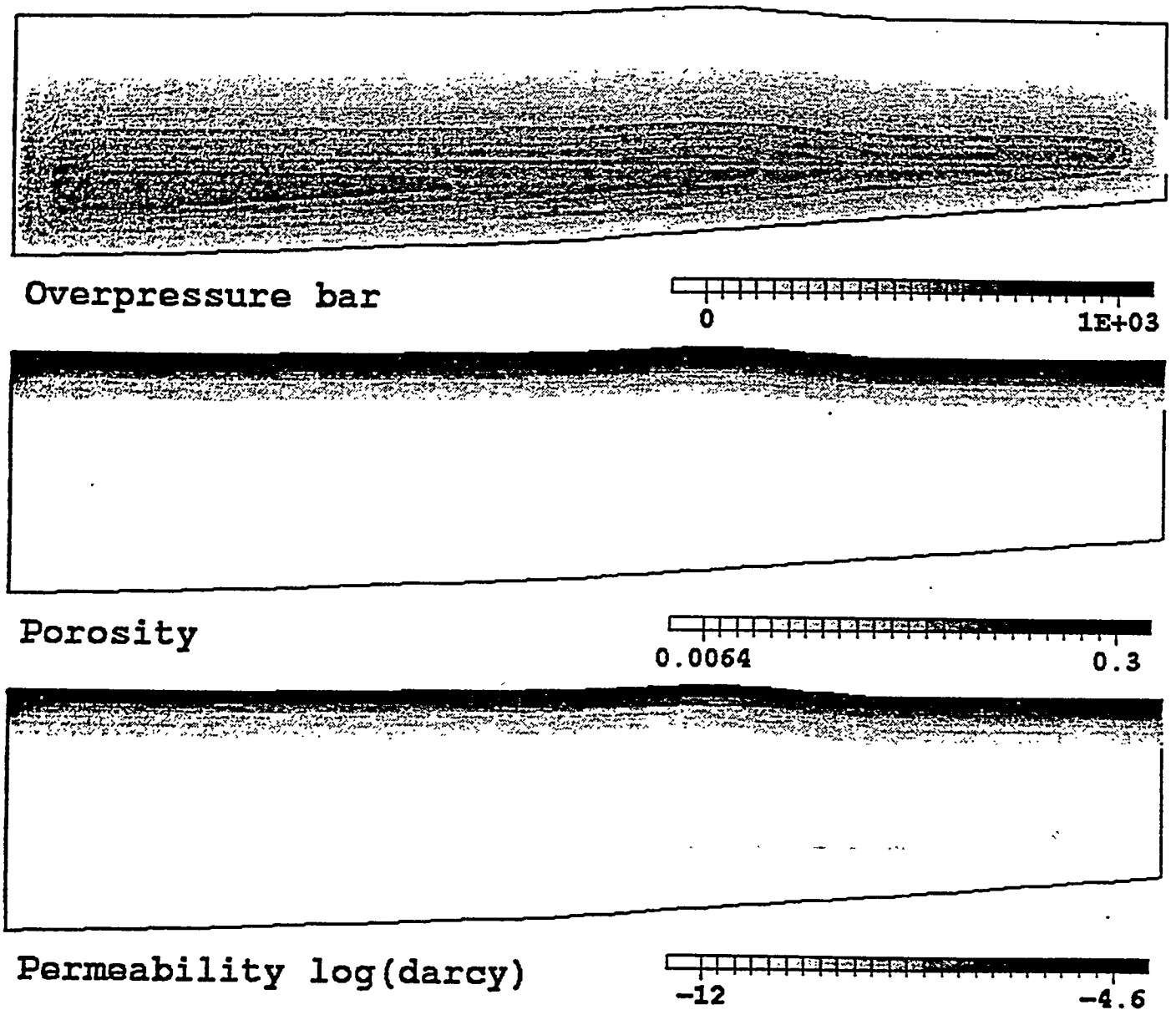

Figure 42-

When the sustained dissipation of overpressure is accompanied by a decreasing mechanical compaction rate, the overpressured compartment may decay to a normally pressured zone. This is demonstrated in Figure 41d and 42g, where the significant overpressure of the lower-most unit at 200 MY is shown to be much less significant at 276 MY, while overpressuring is becoming more significant in the directly overlying region. The same process of overpressuring and normalization may occur in the newly developed overpressured zone. However, overpressure can be maintained if the dissipation rate is maintained at a lower rate than the lower-lying region. Such conditions could be caused by highly impermeable diagenetic seals forming in the lower region accompanied by continual compaction of the overlying region.

Future Objectives

- CIRF.B2 is currently being upgraded to integrate:
  - * hydrofracturing of the rock matrix when overpressure exceeds the least principal compressive stress
  - * thermal maturation models including the ITT and Lopatin models
  - * mass transport of solutes.

Thermal maturation models are being developed to enable us to analyze organic matter maturation timing in a regime involving fluid flow, overpressuring, and hydrofracturing.

The fracture dynamics allows release of fluid pressure by hydro-fracturing, by simulating the corresponding changes in permeability and fluid velocity. Phenomenology for authigenic mineral nucleation has been implemented in the code and is currently being tested. A subroutine has been added which accounts for grain rotation as the grain aspect ratio changes; this allows enhanced grain dissolution at the free-face rather than the vertical

contact in order to accommodate the lithostatic load. This subroutine is currently being tested. Work has begun on the next generation of the textural model, which allows interaction of grains of different mineral species that are in contact. The current model assumes that all grain contact interactions occur between two grains of the same mineralogy. This module accounts for the fact that pressure solution dynamics, notably thickness of the water film and competition for solutes, depend on the mineral composition of the grain with which the grain of interest is in contact.

Three-Dimensional Basin Simulator

CIRF.B3

A basin, with its sedimentary complexity, is a three-dimensional system. A numerical simulation of the fully coupled reaction-transport-mechanical (RTM) processes within it has previously been considered unfeasible. We have now developed and implemented numerical schemes that make this possible. As a result, we have made great progress in developing the capability to predict the location of abnormal pressures, porosity and fracturing, and character of seals and reservoirs within a basin.

The RTM processes incorporated in our three-dimensional basin code are the same as those for CIRF.B2 given in the previous section (also see Appendices A-E). The simulator CIRF.B3 is now being tested and new modules are being integrated. We believe that most major computational difficulties have been met and we will soon be able to simulate the basin evolution, in particular, the spatial distribution of fractures and seals.

Preliminary Results

A number of preliminary simulations of CIRF.B3 have been carried out for the purposes of diagnosis and to demonstrate its ability to make the predictions required for this project.

Genesis of a Basin Scale Overpressured Compartment

A simulation of a basin scale overpressured compartment has been accomplished. A sample simulation is shown in Figures 43-46.

Figure 43 shows a map view of the elliptical simulation domain, showing a fault imposed on the system. Figure 44 shows a schematic cross-section of the simulation domain along the axis AA' of Figure 43 that shows the various lithologies added to the domain during sedimentation. This simulation was a test problem that we designed to evaluate the code. Figure 45 shows the results of one simulation after a time interval of 10 MA involving rapid sediment loading, a 4 MA period of gradual sediment input slowing and a subsequent long period of tectonic quiescence for the remainder of the simulation. A bottom seal formed that followed an analog of a Devonian shale. The top of overpressure formed via a diagenetic seal at around 3 km through pressure solution-mediated compaction. This simulation, involving about 300,000 grid nodes, explicitly calculated overburden stress, a full three-dimensional computation of the fluid pressure, and pressure solution-mediated compaction for user input sediment infilling, basement subsidence, and thermal history.

Figure 45 shows the pressure at 12 MA in the form of overpressure isosurfaces of 200 (a) and 500 (b) bars. These figures are color coded such that the points on the isosurface which are at highest elevation are orange-brown in color and the lowest are blue. The color spectrum indicates intermediate depths on the points of the isosurface. This graph was made using the AVS-based graphical analysis tools we have developed.

The technical triumph of this simulation is that at each time step all variables converge to self-consistency including the material-fixed (moving) grid, the fluid pressure and composition, the grain shape and degree of overgrowth, the (texture dependent) permeability, and the overburden stress. This was made possible due to our pressure module which solves the equation of Darcy flow for a compressible fluid using a mixed method that combines grid refinement, and a partially direct and partially iterative linear solver that

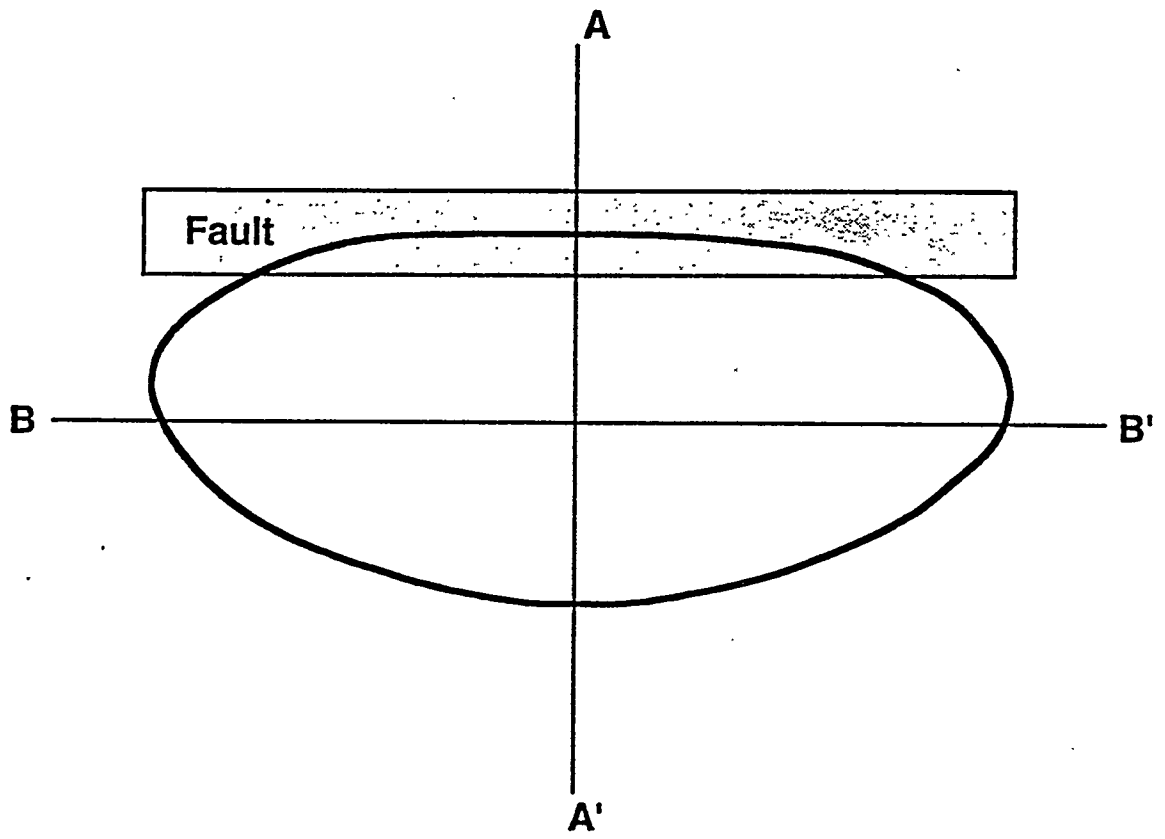

Figure 43- Map view of simulator test case showing cross-section lines A-A' and B-B'. Figure 44 shows cross-section corresponding to A-A'.

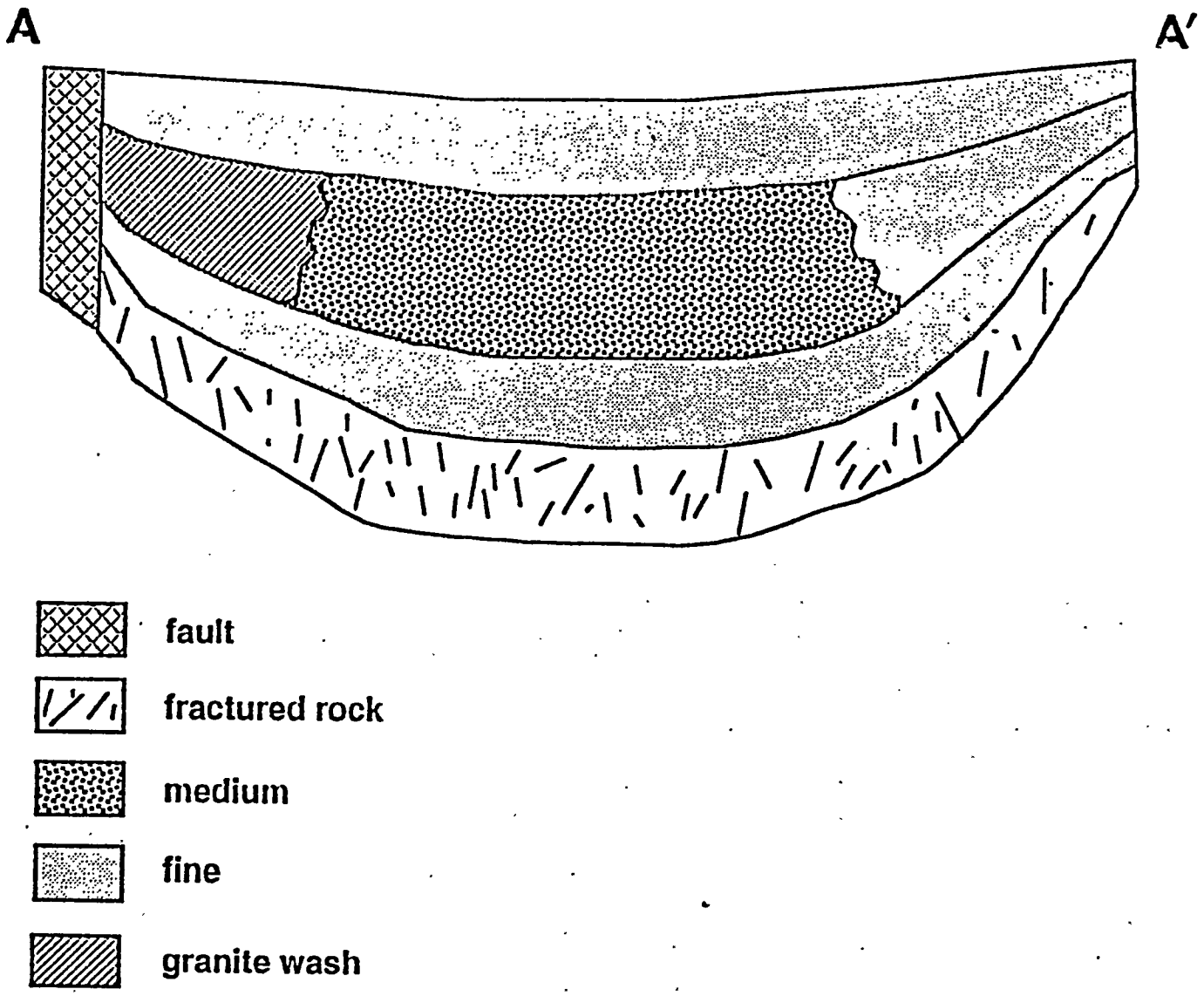

Figure 44- Schematic basin cross-section used for modeling study. Cross-section line along line A-A' in Figure 43.

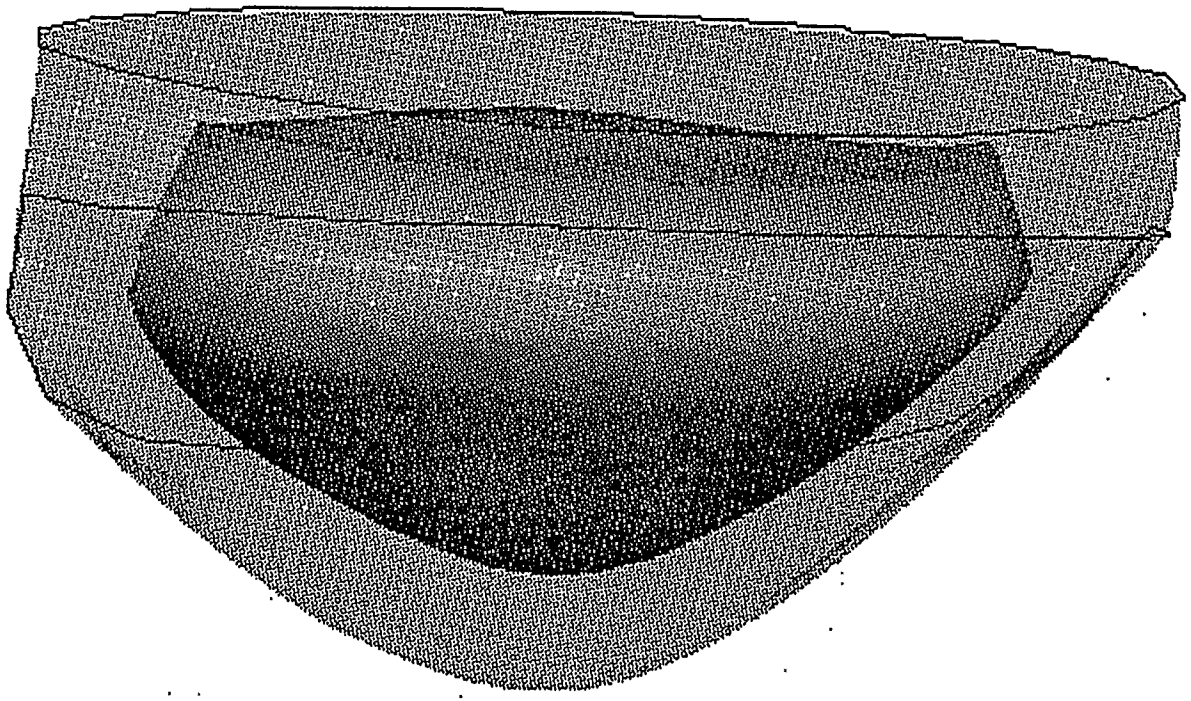

Figure 45- Results of a simulation of a demonstration model. In plan view, the domain is elliptical with dimensions 200x100 km with a sea level of about 0.25 km and a maximum thickness of the sediment pile of 7.2 km for the time slice shown. Figure illustrates the pressure isosurfaces for 200 bars.

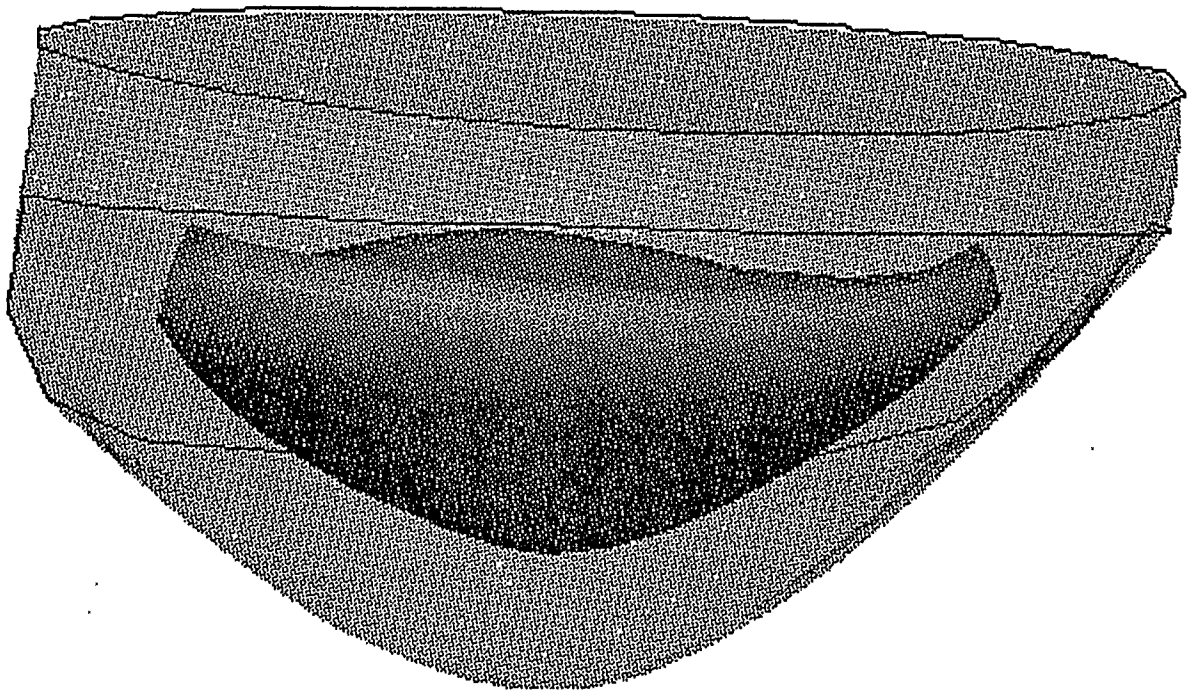

Figure 46- Results of a simulation of a demonstration model. In plan view, the domain is elliptical with dimensions 200x100 km with a sea level of about 0.25 km and a maximum thickness of the sediment pile of 7.2 km for the time slice shown. Figure illustrates the pressure isosurfaces for 500 bars.

solves the full three-dimensional hydrologic problem: The use of this solver surmounts the difficulty of the extreme basin aspect ratio and large range (as many as nine orders of magnitude) of permeability. Also our calculation employs a mass-conserving, finite difference algorithm applied to a moving (rock material point-fixed) grid.

To make the code capable of solving even more lithologically complex problems (the simulation of Figure 45 having 7 distinct formations), the code is being parallelized on the Intel Paragon and other systems via a domain decomposition scheme. The full parallelized code will be completed by early 1995.

Complex Mineral Chemistry Interactions

The development of seals, preservation of porosity and permeability, and the cementation of fractures are strongly influenced by detrital and authigenic mineral content. Ten or more minerals and many more aqueous species are commonly present and couple strongly via fast (equilibrated) and finite rate (kinetic) reactions. Mineral reactions can occur on free-faces and at grain-grain contacts (under stress mediation) and can be strongly influenced by clay coatings and the mineral of the composition grain with which a given grain is in contact.

CIRF.B3 has now been upgraded to include chemical generality and to use an extensive built-in kinetic and thermodynamic data base. In developing CIRF.B3, extensive use was made of the chemical kinetic modules and data base already developed for CIRF.B2.

We illustrate here the use of the model via simulations of a basin with relatively simple sedimentation and subsidence histories (Figures 47 and 48).

In the first simulation, the domain was 334 x 178 x 3 km. The maximum depth of the domain was 3.5 km. Lithologic units present were a siltstone, two very fine sandstones, a fine sandstone, and a coarse sandstone. Minerals present were quartz, K-feldspar, and

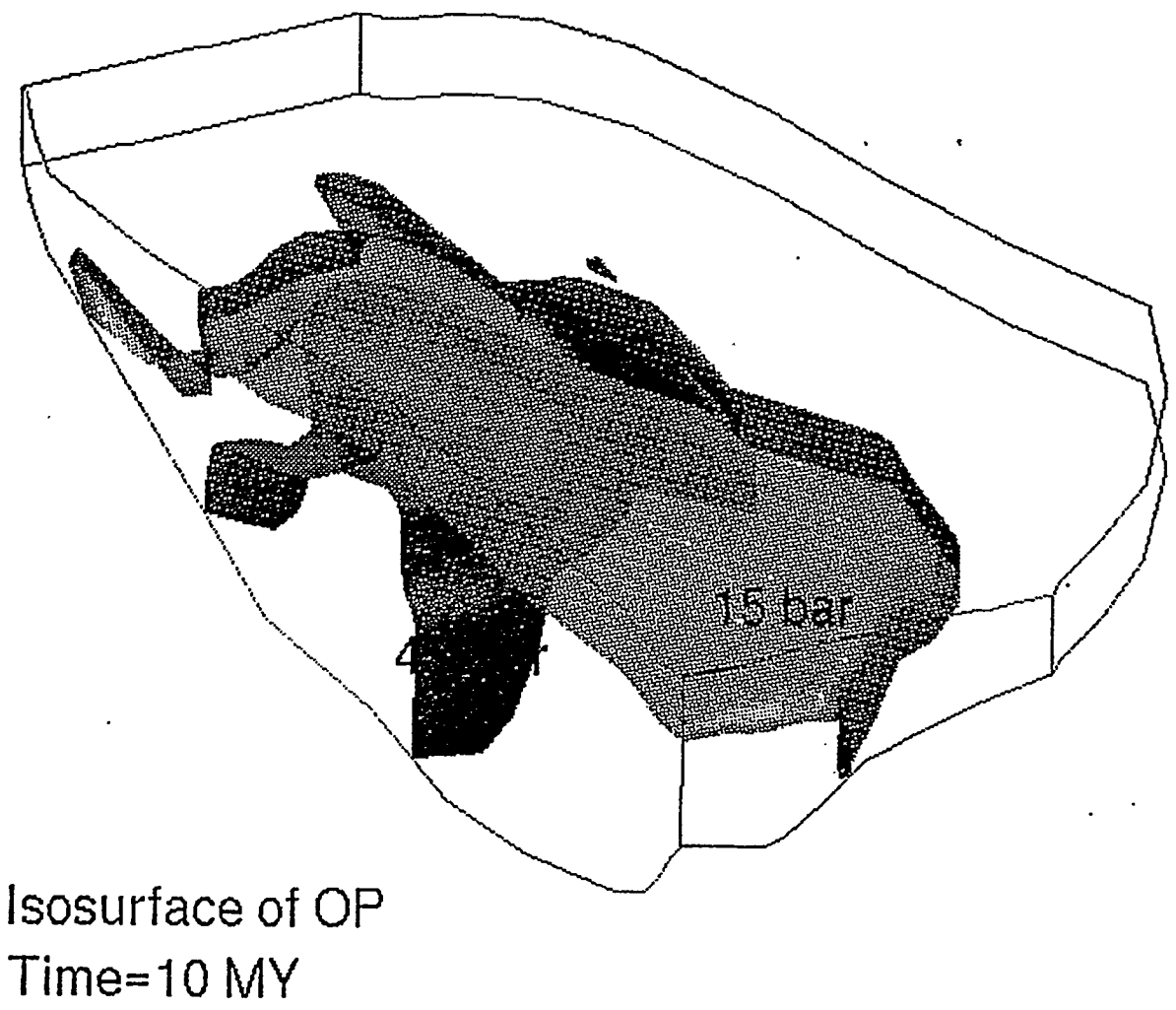

Figure 47- Overpressure isosurface at time=10 million years

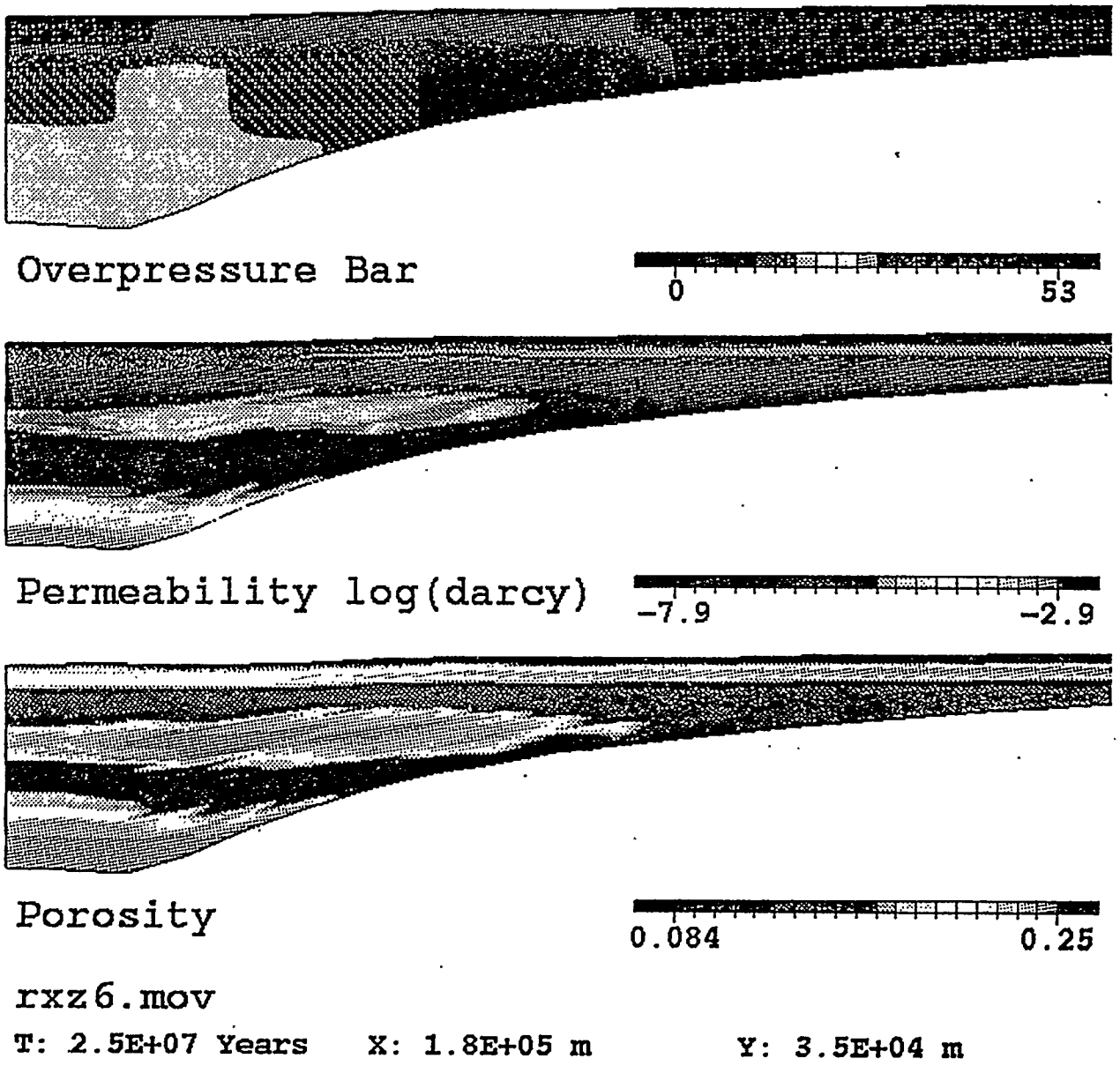

Figure 48- Cross-section through the 3D domain showing relationships between porosity, permeability and overpressured conditions.

muscovite. The boundary condition for fluid pressure was chosen such that the bottom and sides are mass-conservative while the top is maintained at hydrostatic pressure. The subsidence velocity was 22.28 m/MA for t<=22.5 MA, 12.19 m/MA for 22.5<t<=43 MA, and 17.88 m/MA for t>43 MA. The simulation was done on an IBM RS6000.

Figure 47 shows isosurfaces of overpressure of 40 bars and 15 bars at 10 MY of simulation. Overpressure developed because of compaction and thermal expansion. The overpressure is contained because of the formation of diagenetic seals arising through pressure solution-mediated compaction. The configuration of the seals is associated with the interplay of sedimentology and pressure, temperature dependent and texture dependent compaction and overgrowth. Figure 48 is a cross section of the 3D domain showing the inter-relationships between porosity, permeability and overpressure.

(1) A key element of overpressure generation and preservation is basin stress. Solid estimates of stress distribution and its history are required to calculate mechanical and chemical compaction that can generate formation overpressure. Because fracturing occurs when fluid pressure exceeds the least compressive stress, estimates of the time of creation, growth, healing or closure, as well as orientation of fractures rely on estimates of stress distribution and history. In turn, resulting fracture permeability can lead to overpressure loss, escape of fluids from compartments, or the creation of economic tectonically fractured reservoirs in tight sandstones. In short, the ability to estimate stress history based on available data on the overall tectonic history of a basin is a key element of a predictive model of reservoir location, fluid pressure, heterogeneity and producibility.

Two distinct simulation techniques have been attempted. One solution technique is similar to that used by us to calculate fluid pressure. A second stress solver is being developed based on a moving finite element approach. This finite difference stress module is presently being tested on simple cases where mathematically exact results are available so that remaining program errors can be detected and improvements in the solution technique may be developed. Along with testing the mathematical correctness of the finite element

incremental stress solver, we are also determining the optimal preconditioning and linear solution technique to be used.

We have implemented a full three-dimensional stress calculation based on incremental stress theory and on a nonlinear viscous model of plasticity (see Appendix D). The code accepts as input the tectonic motion history of the basement rock. A crudely estimated version of this data is available for many basins based on their general type and chronostratigraphy (and certainly is true for the Piceance region).

(2) The addition of a general three-dimensional sediment inputter to the code has been completed and is being tested. It accepts data about sedimentation, subsidence, and thermal history. More specifically, input data includes:

a) subsidence and sedimentation history (rate, mineralogy and texture);

b) distribution of heat flux at the bottom of the simulation domain, which can change with time; and

c) sea level change history.

A difficulty of sediment history data input is the geometric complexity of the chronostratigraphy. We have devised a novel approach to this problem that greatly reduces the difficulty of going from the data to the program. The strategy is as follows:

a) Well data at discrete map locations are put into a data bank.

b) Isopach maps are computer scanned or drawn with a standard color PC drawing program. In either case these maps are manipulated on the PC and a color TIFF file is created for a series of two spatial dimensional chronostratographic time slices (maps).

c) Our adaptive grid program (see following sections and Appendix I) uses the TIFF file to directly adapt a sediment input and computational grid that refines the grid at the periphery of beds to capture rapid changes of texture across the bed interface.

d) The well sites are located on the adapted grid and an interpolation is carried out in grid index space (not physical space) so as to fill all space with detailed textural data in a way that respects all rapid texture changes across grid boundaries.

Implementation of this method of model development just began in the last quarter of the first year and should be completed in about one more quarter.

Work continues on the finite element stress solver. The elastic module has been coded and tested and has a plasticity module. Preliminary comparison of the predictions of the finite element code with analytical solutions for simple cases or for published results, suggest that the second order finite element method being used is ideal for simulating basin stresses and deformation.

Data Analysis and Data Base

Burial and thermal histories were developed for 18 sites in the Piceance Basin (Figure 49). The burial history curves, temperature history curves, and vitrinite maturation profiles along with the data sets (which include age, burial depths, elevations relative to present-day sea level, geothermal gradients, and paleotemperatures at depth through time) are given in Appendix G. The burial history data and geothermal gradients for the various locations were assembled from published reports (Lorenz, 1985; Johnson and Nuccio, 1986; Nuccio and Johnson, 1989; Johnson and Nuccio, 1993 - see Appendix F for references) and the present-day depths were verified using geophysical logs. Geothermal gradients were chosen to agree, as closely as possible, with the modern-day gradients mapped by Johnson and Nuccio (1986; 1989). These authors assumed that the modern gradients had persisted in the basin back through the time of Mesaverde deposition (74 MA). The appropriateness of the chosen

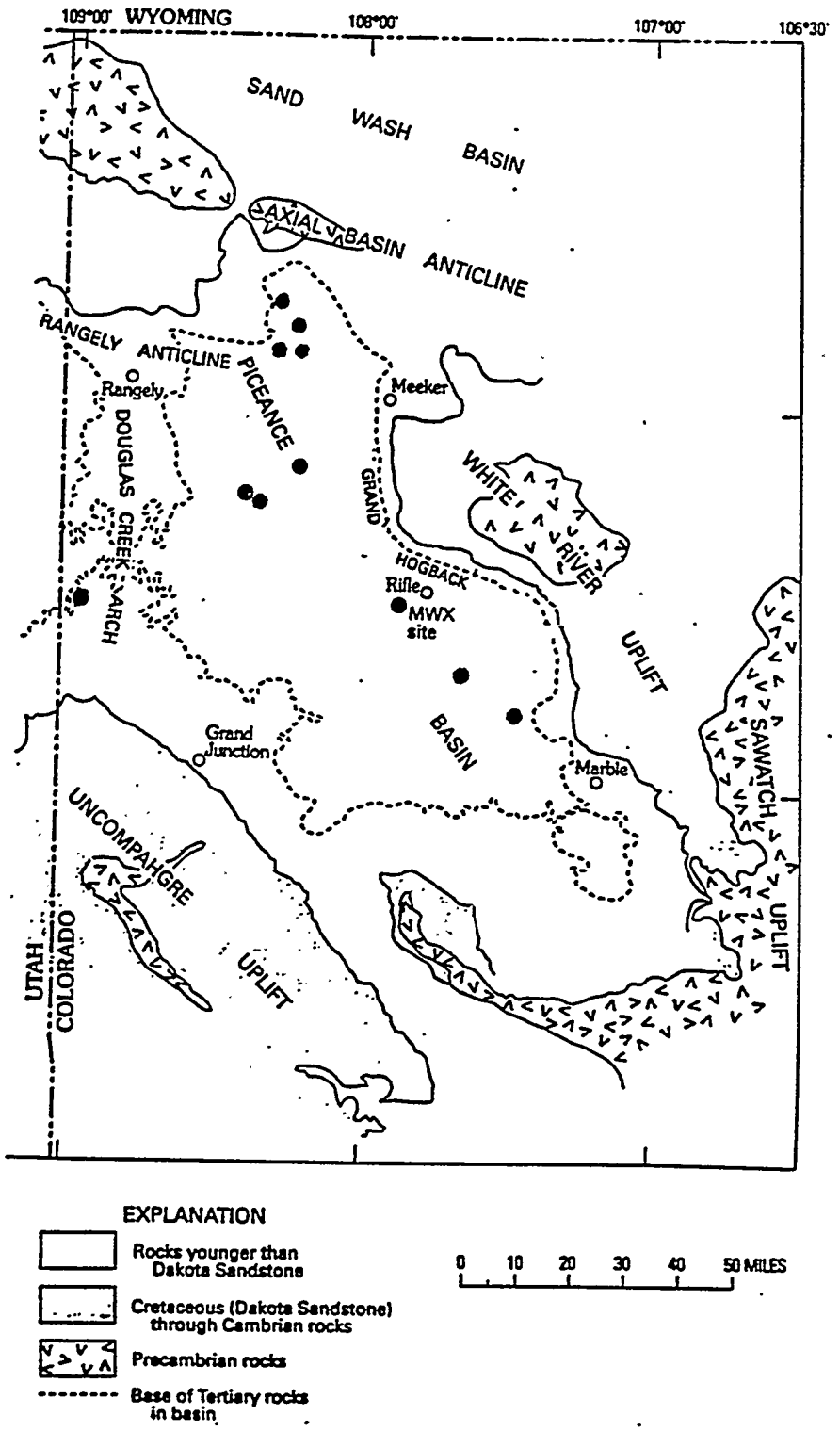

Figure 49- Map of the Piceance Basin showing well locations for which burial and thermal histories have been compiled. (figure modified after Nuccio and Johnson, 1993)

gradients was verified by comparing the measured values of vitrinite reflectance (R_o) from each well site with those calculated using the parallel reaction kinetic model EASY%R_o (Sweeney and Burnham, 1990). The measured R_o values recorded the maximum temperature experienced by the organic maceral vitrinite and are generally accepted as valid indicators of the thermal maturity of organic matter in sedimentary rocks. Geothermal gradients were adjusted from the modern-day values if necessary until the calculated and measured R_o agreed. Paleodepths of burial at some sites were adjusted slightly (a few hundred feet) from those estimated from the published curves in order to bring the measured and calculated R_o values into agreement while retaining a reasonable paleogeothermal gradient. Adjustments to the thermal gradients were made by either increasing or decreasing the paleogradient prior to 30 MA (Table 2), the approximate time at which significant changes occurred in the magmatic and tectonic styles of the basin (Lorenz, 1985). The gradients at all sites for the time period from 30 MA to the present (Table 2) are in general agreement with the modern gradients mapped by Johnson and Nuccio (1986) and Nuccio and Johnson (1989). These data will be further evaluated and adjusted if necessary as more data become available during the course of this study.

A spreadsheet file (Table 3) containing heat flow data for the Piceance Basin as well as thermal conductivity data for 10 lithostratigraphic units representing the time interval from 75 MA to the present was compiled from Law and others (1989). These data will be used in the basin simulator to model the temperature distribution through time.

Several other spreadsheet files were compiled from Sandia reports that contain data on Mesaverde rocks to be used for comparison with the modeling results. These include the following: (1) porosity and permeability data for sandstones, (2) rock-eval data for coals and organic-rich shales, (3) water saturation data, (4) gas composition, and (5) cation exchange capacity.

A petrologic database was created for use in simulations, using data from the MWX site. Over 500 entries containing 25 variables were entered into several spreadsheets. Each

Table 2-
Preliminary thermal gradients at 18 well locations in the Piceance Basin (See Figure 49 for well locations).

Map Symbol	Location (T, R)	Before 30 MA (°C/km)	After 30 MA (°C/km
MWX	6S-94W	25.0	45.6
1	2N-97W	29.0	29.0
2	3N-96W	25.0	29.0
3	4N-97W	29.0	29.0
4	2N-96W	29.0	29.0
5	3S-97W	36.5	36.5
6	3S-97W	36.5	36.5
7	2S-96W	36.5	36.5
8	10S-90W	45.6	45.6
9	9S-92W	45.6	45.6
11	1N-100W	40.0	32.8
12	6S-90W	31.0	36.5
13	5S-100W	32.8	43.7
14	1S-100W	32.8	32.8
15	7S-99W	29.0	43.7
16	2S-98W	36.5	36.5
17	11S-93W	36.5	36.5
18	9S-95W	47.4	47.4

Table 3-
Heat flow and lithologic thermal conductivity data for the MWX site

Thermal Conductivity (W/mK)	Initial Data	Modified Data
Basalt	3.0	3.0
Uinta-Green River	3.0	1.7
Green River	1.0	1.7
Upper Wasatch	2.0	1.7
Middle Wasatch	2.0	1.7
Lower Wasatch	2.0	12.0
Upper Williams Fork	3.9	12.0
Lower Williams Fork	3.9	1.8
Cameo Coal Zone	1.1	1.8
Iles	3.9	1.8
Heat Flow (mW/m^2)	64.0	67.0

spreadsheet is included (Appendix H) which averages values over each interval, as well as units within each interval in some cases.

Data were taken from the appendices of the Sandia Laboratory reports on four intervals at the MWX site; the marine, the paludal, the coastal, and the fluvial intervals (Multiwell Experiment Project Groups, 1987, 1988, 1989, 1990). Each report contained petrographic data sheets from every thin section analyzed. The data on the petrographic sheets contained modes of major and minor detrital minerals, clay minerals, and other authigenic minerals, a porosity estimate, range of and average grain size for each sample, sorting, and petrographer's comments. For the purpose of expediting the completion of a basic database, information on minor and trace detrital and authigenic minerals, qualitative estimations of clay compositions, and detailed comments were not included in the database, because these are considered less important in basin diagenetic processes. Included in the database are the textural parameters (grain size range and average, sorting and angularity of grains) and porosity and modes of the major detrital and authigenic minerals. A scheme was developed to quantify semi-quantified clay mineral modes; another scheme is being developed to assign mineral composition to the lithic fragments category.

The purpose of developing this database is to have reasonable estimates of lithologic composition of the rocks used for simulations. The codes require textural and compositional input because lithology is an important factor influencing reservoir evolution. The mineralogy of the sediments affects the precipitation and dissolution of grains, as well as the chemistry of the pore waters. Grain textures affect the rates at which diagenetic processes occur. Lithologic characteristics are strongly coupled with mechanical processes that are occurring. For example, the development of fluid pressures affected by external forces on the system (tectonics). Any model that attempts to predict the distribution and timing of fracturing based on processes occurring from within, as well as external to the basin, must consider the lithology of the rock and the lithologic changes that occur during diagenesis. This data, as well as data on mineral paragenesis (to be collected using a petrographic image analysis system) will allow the model to be calibrated.

At this point, the petrographic data base has a minimum of important information for the Mesaverde Group. It would be beneficial to have basic petrographic data from the Wasatch Formation and the Green River Formation, preferably from the MWX or Rulison Field area, as well. Lithologic data from the Mancos Formation would also be useful, although the kind of data needed is likely not available. Of secondary importance would be locating other sites in the Piceance Creek Basin with general lithologic information to verify lateral lithologic variations across the basin.

Organic geochemical data for the paludal interval of the Mesaverde Group have been compiled, evaluated, and found to be adequate for modeling.

Mineralogic and textural data, and burial history information compiled at the MWX site have been formatted for preliminary one-dimensional runs using CIRF.B2. Burial history information at eleven sites, and grain texture information from the MWX site are being formatted for preliminary runs using CIRF.B3.

CIRF.B3 is written to accept sediment, basement/basin bottom and ocean depth data on a regular rectangular grid in the horizontal plane. We are using a software package that takes the available data (i.e., at the various ("randomly placed") well sites) and interpolate and extrapolate it to the regular grid required by CIRF.B3. The procedures we are working out will also allow us to relatively easily apply the isopach maps being developed by ARI personnel to our modeling of the Piceance Basin.

Organic Reactions and Multiphase Flow

Introduction

The generation of overpressures and fractures may be dramatically affected by the presence of nonaqueous fluids (oil or gas). The generation of these phases from kerogen or other petroleum phases and coal can cause abnormal pressures because of changes in reaction

volume. Capillarity can alter flow characteristics so as to sustain large pressures, thereby, promoting fracturing. The presence of oil or gas may suppress fracture healing and alter rock rheology.

To account for these phenomena we are developing a number of models, techniques and computational modules. These advances are as follows.

Simple Methane/Aqueous Fluid Liquid-Gas Model

To address the major questions arising in the analysis of fractured gas reservoirs, we are developing a two phase capability for CIRF.B3. The model will account for two fluid phase flow, capillarity, exchange equilibria between the aqueous liquid and the gas, and a methane forming reaction, and will be developed in three steps to insure useful results at an early stage in the project.

Basic Two Phase Model

As suggested in Figure 50 there will be the possibility for two phases in a pore. The gas phase will contain methane and water vapor only. The liquid phase will contain water, methane and the host of ions and complexes arising from mineral dissolution/growth reactions already accounted for in CIRF.B3. The thermodynamics of the aqueous phase is already contained in CIRF.B3.

The exchange equilibrium between the liquid and gas phase will be according to Henry's law for methane and Raoult's law for water. A number of reactions of the type solid carbonaceous matter to methane will account for the thermally induced generation of methane at depth. The two phase flow is by the "black oil" model. This module is approximately 90% complete and when verified will be put into CIRF.B3.

Material exchanges between phases in a pore

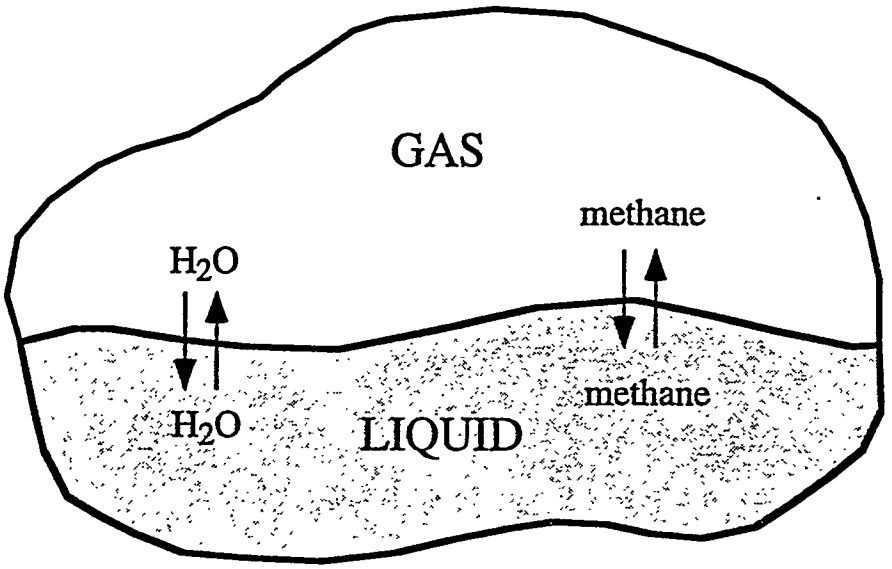

Figure 50- Schematic view of conceptual pore showing gas and water phases and the exchange of water and methane between phases.

More complex chemistry

In this model we allow for more aqueous phase species to equilibrate with the gas. These species include CO_2, H_2O, benzene, and other C_n(low n) species. This will give us a better estimation of pressure and an estimate of gas composition and its coupling to the mineral reaction (for example, calcite in the presence of CO_2(gas)). This has implications for cementation during healing of fractures or when their dissolution-induced apertures increase. At this time, only a thermodynamic module for the exchange equilibrium has been developed extensively (approximately 80% complete). This model is as follows.

Thermodynamics of Gas/Liquid Exchange

The analysis of the phenomena of interest requires an accurate model of the exchange equilibria between a number of fluid phases. Those known by us to have been encountered to date are the gas phase and aqueous, oil, and CO_2-rich liquids (or supercritical fluids). One must be able to calculate automatically which of these phases exist and the saturation (% pore volume) and composition of each. In the context of reaction-transport modeling one must be able to do this for the pores in each macrovolume element for given total number of moles per pore (for all phases) and, self-consistently, determine these total numbers of moles via equations that conspire inter-macrovolume element mass.

Because the number of phases present must be continuously calculated, the interphase exchange equilibrium requires constant testing with all possible phases. To avoid this, we are taking a free energy optimization approach. The appropriate free energy is that which becomes a minimum at equilibrium when system volume (here the pore volume) is constant.

Our approach has several central elements:

* An equation of state relating pressure (p) to temperature, mole fractions and total number of moles (of all N species). An example of the excellent fit that

our equation of state yields for the illustrative cases of water and benzene are seen in Figure 51. We are in the process of obtaining an optimized parameterization of our equation of state that accounts for a wide range of aqueous species and organic species and phases.

* We have devised a minimization method based on the simulated annealing approach to solve the multi-phase exchange equilibrium problem.

A preliminary result of our multi-phase equilibrium simulator is seen in Figure 52. Shown is the case of water, methane, pentane, and CO_2. A preliminary result is seen in Figure 52 for a water, methane-dominated system.

Future Objectives

In order to keep on schedule we are making a very concerted effort to have a simplified organic reaction model in operation by the first quarter of year II. The organic reaction model should be completed in the second quarter of year II. The more complete will be implemented in the next one or two quarters due to the more exploratory nature of this module, and because precise estimates of its completion time frame are more difficult to outline.

Grid Optimization For Simulation and Model Building

Prediction of fracturing in a basin requires the accurate calculation of pore fluid pressure, rock stress, and rock texture. Both the magnitude and spatial distribution of these quantities determine the characteristic and spatial distribution of fractures.

In our preliminary calculations we have found that the accuracy of fluid pressure and rock stress calculations and predictability depend strongly on the spatial resolution of the grid

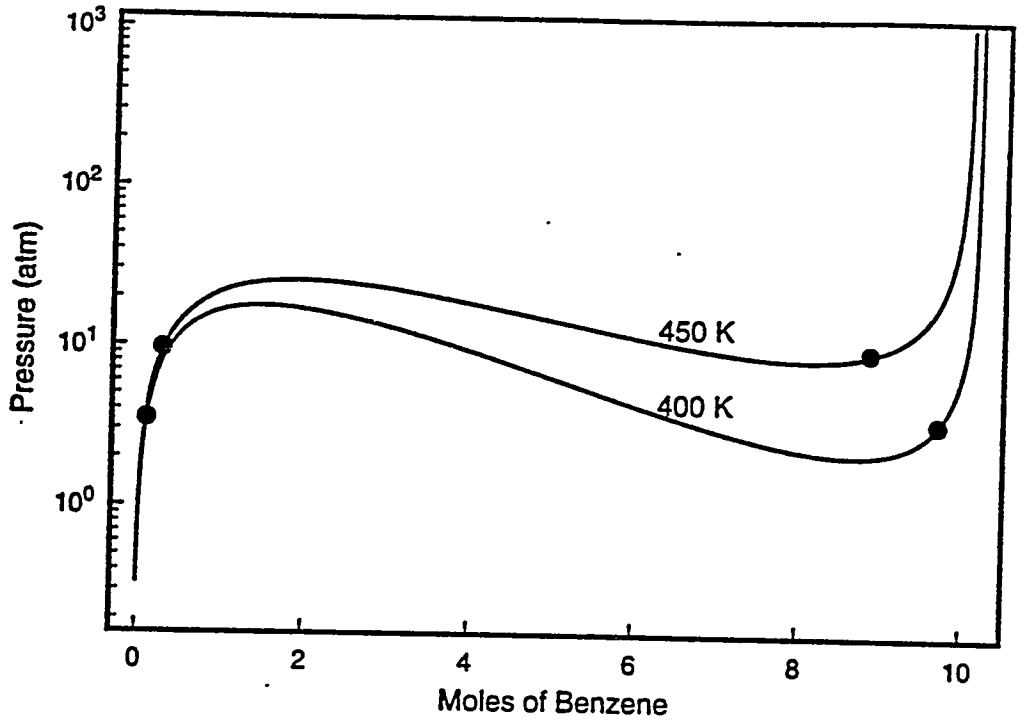

Table. Theoretical modeling of experimental T-P data of Benzene

Temperature (K)	Equil. P(atm) (experimental)	Gas P(atm) (Theoritical)	liquid P(atm) (Theoritical)	Maximum Error(%)
375.00	1.90575	1.87199	2.11010	10.72283
400.00	3.48581	3.49209	3.47124	0.41821
425.00	6.02023	5.99878	5.49900	8.65795
450.00	9.58401	9.33571	9.33421	2.60646
475.00	14.80385	14.85036	15.74981	6.38994
500.00	21.35702	21.60720	22.29405	4.38744
525.00	30.40711	29.22155	25.86751	14.92941

Figure 51- Graphical representation of a Van der Waals equation of state expanded to account for more phase density terms and arbitrary hydrocarbon mixtures. The lower table shows the data table for benzene. Dots on graph indicate experimental results for modeled liquid-gas equilibrium, indicating good agreements between simulated and theoretical values.

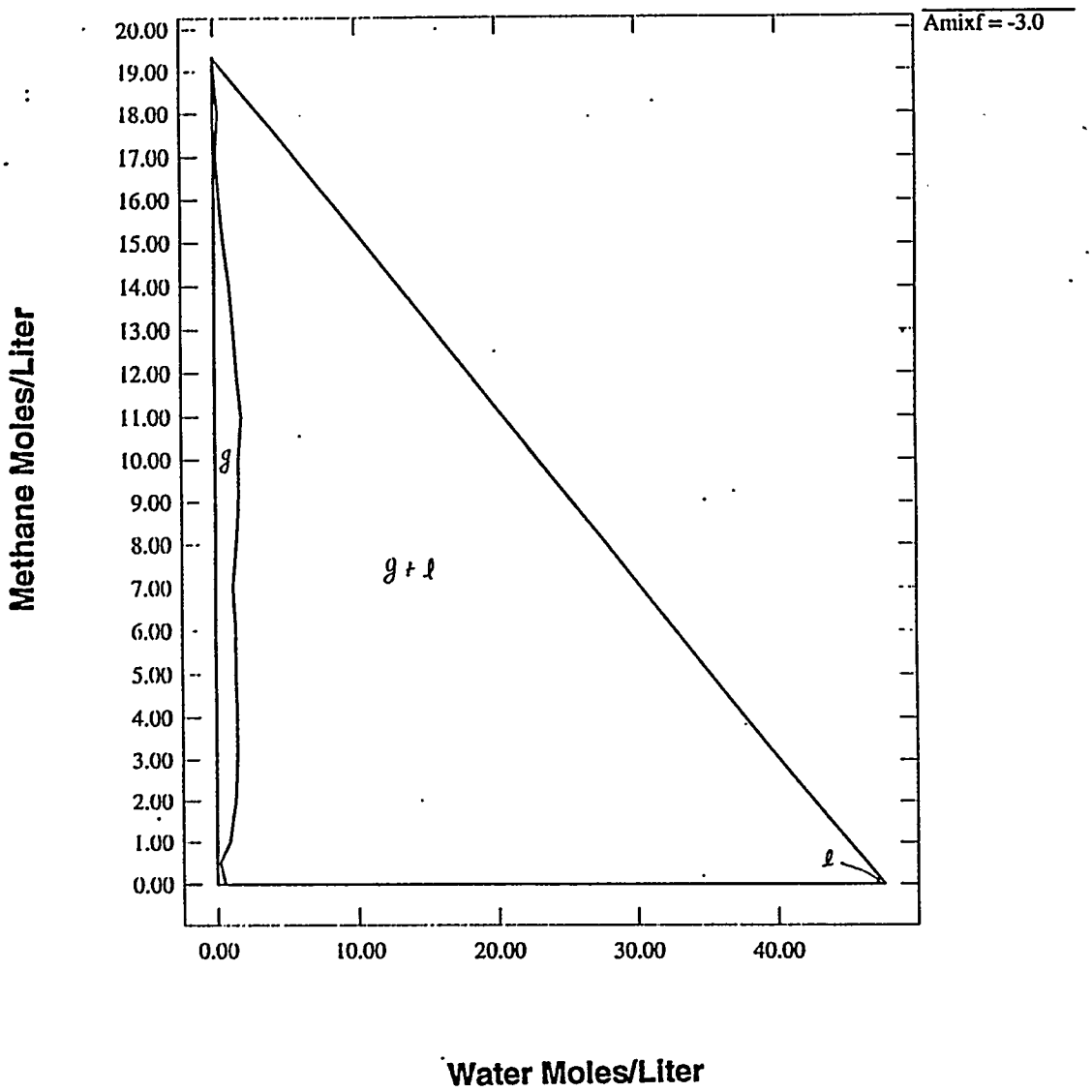

Figure 52- Determination of states of water/methane system using the free energy minimization technique. Shown is the plane of total number of moles of water per pore volume and total number of moles of methane per pore volume. Zones wherein only gas (g), only liquid (l) or two phases (g+l) coexist in the pore are delineated. The volume percentage and composition of each phase is also calculated (not shown). The diagonal line indicates the high density limit of validity for the Van der Waals equation of state used. The temperature of 190 degrees (Celsius) is greater than critical for methane so no liquid exists for low total water content.

on which these calculations are performed. More precisely, it is necessary for the grid to be sufficiently fine in regions where rock properties change dramatically (e.g., at the interface of a sandstone and a shale).

An immediate need for a more precise grid has been encountered in the sediment input module for CIRF.B3. As sediment is added layers of calculational grid must also be added. The gridding we use for our calculation has cubic logic. Thus, space is divided into an array of exactly fitting distorted bricks. One layer of grid has the form of a set of quadrilaterals as suggested in Figure 53. However, in order to capture a set of lenticular sand or other bodies, for example, it is preferable to add the layer of grid in a distorted way so that the quadrilaterals are concentrated at the periphery of a sedimentary feature. An example is seen in Figures 54 and 55.

To address this problem we have adopted a procedure whereby the grid is automatically refined at regions of textural contrast. Our algorithm is unique as required by the special demands of our computational approach for predicting pressure and stress. The approach is as described in Appendix H.

Graphical Interpretation Modules

The prediction of the fracture network and other rock properties by the model is in the form of the numerical values of fracture length, aperture and orientation, porosity, fluid pressure, and other variables at each node of our three-dimensional, irregular brick grid. To visualize this data and compare it to similar data from the MWX site we are developing graphics modules based on the AVS graphics language. There will be three ways to view the data:

* iso-surfaces of chosen variables

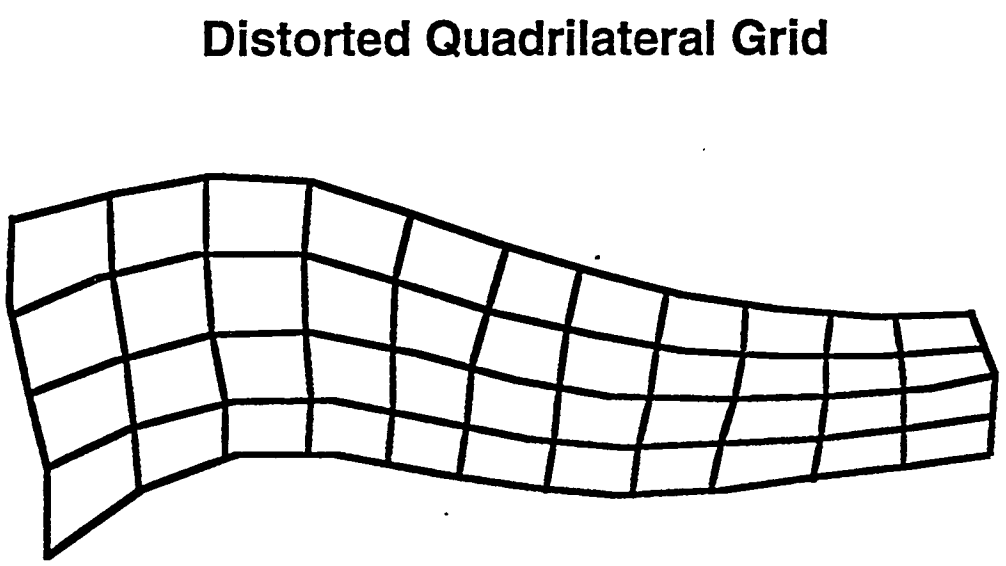

Figure 53- Typical quadrilateral grid. Note how grid attempts to maintain orthogonality despite exterior shape constraints.

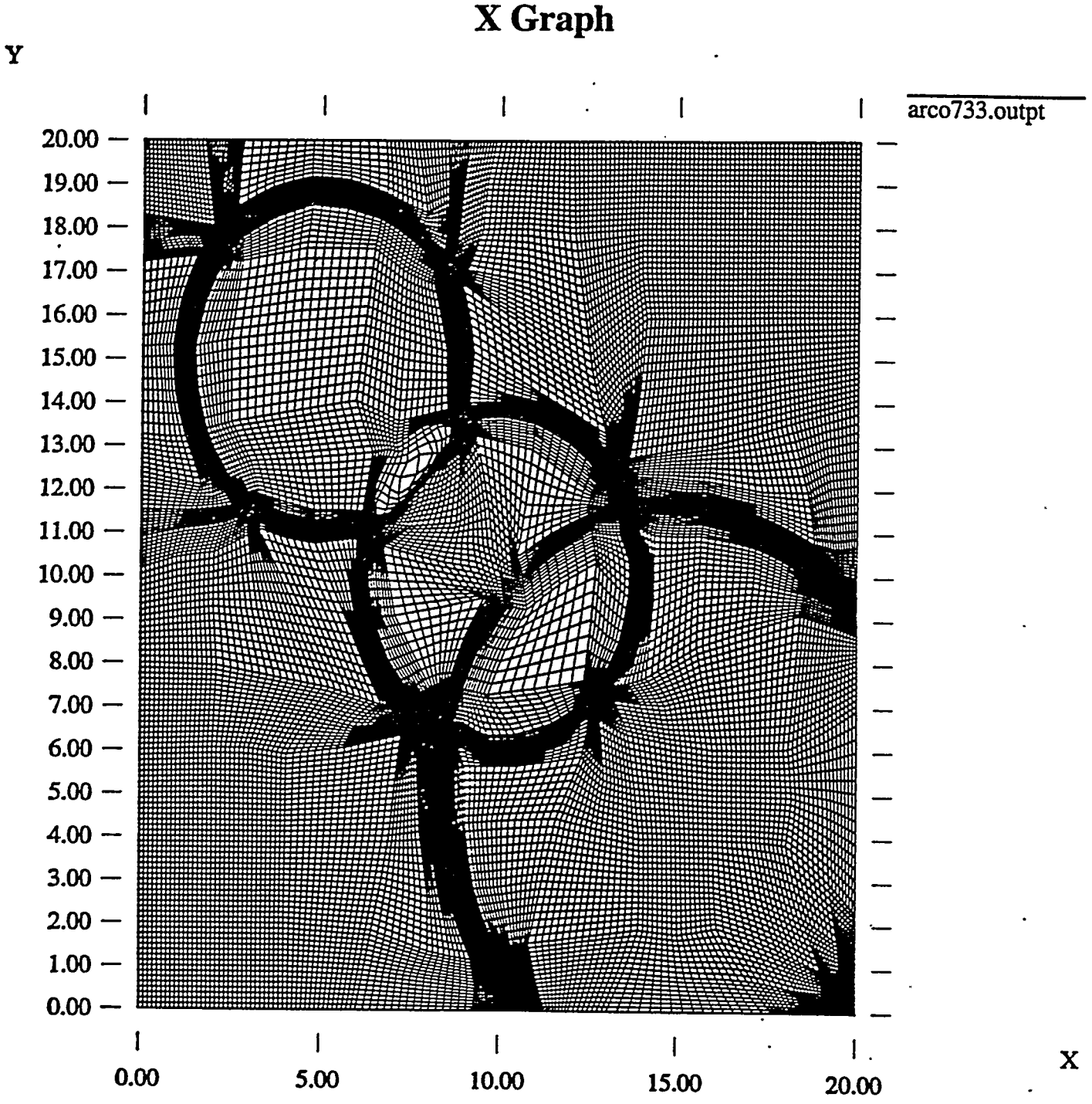

Figure 54- Computationally adapted grid used to capture characteristics of three lenticular sedimentary bodies.

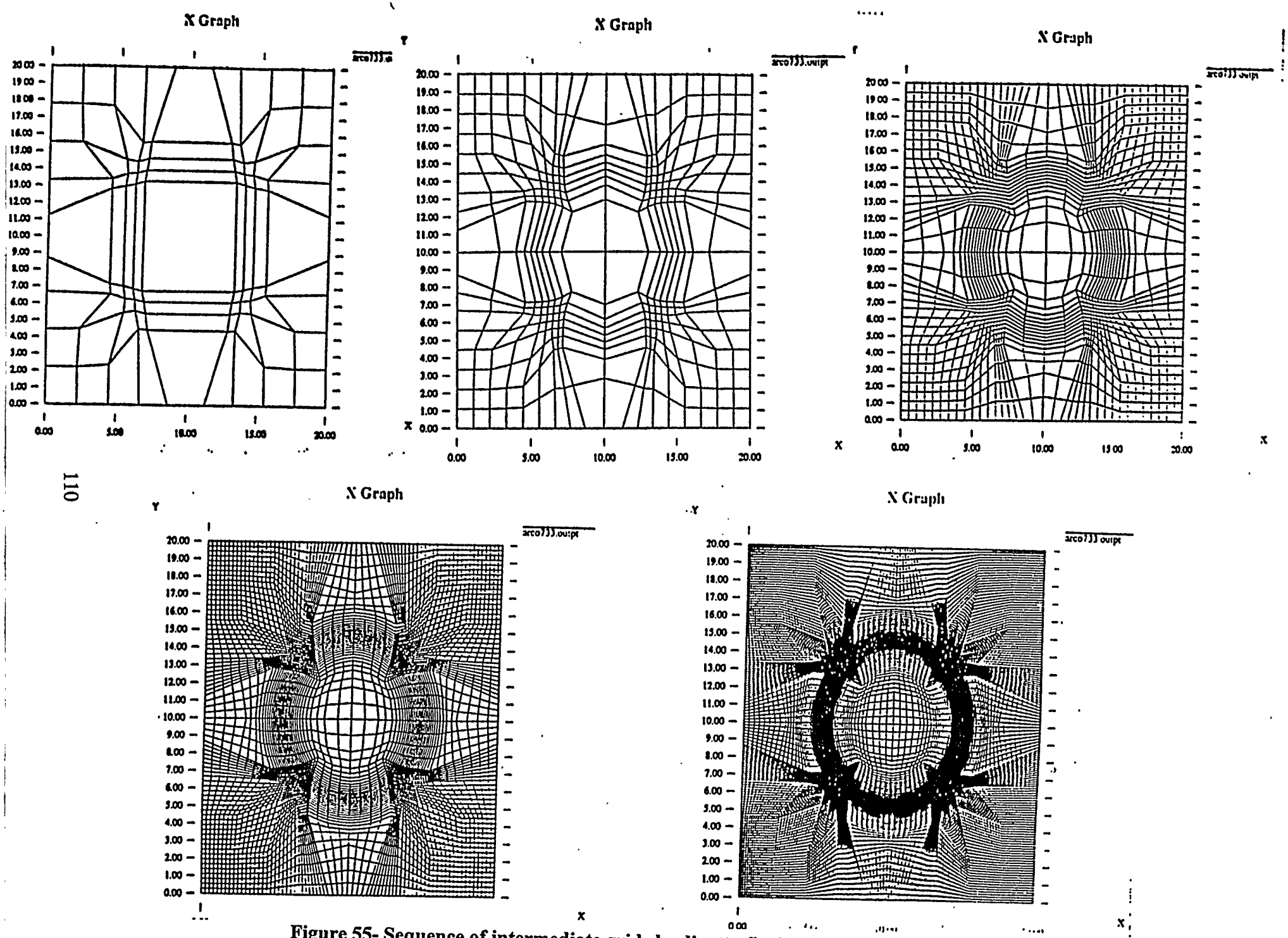

Figure 55- Sequence of intermediate grids leading to finely-adapted grid using our multiple grid-splitting adaption method.

* contour maps of chosen variables on specified planes cutting through the basin

* pressure-depth or other one-dimensional plots along a graphically chosen "well" at any point in the horizontal plane.

At this time the iso-surface option is complete and gives the results as seen in Sect. II of this report. By next quarter we believe that all three graphics options will be completed except for a relatively minor amount of work needed to make them more convenient to use.

Conclusions

The numerical model being created at Indiana University represents a potent addition to the arsenal of tools used for fractured basin analysis. Through the use of this model, the complex evolution of fracture development and related fracture-controlling pheonomena can be realistically modeled. Because fractured reservoir conditions are critical to the economic development of tight gas sand reservoirs, the ability to determine the timing of fracture genesis relative to gas generation and migration represents a critical piece of information. In the future, a carefully calibrated basin model may provide the framework for a greatly simplified, and less expensive alternative to conventional basin analyses using advanced seismic, drill core, geochemical and geologic studies. In this context, the numerical basin model, when properly calibrated, may represent an advanced method for basin exploration.

ACCOMPLISHMENTS TO DATE AND PROJECT STATUS

The preliminary results obtained from the integrated approach to fracture detection outlined in this report are being applied to understand the origin, location and spatial geometry of fractured reservoirs. At this point in the project, there are two primary tasks that have been addressed. The first of these is a geologic characterization of the basin, and the second is the numerical modeling effort. These two tasks are being conducted in parallel by ARI and Indiana University, respectively. The status of each of these tasks will be

discussed separately. The project is on schedule and all work is proceeding as planned.

Geologic Characterization Of Basin

Geologic characterization of the Piceance Basin is following a systematic basin partitioning approach. The basin has been initially partitioned by identifying gas saturated portions of the basin using a gas-centered basin model. The Parachute and Rulison fields have been studied in detail to determine fracture genesis. These two fields then, represent an analog to use in developing an exploration model for applying fracture detection methods to locate other fractured areas in the basin.

Preliminary assessment of the basin involved delineating the location of gas and water-saturated areas. Because we are only interested in the gas-bearing portion of the basin, this screening is a critical first step in our integrated basin analysis. A detailed basin-scale study of the gas and water-saturated zones has been completed for the Williams Fork, Cozzette and Corcoran sandstones. The majority of the basin is gas-saturated for all three reservoir horizons. A zone of overpressure is found in the east-central basin whose upper boundary is located just above the Cameo Coal Group and whose lower boundary is the top of the Rollins Sandstone. Water saturation is more difficult to unequivocally interpret, however, it appears that all reservoir horizons have been breached to meteoric influx along the basin margins. The differential influx of this water for the different reservoir horizons appears to be controlled by lateral continuity and homogeneity of the different reservoir horizons. Laterally continuous marine sandstones appear to show the greatest amount of meteroic influence while the discontinuous fluvial sands of the Williams Fork appear to be hydrodynamically isolated.

To understand the relationship between production, stratigraphy and structural geology, a detailed field study was performed in the Parachute-Rulison fields. Detailed structural maps and gas field studies at Parachute and Rulison fields show that production is greatest in those areas where small folds are present. Greatest production is found at surfaces of maximum flexure where fracturing should be most intense. Interestingly, the

orientation of the small folds parallel production trends and neither feature lies parallel to natural fractures measured at the MWX site. This relationship suggests that the small structures enhance the existing fracture permeability or create new fracturing. The latter interpretation is preferred, given that the existing models for basin fracturing suggest that fracturing should be equally well-developed everywhere in the paleo-overpressured zone. Because this relationship is not observed, it is more likely that the small structure generate additional fractures, perhaps allowing communication between the existing natural fractures formed earlier. From 2D seismic data, it appears that there is basement influence on the localization of overlying structures. Because of this relationship, we are attempting to characterize both the shallow, thin-skinned deformation and also the basement structural features. The relationship between the thin-skinned deformation and the basement is being investigated by the combined use of high-resolution aeromagnetics and 2D seismic.

Preliminary structural mapping of the basin on several datums (Top Ohio Creek Conglomerate, Top Rollins Sandstone, Top Cozzette Sandstone, Top Corcoran Sandstone) and isopachs for these same intervals have been created. From this work, we are able to clearly document small-scale structural features, similar to those at Parachute-Rulison, that control the development of fractured reservoirs. Additional effort has focused on the creation of regional stratigraphic cross-sections to elucidate the stratigraphic correlations and complexity within the basin. We have established a computer database containing stratigraphic and structural information for all wells in the Piceance Basin. The use of computer-based mapping systems allows us to rapidly generate maps illustrating the relationships between depositional systems and structural features. Analysis of depositional systems is important to identify the relationship between structure and stratigraphy, and to delineate locations where exceptional reservoir sands are located throughout the basin.

Analysis of basement fault blocks and surficial manisfestation of these structures is accomplished by an integrated analysis of remote sensing, high-resolution aeromagnetic data, 2D seismic and subsurface geologic mapping. To date, remote sensing imagery analysis has interpreted linear features for SLAR (side-looking airborne radar) and TM (thematic mapper)

data sets. Preliminary statistical analysis of the linears is underway and the linear features are being investigated by both the structural domain and by the surface bedrock geology in the area where the linear is mapped. It is thought that delineation of linear features trends by these two characteristics will highlight the differences produced by lithology and by linear features that formed at different times. Also, this technique will reveal differences in linear features that formed as the result of different stress regimes operating around the basin. Integration of this interpretation with mapped interpreted faults, joints and other fractures will commence in the near future.

Additional information about basement fault blocks and their subsurface geometry is provided by high-resolution aeromagnetic data. The high-resolution aeromagnetic survey being flown by World Geoscience commenced in early October and is approximately 65% complete. It is anticipated that this survey will be completed by the beginning of November and we will be able to have preliminary intrepretations by early December to integrate with the 2D seismic interpretation. These two geophysical data sets, integrated with the remote sensing, 2D seismic, and structural interpretation, will allow us to delineate the basement fault block geometries and their influence on surficial fracturing.

A complete and extensive reference list on both topical subjects (e.g. tight gas sands, fractures, western basins) and Piceance Basin-specific papers have been collected and synthesized. This computer database of reference materials has been given to several interested operators. We are continually updating this database as more relevant material is accessed.

We have presented two talks on the Piceance Basin. The first addressed the gas and water-saturated zones in the Piceance and the relationship between production and structure in Parachute and Rulison fields. This information was presented as a poster at the AAPG Annual Convention in Denver. An oral presentation was made at the RMAG Biennial Gas Conference in Denver on the use of the integrated exploration methodology for fractured tight gas reservoir detection and optimization. Industry and academic feedback at both

presentations was highly favorable and interest in the project is high.

Numerical Modeling Of Basin

This effort, occuring in parallel with the geologic characterization effort, involves writing and testing of computer code to model the geologic evolution and fracture genesis of the Piceance Basin. The physical, chemical model and computer simulator are to be used in planning and interpreting fracture detection efforts in petroleum exploration.

The simulator is based on the equations of grain and fluid-phase reactions, pressure solution-mediated and mechanical compaction, mass and energy transport, incremental stress rock rheology and fracture kinetics. The coupling of all these processes is fully accounted for in order to yield a fully self-consistent calculation. The simulator is being written in both two (cross-sectional) dimensional and three dimensional versions for preliminary and complete modeling, respectively.

Data from the MWX site has been analyzed and put into a computer data base. This data, augmented by that from ARI, will be used to test and calibrate the model.

Organic reactions and multi-phase flow were not part of the original workplan. Because of its importance to fracturing in the Piceance Basin, considerable time has been expended to account for the effect of thermally generated gas overpressuring on fracturing.

During code improvement, a technology of computational grid adaptation was devised in order to obtain the accuracy in the prediction of fluid pressures and rock stresses needed for fracture prediction. This technology is also providing a key part of the strategy for entering the complexity of sedimentary history for full three-dimensional modeling by allowing the input of scanned isopach maps into the simulation. Graphical analysis tools needed to visualize the results are also being developed.

All aspects of the project are occurring as planned. Preliminary simulation results have been obtained for several of the program modules and these results show close agreement between calculated and known results. This success leads additional support for the correctness of the calculations and verifies the potential utility for a fully self-consistent basin simulator.

REFERENCES

Brown, C.A., Smagala, T.M. and Haefele, G.R., 1986, Southern Piceance Basin Model-Cozzette, Corcoran and Rollins Sandstones, In: Spencer, C.W. and Mast, R.F. eds., *Geology of Tight Gas Reservoirs*, AAPG Studies in Geology #24, 207-219.

Grout, M.A., Abrams, G.A., Tang, R.L., Hainsworth, T.J., Verbeek, E.R., 1991, Late Laramide Thrust-related and Evaporite-domed Anticlines in the Southern Piceance Basin, Northeastern Colorado Plateau, American Association of Petroleum Geologists Bulletin, 75 (2) 205-218.

Gunneson, B., Wilson, M. and Labo, J., 1994, A structural history of the Divide Creek Anticline, Piceance Basin, Northwest Colorado, Poster Session, AAPG Annual Meeting, Spring 1994, p. 160.

Law, B.E. and Dickinson, W.W., 1985, Conceptual model for origin of abnormally-pressured gas accumulations in low-permeability reservoirs, American Association of Petroleum Geologists Bulletin, 69 (8) 1295-1304.

Lorenz, J., 1985, Predictions of Size and Orientation of Lenticular Reservoirs in the Mesaverde Group, Northwestern Colorado, Society of Petroleum Engineers SPE/DOE 13851, in: Proceedings of the 1985 SPE/DOE Joint Symposium on Low Permeability Reservoirs, 23-28.

Lorenz, J. , Warpinski, N.R., Teufel, L., Branagan, P. T., Sattler, A.R., and Northrop, D.A., 1988, Results of the Multiwell Experiment, EOS (Transactions of the American Geophysical Union) v. 69 (35), 817, 825-826

Lorenz, J. , Teufel, L. and Teufel, N., 1991, Regional Fractures II: Fracturing of Mesaverde reservoirs in the Piceance Basin, American Association of Petroleum Geologists Bulletin, 75, 1738-1757.

Lorenz, J. , Teufel, L. and Teufel, N., 1991, Regional Fractures I: A mechanism for the formation of regional fractures at depth in flat-lying reservoirs, American Association of Petroleum Geologists Bulletin, 75, 1714-1737.

Martinez, C. and Duey, H., 1982, Rulison Field, in: Crouch, M.C., ed., *Oil and Gas fields of Colorado, Nebraska and Adjacent Areas*, Rocky Mountain Association of Geologists Publication, Volume 2, 444-449.

Meissner, F.F., 1978, Patterns of source-rock maturity in nonmarine source-rocks of some typical western interior basins, in: *Nonmarine Tertiary and Upper Cretaceous source rocks and the occurence of oil and gas in west-central U.S.*, Rocky Mountain Association of

Geologists, Continuing Education Lecture Series, 1-37.

Mercer, J.C., Frohne, K.H., 1986, Production Characterization of Tight Lenticular Gas Sands in the Rulison Area of Western Colorado, SPE Unconventional Gas Technology Symposium Proceedings, SPE 15248, 1-6.

Peterson, R.E., 1984, Geological and Production Characteristics of the Nonmarine Part of the Mesaverde Group, Rulison Field Area, Piceance Basin, CO, SPE/DOE/GRI Joint Symposium on Unconventional Gas Recovery, SPE 12835, 47-56.

Reinecke, K. M., Rice, D. D. and Johnson, R. C., 1991, Characteristics and Development of Fluvial Sandstone and Coalbed Reservoirs of Upper Cretaceous Mesaverde Group, Grand Valley, Colorado, in: *Coalbed Methane*, Rocky Mountain Association of Geologists Publication, 209-225.

Spencer, C.W., 1987, Hydrocarbon generation as a mechanism for overpressuring in Rocky Mountain Region, American Association of Petroleum Geologists Bulletin, 71 (4) 368-388.

Stone, D.S., 1986, Geology of the Wilson Creek Field, Rio Blanco County, Colorado, in: *New Interpretations Northwest Colorado*, Rocky Mountain Association of Geologists Publication, 229-246.

Taylor, O.J., 1987, Oil Shale, Water Resources, and Valuable Minerals of the Piceance Basin, Western Colorado: the Challenge and Choices of Development, U.S. Geological Survey Professional Paper #1310, 143 p.

Waechter, N.B., Johnson, W.E., 1986, Pennsylvanian-Permian Paleostructure and Stratigraphy as Interpreted From Seismic Data in the Piceance Basin, Northwest Colorado, in: *New Interpretations Northwest Colorado*, Rocky Mountain Association of Geologists Publication, 51-64.

NOTE: Significant amounts of extremely detailed data characterizing the geology and reservoir properties of Rulison field have been collected as part of the Department of Energy's Multiwell Experimental Site (MWX). The texts by Lorenz and Lorenz et al., referenced above, provide a partial listing of the key references for this area.

Additional references for the modeling section may be found in Appendix F

APPENDICES

Appendix A

Multimineralic Model of Pressure Solution Mediated Compaction

A. Park and P. Ortoleva

Laboratory for Computational Geochemistry

Department of Chemistry
Indiana University
Bloomington, IN 47405

Abstract

Modeling the formation of diagenetic pressure seals and fluid compartments requires an accounting of compaction and, in particular, pressure solution-mediated compaction in a multi-mineralic system. A model is proposed here that incorporates a new multimineralic pressure solution-mediated rock rheology with a grain-grain contact reaction rate that accounts for variations of grain geometry and mineralogy. The model is based on the water-film diffusion mechanism. The pressure solution contact rate law is of the diffusion-limited type and is even valid for cases where the diffusion coefficient of a solute along the contact can be different for each solute. Finally, a statistical account is made of the fact that the behavior of the contact between any two grains may differ significantly with the mineral identity of each of the two grains.

I. Introduction

Basin diagenesis involves the coupling of reaction, transport and mechanical (RTM) processes. As these processes can be strongly coupled, a complete understanding of the lithologic heterogeneity, texture, stresses, fluid pressure, and other features of sedimentary basin dynamics is required for the development of an integrated model.

The focus of the present work is the nature of compaction in multimineralic rocks and the resulting changes of porosity and other textural variables over geologic time. The problem is complicated in a number of distinct ways. Those we attempt to address here focus on pressure solution mediated effects as follows:

* Molecular products of the pressure dissolution of one mineral can promote the precipitation or dissolution of others;
* Changes in mineralogy due to reaction will in general change macroscopic poroelastic rock strength and other parameters, and thereby the stress distribution and pressure solution;
* The nature of pressure solution for a given mineral can strongly depend on the mineral identity of the grain with which it is in contact;
* Like for other reactions, pressure solution can be strongly affected by the pressure, temperature and composition of the pore fluid; and
* As mineralogy and texture affect mechanical response, it is even more difficult to separate mechanical from pressure solution-mediated compaction effects in multimineralic systems.

A model is set forth of pressure solution in multimineralic rocks. This model underlies our basin simulators CIRF.B2 and CIRF.B3 (see Park and Ortoleva, this volume and Maxwell, Qin, Sakrani and Ortoleva, this volume). The model allows for the coupling wherein the pressure solution-mediated reactions of one mineral are affected by that of its surroundings through the mineralogy and texture of the latter and the stress applied on a macroscopic volume element containing that grain (see Fig. 1).

In Sect. II we set forth our model of multimineralic pressure solution. It is based on the water film diffusion (WFD) mechanism. In Sect. III we pose and solve the mass balance problem for multi-solute species steady state contact diffusion. This calculation is needed to obtain the

effective (i.e., diffusion-limited) rates of contact reactions. The basin model is reviewed in Sect. IV as is our strategy for developing the simulator.

II. The Pressure Solution Model

Grains of mineral i are described by a set of three truncation lengths L_{xi}, L_{yi}, L_{zi} that fix the two horizontal dimensions and the vertical (z) dimension, and a fourth length variable L_{fi} that fixes the grain radius for truncated spheres and, more generally, is a coordinate that keeps bookkeeping on growth normal to the free face in contact with the pore fluid. The truncation length parameters likewise keep bookkeeping on growth/shortening on the x, y, z contacts.

The dynamics of the L_{gi} (g=x,y,z,f) are generated by

$$\frac{DL_{\gamma i}}{Dt} = G_{\gamma i}, \quad g = x, y, z, f. \tag{II.1}$$

Grain volume evolves via

$$\frac{DV_i}{Dt} = \sum_{\gamma=x,y,z,f} A_{\gamma i} G_{\gamma i} \tag{II.2}$$

where $A_{\gamma i}$ is the nominal area of the γ-type surface of a mineral i grain. The porosity is given by the usual formula

$$\phi = 1 - \sum_{i=1}^{M} n_i V_i \tag{II.3}$$

where n_i is the number of i-grains per rock volume.

A. Surface Area Relations

The geometry of grains, their packing and the effect on these parameters due to changes in the $\underline{L}_i$ ($\underline{L}_i = \{L_{xi}, L_{yi}, L_{zi}, L_{fi}\}$) is very complex. Here we make the very simplest assumption--i.e., the $A_{\gamma i}$ can be written as explicit functions of the $\underline{L}_i$ and the porosity.

Let a superscript "o" indicate the value of a quantity at the initial instant (or at sediment deposition). Then we adopt the formula

$$A_{fi} = \left(\frac{\phi}{\phi^o}\right)^{2/3} \left(\frac{L_{fi}}{L_{fi}^o}\right)^2 A_{fi}^o. \tag{II.4}$$

This formula has the following properties:

1. A_{fi} has its correct value in the "o"-state.
2. A_{fi} goes to zero as $\phi \rightarrow 0$ and does so as $\phi^{2/3}$--i.e., as roughly proportional to the surface area of a pore.
3. A_{fi} tends to increase as does L_{fi}^2, in agreement with the behavior of spheres in a loose packing.

B. Grain Nominal Contact Areas A_{xi}, A_{yi}, A_{zi}

We make the geometric assumption that as $A_{fi} \rightarrow 0$ the grains are roughly rectangular bricks with side dimensions L_{xi}, L_{yi} and L_{zi}. With this we assert the following relation (interpolation)

$$A_{zi} = L_{xi}L_{yi} + \left[A_{zi}^o - L_{xi}L_{yi}\right]\frac{A_{fi}}{A_{fi}^o}. \qquad \text{(II.5)}$$

Thus A_{zi} has its correct value $\left(A_{zi}^o\right)$ in the "o"-state (or at sediment input) but as A_{fi} vanishes then $A_{zi} \rightarrow L_{xi}L_{yi}$. Similar expressions hold for A_{xi} and A_{yi}; for them $L_{xi}L_{yi}$ is replaced by $L_{yi}L_{zi}$ and $L_{xi}L_{zi}$, respectively.

An alternative A_{zi} formula is a logarithmic interpolation as follows:

$$A_{zi} = \left(A_{zi}^o\right)^q \left(L_{xi}L_{yi}\right)^{1-q} \qquad \text{(II.6)}$$

$$A_{zi}^o = A_{zi} \text{ at } t = 0 \qquad \text{(II.7)}$$

$$q = \frac{2}{\frac{A_{fi}^o}{A_{fi}} + \left(\frac{\phi^o}{\phi}\right)^{2/3}}. \qquad \text{(II.8)}$$

This expression has the properties that $A_{zi} \rightarrow L_{xi}L_{yi}$ as $\phi \rightarrow 0$, and $A_{zi} \rightarrow 0$ as A_{fi} increases. The latter limiting behavior simulates the effect whereby dissolving the free face decreases the contact areas and, in turn, increases stress at the contacts.

C. Effects Of Grain-Grain Contact Mineralogy

Petrologic evidence suggests that pressure solution of a given mineral can strongly depend on the mineral identity of grains with which it is in contact. The classical case is the promoting role of phyllosilicates on the pressure solution of a host of minerals including quartz, garnet and carbonates (see Fig. 2). This may be accounted for in the present model.

The role of phyllosilicates in promoting pressure solution has been suggested to be that diffusion along the contact between the two mineral types is enhanced over that of two non-phyllosilicate grains. If this is the mechanism of phyllosilicate enhancement then the following crude statistical approach describes the process adequately. Let $G_{i\gamma j}$ be the rate of change of L_{ig} due to pressure solution when the i-grain is in contact with a j-grain. Let $\zeta_{i\gamma j}$ be defined as the fraction of γ-contacts (γ=x,y,z) that an i-grain has with a j-grain:

$$\sum_{j=1}^{M} \zeta_{i\gamma j} = 1. \qquad \text{(II.9)}$$

We suggest the simple uncorrelated textural approximation

$$\zeta_{i\gamma j} = \frac{n_j A_{\gamma j}}{\sum_{j'=1}^{M} n_{j'} A_{\gamma j'}}. \qquad \text{(II.10)}$$

As a result of the lack of correlation in this model--i.e., it is no more likely to have a quartz grain near a quartz grain than to a feldspar grain--$\zeta_{i\gamma j}$ does not depend on i. Using this (or other assumed form) of $\zeta_{i\gamma j}$ we then write

$$G_{\gamma i} = \sum_{j=1}^{M} \zeta_{i\gamma j} G_{i\gamma j}, \quad \gamma = x, y, z. \qquad \text{(II.11)}$$

The implication of this statement is not that the $L_{i\gamma}$ dynamics is dictated by some averaged contact. Rather, if $\zeta_{i\gamma j}$ does not vary too strongly in time then $L_{\gamma i}$ represents a $\zeta_{i\gamma j}$ average of "$L_{i\gamma j}$", the dimension of an i-grain in the γ-direction for i-grains in contact with j-grains on one side and j′-grains on the other (along the γ-direction). However, as $\zeta_{i\gamma j}$ clearly changes in time, this interpretation has limited validity. Nonetheless, the above formulation we believe captures

most of the semi-quantitative aspects of the dependence of pressure solution on contact grain mineral identity.

D. Grain Stresses

The contact stresses are calculated in the present model via a crude averaging procedure. Let $<\cdots>$ indicate a solid fraction average: for a quantity Q_i for mineral i we write

$$<Q>=\frac{1}{1-\phi}\sum_{i=1}^{M} Q_i n_i V_i . \qquad \text{(II.12)}$$

Next we assert that all normal nominal contact stresses P_{zi} are the same--i.e., any given grain is in contact with another grain of any mineral on the average. Thus putting $P_{zi} = P_z$ we assert

$$-\sigma_{zz}^{m}\langle L_x L_y\rangle = \langle A_z\rangle P_z + \left[\langle L_x L_y\rangle - \langle A_z\rangle\right] p \qquad \text{(II.13)}$$

with similar expressions being adopted for P_x and P_y. These formulae complete the model once the form of the rate laws (G_{zi}, etc.) are set forth.

E. Creation of New Minerals

Questions of the transition to stress support when nucleated grains grow introduces another modeling challenge. Our approach is as follows. A logical variable is introduced for each mineral allowed. This variable is set true for all minerals present in the initial sediment and false for those would-be minerals (at every material point). If a nucleation threshold is exceeded, a mineral not present at a given point can commence to grow in the pore against fluid pressure on <u>all</u> faces (x,y,z,f). Thus in the growth laws for the new nonstress-supporting mineral G_x, G_y and G_z are set to G_f. These minerals may continue to grow until their maximum size (L_x, L_y, L_z, L_f) exceeds a critical pore-bridging length ℓ_b; at this point the mineral's length rates G_x,G_y ,G_z for the supporting dimensions are calculated by the usual WFD law as if the grains of this mineral were always present.

An estimate of the pore bridging length is obtained as follows. The volume fraction of the rock that is pore space (f) is set equal to the total free face area per rock volume times the bridging length. Thus

$$\ell_b \sum_{i=1}^{M} A_{fi} n_i = \phi. \qquad \text{(II.14)}$$

For low porosity ℓ_b is small. For large total A_f, ℓ_b is also small--i.e., the pore domain is very contorted (so the area is large) and hence ℓ_b must be small so that the pore volume is as specified.

F. Free Face Erosion Of A Grain

Another problem arises when a mineral loses stability and commences to dissolve at its free face. Under this situation a grain may be reduced to a thin column or other structure with $L_f << L_x, L_y, L_z$. In reality, such a texture is not found at depth due to the possible operation of three processes:

(a) the grain is not free-standing but is being replaced, often pseudomorphically;

(b) under strongly non-hydrostatic stress such a configuration would be a house-of-cards configuration destined for collapse by rotation of the eroding grain; and

(c) the great stress that can be created within such a thin column would cause its deformation by a plastic mechanism or even grain breakage.

A combination of these processes may be actually taking place in many situations.

Here a crude dissolution/rotation model is adopted. It is assumed that the grains tend to slip and rotate when their L_f passes below the minimum of L_x, L_y, L_z by a factor $\lambda<1$. In the present code this is always assumed to be L_z as the greatest principal stress direction is typically z. Rotation is envisioned as a process of decreasing the characteristic length in the z direction (L_z) while increasing it in the free-face direction L_f at constant volume. We write

$$\frac{DL_z}{Dt} = G_z + H \qquad \text{(II.15)}$$

$$\frac{DL_f}{Dt} = G_f - \frac{A_z}{A_f} H. \qquad \text{(II.16)}$$

Note from (II.2) for the rate of change of volume that the H-term does not change grain volume. In reality, one cannot rotate the grain without also changing at least one of L_x, L_y but we neglect this here for simplicity.

The rotational z-shortetning rate H is assumed to be in the form

$$H = \theta(\lambda L_z - L_f)\theta(-G_f)G_f\left(\frac{L_z}{L_f}\right)^{\beta} \qquad \text{(II.17)}$$

where θ is 1 when its argument is positive and zero otherwise. The process is envisioned to be promoted by ongoing free face dissolution. It occurs when L_f falls below λL_z. It is accelerated as L_z/L_f increases with an exponential factor b and is increased as a rate of dissolution increases, the notion being that rotation and dissolution go in step.

In our simulations we have taken $\gamma = .75$ and $\beta = 1$. These choices seem to give reasonable textures--i.e., thin columnar grains ($L_f << L_z$) are not created while some L_f decrease can occur without any appreciable rotation occuring. We do not claim these choices of parameters or the form of H adopted has any theoretical justification in the real kinetics of grain boundary slip or the processes (a) - (c) noted above.

Free face dissolution can eventually completely remove a grain. If this occurs (i.e., grain volume goes to zero at some space-time point) then the logical presence variable for that mineral at that material point is set to false. Should conditions change and that grain can renucleate then the process of the previous subsection can take place.

G. Compaction and Grain Number Density Dynamics

The conservation of grains yields a useful equation for the grain number densities n_i. First we have

$$\frac{\partial n_i}{\partial t} = -\vec{\nabla} \bullet (n_i \vec{u}). \qquad \text{(II.18)}$$

Let

$$n = \sum_{i=1}^{M} n_i \qquad \text{(II.19)}$$

define the total number of grains of all types per system volume. Then rearrangement yields

$$\frac{D\ln n}{Dt} = -\vec{\nabla} \bullet \vec{u} \equiv -tr\dot{\underline{\underline{\varepsilon}}} \qquad \text{(II.20)}$$

where $\dot{\underline{\underline{\varepsilon}}}$ is the rate of strain tensor. Next define the number density fractions $\hat{n}_i$ via

$$n_i = \hat{n}_i n. \qquad \text{(II.21)}$$

Then the above results can be combined to yield

$$\frac{D\hat{n}_i}{Dt} = 0. \qquad \text{(II.22)}$$

Hence in any material point the number density fractions are constant. In numerical simulations this means that if the discretization grid moves with the rock flow velocity $\bar{u}$ then the $\hat{n}_i$ at each grid point are constant. Thus we need only calculate n and hence the rate of strain.

Our model for rock deformation and compaction is based on the incremental stress theory (see Appendices E1,2). In the incremental stress theory, we use a nonlinear viscosity model. The mechanical compaction viscosity η is introduced and is taken to depend strongly on texture to reflect the tendency for mechanical compaction to be significantly diminished as a stable configuration is obtained. For example

$$\eta = \eta_0 \exp\left(\phi^*/\phi\right)^q \qquad \text{(II.23)}$$

for constants η_0. q (>0) makes η become very large once the porosity passes below a conjectured mechanically stable porosity ϕ^*. We expect ϕ^* to be in the interval $.2 < \phi^* < .4$ depending on sorting, with ϕ^* being lowest for poorly sorted rocks.

III. Pressure Solution Rate Laws

The pressure solution rates $G_{\gamma i}$ may be obtained in the steady state approximation in the form of implicit nonlinear equations. Here we illustrate this for the case of a WFD contact.

A. Basic Steady State Phenomenology

Let Y_α and Y_α^z be the activity of species α in the pore fluid and in the center of the z-contact, respectively. Then for a mineral reacting according to

$$\text{mineral} \Leftrightarrow \sum_{\alpha=1}^{N} \nu_\alpha \text{ (aqueous solute } \alpha) \qquad \text{(III.1)}$$

we develop G_z as follows. First we assume that G_z takes the mass action form

$$G_z = k\left\{ \prod_{\nu_\alpha>0} \left(Y_\alpha^z\right)^{\nu_\alpha} \Big/ K - \prod_{\nu_\alpha<0} \left(Y_\alpha^z\right)^{-\nu_\alpha} \right\} \qquad \text{(III.2)}$$

for rate coefficient k and equilibrium constant K. The flux J_α of α out of the z-contact is taken to be

$$J_\alpha = D_\alpha^z \left(Y_\alpha^z - Y_\alpha\right) \Big/ L_z \qquad \text{(III.3)}$$

for contact radius L_z. Then at steady state

$$J_\alpha = D_\alpha^z \left(A_\alpha^z - A_\alpha\right) \Big/ L_z . \qquad \text{(III.4)}$$

Combining (III.3,4) yields a complicated set of equations for the Y_α^z.

B. An Implicit Equation for the Rate

The main objective of the above calculation is to obtain an expression for G_z in terms of the pore fluid activities $\underline{Y}$. This can actually be accomplished directly without the need for first solving the steady state equations for Y_α^z in terms of the $\underline{Y}$ and then putting the result in (III.2). Rather, we obtain a nonlinear equation for G_z itself.

First solve (III.4) for Y_α^z in the form

$$Y_\alpha^z = Y_\alpha + \Lambda_\alpha G_z \qquad \text{(III.5)}$$

$$\Lambda_\alpha = \nu_\alpha \rho A_z / 2\pi \Delta_z D_\alpha^z . \qquad \text{(III.6)}$$

Combining this with the mass action law (III.2) yields

$$G_z = k\left\{ \frac{1}{K} \prod_{\nu_\alpha>0} \left[Y_\alpha + \Lambda_\alpha G_z\right]^{\nu_\alpha} - \prod_{\nu_\alpha<0} \left[Y_\alpha + \Lambda_\alpha G_z\right]^{-\nu_\alpha} \right\}. \qquad \text{(III.7)}$$

This is an equation which can be solved for G_z. For simple cases like quartz $\Leftrightarrow SiO_2$ or calcite $\Leftrightarrow CO_3^{2-}$ this equation can be solved explicitly in simple form. For more complex cases this problem is solved in the CIRF.B codes using a combination of bisection and Newton-Raphson methods.

Even more complex formulae arise when explicit account of the effect of the mineral identity of contacts is made as was done in Sect. II.C.

C. Further Assumptions on the Rate Laws

1. Free energies and the equilibrium constants

In the present model we make a number of simplifying assumptions for the thermodynamics. For aqueous species α the chemical potential μ_α is taken in the form

$$\mu_\alpha = \mu_\alpha^*(1,T) + RT\ell n\gamma_\alpha c_\alpha + \bar{V}_\alpha(p-1) + \beta_\alpha(p-1)^2/2 \qquad \text{(III.8)}$$

where $\bar{V}_\alpha$ is the partial molar volume, β_α is the partial compressibility, γ_α is the Debye-Huckle activity coefficient (as implemented in EQ3/6, 1992 release) and μ_α^* is the reference chemical potential. Note that γ_α depends on c_α only through the ionic strength I. With this equilibria for the aqueous reaction

$$\sum_\alpha \omega_\alpha (\text{aqueous solute } \alpha) = 0 \qquad \text{(III.9)}$$

takes the form

$$\prod_{\alpha=1}^{N} (\gamma_\alpha c_\alpha)^{\omega_\alpha} = K(p,T) \qquad \text{(III.10)}$$

$$-RT\ell n\ K = \sum_{\alpha=1}^{N} \omega_\alpha \left\{ \bar{V}_\alpha(p-1) + \frac{1}{2}\beta_\alpha(p-1)^2 + \mu_\alpha^* \right\}. \qquad \text{(III.11)}$$

For a mineral reaction in the form mineral $= \sum_\alpha \nu_\alpha$ for aqueous species α the above result is obtained except that $-RT\ell nK$ has an additional contribution $-\mu$ where μ is the solid free energy at the site (x,y,z or f) of reaction. From Kamb (1959) we adopt

$$\mu = \mu^o + \frac{P}{\rho} + \frac{\mathrm{tr}(\underline{\underline{\sigma}}\,\underline{\underline{\varepsilon}})}{2\rho^o}. \qquad \text{(III.12)}$$

Here μ^o is the molar free energy of the mineral in the stress-free state; P is the normal stress at the site (i.e., p_z for an actual z-contact); ρ and ρ^o are the molar densities in the stressed ($\underline{\underline{\sigma}} \neq \underline{\underline{0}}$) and unstressed ($\underline{\underline{\sigma}} = \underline{\underline{0}}$) states; $\underline{\underline{\sigma}}$ is the stress tensor at the site of reaction; $\underline{\underline{\varepsilon}}$ is the corresponding strain (linearly related to $\underline{\underline{\sigma}}$ through the compliance tensor). For simplicity the compliance tensor is taken to be that for an isotropic elastic medium and hence represents an average of compliances for anisotropic crystals (see Dewers and Ortoleva, 1990, for more details).

2. Rate coefficients and equilibrium constants

Rate coefficients are taken to be of the Arrhenius form while equilibrium constants (taken from the EQ3/6 database) are re-evaluated as temperature polynomials. The dependence of the water film thickness on stress, temperature, and fluid pressure and composition is according to the theory and data as in Renard and Ortoleva (this report).

D. Conservation of Pore Fluid Solute Mass

In the present model we investigate the effect of local diagenetic reactions. Thus we neglect transport between rock volume elements. With this we obtain

$$\frac{\partial \phi c_\alpha}{\partial t} = -\vec{\nabla} \bullet (\phi c_\alpha \vec{u}) - \vec{\nabla} \cdot \vec{J}_\alpha^{rel} + \sum_{k=1}^{N_a} \omega_{\alpha k} W_k - \sum_{k=1}^{N_m} \nu_{\alpha ik} \rho_{i(k)} \sum_{\gamma=x,y,z,f} A_{\gamma i(k)} G_{\gamma ik} \quad \text{(III.16)}$$

where ρ_i is the molar density of mineral i and the $\omega_{\alpha k}$ are the stoichiometric coefficients for the N_a aqueous reactions, the k^{th} of which has rate W_k, $k = 1,2,\cdots,N_a$. Also i(k) indicates the mineral, i, that takes place in the k^{th} reaction written

$$\text{mineral } i(k) = \sum_{\alpha=1}^{N} \nu_{\alpha k} (\text{pore fluid species } \alpha). \quad \text{(III.17)}$$

The above conservation of mass equation may be reduced in a number of ways to a good approximation.

First the porosity ϕ is given by

$$\phi = 1 - \sum_{i=1}^{M} n_i V_i. \quad \text{(III.18)}$$

Hence, using (II.30) for n_i,

$$\frac{D\phi}{Dt} = -(1-\phi) tr \dot{\underline{\underline{\varepsilon}}} - \sum_k n_{i(k)} A_{\gamma i(k)} G_{\gamma k}. \quad \text{(III.19)}$$

These two results can be combined to show that when terms like $c_\alpha G_\alpha$ are neglected relative to terms like $\rho_i G_{\gamma i}$ (as $c_\alpha \ll \rho_i$); with this, we obtain

$$\phi \frac{Dc_\alpha}{Dt} = \sum_{k=1}^{N_a} \omega_{\alpha k} W_k + \sum_{k\gamma} \nu_k \rho_{i(k)} A_{\gamma i(k)} G_{\gamma k}. \quad \text{(III.20)}$$

We assume that the aqueous reactions are relatively fast for the geochemical processes of interest here. Thus we have the equilibrium conditions $W_k=0$, $k=1,2,\cdots,N_a$. Assuming none of these aqueous reactions are not thermodynamically redundant, this yields N_a equations for the c_α. These may be written in the form

$$\sum_{\alpha=1}^{N}\omega_{\alpha k}\mu_\alpha(\underline{c},p,T)=0 \qquad \text{(III.21)}$$

where μ_α is the chemical potential of species α. The form of the μ_α adopted is given in Sect. III.C1.

Next we introduce a set of $N-N_a$ row vectors $\underline{Y}^{(\lambda)}$ such that

$$\sum_{\alpha=1}^{N}a_\alpha^{(\lambda)}\omega_{\alpha k}=0,\quad k=1,2,\cdots,N_a,\quad \lambda=1,2,\cdots,N-N_a. \qquad \text{(III.22)}$$

The first $N-N_a-M$ of these can be chosen such that

$$\sum_{\alpha=1}^{N}a_\alpha^{(\lambda)}\nu_{\alpha i}=0,\quad k=1,2,\cdots,N_a. \qquad \text{(III.23)}$$

Multiplying (III.17) by $\underline{a}^{(\lambda)}$ and summing over α we obtain

$$\frac{D\chi^{(\lambda)}}{Dt}=-\phi\chi_\alpha tr\dot{\underline{\underline{\varepsilon}}},\quad \lambda=1,2,\cdots,N-N_a-M \qquad \text{(III.24)}$$

$$\frac{D\chi^{(\lambda)}}{Dt}=-\phi\chi_\alpha tr\dot{\underline{\underline{\varepsilon}}}-\sum_{\gamma i}\nu_i^{(\lambda)}\rho_i A_{\gamma i}G_{\gamma i},\quad \lambda=N-M-N_a+1,\cdots,N-N_a \qquad \text{(III.25)}$$

where

$$\chi^{(\lambda)}=\phi\sum_{\alpha=1}^{N}a_\alpha^{(\lambda)}c_\alpha \qquad \text{(III.26)}$$

$$\nu_k^{(\lambda)}=\sum_{\alpha=1}^{N}a_\alpha^{(\lambda)}\nu_{\alpha k}. \qquad \text{(III.27)}$$

The first set of χ's represent conserved quantities, i.e., they only change due to the rate of rock dilitation $tr\dot{\underline{\underline{\varepsilon}}}$. For example, if Mn^{2+} does not take place in any mineral reaction then a χ representing the total concentration of Mn^{2+} in all complexes or the bare form is a constant. The

second group of χ's are changed because the ion pools they represent are changed by mineral reactions.

E. Other Aspects of the RTM Model

The model accounting for stresses and pore fluid pressure (using Darcy's law) are the same as those discussed in Sonnenthal and Ortoleva (1993). The temperature distribution is specified by a geothermal gradient and the sedimentation and sea-level information is supplied to the simulator by the user, as is the history of the basement rock-sediment interface so as to account for subsidence or uplift.

IV. Remarks

The above multimineralic pressure solution and other aspects of the RTM model are the basis of the CIRF.B basin diagenesis simulators. CIRF.B has both two (CIRF.B2) and three (CIRF.B3) spatial dimensional options. The CIRF.B2 and CIRF.B3 codes in their preliminary forms are now operational. Augmentations of CIRF.B being carried out include the incremental stress solver (as described in Tounsi and Ortoleva, 1993), fracture kinetics (see Sonnenthal and Ortoleva, 1994) and ionic strength corrected thermodynamics (as in Chen et al., 1993).

References

Bayly, B. (1982) In Atlas of Deformational and Metamorphic Rock Fabrics, G.J. Borradaile, B.M. Bayly and L.M. Powell, eds., New York, Springer Verlag.

Dewers, T. and Ortoleva, P. (1990) "A Coupled Reaction/Transport/Mechanical Model for Intergranular Pressure Solution, Stylolites, and Differential Compaction and Cementation in Clean Sandstones", Geochim. Cosmochim. Acta 54, 1609-1625.

Eshelby. J.D. (1957) in Proceedings of the Royal Society of London A241, 376.

Geo-Chemical Research Associates, Inc. (1993) "CIRF: Models, Numerical Techniques and Graphical Analysis".

Maxwell, M. and Ortoleva, P. (1993) "Simulating a Three-Dimensional Basin-Wide Overpressured Compartment", Quarterly Report for the Gas Research Institute, October, 1992-January, 1993, 39-57.

Pettijohn, F.J. (1975) Sedimentary Rocks, 3rd edition, Harper and Row, San Francisco. p. 628.

Potdevin, J.L., Chen, W., Chen, Y. and Ortoleva, P. (1992) "CIRF, A General Reaction-Transport Code: Mineralization Fronts Due to the Infiltration of Reactive Fluids", in Water-Rock Interaction, Vol. 2, Y.K. Kharaka and A.S. Maest, eds, 1047-1054.

Sonnenthal, E. and Ortoleva, P. (1994) "Numerical Simulations of Overpressured Compartments in Sedimentary Basins". In Deep Basin Compartments and Seals, AAPG Memoir, to appear.

Tounsi, F. and Ortoleva, P. (1994) "Coupled Texture Dynamics and Deformation in a Sedimentary Basin", in preparation.

Appendix B

Water Films at Grain-Grain Contacts: Debye-Hückel, Osmotic Model of Stress, Salinity and Mineralogy Dependence

F. Renard and P. Ortoleva
Departments of Chemistry and of Geological Sciences
Indiana University
Bloomington IN 47405

Abstract

A key problem in the theory of pressure solution is the nature of the water film that is believed to provide the reaction and transport medium in the water film diffusion (WFD) mechanism. To allow for WFD pressure solution such a film must exist for large differences between the stress applied across the contact and the fluid pressure in the pore. Since the film is believed to be tens to hundreds of angstroms thick and the evidence is that only one or two water layers can be tightly bound to a grain surface, it is perplexing to explain the existence of such films. Even if the film is ice-like, the yield stress for ice is at most a few bars, far less than the hundreds of bars of deviatoric stress encountered in stressed contacts in a basin.

Here we show that the charged surface of a mineral can attract counter-ions from the pore and, by the related change of osmotic pressure, keep water within the contact. Simply put, the counter-ions in the water film increase the salinity in the film relative to that in the pore. This lowers the free energy of water in the contact to a degree that balances the increase in free energy of water due to the elevated pressure in the film. These notions are made more precise by combining the theory of the Debye-Hückle double layer with equations of osmotic pressure. The resulting D-H/O theory predicts the dependence of the water film thickness on stress across the contact, composition of the pore fluidand the identity of the minerals involved.

THE PHYSICAL PICTURE

A charged mineral surface attracts a counterbalancing charge cloud in the solution as suggested in Fig. 1 Thus the concentration of dissolved solutes near the surface exceeds that far from it. Osmotic equilibrium can then be set up with elevated fluid pressure developing in the region of appreciable counterbalancing charge density. The incoming water tends to displace the counterbalancing charge while the strong Coulomb attraction keeps the counterbalancing charge localized to near the surface. Thus a layer of compressed fluid is created near the grain surface.

The osmotic layer is bound yet still a liquid. In this way a truly water (and not a solid-like) water film can exist within a stressed grain contact.

It might be asserted that the water film could be ice-like (or otherwise solid in structure) and can thereby sustain stress. Thus for a solid model the water film might be conjectured to exist when the stress normal to the contact is less than the fluid pressure within the pore plus the yield stress. For ice the latter is only a few bars and hence one expects that a solid-like water film failure model does not tell the whole (if any) of the story. Indeed, direct observations suggest that such a solid-like layer does not exceed a few angstroms in thickness and is thereby one or two orders of magnitude less than generally accepted (or at least conjectured) layer thicknesses of ten to one hundred angstroms.

SIMPLE MODEL

A simple model of the D-H/O layer for a stressed contact is suggested in Fig. 1. The difference between p_z (the stress across the contact) and p_o (the pore fluid pressure) is set equal to the classical osmotic pressure:

$$p_z - p_o = -\frac{\mathcal{R}T}{\overline{V}_w} \ell n \left(\frac{x_w}{x_w^o} \right) \qquad (1)$$

where $\overline{V}_w$ is the molar volume of water and x_w and x_{w0} are the mole fractions of water within the contact and within the pore fluid, respectively.

In this simple model the simplifying assumption is made that the counterbalancing charge is spread out uniformly within the contact. If Γ is the moles of surface charge per area and Δ is the water film thickness then the concentration of (uniformly smeared) compensating charge within the contact is $2\Gamma/\Delta$, the 2 coming from the assumption that the grain surface on either side of the contact has the same charge. Then if C_o is the total molar concentration of all solutes within the pore one has

$$x_w = \left\{1+\bar{V}_w\left[C^o+2\Gamma/\Delta\right]\right\}^{-1},\ x_{w0} = \left\{1+\bar{V}_w C^o\right\}^{-1}. \qquad (2)$$

Combining (1,2) we may determine Δ as a function of p_z - p_o:

$$\Delta(p_z\text{-}p_o, C_o, \Gamma, T) = \frac{2\Gamma}{C_0\left\{\exp\left[\frac{\bar{v}_w(p_z-p)}{RT}\right]-1\right\}} \qquad (3)$$

Thus one determines the predicted water film thickness as a function of contact normal stress, salinity and temperature.

Results for Δ when the pore fluid concentration is on the order of that for SiO_2(aq) in equilibrium with quartz is seen in Fig. 2. The water film thicknesses are close to those one might expect. Furthermore, the water film is appreciable (several angstroms) even when p_z-p_o is hundreds of bars. This latter stability is needed if pressure solution is expected to operate at several kilometers depth in a sedimentary basin.

D-H/OSMOTIC MODEL

While the simple model results are encouraging, several questions emerge.

* The distribution of compensating charge is not uniform but is presumably distributed according to the Debye-Huckle double layer theory.
* The elevated pressure in the osmotic layer will have a complex effect on the D-H layer structure--attracting ions with negative partial molar volumes and expelling solutes with positive ones.
* What happens when the surface charge is pH or otherwise fluid composition dependent?

In the present model we address only the first two issues.

The voltage $\mathcal{V}$ within the water film satisfies Poisson's equation

$$\frac{d^2\mathcal{V}}{dz^2} = -\frac{4\pi\mathcal{F}}{\varepsilon}\sum_{\alpha=1}^{N} z_\alpha c_\alpha \qquad (4)$$

where z is distance across the film (lying within $-\Delta/2 < z < +\Delta/2$). The dielectric constant ε is taken to be constant; $\mathcal{F}$ is Faraday's constant and c_α is the concentration of solute α in the aqueous solution and z_α is its valence.

An overall equilibrium is assumed between the pore fluid and the contact fluid. If μ_α is the chemical potential of species α (=1,2,···,N,w, w being H_2O, the solvent), then the aforementioned equilibrium implies

$$\mu_\alpha(p,T,\underline{c}) = \mu_\alpha(p_o,T,\underline{c}^o) \qquad (5)$$

where $\underline{c} = \{c_1,c_2,...,c_N,c_w\}$ and $\underline{c}(z)$ and $p(z)$ are to be determined from the D-H osmotic theory.

In order to simplify the calculations, first assume the solution is dilute (the effect of Pitzer-type corrections were also used--see below). For the solutes therefore one has

$$\mu_\alpha = \mu_\alpha^* + p\overline{V}_\alpha + \mathcal{R}T\ell n a_\alpha + z_\alpha\mathcal{F}\mathcal{V} - \mathcal{R}Te^{\frac{-(z-\gamma_1)}{\gamma_2}} \quad \alpha \neq w \qquad (6)$$

where $a_\alpha = \gamma_\alpha c_\alpha$ for reference potential μ_α^*. a_α is the activity of the species α, γ_α the activity coefficient. The equilibrium (5) yields, taking $\mathcal{V} = 0$ in the pore,

$$a_\alpha = a_{\alpha 0}\exp\left\{\frac{-1}{\mathcal{R}T}\left[(p-p_o)\overline{V}_\alpha + z_\alpha\mathcal{F}\mathcal{V}\right]\right\}. \qquad (7)$$

Thus the c_α in (4) can be eliminated. A further equation needed to yield $p(z)$ is obtained from the osmotic condition. For water we assume

$$\mu_w = \mu_w^* + p\overline{V}_w + \mathcal{R}T\ell n a_w + \mathcal{R}Te^{\frac{-(z-\gamma_1)}{\gamma_2}}. \qquad (8)$$

Equilibrium between the pore and the film then yields the $e\left(-\frac{z-\gamma_1}{\gamma_2}\right)$ term represents a repulsion potential, z being the distance from the surface. It is known that on every mineral surface, one layer of water is strongly attached, and it is almost impossible to remove it. This potential, with $\gamma_1 = 2$ angstroms and $\gamma_2 = 0.1$ angstrom allows a strong

binding of a monolayer of water molecules on the mineral surface. Thus a minimum thickness of 4 angstroms for the water film is preserved

$$\left(p-p^{o}\right)\bar{V}_{w}=-\mathcal{R}T\ell n\left(\frac{a_{w}}{a_{w0}}\right)-\mathcal{R}Te^{\frac{-(z-\gamma_{1})}{\gamma_{2}}}. \qquad (9)$$

The activity of water, a_w, is calculated through the osmotic coefficient once all the activities c_α are known. $\underline{c}$ can be expressed in terms of a_w by combining (7) and (9) to obtain

$$\gamma_{\alpha}c_{\alpha}=\gamma_{\alpha}^{o}c_{\alpha}^{o}\left(\frac{a_{w}}{a_{w}^{o}}\right)^{\bar{V}_{\alpha}/\bar{V}_{w}}e^{-z_{\alpha}\mathcal{F}\mathcal{V}/\mathcal{R}T}\bullet\exp\left[\left(\frac{V_{\alpha}}{V_{w}c_{\alpha}}+1\right)\exp\left(-\frac{(z-\gamma_{1})}{\gamma\varepsilon}\right)\right]. \qquad (10)$$

Therefore (10) is a nonlinear algebraic equation for x_w in terms of $\underline{c}^o$, all the c_α and $\mathcal{V}$ once the dependence of a_w and γ_α on $\underline{c}$ is delineated. This kind of equation is written for all the species α. We solve the resulting system of nonlinear equations by iterations.

In this way the D-H osmotic problem is reduced to solving Poisson's equation for $\mathcal{V}$ with a c_α-dependent charge density coupled to a nonlinear algebraic equation relating $\bar{c}_\alpha$ and $\mathcal{V}$. This nonlinear problem can be solved numerically via an iteration scheme.

To complete the calculation we need to consider various types of boundary conditions. Conditions on the voltage at $z = \pm\Delta/2$ needed to solve Poisson's equation may be obtained by integrating Poisson's equation across the fixed charge sheet, assumed to reside at $z = \pm\Delta/2$. Thus Poisson's equation is augmented to be

$$\frac{-\varepsilon}{4\pi}\frac{d^{2}\mathcal{V}}{dz^{2}}=\sum_{\alpha=1}^{N}z_{\alpha}\mathcal{F}c_{\alpha}+\Gamma\left[\delta\left(z-\frac{\Delta}{2}\right)+\delta\left(z+\frac{\Delta}{2}\right)\right]. \qquad (11)$$

Integrating over a small interval about $z = +\Delta/2$ yields

$$-\frac{\varepsilon}{4\pi}\left\{\frac{d\mathcal{V}}{dz}\left(\frac{\Delta}{2}+0^{+}\right)-\frac{d\mathcal{V}}{dz}\left(\frac{\Delta}{2}+0^{-}\right)\right\}=\Gamma \qquad (12)$$

where 0^+ and 0^- are positive and negative infinitesimals, respectively. But inside the grain ($z > \Delta/2$) there are no charges so that $\mathcal{V}$ is constant and hence d /dz is zero there. Thus we have

$$\frac{d\mathcal{V}}{dz}\left(\frac{\Delta}{2}+0^{-}\right)=\frac{4\pi\Gamma}{\varepsilon}. \tag{13}$$

Another boundary condition is a condition of symmetry about z = 0, where $d\mathcal{V}/dz = 0$.

It might be questioned as to whether the compensating charge actually balances the surface charge. Integrating Poisson's equation over the interval $-\frac{1}{2}\Delta+0^{+} < z < +\frac{1}{2}\Delta+0^{-}$, i.e., over the film but not including the fixed charge layer, and using the boundary conditions on $d\mathcal{V}/dz$ at $\pm\frac{1}{2}\Delta+0^{+}$ one obtains

$$\int_{-\frac{1}{2}\Delta+0^{+}}^{\frac{1}{2}\Delta+0^{-}} dz \sum_{\alpha=1}^{N} z_\alpha c_\alpha = 2\Gamma. \tag{14}$$

Thus the charge within the water film is exactly compensating.

THERMODYNAMICS OF THE RELATION BETWEEN Δ AND P_Z

The calculation of the dependence of Δ on p_z must be done through a careful consideration of the thermodynamics of the water film. In particular, we now show that the compressive stress applied to the solid across the water film, i.e., p_z, must be obtained as the derivative of an appropriate free energy with respect to Δ.

The compression of the water film is carried out at constant chemical potential and temperature. Thus we seek a free energy whose derivative with respect to volume (and ultimately Δ) is the pressure doing the overall ("piston") compression--i.e., p_z. The Gibb's free energy of the film considered as a totality, i.e., G^{film}, is related to the piston pressure p_z, the total number of moles n_α^{film} and temperature via Euler's theorem

$$G^{film}\left(p_z,\left\{n_\alpha^{film}\right\},T\right)=\sum_{\alpha=w}^{N} n_\alpha^{film}\mu_\alpha^{film} \tag{15}$$

and furthermore

$$dG^{film}=\sum_{\alpha=w}^{N}\mu_\alpha^{film}dn_\alpha^{film}+V^{film}dp_z-S^{film}dT. \tag{16}$$

On the other hand, the transformed function Ω^{film},

$$\Omega^{film}\equiv G^{film}-\sum_{\alpha=w}^{N}\mu_\alpha^{film}n_\alpha^{film}-p_zV^{film} \tag{17}$$

has increment

$$d\Omega^{film} = -\sum_{\alpha=w}^{N} n_\alpha^{film} d\mu_\alpha^{film} - p_z dV^{film} - S^{film} dT. \tag{18}$$

Thereby

$$p_z = -\left(\frac{\partial \Omega^{film}}{\partial V^{film}}\right)_{\underline{\mu}^{film},T} \quad \text{where } \underline{m}^{film} = (m_1, m_2, ..., m_N). \tag{19}$$

For the film of area $\mathcal{A}$, $V^{film} = A\Delta$ and hence

$$p_z = -\frac{1}{\mathcal{A}}\left(\frac{\partial \Omega^{film}}{\partial \Delta}\right)_{\underline{\mu},T}, \tag{20}$$

a key result of the D-H/Osmotic theory.

The macroscopic thermodynamics of (4-9) can now be related to the mesoscopic theory of the previous section as follows. In every volume element we define the free energies G and Ω as above:

$$G = \sum_{\alpha=w}^{N} n_\alpha \mu_\alpha \tag{21}$$

$$\Omega = G - \sum_{\alpha=w}^{N} n_\alpha \mu_\alpha - pV = -pV. \tag{22}$$

Then the Ω-energy density $\omega = \Omega / V$ can be used to obtain Ω by integrating over the film

$$\Omega^{film} = \int_{film} d^3r w = -\int_{film} d^3r p. \tag{23}$$

Then using $d^3r = \mathcal{A}dz$ we obtain via (22)

$$p_z = \frac{\partial}{\partial \Delta}\Big)_{\underline{\mu},T} \int_{-\frac{\Delta}{2}}^{\frac{\Delta}{2}} dz p(z;\Delta). \tag{24}$$

Note that as $p(z,\Delta)$ depends on Δ through the solution of the D-H/Osmotic model, p_z is not simply $[p(\Delta/2,\Delta) + p(-\Delta/2,\Delta)]/2$. Rather, p_z depends on the distribution of p across the entire film (i.e., $-\frac{\Delta}{2} < z < \frac{\Delta}{2}$).

SURFACE CHARGE

Many minerals have surface charge. There are three different mechanisms to create a surface charge :

1) Chemical reaction at the surface of the mineral can modify its electroneutrality. For example, in quartz, the (Si-OH) group can gain or lose a proton and become charged (Stumm, 1981; Brady, 1992). In this case the charge depends strongly on the pH. In the same way, clays in contact with water can gain negative charges by losing cations which go in solution. The mechanisms of these reactions are controlled by the rates of complexations and ionizations at the surface of the solid (van Cappellen, 1993).

2) Surface charge may be caused by lattice imperfections at the surface of the crystal and substitutions in the silicate framework. For example, if Al^{3+} replaces Si^{4+} in a tetrahedral site, a positive charge is lost, and the surface becomes negative. This mechanism appears in clays (smectites, micas) and makes their surface charged.

3) A surface charge may also be established by adsorption of a surfactant ion, because of Van der Waals attractions or hydrogen bonds (Stumm, 1981).

SURFACE CHARGE DATA

Different methods have been used to measure the surface charge of minerals. In many of them, the adsorption of compensated ions is studied to estimate the concentration of charges on the mineral surface (Anderson, 1991; van Cappellen, 1993). Unfortunely, few experiments have been done and there is a lack of surface charge data for many minerals. Table 1 shows data for some common minerals.

THE THERMODYNAMIC PROPERTIES OF THE SOLUTION

We assume that the compensating ions in the solution are Na^+ and Cl^-. To calculate their activities, we use a Pitzer approach.

During the past few years Pitzer and co-workers have developed a set of equations that describe the thermodynamic properties of electrolyte solutions (Pitzer and Mayorga,

1973; Pitzer, 1973, 1987, 1991). These equations are based on an extended Debye-Hückel theory.

The case of a solution of NaCl has been studied in detail (Pitzer, 1984). The osmotic coefficient for water (ϕ), and the logarithms of the activities of sodium (γ_{Na}) and chloride (γ_{Cl}) ions are given in the following equations :

$$\phi - 1 = \frac{2}{m_{Na} + m_{Cl}} \left[\frac{-A^{\phi} I^{3/2}}{1 + bI^{1/2}} + m_{Na} m_{Cl} \left(B^{\phi}_{NaCl} + ZC_{NaCl} \right) \right] \tag{25}$$

where b is a universal parameter with the value 1.2 $kg^{1/2}.mole^{-1/2}$, m_{Na} and m_{Cl} are the molalities (mole/kg of solvent) of Na^+ and Cl^- respectivily and I is the ionic strength of the solution. By definition :

$$I = \frac{1}{2}(m_{Na} + m_{Cl}). \tag{26}$$

The activity of water a_{H_2O} is easily expressed by the osmotic coefficient (Wood, 1975).

$$\ln\left(a_{H_2O}\right) = -\frac{m_{Na} + m_{Cl}}{55.51}\phi \tag{27}$$

$$\begin{aligned} \ln(\gamma_{Na}) &= F + m_{Cl}(2B_{NaCl} + ZC_{NaCl}) + m_{Na} m_{Cl} C_{NaCl} \\ \ln(\gamma_{Cl}) &= F + m_{Na}(2B_{NaCl} + ZC_{NaCl}) + m_{Na} m_{Cl} C_{NaCl} \end{aligned} \tag{28}$$

F is a Debye-Hückel term depending only on the ionic strength, which describes long range interactions between the ions. The other terms, B_{NaCl} and C_{NaCl}, take in account short range interactions between Na^+ and Cl^-. The functions F and z are definied by :

$$F = f^{\gamma} + m_{Na} m_{Cl} B'_{NaCl} \tag{29}$$

where

$$f^{\gamma} = -A^{\phi}\left[\frac{I^{1/2}}{1 + bI^{1/2}} + \frac{2}{b}\ln\left(1 + bI^{1/2}\right) \right] \tag{30}$$

$$Z = m_{Na} + m_{Cl} \tag{31}$$

A^{ϕ} is the Debye-Hückel parameter (0.3915 $kg^{1/2}.m^{-1/2}$ at 25ºC)

$$A^{\phi} = \frac{1}{3}\left(\frac{2\pi N_A \rho_w}{1000}\right)^{1/2}\left(\frac{e^2}{k\varepsilon_w T}\right)^{3/2} \quad (32)$$

with N_A Avogadro's number, e the electronic charge, k Boltzmann's constant, ρ_w and ε_w the density and dielectric constant of pure water. These last two parameters are sensitive to pressure and temperature. Bradley and Pitzer (1979) have fitted the variations of the dielectric constant of water with P and T.

The parameter A^{ϕ} has been studied by many authors (Ananthaswamy, 1984; Archer, 1990; Bradley and Pitzer, 1979) but for practical calculations, one can use the equation for A^{ϕ} given by Clegg and Withfield (1991) for a temperature between 273°K and 373°K.

$$A^{\phi} = 0.13422\,(4.1725332 - 0.1481291\,T^{0.5} + 1.518805e^{-5}\,T^2 - 1.8016317e^{-8}\,T^3 + 9.3816144e^{-10}\,T^{3.5})$$

Terms B_{NaCl} in the former equations depend on the ionic strength. Pitzer et al. (1991) give the expressions of these parameters.

$$B^{\phi}_{NaCl} = \beta^{(0)}_{NaCl} + \beta^{(1)}_{NaCl}\exp\left(-\alpha I^{1/2}\right) \quad (33)$$

$$B_{NaCl} = \beta^{(0)}_{NaCl} + \beta^{(1)}_{NaCl} g\left(\alpha I^{1/2}\right) \quad (34)$$

$$B'_{NaCl} = \frac{\beta^{(1)}_{NaCl} g'\left(-\alpha I^{1/2}\right)}{I} \quad (35)$$

$\alpha = 2$ and the functions g(x) and g'(x) are :

$$g(x) = \frac{2}{x^2}\left(1-(1+x)e^{-x}\right) \quad (36)$$

$$g'(x) = -\frac{2}{x^2}\left(1-\left(1+x+\frac{1}{2}x^2\right)e^{-x}\right) \quad (37)$$

The values of $\beta^{(0)}_{NaCl}$, $\beta^{(1)}_{NaCl}$, C^{ϕ}_{NaCl} and C_{NaCl} at 25°C, 1 bar, have been measured :

$\beta^{(0)}_{NaCl}$ (kg / mole)	$\beta^{(1)}_{NaCl}$ (kg / mole)	$C^{\phi}_{NaCl} = 2C_{NaCl}$ ($kg^2/mole^2$)
0.0764	0.277	0.0014

Pitzer (1984) gives the variations of these parameters with the temperature (between 273°K and 573°K), the pressure (between 1 bar and 1 kbar), for ionic strength less than 6 mole/kg.

Table 1. Surface charge for different minerals.

Mineral	Surface charge (Coulomb / m^2)	pH range	Ref.
Alumina	0 ; - 0.06	4 ; 11	(1)
Alumina	0.3 ; 0	3 ; 6.5	(3)
Alumina	0 ; - 0.3	6.5 ; 10	(3)
Amorphous silica	- 0.0048	5	(2)
Amorphous silica	- 0.048	7	(2)
Amorphous silica	- 0.48	11	(2)
Silica	0 ; - 0.75	4 ; 10	(4)
Silica	- 0.48 ; - 0.96	> 2.5	(5)
Montmorillonite	0.12 ; 0	0 ; 2	(6)
Montmorillonite	0 ; - 0.2	2 ; 4	(6)
Montmorillonite	0.12	-	(8)
Smectites	- 0.12 ; - 0.17	-	(8)
kaolinite (edge)	0 ; - 1.2	3.5 ; 10	(1)
kaolinite (edge)	- 0.6	7	(1)
kaolin	-0.18; +0.63	0-10	(9)
muscovite	-0.81;+0.54	3-9	(9)
$MnCO_3$	1.45 ; 0	4 ; 5.5	(7)
$MnCO_3$	0 ; - 1.98	5.5 ; 8	(7)
$CaCO_3$	1.45 ; 0	6 ; 8	(7)
$CaCO_3$	0 ; - 1.45	8 ; 12	(7)
$CaCO_3$	0.1 ; 0	6 ; 8	(6)
$CaCO_3$	0 ; - 0.2	8 ; 10	(6)

References : (1) Zhou (1992), (2) Brady (1992), (3) Brady (1994), (4) Yates (1975), (5) Baudin (1990), (6) Stumm, (7) van Cappellen (1993), (8) Villemure (1990), (9) Herrington et al (1992).

RESULTS AND DISCUSSION

Poisson's equation

Profiles of voltage and concentration across the water film are shown in figure 3. As the surface charge is negative the concentration of the compensating ion, Na^+, is high near the mineral surface. The concentration of Cl^- is low in the same region. In the

middle of the water film the two concentrations are equal to respect electroneutrality. The voltage decreases from a value of - 0.11 V near the grain, to - 0.0001 V in the middle of the water film.

The relationship between the pressure and the water film thickness

Equation (4) gives pressure as a function of Δ. In double logarithmic scales the curves can be fitted by straight lines. We obtain a linear relationship between the logarithms of the pressure (bars) and Δ (angstroms):

$$\ln(\Delta) = a + b\ln(P) \qquad (38)$$

where a and b are constants depending on surface charge and temperature. We have calculated such curves for different surface charges between - 0.01 and - 0.15 C/m^2 (fig. 4) and found the charge dependence of a and b to be

$$a = 9.3925 + 5.88\,\sigma + 26.96\,\sigma^2$$

$$b = -1.008 - 0.41\,\sigma$$

where σ is the surface charge (C/m^2).

If we develop the exponentional in equation (3) of our simple model, we obtain:

$$\Delta \approx \frac{C}{(p_z - p_0)} \qquad (39)$$

where C is a constant. In the complete Debye-Huckel/Osmotic model, we have :

$$\Delta \approx C'(p_z - p_0)^b \qquad (40)$$

where C' is a constant and b has a value close to -1. The two equations (39) and (40) are similar. The only difference is the value of the constants C and C'. $C = 5 \times 10^{-8}$ and $C = 8 \times 10^{-7}$ for P in bars and Δ in m. There is a factor 16 between these two numbers. At the same pressure, the DH/O theory gives a bigger water film thickness.

Application: evolution of the rate of pressure solution by the water film diffusion mechanism

Ortoleva and co-workers (Dewers and Ortoleva, 1990) have proposed the following expression to estimate the rate of pressure-solution by water film diffusion.

$$G_{WFD} = -\frac{2\pi\Delta D\left(c_{contact} - c_{pore}\right)}{\rho_{quartz} A} \qquad (41)$$

where G_{WFD} is the rate of pressure solution (in m/s), water film thickness Δ, coefficient of diffusion inside the film of water D, concentrations of dissolved silica inside the contact and inside the pore fluid, $c_{contact}$ and c_{pore}, respectivily, molar volume of quartz ρ_{quartz} (6.0085×10^{-7} m^3/mole) and surface of the contact A. Using our equation for Δ, we can determine the rate of pressure solution versus depth.

For this, we assume that the diffusion mechanism is like that of water when the water film is sufficiently thick. The coefficient of diffusion is taken to be 10^{-10} m^2/s. When the water film is thiner than 2 layers of water molecules (4 Angstroms), the diffusion process slows down and we adopt a coefficient of diffusion more like that of solids, in the order of 10^{-15} m^2/s.

Figure 5 shows that the pressure solution by water film diffusion is most efficient between 1000 and 3000 m, corresponding to the depth where the loss of porosity is greatest in a sedimentary basin. The pressure solution rate depends on a driving force, which is the difference of the concentrations of silica between the contact area and the pore fluid, and on the diffusion rate inside the film. The driving force increases with depth, due to the increasing pressure on the contact area. On the contrary, the water film thickness decreases as a result of the increasing pressure. The competition between these two factors leads to a curve with a maximum of pressure solution at 2000 m. At deeper depth, the pressure solution is less efficient. This is an argument to explain the preservation of porosity at depth greater than 3000 m.

In an overpressured compartment, the water film layer becomes thicker and the pressure solution rate increases. This can explain why the reduction rate of porosity is higher in these regions.

CONCLUSIONS

The purpose of this study was to estimate the influence of electric charge on the surface of the grain and the water film inside the contact between two grains.We have obtained a relationship between the thickness of this film of water, stress across the contact and fluid pressure, and the surface charge. For the case where the two minerals making the contact are the same. This relationship should change if the two surface charges are different, for example if a grain of quartz is in contact with a sheet of mica. However, when the two minerals bounding the contact are different, the symmetry in the profiles of concentration and voltage of figure 3 are skewed toward one of the minerals.

Many points have not yet been studied. Particularly, the influence of temperature on the thickness of the water film, through the dielectric constant, may be important. Another problem is the roughness of the mineral surface. We assumed that the surface of contact was flat. This may be a fair estimation for micas sheets, but it becomes less realistic in the case of quartz for example.

This study shows that water film can be sustained under large stress across a cotnact. Thus the water film diffusion mechanism can operate under high stress. Our Debye-Huckel/Osmotic model is a first step in the study of the water film structure and it has raised many interesting issues.

Acknowledgements

This research was supported by grants from the Institut Francais du Petrole, the U.S. Department of Energy and a contract with the Gas Research Institute.

References

Ananthaswamy J. and Atkinson G. (1984) Thermodynamics of concentrated electrolyte mixtures. 4. Pitzer-Debye-Hückel liminting slopes for water from 0 to 100°C and from 1 atm to 1 kbar. *J. Chem. Eng. Data* **29**, 81-87.

Anderson S. J. and Sposito, G. (1991) Cesium-adsorption method for measuring accessible structural surface charge. *Soil Sci. Soc. Am. J.* **55**, 1569-1576.

Archer D. G. (1990) Effect of revisions of Debye-Huckel limiting law coefficients on the thermodynamic parameters for strong electrolytes. *J. Chem. Eng. Data* **35**, 340-344.

Baudin I., Ricard A. and Audebert, R. (1990) Adsorption of dextrans and pullulans at the silica-water interface; hydrodynamic layer thickness measurements; role in the fouling of ultrafiltration membranes. *J. Colloid Int. Sci.* **138**, 324-331.

Bradley D. J. and Pitzer K.S. (1979) Thermodynamics of electrolytes. 12. Dielectric properties of water and Debye-Huckel parameters to 350°C and 1 kbar. *J. Phys. Chem.* **83**, 1599-1603.

Brady P.V. (1992) Silica surface chemistry at elevated temperatures. *Geochim. Cosmochim. Acta* **56**, 2941-2946.

Brady P.V. (1994) Alumina surface chemistry at 25, 40 and 60°C. *Geochim. Cosmochim. Acta* **58**, 1213-1217.

van Cappellen P., Charlet L, Stumm W. and Wersin P. (1993) A surface complexation model of the carbonate mineral-aqueous solution interface. *Geochim. Cosmochim. Acta* **57**, 3505-3518.

Clegg L., and Whitfield M. (1991) Activity coefficients in natural waters, chap 6. in *Activity Coefficients In Electrolytes Solution* , Pitzer K.S., CRC Press. 542 p.

Dewers T. and Ortoleva P. (1990) A coupled reaction/transport/mechanical model for intergranular pressure solution, stylolites, and differential compaction and cementation in clean sandstones. *Geochim. Cosmochim. Acta* **54**, 1609-1625.

Herrington, T.M., Clarke, A.Q. and Watts, J.C. (1992) The surface charge of kaolin. *Colloids and Surfaces* **68**, 161-169.

Hunter R. J. (1986) *Foundations of Colloid Science, Vol. 1*, Oxford Science Publications, 673 p.

Pitzer K.S. (1973) Thermodynamic of electrolytes. I. Theoretical basis and general equations. *J. Phys. Chem.* **77**, 268-277.

Pitzer K.S. and Mayorga G. (1973) Thermodynamic of electrolytes. II. Activity and osmotic coefficients for strong electrolytes with one or both ions univalent. *J. Phys. Chem.* **77**, 2300-2308.

Pitzer K. S. (1987) Thermodynamic model fore aqueous solutions of liquid-like density, in Carmichael I. S. E. & Eugster H. P. *Thermodynamic modeling of geological materials: Minerals, fluids and melts, Reviews in mineralogy* **17**, 97-142.

Pitzer K. S., Pelper J. C. and Busey R. H. (1984) Thermodynamic properties of aqueous sodium chloride solutions. *J. Phys. Chem. Ref. Data.* **13**, 1-102.

Pitzer K. S. (1991) *Activity coefficients in electrolytes solution.* 2nd edition. CRC Press. 542 p.

Stumm W. and Morgan J. J. (1981) *Aquatic Chemistry: An Introduction Emphasizing Chemical Equilibria in Natural Waters.* Second edition, Wiley, 780 p.

Villemure G. (1990) Effect of negative surface-charge densities of smectite clays on the adsorption isotherms of racemic and eniantomeric tris(2,2'-bipyridyl)ruthenium (II) chloride. *Clays and Clay Minerals* **68**, 622-630.

Wood J. R. (1975) Thermodynamics of brine-salt equilibria - I. The systems NaCl-KCl-$MgCl_2$-$CaCl_2$-H_2O and NaCl-$MgSO_4$-H_2O at 25° C. *Geochim. Cosmochim. Acta* **39**, 1147-1163.

Yates D. E. and Healy T. W. (1975) The structure of the silica/electrolyte interface. *J. Colloid and Interface Sci.* **55**, 9-19.

Zhou Z and Gunter W. D. (1992) The nature of the surface charge of the kaolinite. Clays and Clay Minerals 40, 365-368.

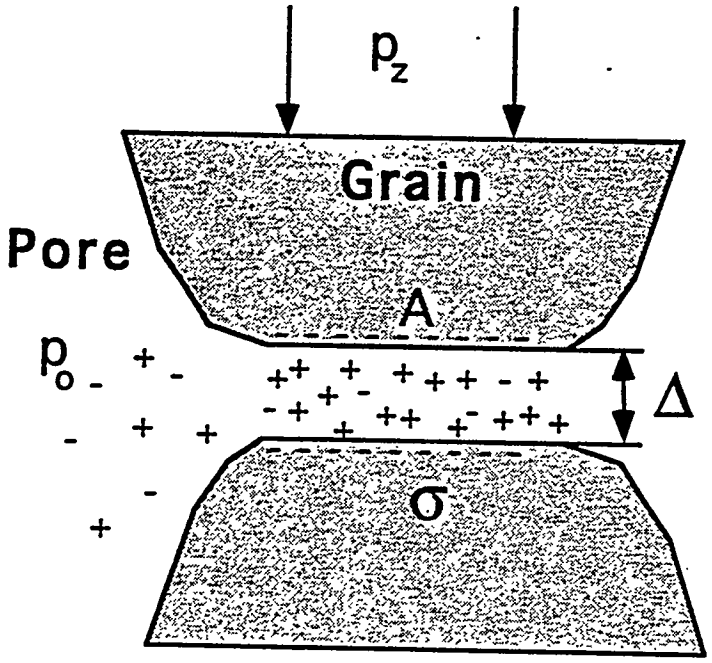

Fig. 1 Distribution of the electric charges in a schematic grain-grain contact. Here the negative charges of the surface of the grain are compensated by a cloud of positive ions in the water film of the contact. The compressive stress in the grain across the contact is p_z, the pressure of the pore fluid is p^o. σ is the surface charge, A the surface of the contact.

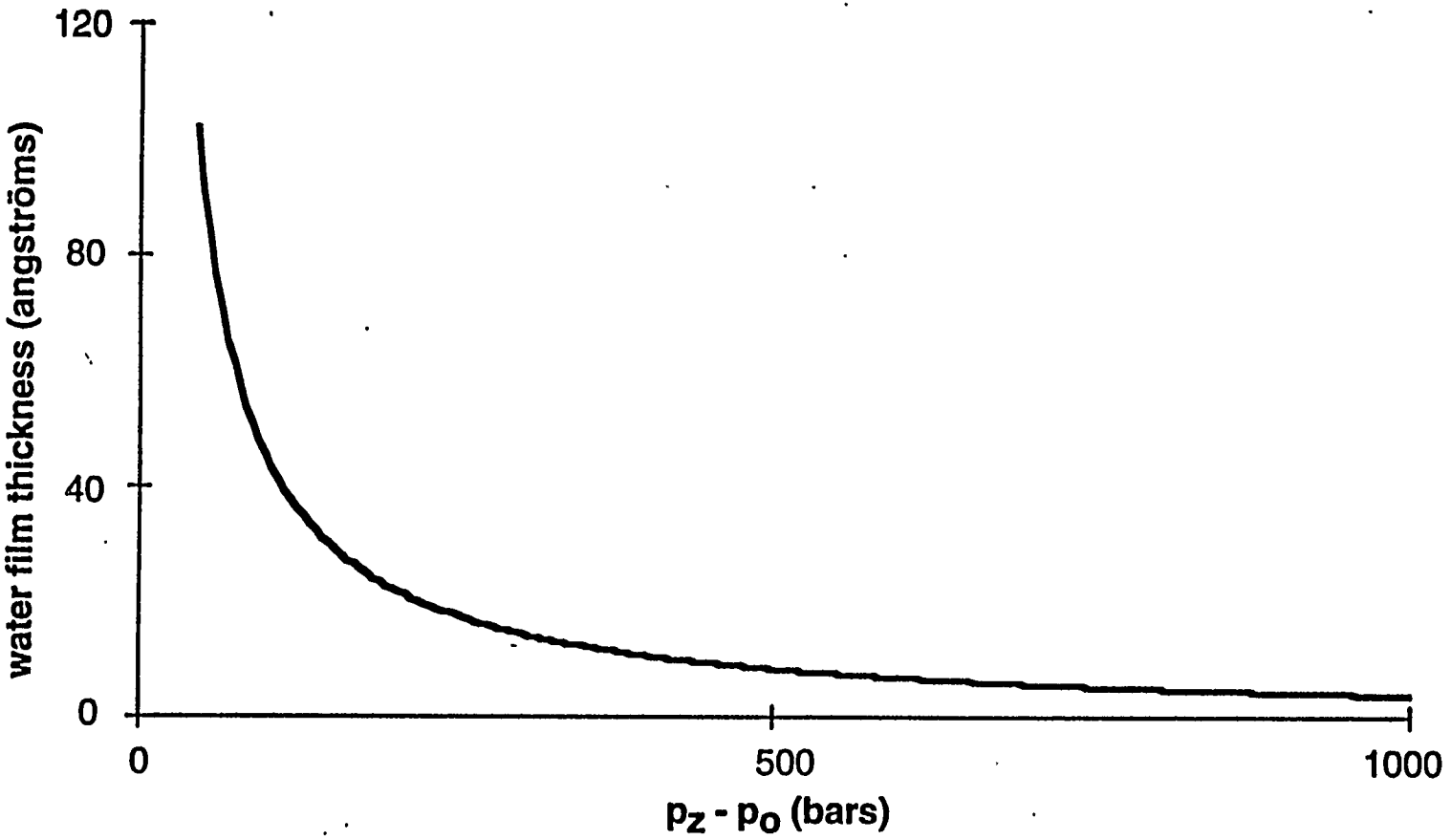

Fig. 2 Preliminary prediction of water film thickness Δ as a function of the difference between the compressive stress p_z, normal to the contact and fluid pressure p^o in the pore, for a temperature of 100°C. A positive charge density of - 0.1 C/m^2 (measured from muscovite--see Hunter, 1986) was chosen. We believe the theory will be able to predict the variations of Δ with mineral identity, presence/absence of clay in the contact, pore fluid salinity, pH and composition and temperature. Our Debye-Hückel/osmotic model seems to be a major advance in the theory of pressure solution.

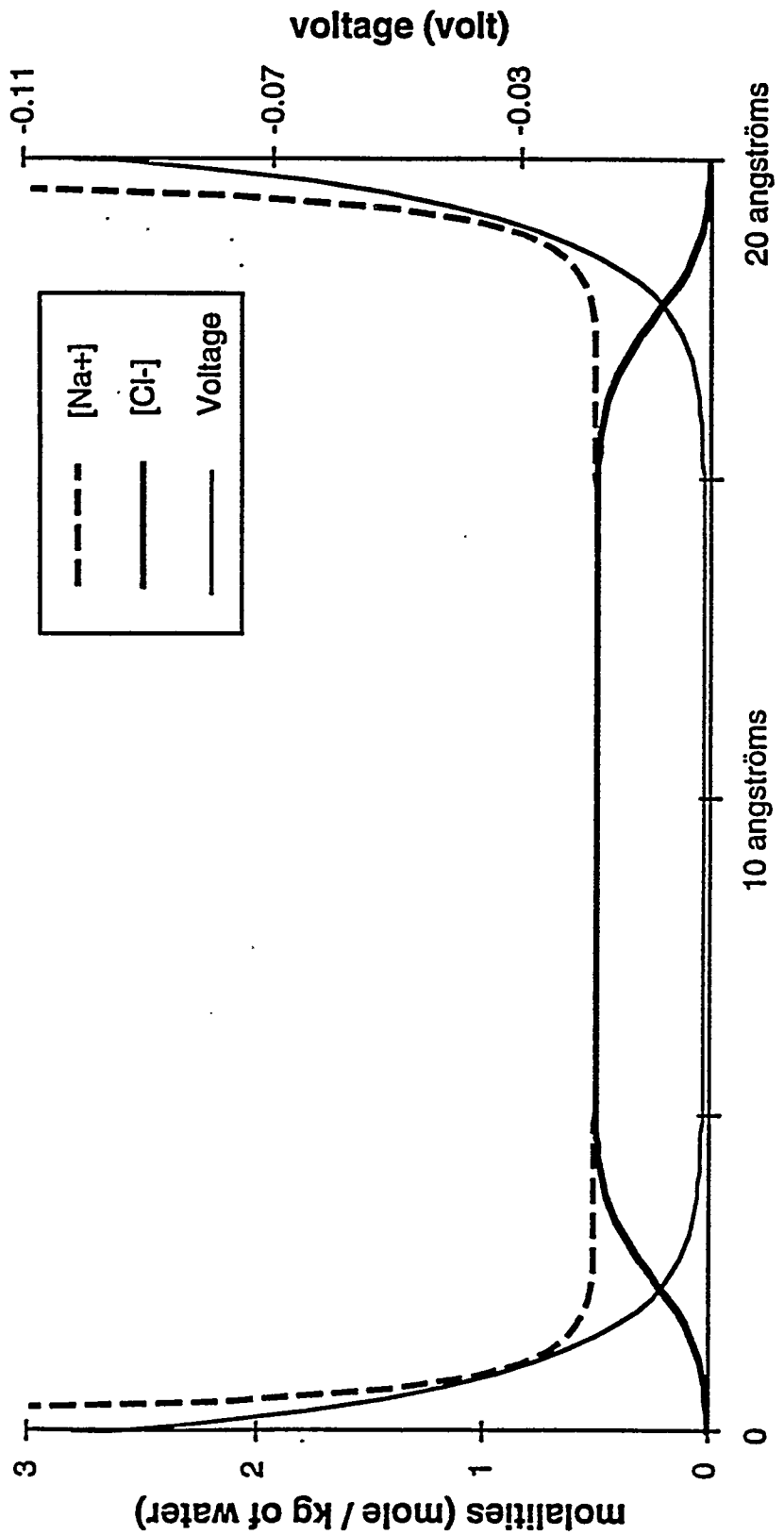

Fig. 3 Profile of the voltage and the concentrations inside the contact, across the water film. Parameters used to solve the equations III. 1 and III. 9 were : $\sigma = -0.05$ C/m2, concentration in the pore fluid 0.5 mole/kg of water and $\Delta = 20$ angstroms.

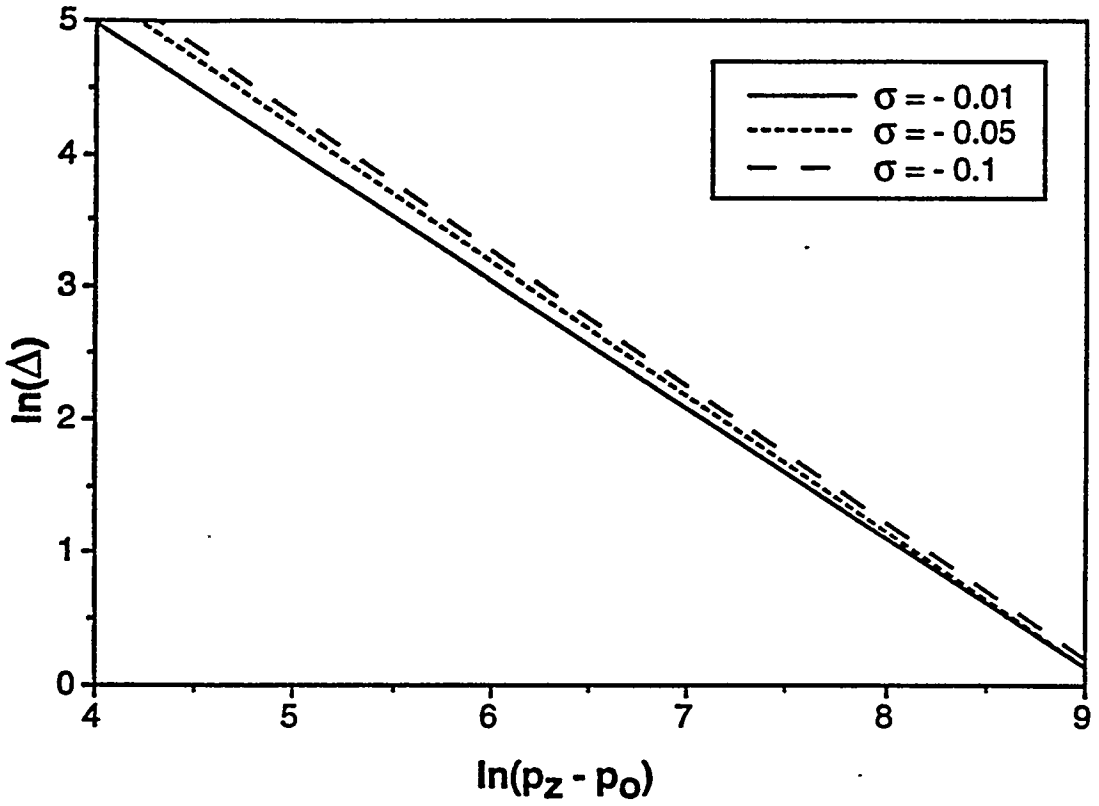

Fig. 4 Dependence of water film thickness on deviatoric stress ($p_z - p^o$) for a range of surface charge densities according to the D-H/O model.

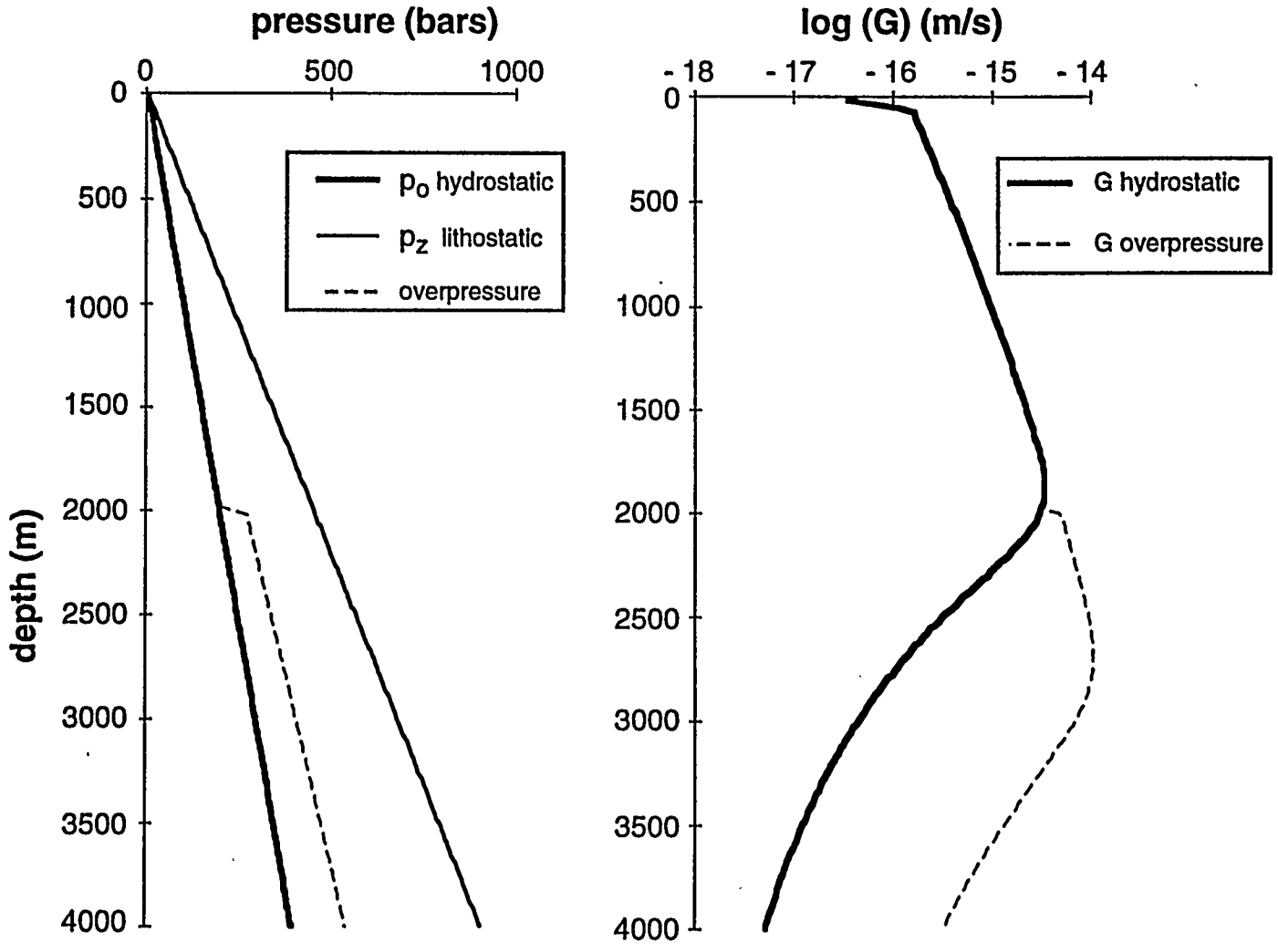

Fig. 5 Dependence of pressure solution rate as in equation VIII.1 with (and via the geothermal gradient of temperature) showing the interplay between the increase in rate due to increasing deviatoric stress and the decrease associated with the decrease Δ. Parameters used where a constant gradient of temperature (30°/km) and a surface charge of - 0.1 C/m^2.

Appendix C

Fracture Nucleation, Growth and Cement Infilling: A Mechano-Chemical Model

C. Qin, A. Park, F. Renard and P. Ortoleva

Laboratory for Computational Geochemistry

Department of Chemistry
Indiana University
Bloomington, IN 47405

Abstract

The kinetics of fracture nucleation, growth and healing plays a central role in determing the characteristics of gas producibility in tight gas sandstone reservoirs. They may comprise the major component of the internal permeability. Fracturing and healing of seals can determine limits on overpressures and the leakage of petroleum from overpressured compartments or the injection of petroleum into underpressured ones. To predict the producibility of potential tight gas sandstone reservoirs, we develop a fracture kinetics model. The model integrates diagenesis, mechanical fracture kinetics and chemical cement infilling.

The purely mechanical notion of fracturing is modified to capture key elements of the interplay between fracturing and diagenesis. Consider now a macroscopic theory of fracturing that places it in a context of pressure solution and elastic and plastic deformation in the surrounding matrix. The model is implemented in a basin simulator CIRF.B and illustrative simulations are presented.

The goals of the model proposed here are as follows:

(1) Predict the effects of burial, thermal and tectonic history on fracture and fracture network properties;

(2) Delineate the effects of the texture and mineralogy of a rock on the characteristics of the fractures and the mineralogy and characteristics of infilling cements; and

(3) Show how fracturing and infilling effect the overall magnitudes, timing and spatial distribution of flows, over- and under-pressures and pressure seals and compartments in a sedimentary basin.

Addressing these questions is central to our understanding of a sedimentary basin and for the exploration and production of petroleum in fractured reservoirs.

I. Introduction

A number of factors determine the characteristics of fractures. Mechanical factors determine the tendency for the rock to part at some surface; elastic and plastic responses can affect aperture, shape and size. Diagenesis can lead to the cement infilling of fractures and, through pressure solution, change the shape, size and aperture of fractures. Hence, fracturing is a result of the complex interplay of mechanical and chemical processes.

The purpose of the present work is to develop a macroscopic theory of the mechano-chemistry of subcritical fractures and their role in basin diagenesis. The basic model adopted is as suggested in Fig. 1. The individual fractures are treated as features like grains so that they are descriptive elements in a macroscopic theory. The pressure solution, elastic response, plastic flow and fracturing are placed within a unified context via the formalism of incremental stress theory.

The fracture as a descriptive element is treated as a "typical fracture". Then an array of features is treated in terms of the dynamics of the typical fracture, a fracture number density and the kinetics of cement infilling/dissolution within the fracture. The dynamics of an individual fracture depends on the local stress environment. The latter can be strongly modified by the local rock rheological properties which in turn depends on the individual fracture characteristics and the number density of fractures. In short, fracturing during diagenesis presents itself as a tightly coupled mechano-chemical system.

In the section to follow we outline the model and kinematic aspects of the fracture model and then analyze the specific mechanical and chemical phenomenological laws we propose.

II. The Basic Model

Fractures are considered to have the geometry as in Fig. 2. They are taken to be of radius r and aperture a as defined there. Each fracture has void volume $\mathcal{V}$. If η is the number of such fractures per unit volume of the unfractured matrix then the fracture volume of a rock of

unfractured volume Ω is $\Omega\eta\mathcal{V}$. The matrix has volume Ω so the total fractured rock volume Ω_{tot} is given by

$$\Omega_{tot} = \Omega(1+\eta\mathcal{V}).$$

With this we have

$$\tilde{n} = \left\{\begin{matrix}\text{number of grains per} \\ \text{whole rock volume}\end{matrix}\right\} = \frac{n}{1+\eta\mathcal{V}}$$

$$\tilde{\eta} = \left\{\begin{matrix}\text{number of fractures per} \\ \text{whole rock volume}\end{matrix}\right\} = \frac{\eta}{1+\eta\mathcal{V}} \qquad \text{(II.1)}$$

where n is the number of grains per unit volume of matrix.

Fracture radius change rate is expressed as

$$\frac{dr}{dt} = \mathcal{G} + \mathcal{H}, \quad \begin{matrix}\mathcal{G} = \text{growth rate } (\geq 0) \\ \mathcal{H} = \text{healing rate}\end{matrix} \qquad \text{(II.2)}$$

Here $\mathcal{G}(\leq 0)$ is the growth rate due to mechanical fracture extension; $\mathcal{H}$ is a contribution to dr/dt from cement infilling (a negative contribution) or dissolution (a positive contribution) or other irreversible terms associated with the visco-plastic deformation of the matrix around the fracture.

The fracture extension rate $\mathcal{G}$ is taken from the classical theory (Dunnington 1967; Wang et al., 1983; Atkinson, 1984; Segall, 1984; Smith and Evans, 1984; Swanson, 1984; Pollard and Aydin, 1988; Sleep, 1988). Let p^* be minus the least principle stress ($-\sigma_{xx}^m$ when the least principle stress is in the x (horizontal) direction) plus the fracture extension force as arises in the classical theory of fracture length extension rate. Then have

$$\mathcal{G} = \begin{cases} v_f(1-e^{-U/\mathcal{R}T}), & p > p^* \\ 0, & p \leq p^* \end{cases} \qquad \text{(II.3)}$$

Here v_f and U are as per the Atkinson mechanical fracture extension rate. The rate $\mathcal{G}$ is the fracture growth rate that is assumed to be nonzero for $p > p^*$.

A fracture shortening process would occur when the matrix is compacting due to pressure solution in the direction parallel to the fractures. Suppose the fractures are vertical--along the z-direction. Then

$$\mathcal{H}^{matrix\ ps} = \frac{r}{1-\phi}\sum_{i=1}^{M}\frac{G_{zi}}{L_{zi}} \qquad \text{(II.4)}$$

assuming the system is composed of M minerals with periodic truncated sphere packing (Dewers and Ortoleva, 1990) where m_i, L_{zi}, and G_{zi} are the volume fraction, grain height, and grain dissolution rate in vertical direction of the i-th mineral respectively and ϕ is the porosity of the medium..

The fracture aperture a is commonly assumed to obey an elastic relationship (Sleep, 1988)

$$a = \begin{cases} Yr(p - P_l), & p > P_l \\ 0, & p < P_l \end{cases} \tag{II.5}$$

for forefactor Y and least principle compressive stress P_l. In the present model we take $P_l = -\sigma_{xx}^m$ for the least compressive stress being horizontal as above. When we have other (irreversible) processes taking place, we adopt a model suggested by incremental stress theory (Zienkiewicz and Cormeau, 1974). A small variation δa in time increment δt takes

$$\delta a = Y\delta(r(p\text{-}P_l)) + h\delta t. \tag{II.6}$$

The rate of change of aperture a due to cementation and visco-plastic (irreversible, mechanical) closure is denoted by h. We might add all healing and visco-plastic contributions roughly as follows

$$h = h^{infill} + a\left(\dot{\varepsilon}_{\perp}^{vp} + \dot{\varepsilon}_{\perp}^{ps}\right) \tag{II.7}$$

$$\mathcal{H} = \mathcal{H}^{infill} + \mathcal{H}^{matrix\,ps} + r\left(\dot{\varepsilon}_{||}^{vp} + \dot{\varepsilon}_{||}^{ps}\right) \tag{II.8}$$

where superscript "infill" refers to all precipitation processes; $\dot{\varepsilon}_{||}^{vp}$ and $\dot{\varepsilon}_{||}^{ps}$ are the rates of strain in the fracture parallel direction (and similarly for the normal direction). Also $\mathcal{H}^{infill}$ and h^{infill} are related as in (II.13). The formulae for the $\dot{\varepsilon}$ contributions are related to the macroscopic rates of strain but require adjustment due to the local stress environment near the fracture. They will not be dealt with further here.

To make an explicit connection between h^{infill} and $\mathcal{H}^{infill}$ we use the geometry and notation of Fig. 3. First note

$$S + \frac{1}{2}a = R \tag{II.9}$$

$$S^2 + r^2 = R^2. \tag{II.10}$$

These may be combined to yield

$$\frac{r^2}{a}+\frac{a}{4}=R. \tag{II.11}$$

But during cementation without elastic closure $\frac{dR}{dt}=\frac{1}{2}\frac{da}{dt}$ (by our assumed fracture geometry).

Hence

$$\frac{2r}{a}\mathcal{H}^{infill}+\left(\frac{1}{4}-\frac{r^2}{a^2}\right)h^{infill}=\frac{1}{2}\frac{da}{dt}. \tag{II.12}$$

And

$$\mathcal{H}^{infill}=\left(\frac{a}{8r}+\frac{r}{2a}\right)h^{infill}. \tag{II.13}$$

Such a relation would also hold for any infilling process (i.e., calcite, multi-mineralic, etc.)

III. Fracture Infilling Cement Model

All minerals of the chemical model, including those present or which can nucleate, are allowed to initiate in the fracture once it develops a nonzero radius. All these potential cement-forming grains grow like nucleating grains as treated in the nucleation model for the matrix. The algorithm is as follows:

1. At the time of fracture initiation all allowed minerals are tested for exceeding a nucleation threshold special for fractures.
2. Those minerals indicating that they can nucleate (at the nucleation criterion for the free face) can commence to grow at the free face rate for that mineral.
3. The minerals grains once growing can also dissolve.
4. The number density for the nucleated grains is the same for all minerals and is a special value for the fracture infilling problem.
5. Once the fracture is completely infilled, the grains within it grow/dissolve with a normal pressure ($p \rightarrow p_{frac}$) which is given by

$$p_{frac}=-\frac{1}{3}tr\underline{\underline{\sigma}}^m. \tag{III.1}$$

Here $\underline{\underline{\sigma}}^m$ is the macrostress in the rock

$$tr\underline{\underline{\sigma}}^m=\sigma_{xx}^m+\sigma_{yy}^m+\sigma_{zz}^m. \tag{III.2}$$

The switch between p and p_{frac} is smoothly given by $\hat{p}(\xi)$

$$\hat{p} = p + (p_{frac} - p)\frac{\xi^2(1+\xi_c^2)}{\xi_c^2+\xi^2} \tag{III.3}$$

where ξ is the fraction of the fracture volume filled by cement and ξ_c is a number very close to 1. Note $\hat{p}$ virtually equals p when ξ is smaller than ξ_c and approaches to p_{frac} quickly after ξ exceeds ξ_c.

6. The fracture filling cement coats the walls of the fracture with an assumed smooth, low porosity coating. As in Fig. 2 the coating thickens with normal velocity w. In a time δt a thickness $w\delta t$ is added. But also a volume addition can be calculated from grain growth kinetics.

The volume added in a small patch of area A is

$$Aw\delta t = \sum_{i=1}^{M} \dot{v}_i^{frac.}\delta t A\Gamma. \tag{III.4}$$

where $\dot{v}_i^{frac.}$ is the fracture fill mineral growth mediated fracture volume decrease rates. Γ is the number of mineral grains allowed per area of fracture at the wall rock. The number density of mineral i grains in the fracture is

$$n_i^{fract} = Aw\Gamma \tag{III.5}$$

From (III.4) we have

$$w = \sum_{i=1}^{M} \dot{v}_i^{frac.}\Gamma \tag{III.6}$$

and

$$h^{infill} = 2w. \tag{III.7}$$

Next when the fracture is filled then further growth goes with p_{frac} not p. But $\underline{\underline{\sigma}}^m$ as above should be modified to account for the extra local force in dilating the rock.

$$\underline{\underline{\sigma}}^m \to \underline{\underline{\tilde{\sigma}}}^m = \underline{\underline{\sigma}}^m + \frac{\left(\mathcal{V}_{frac} - \mathcal{V}^{just\,filled}\right)}{\beta\mathcal{V}^{just\,filled}}\underline{\underline{I}} \tag{III.8}$$

where β is the rock bulk modules.

Conservation of solute mass in a macrovolume element containing many matrix grains and fractures yields

$$\frac{\partial \phi c_\alpha}{\partial t} = -\overline{\nabla} \bullet \vec{J}_\alpha + \sum_{k=1}^{N_f} \omega_{\alpha k} W_k + \sum_{k=1}^{N_m} \nu_{\alpha k} \rho_{i(k)} \sum_{\gamma=x,y,z,f} n_{i(k)} A_{\gamma i(k)} G_{\gamma k}$$

$$+ \sum_{k=1}^{N_m} \nu_{\alpha k} \rho_{i(k)} \frac{\eta}{1+\mathcal{V}\eta} n_{i(k)}^{frac} \sum_{\gamma=x,y,z,f} G_{\gamma k}^{cem.} A_{\gamma i(k)}^{cem.} . \qquad \text{(III.9)}$$

where $\mathcal{V}(r,a)$ is given by

$$\mathcal{V} = \frac{\pi}{6} a \left(3r^2 + \frac{a^2}{4} \right) \qquad \text{(III.10)}$$

and

$$\dot{v}^{cem} = \sum_{k=1}^{N_m} n_{i(k)}^{frac} \sum_{\gamma=x,y,z,f} \frac{\partial \mathcal{V}^{grain}}{\partial L_{\gamma i(k)}} G_{\gamma k}^{cem.} . \qquad \text{(III.11)}$$

References

Atkinson, B.K., 1984. Subcritical crack growth in geological materials. Journal of Geophysical Research 89, 4077-4114.

Dewers, T. and Ortoleva, P., 1990. A Coupled Reaction/Transport/Mechanical Model for Intergranular Pressure Solution, Stylolites, and Differential Compaction and Cementation in Clean Sandstones. Geochim. Cosmochim. Acta 54, 1609-1625.

Dunnington, H.V., 1967. Aspects of diagenesis and shape change in stylolitic limestone reservoirs, In Proceedings of the 7th World Petroleum Congress, Mexico, 1967, v. 2, p. 337-352.

Pollard, D.D. and Aydin, A., 1988. Progress in understanding jointing over the past century. Geological Society of America Bulletin 100, 1181-1204.

Segall, P., 1984. Rate-dependent extensional deformation resulting from crack growth in rock. Journal of Geophysical Research 89, 4185-4196.

Sleep, N.H., 1988. Tapping of melt by veins and dikes. Journal of Geophysical Research 93, 10255-10272.

Smith, D.L. and Evans, B., 1984. Diffusional crack healing in quartz. Journal of Geophysical Research 89, 4125-4136.

Swanson, P.L., 1984. Subcritical crack growth and other time- and environment-dependent behavior in crustal rocks. Journal of Geophysical Research 89, 4137-4152.

Wang, J.S.Y., Tsang, C. and Sternbentz, R.A., 1983. The state of the art of numerical modeling of thermohydrologic flow in fractured rock masses. Environmental Geology 4, 133-199.

Zienkiewicz, O.C. and Cormeau, I.C., 1974. Visco-plasticity--plasticity and creep in elastic solids--a unified numerical solution approach. Int. J. Numer. Methods Eng. 8, 821-845.

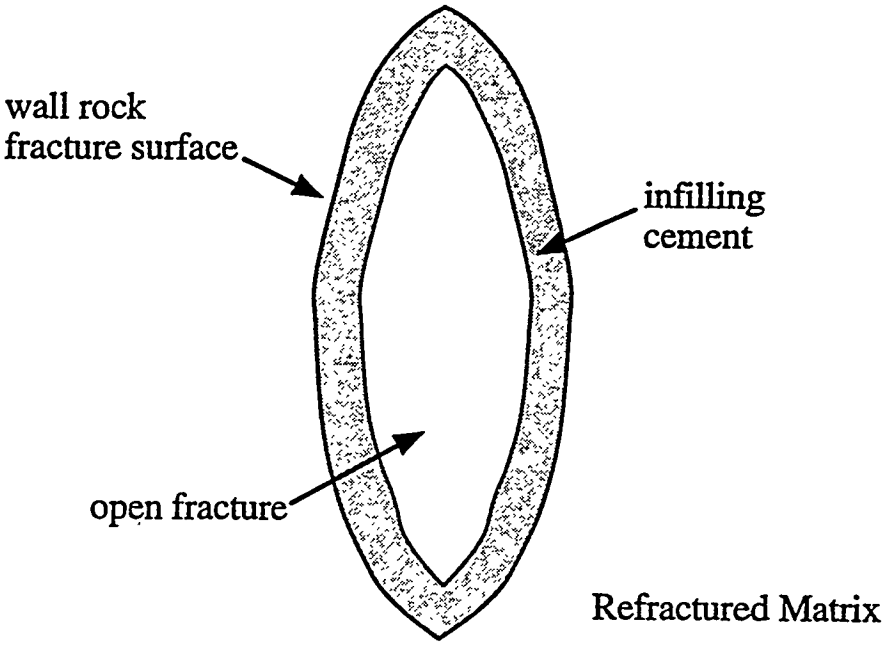
wall rock
fracture surface
infilling
cement
open fracture
Refractured Matrix

Fig. 1

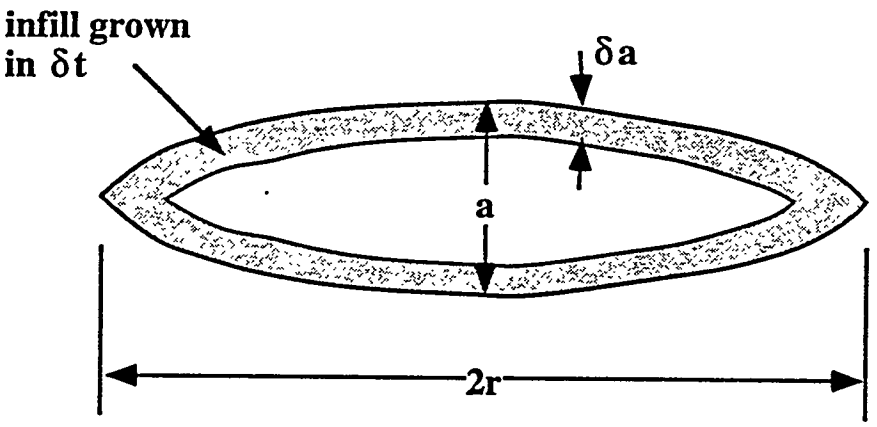

Fig. 2 Fracture radius r and aperture a defined along with the assumed geometry of infilling cements

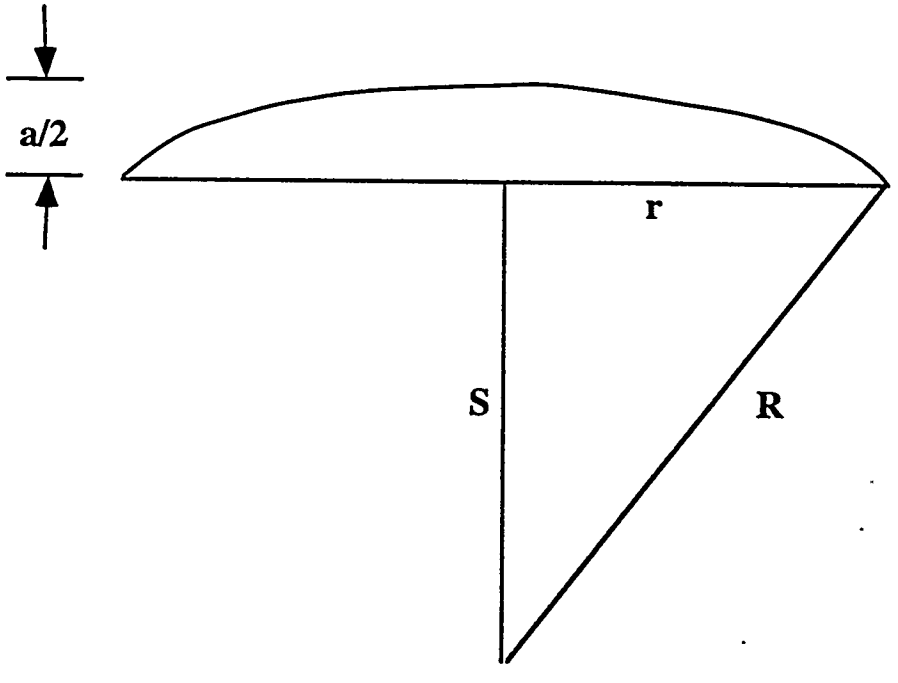

Fig. 3 Cross-section of spherical cap showing geometry variables used in calculating rate relations and fracture volume.

Appendix D1

Three Dimensional Basin Incremental Stress Modeling and Finite Difference Simulation

K. Sakrani, J.M. Maxwell and P. Ortoleva

Laboratory for Computational Geochemistry
Indiana University
Bloomington IN 47405

I. INTRODUCTION

A central aspect of naturally fractured tight gas reservoirs is the evolution of the distribution of stress within the basin. As there is a great deal of coupling between the evolution of stress and of fluid pressure and diagenetic reactions, we require a rock rheologic fomulation which can integrate the stress evolution into that of the other quantities. The theory that presents itself for this integration is incremental stress theory.

The objective here is to present an introduction to incremental stress theory to show how it naturally allows for the coupling to other processes. In particular we illustrate the types of rock rheologic models that we believe will capture the evolution of a naturally fractured tight gas reservoir.

The fundamental descriptive variable for the mechanical problem is the rock deformation velocity $\bar{u}$. With it we can trace the time course of any material point through time. The rate of strain tensor is given by the spatial derivatives of $\bar{u}$. In the incremental stress this net rate of strain is given by the sum of elastic and inelastic contributions. In our model the latter has three contributions - one each from irreversible mechanical deformation (viscous or plastic term), a pressure solution term and, finally, a term from fracturing.

This formulation allows for the key feedback between stress and the various processes. For example, fracturing causes overall rock dilitation which, in turn, causes extra stress which can, in turn, tend to repress further fracture growth or opening.

In the remainder of this presentation we give our model as formulated to date and suggest a finite difference numerical simulation technique for solving the problem. In the companion piece (Tounsi and Ortoleva, 1994) gives a finite element treatment and presents preliminary results.

II. BASIN INCREMENTAL STRESS MODEL AND CALCULATION

The basis of our calculation is the incremental stress rheology and the force balance condition. The calculation focuses on the determination of the rock deformation velocity $\vec{u} = (u_1,u_2,u_3)$ as observed in the laboratory coordinate system $\vec{r} = (x_1,x_2,x_3)$. The macroscopic rate of strain $\dot{\underline{\underline{\varepsilon}}}^m = \frac{1}{2}\left(u_{i,j} + u_{j,i}\right)$ has several contributions:

$$\dot{\underline{\underline{\varepsilon}}} = \underline{\underline{\underline{\underline{C}}}}^{-1} \frac{D}{Dt}\left(\underline{\underline{\sigma}} + \alpha p \underline{\underline{I}}\right) + \dot{\underline{\underline{\varepsilon}}}^{ir}. \tag{II.1}$$

Here $\underline{\underline{\underline{\underline{C}}}}$ is the fourth rank tensor of elasticities, α is the Terzaghi effective stress coefficient, p is fluid pressure and $\underline{\underline{I}}$ is the identity tensor. In cases when the rock twisting is not important, the material time derivative D/Dt is related to the laboratory time derivative $(\partial/\partial t)_{\vec{r}}$ and the $\vec{r}$-gradient $\vec{\nabla}$ via

$$\frac{D}{Dt} = \frac{\partial}{\partial t} + \vec{u} \bullet \vec{\nabla}. \tag{II.2}$$

The theory is completed by the force balance conditions

$$\sum_{j=1}^{3} \frac{\partial \sigma_{ij}}{\partial x_j} = f_i \tag{II.3}$$

for body force component f_i and giving the specific rheology--i.e., dependence of $\dot{\underline{\underline{\varepsilon}}}^{ir,m}$ on stress, fluid composition and pressure and rock texture (see Sect. III).

The kinematics and numerical computation of the above problem is made somewhat complicated by the mixed formulation involving laboratory gradients and material time derivatives. Consider a reformulation in terms of curvilinear, material-fixed coordinates $\vec{\xi}$. Each material point is labeled with a unique $\vec{\xi}$ and hence $\vec{\xi}(\vec{r},t)$ yields the identity of the material point at $(\vec{r},t)$. Similarly, $\vec{r}\left(\vec{\xi},t\right)$ is the location of material point $\vec{\xi}$ at t. The transformations $\vec{r} \Leftrightarrow \vec{\xi}$ are assumed unique and sufficiently smooth. Thus all Jacobians are defined and we do not account for discontinuous phenomena like macroscopic breakage. Finally, as the material points move with $\vec{u}$ we have

$$\left(\frac{\partial \vec{r}}{\partial t}\right)_{\vec{\xi}} = \vec{u} \tag{II.4}$$

and furthermore D/Dt is $(\partial/\partial t)_{\vec{\xi}}$.

Because D/Dt is the constant $\vec{\xi}$ time derivative, it is convenient to reformulate the laboratory gradients $\vec{\nabla}\left(=\left(\frac{\partial}{\partial x_1},\frac{\partial}{\partial x_2},\frac{\partial}{\partial x_3}\right)\right)$ in terms of $\vec{\xi}$-derivatives. Consider a quantity $\psi\left(\vec{\xi},t\right)$. Then

$$\frac{\partial \psi}{\partial x_i}=\sum_{j=1}^{3}\frac{\partial \psi}{\partial \xi_j}\Lambda_{ji} \tag{II.5}$$

$$\Lambda_{j1}\equiv\left(\frac{\partial \xi_j}{\partial x_1}\right)_{x_2x_3t} \tag{II.6}$$

and similarly for Λ_{j2}, Λ_{j3}. The Jacobian Λ_{ji} translates from $\vec{\xi}$ to $\vec{r}$ gradients. From a conceptual and computational point of view it is useful to relate Λ_{ji} to the inverse Jacobian $\left(\partial x_i/\partial \xi_j\right)$. This is particularly useful because we can conveniently choose ξ_i to have integer value at computational grid nodes, the latter's position advancing in time via the deformation velocity. Thus $D\underline{\underline{\sigma}}^m/Dt$ can be simply discretized as, say, a discrete difference of $\underline{\underline{\sigma}}^m$ at a given grid node at time t + δt minus its value at t for small δt.

First note that the transformation can be written $x_i = x_i(\xi,t)$. Taking $\partial/\partial x_k$ of both sides

$$\delta_{ik}=\sum_{j=1}^{3}\left(\frac{\partial x_i}{\partial \xi_j}\right)\Lambda_{jk} \tag{II.7}$$

where δ_{ik} is the Kroniker delta. Thus Λ_{jk} can be calculated from the grid derivatives $\left(\partial x_i/\partial \xi_j\right)$, For example, taking ξ to be the grid indices on a rock-fixed grid with six sided elements,

$$\frac{\partial x_i}{\partial \xi_i}\approx\frac{x_i(\xi_1+1,\xi_2,\xi_3,t)-x_i(\xi_1-1,\xi_2,\xi_3,t)}{2} \tag{II.8}$$

for a central difference discretization.

With this formulation we may transform the rheology (II.1) and force balance condition (II.3) into a problem on (ξ,t) space (i.e., not involving laboratory gradients mixed with material time derivatives). This was the approach used in deriving the results of Maxwell and Ortoleva (1994). The ξ,t partial differential equations were solved on a cubic $\vec{\xi}$-grid using finite differences.

III. BOUNDARY CONDITIONS AND GRIDS

The stress boundary conditions to be invoked are chosen to reflect a range of important basin histories and to not introduce any artifacts that interfere with the natural system (wherein there are no lateral boundaries except the entirety of the planet surface). Furthermore, we choose a grid structure that reflects basin geometry and, furthermore, tends to simplify computation of the boundary conditions.

The system is taken to be ovoid in plan view and to have vertical sides as suggested in Fig. 1. At the top of the sediment pile the normal stress is specified to be fluid pressure p_o applied by the overlying ocean water column. If $\underline{n}$ is the outward normal and $\underline{\tau}_1$ and $\underline{\tau}_2$ are a set of unit vectors normal to $\underline{n}$ and to each other. Then if the tangential shear is zero at the top of the pile we have

$$\left.\begin{aligned} \underline{n} \bullet \underline{\underline{\sigma}}^m \bullet \underline{n} &= -p_o \\ \underline{\tau}_1 \bullet \underline{\underline{\sigma}}^m \bullet \underline{n} &= 0 \\ \underline{\tau}_2 \bullet \underline{\underline{\sigma}}^m \bullet \underline{n} &= 0 \end{aligned}\right\} \text{ at top of basin.} \qquad \begin{aligned} &\text{(III.1)} \\ &\text{(III.2)} \\ &\text{(III.3)} \end{aligned}$$

On the bottom of the basin, the sediment-basement interface, the dynamics is assumed fixed by the tectonic history. Thus if $\underline{U}(\xi^b,t)$ is the velocity of material points ξ^b at the bottom of the basin, we have

$$\underline{u}(\xi^b,t) = \underline{U}(\xi^b,t) \text{ at basin bottom.} \qquad \text{(III.4)}$$

On the sides of the basin the horizontal velocity (u_1,u_2) is specified to be $u_1^s\left(\underline{\xi}^s,t\right),u_2^s\left(\underline{\xi}^s,t\right)$ for material points ξ^s on the side of the basin. The gridding consists of stacked layers like those seen in Fig. 2. Each layer with the center point removed maps onto a square grid in ξ_1,ξ_2 space. In any discretization a function is "continued" to the center point by interpolating it as a linear function of ξ_1,ξ_2 fit by least squares with all the points $\xi_1 = 1$ comprising the innermost circle. The layers are stacked with increasing ξ_3 for each layer like that of Fig. 3.

The outward normals can be easily calculated. For example, the normal at the top boundary, where $\xi_3 = N_3$, is given by the laboratory gradient $(\underline{\nabla})$ of ξ_3 at $\xi_3 = N_3$:

$$\underline{n} = \frac{\nabla \xi_3}{|\nabla \xi_3|} \text{ at } \xi_3 = N_3. \tag{III.5}$$

To allow for vertical shortening due to compaction to take place naturally, we do not impose the vertical velocity u_3 on the sides but allow them to compact "freely" by assuming that the vertical shear is zero at the side. Letting $\underline{e}_3$ be a unit vector in the vertical, upward, direction and $\underline{n}$ be an outward normal to the sides we have

$$\left.\begin{array}{r} u_1, u_3 \text{ given} \\ \underline{e}_3 \bullet \underline{\underline{\sigma}}^m \bullet \underline{n} = 0 \end{array}\right\} \text{ at basin sides.} \tag{III.6}$$

The tangents $\underline{\tau}_1$ and $\underline{\tau}_2$ can be given by

$$\underline{\tau}_1 = \frac{\nabla \xi_1}{|\nabla \xi_1|} \tag{III.7}$$

$$\underline{\tau}_2 = \underline{n} \times \underline{\tau}_1. \tag{III.8}$$

IV. RHEOLOGY

The strain rate for irreversible processes is divided into three contributions:

$$\underline{\underline{\dot{\varepsilon}}}^{ir} = \underline{\underline{\dot{\varepsilon}}}^{vp} + \underline{\underline{\dot{\varepsilon}}}^{ps} + \underline{\underline{\dot{\varepsilon}}}^{f} \tag{IV.1}$$

where the notation

vp - visco-plastic

ps - pressure solution

f - microfracture

is adopted. The incremental stress approach is to separate purely mechanical (i.e., not chemically reactive (ps)) processes from grain boundary slip or individual grain mechanical deformation (vp) and fracture contributions.

Admittedly it is not straightforward to completely separate these processes out. For example, pressure solution may remove barriers to grain boundary slip and hence facilitate $\underline{\underline{\dot{\varepsilon}}}^{vp}$. In our work we shall address this point by introducing a specific formula for $\underline{\underline{\dot{\varepsilon}}}^{ps}$ and then assume that certain shearing and compaction dynamics associated with pressure solution-assisted processes (like grain boundary slip) are accounted for in $\underline{\underline{\dot{\varepsilon}}}^{vp}$.

In the present study we adopt a nonlinear viscosity model for $\underline{\underline{\dot{\varepsilon}}}^{vp}$:

$$\underline{\underline{\dot{\varepsilon}}}^{vp} = \underline{\underline{\underline{\eta}}}^{-1}\left(\underline{\underline{\sigma}}^{m} + \tilde{\alpha} p \underline{\underline{I}}\right) \tag{IV.2}$$

where $\tilde{\alpha}$ is an effective stress coefficient, generally taken to be unity for visco-plasticity. The fourth rank tensor of viscosities $\underline{\underline{\underline{\eta}}}$ is taken in the form

$$\eta_{ijkl} = \nu \delta_{ij}\delta_{kl} + \mu\left[\delta_{ik}\delta_{jl} + \delta_{il}\delta_{jk}\right] \tag{IV.3}$$

where ν and μ are bulk and shear viscosity coefficients. The inverse viscosity coefficients are taken to depend on stress via

$$\mu^{-1} = \mu_0^{-1} + \left(\mu_\infty^{-1} - \mu_0^{-1}\right) h(\xi) \tag{IV.4}$$

$$\nu^{-1} = \nu_0^{-1} + \left(\nu_\infty^{-1} - \nu_0^{-1}\right) h(\xi). \tag{IV.5}$$

where $\nu_0, \mu_0, \nu_\infty, \mu_\infty$ are values of the viscosity coefficients in the unplastified and plastified medium, respectively. ξ is the yield function that has the form:

$$\xi = \frac{6\sin\Psi}{3-\sin\Psi}\bar{\sigma} + \sqrt{3\,J_2} - \frac{6c\cos\Psi}{3-\sin\Psi} \tag{IV.6}$$

where Ψ is the angle of internal friction, c the cohesion, $\bar{\sigma}$, J_2 are stress invariants.

$$\bar{\sigma} = \frac{1}{3} tr \underline{\underline{\sigma}}^m \tag{IV.7}$$

$$s_{ij} = \sigma_{ij}^m - \delta_{ij}\bar{\sigma} \tag{IV.8}$$

$$J_2 = \frac{1}{2} s_{ij} s_{ij}. \tag{IV.9}$$

$h(\xi)$ is a function that makes a smooth transition between 0 and 1 as ξ passes through zero.

$$h(\xi) = \frac{e^{(\xi/\Delta)}}{1+e^{(\xi/\Delta)}} \tag{IV.10}$$

for a transition width Δ. As the yield limit is exceeded ($\xi \geq 0$) the rock viscosity drops and the material undergoes viscoplastic flow. In work in progress we are combining the nonlinear viscosity model above with notions from liquid crystal theory to obtain a model of induced tensor viscosity that accounts for the orientation of fracture planes and the resulting induced special directions of weakness.

The pressure solution contribution is taken to be diagonal and its form is discussed in Park and Ortoleva (1994). The microfracture model adopted is as outlined in Qin et al. (1994). From them one may obtain an expression for $\dot{\underline{\underline{\varepsilon}}}^{ps}$ and $\dot{\underline{\underline{\varepsilon}}}^{f}$.

V. REMARK

Our incremental stress basin modeling via the finite difference approach is presently not complete. Results using a finite element simulation approach are presented in Tounsi and Ortoleva (1994).

References

Dewers, T. and P. Ortoleva (1994) Nonlinear Dynamical Aspects of Deep Basin Hydrology: Fluid Compartment Formation and Episodic Fluid Science, Am. J. Sci. 294, 713-755.

Maxwell, J.M. and P. Ortoleva (1994) Basin Reaction, Transport, Compaction, Sedimentation and Energy Balance: Three Dimensional, Finite Difference Simulator - see Appendix E1.

Ortoleva, P.J. (1994) Geochemical Self-Organization, New York, Oxford University Press, 411 p.

Ortoleva, P.J. (1994) Nonlinear Chemical Waves, Chichester, John Wiley and Sons, 302 p.

Park, A. and P. Ortoleva (1994) Multimineralic Model of Pressure Solution Mediated Compaction - see Appendix A.

Qin, C., A. Park, F. Renard and P. Ortoleva (1994) Fracture Nucleation, Growth and Cement Infilling: A Mechano-Chemical Model - see Appendix C.

Sonnenthal, E. and P. Ortoleva (1994) Numerical Simulations of Overpressured Compartments in Sedimentary Basins, Basin Compartments and Seals, AAPG Memoir (in press)

Tounsi, F. and P. Ortoleva (1994) Three-Dimensional, Finite Element Solver for Basin Incremental Stress Modeling - see Appendix D2.

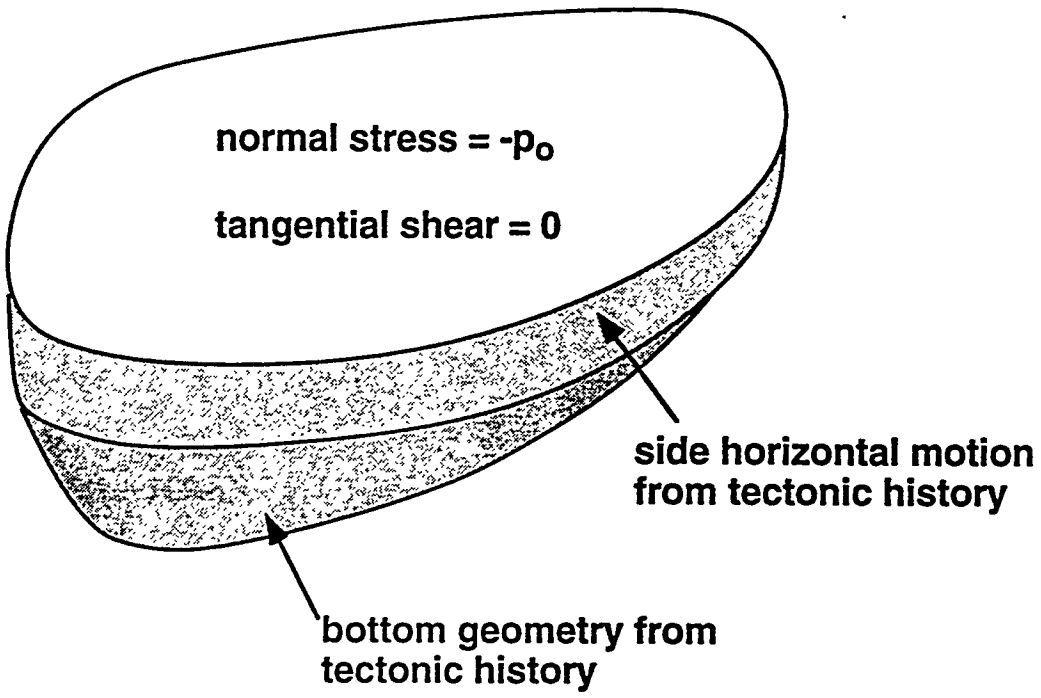
normal stress = -p_o
tangential shear = 0
side horizontal motion
from tectonic history
bottom geometry from
tectonic history

Fig. 1

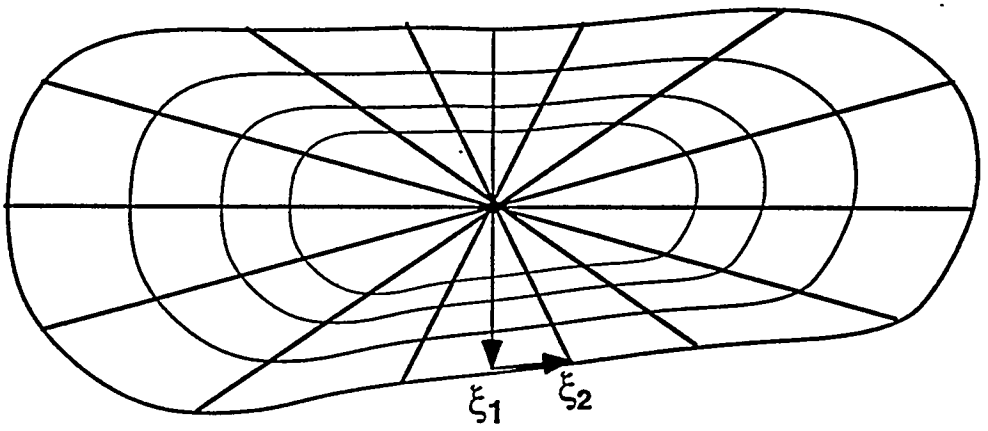

Fig. 2

Appendix D2

Three-Dimensional, Finite Element Solver for Basin Incremental Stress Modeling

F. Tounsi and P. Ortoleva

Laboratory for Computational Geochemistry
Indiana University
Bloomington, IN 47405

Abstract

The calculation of the stress is key to the prediction of the location and characteristics of naturally fractured tight gas reservoirs. Seals and preservation of naturally fractured tight gas reservoir interior porosity and permeability depend on pressure solution- and mechanically-mediated compaction and fracture growth and cement infilling. Prediction of these effects depends critically on the accurate computation of stress and their variation in space and time.

To ensure that the naturally fractured tight gas reservoir project will stay on schedule we have started a finite element solver for the stress to implement the incremental stress approach.

I. Numerical Approach

Our computational approach is based on a finite element descretization. Our formulation is based on an elastic, visco-plastic, pressure solution and fracture rheology (see Appendix D1 of this report):

$$\dot{\varepsilon} = \dot{\varepsilon}^{vp} + \dot{\varepsilon}^{e} + \dot{\varepsilon}^{o} \tag{I.1}$$

where

$$\dot{\varepsilon}^{vp} = \eta^{-1}(\sigma) \tag{I.2}$$

$$\dot{\varepsilon}^{e} = C^{-1}\frac{D}{Dt}(\sigma + \alpha p I) \tag{I.3}$$

$\dot{\varepsilon}^{o}$ = rate of strain from pressure solution and fracturing. (I.4)

To account for the large deformation of the basin an Eulerian-Lagrangian approach is used. The pure Eulerian and pure Lagrangian limits are special cases included in the formulation. The equations are discretized using an isoparametric, moving finite element to which reduced integration is applied. The resulting scheme is iterative with respect to the nonlinearity of the rheology. The symbolic manipulation code Maple was used to develop the code. This allows for easy extension and upgrading of algorithms, phenomenology and order of accuracy.
The elements used are distorted bricks and are second order in the calculation of the deformation velocity $\underline{u}$. This allows for a more accurate calculation of stress $\underline{\underline{\sigma}}$ as $\underline{\underline{\sigma}}$ is obtained from the spatial derivatives of $\underline{u}$. Finally, the boundary nodes are advected so that they remain on the material boundary of the domain.

II. Preliminary Results

Test cases were conducted using a basin-like geometry with an aspect ratio of 80. The boundary conditions shown in Fig. 1 are used. Various aspects of the code were tested. First the incremental viscoplastic rheology was tested on a basin collapsing and compacting under gravity. Fig. 2 shows the basin in its final configuration. The lower half of the domain has yielded and shows increasing compaction close to the bottom. The upper half remains elastic and in downward rigid body motion throughout the calculation. The vertical stress in the basin is

shown by color intensity (blue is highest). The actual stresses are found to agree within machine accuracy with the exact solution for this one dimensional problem.

The second test verifies the code's capability to resolve gradient of shear stress and movement with big aspect ratio. Fig. 3 shows a basin with a bottom subjected to a downward vertical velocity field and the lateral walls remain vertical. A diagram of shear and moment (Fig. 4) shows close agreement with the results from Beam Theory. These two tests verify the code's predictive capability of the basin's stress state. Large scale and long time computations are being undertaken to demonstrate the robustness of the code.

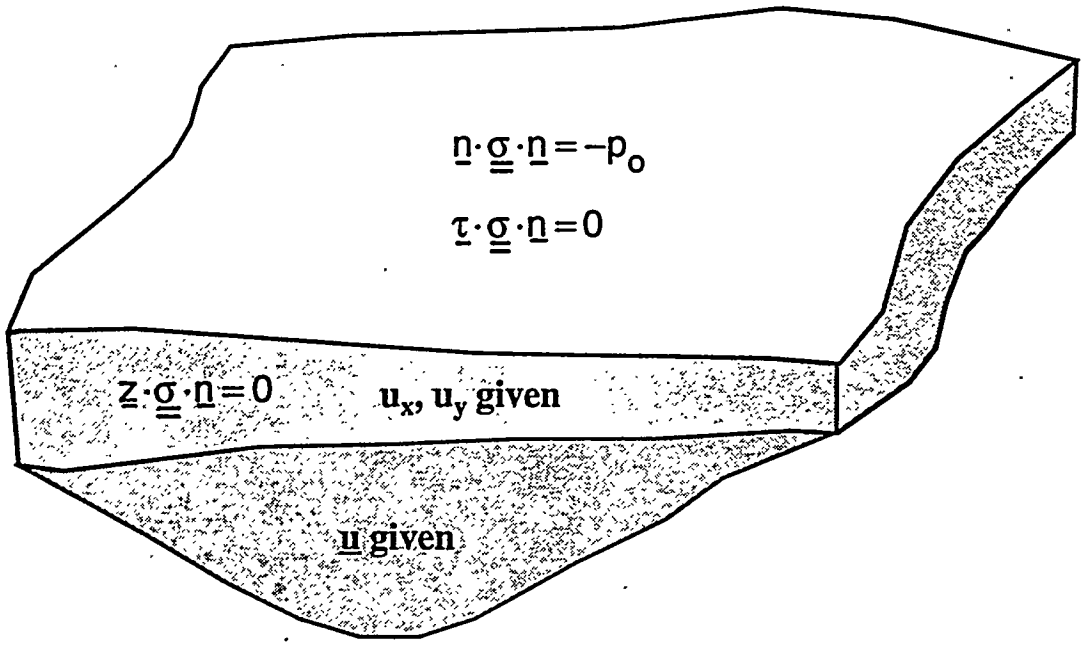

Fig. 1 Conditions at boundary of basin simulation domain allow for imposition of ocean bottom normal pressure p_o and no shear at the top (τ being a tangent vector and $\underline{\tau}$ being a normal vector). At the bottom the tectonic history fixes the evolution of the deformation velocity $\underline{u}$. On the sides (lightly shaded) the horizontal deformation velocity (u_x, u_y) is imposed, to allow the natural compaction dynamic to take place near the sides a no verticle tangential sheer condition is invoked.

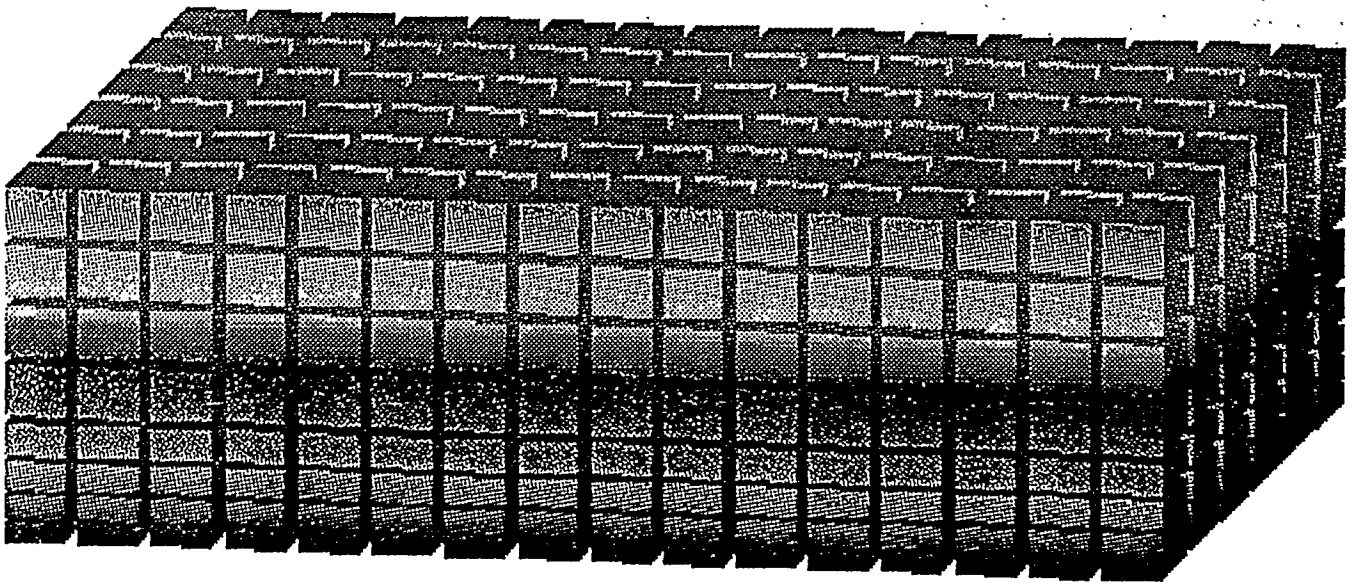

Fig. 2 Basin mechanical compaction under gravity: vertical stress (blue = negative maximum stress) is indicated as a color contour map on the front surface. The gridding used is also shown. The basin's length and thickness are 400 km and 5 km (thickness exaggerated).

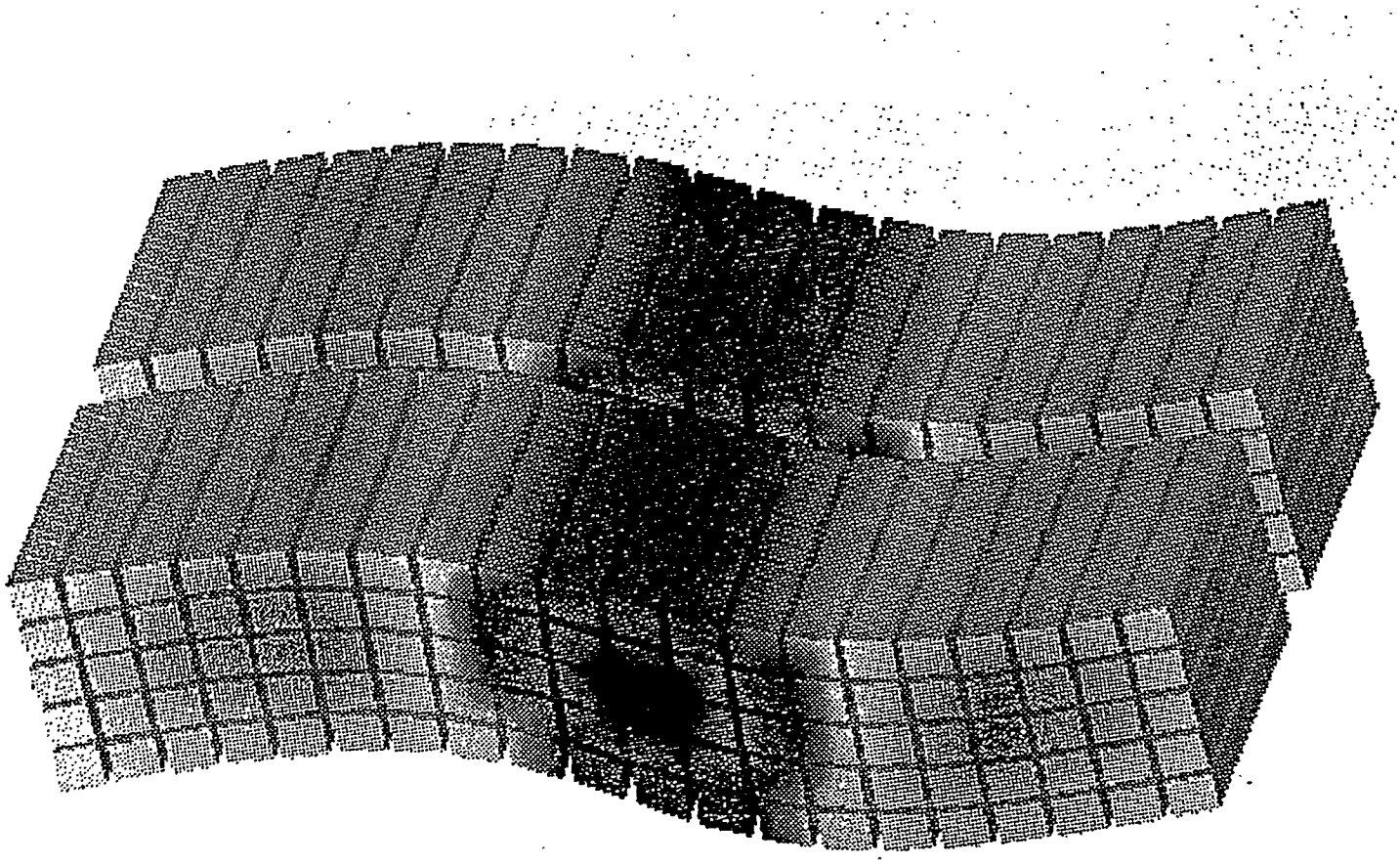

Fig. 3 Side view of basin under shear due to relative motion of right side due to imposed downward velocity from basement fault motion. Color contour map of shear stress is shown on front face. Relative motion across displacement plane is exaggerated to clarify the nature of the deformation. Same basin dimensions as previously.

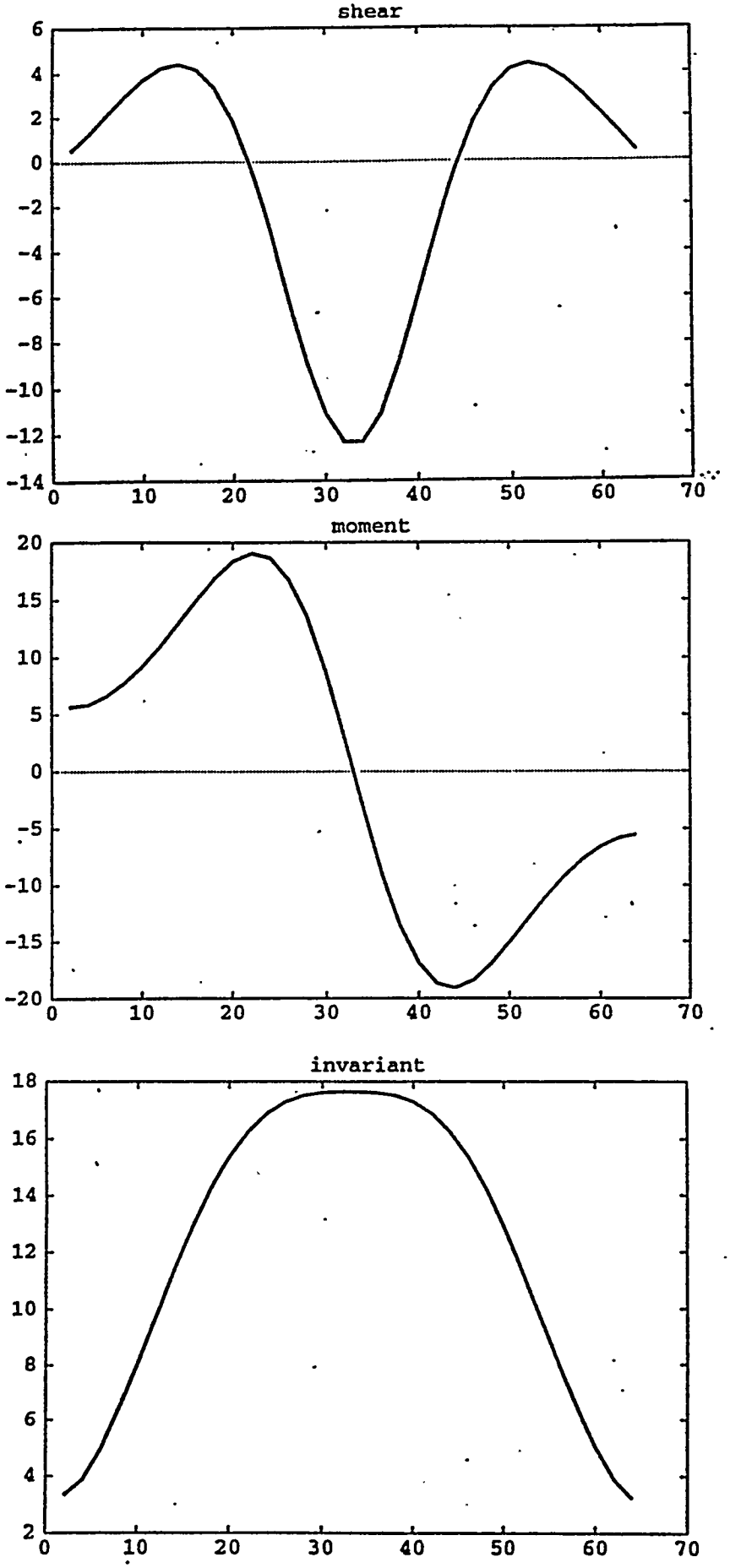

Fig. 4 Shear, moment, second stress in variant at the lower face of the basin.

Appendix E1

Basin Reaction, Transport, Compaction, Sedimentation and Energy Balance: Three Dimensional, Finite Difference Simulator

J.M. Maxwell and P. Ortoleva

Laboratory for Computational Geochemistry
Indiana University
Bloomington, IN 47405

I. The Model

A basin, with its sedimentary complexity, is a three-dimensional system. A numerical simulation of the fully coupled reaction-transport-mechanical (RTM) processes within it have heretofore been considered unfeasible. We have now developed and implemented numerical schemes that make this possible. As a result, we have made great progress in attaining the capability to predict the location of abnormal pressures, porosity and fracturing and the character of seals and reservoirs within a basin for E&P applications in general, and for this naturally fractured tight gas reservoir project in particular.

The RTM processes being incorporated in our three-dimensional basin RTM code are the same as those for CIRF.B2 given in Park and Ortoleva (1994). The simulator CIRF.B3 is now at a stage of testing and module integration. We believe that most major computational difficulties have been met and we will soon be able to simulate the basin evolution and in particular the spatial distribution of fractures and seals.

II. Numerical Approach

The numerical technique used to solve the basin hydrologic and energy balance equations is based on a finite difference descretization. The grid is composed of a set of distorted bricks so that it maps onto a cubic grid in node index space. The grid nodes move with rock deformation velocity. New planes of grid nodes are added with both the addition of sediment as well as in the interior to resolve large gradients of rock properties that may develop as a result of diagenesis or due to changes in sedimentation. The descretization takes account of the fact that the grid moves with rock defomation. Furthermore, the descretization is mass conserving.

Ultimately the descretization equations require the solution of very large sets of linear equations. These are solved using a mixed direct/iterative method. The method is based on an ADI approach with a grid node line solver using pivoting and iterative refinement. Thereby, our solver can survive for the problems of very large aspect ratios and variation of parameters (such as permeability) of nine orders of magnitude across the basin.

III. Preliminary Results

A number of preliminary simulations of CIRF.B3 have been carried out for the purposes of diagnosis and to demonstrate its ability to make the predictions required for this project.

1. Genesis of a Mega-Compartment

A first simulation of a basin-wide region of overpressuring (mega-compartment) has been carried out. A sample simulation is shown in Figs. 1-3. The simulation was carried out on a DEC Alpha with 370 Mb internal memory and required 5 CPU days to complete.

The number and range of the control variables (sedimentology and tectonics) that affect basin evolution, and in particular diagenesis, give each basin its individual character. Evolution of this megacompartment proceeds in several stages which for this preliminary study we caricaturize as follows (see Figs. 1 and 2). As sediment is added the lower shale achieves sufficient depth that it compacts. Compaction elevates pressure within the shale and that developed overpressure eventually represses further compaction in the interior of the shale and may lead to the development of tight, naturally fractured reservoirs. However, at the periphery of the shale, fluid is lost to the surrounding, more permeable beds. This causes a rind of more highly compacted rock temporarily bounding the shale on top and bottom. Thereby, in this early stage the shale becomes a bed-localized compartment.

With further burial the medium grain size material and its more active near-fault and far-from-fault finer sediment are added. Further burial adds the finer overburden. In time the medium material becomes enclosed in faster compacting sediment. This compacting envelope eventually develops significant overpressure and serves as a shell with complete three dimensional closure.

In the third stage fluid squeezed from the surrounding seals and compaction of the interior lead to overpressuring of the interior. Finally, a steady state is obtained wherein fluid leakage from the interior is just balanced by compaction. This "eustetic" state is long lived (i.e., on the 100 MA time frame) if the surrounding seals are of sub-nanodarcy permeability (Ortoleva et al., 1994).

This simulation illustrates this scenario. The domain and sedimentary history are those suggested in Figs. 1 and 2. At the end of the simulation the basal, top and side seals have completed. The minimum permeability of the surrounding is 0.01 nanodarcy. This is in stark contrast to the permeability in the interior which is 1.0 millidarcy and that of the uncompacted fine material at the very top of the basin, where it is 10^{-2} Darcy. Three dimensional closure to form the megacompartment has been obtained.

Fig. 3 shows the results of the simulation after an epoch of 10 MA of rapid sediment loading, a 4 MA period of gradual slowing of sediment input and subsequent long period essentially quiescent for the remainder of the simulation. A bottom seal formed that followed the shale. The top of overpressure formed via a diagenetic seal at around 3 km through pressure solution-mediated compaction. This simulation involved about 300,000 grid nodes and explicitly calculated overburden stress, a full three-dimensional computation of the fluid pressure, and pressure solution-mediated compaction for the prescribed sediment infilling, basement subsidence and thermal history.

Fig. 3 shows the pressure at 12 MA in the form of overpressure isosurfaces of 200 (a) and 500 (b) bars. These figures are color coded such that the points on the isosurface which are at highest elevation are orange-brown in color and the lowest are blue with the color spectrum between indicating intermediate depths on the isosurface.

The technical triumph of this simulation is that at each time step all variables are converged to self-consistency including the material-fixed (moving) grid, the fluid pressure and composition, the grain shape and degree of overgrowth, the (texture dependent) permeability and the overburden stress. This was made possible due to our pressure module which solves the equation of Darcy flow for a compressible fluid using a mixed method combining grid refinement, and partially direct and partially iterative linear solver that computes the full nonlinear problem and surmounts the difficulty of the basin's extreme aspect ratio. Also our calculation employs a mass-conserving, finite differencing on a moving (rock material point-fixed) grid.

To make the code capable of solving even more lithologically complex problems (the simulation of Fig. 3 having 7 distinct formations), the code is being parallelized on the Intel Paragon and other systems via a domain decomposition scheme. The full parallelized code will be completed by the first quarter of 1994. A version with local grid refinement has also been developed.

2. Effects of Thermal Transport and Fracturing

The results shown above do not take account for a self-consistent calculation of temperature (a constant geothermal gradient was assumed) and fracturing. Both of these effects have now been included in the code and are presently being tested.

References

Ortoleva, P. Z. Al-Shaieb and J. Puckette, 1994. Genesis and Dynamics of Basin Compartments and Seals. (submitted for publication, American Journal of Science)

Park, A. and P. Ortoleva, 1994. Multimineralic Model of Pressure Solution Mediated Compaction. (see Appendix A)

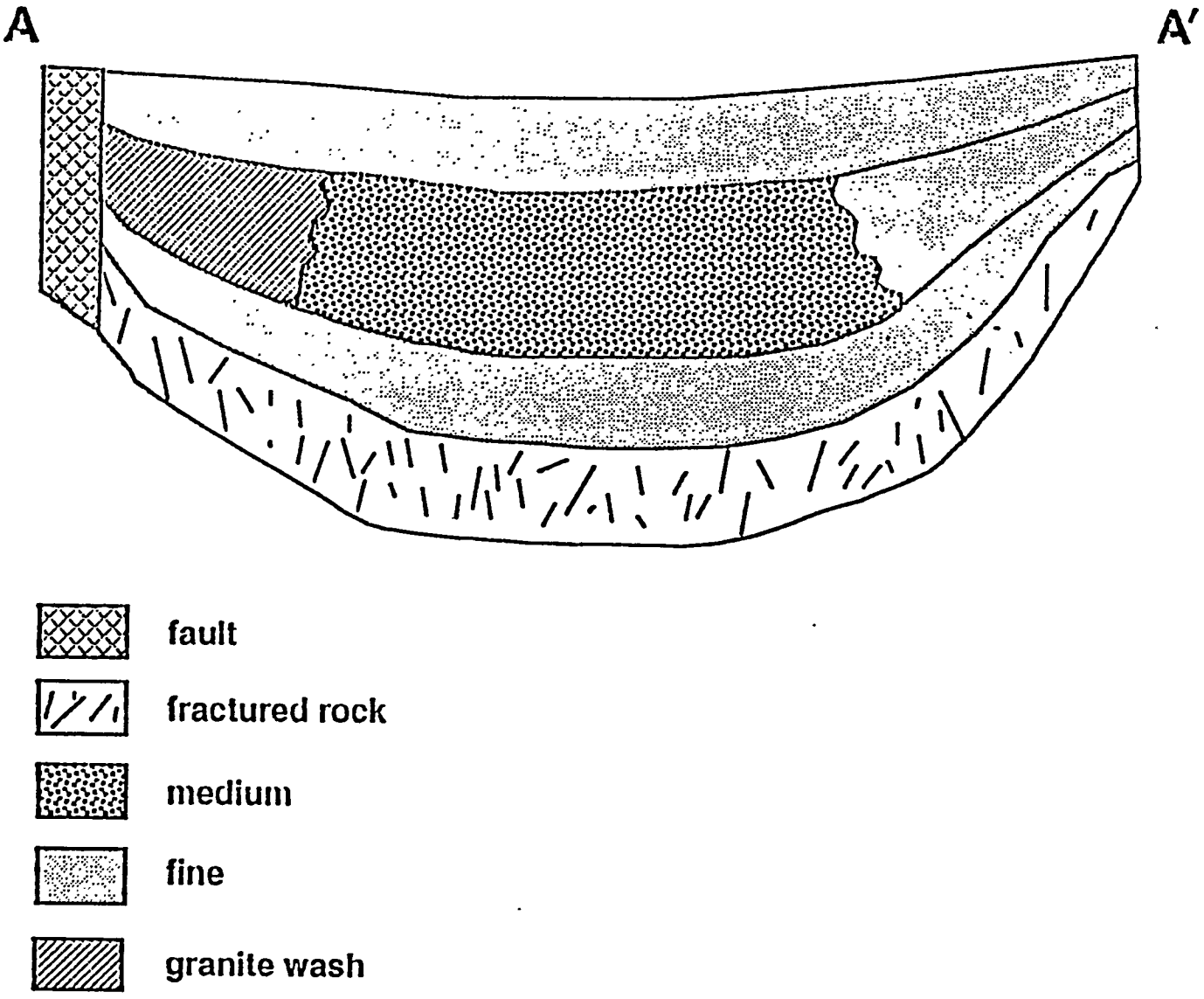

Fig. 1 Schematic basin cross-section used for modeling study. AA' transect as in Fig. II-1.

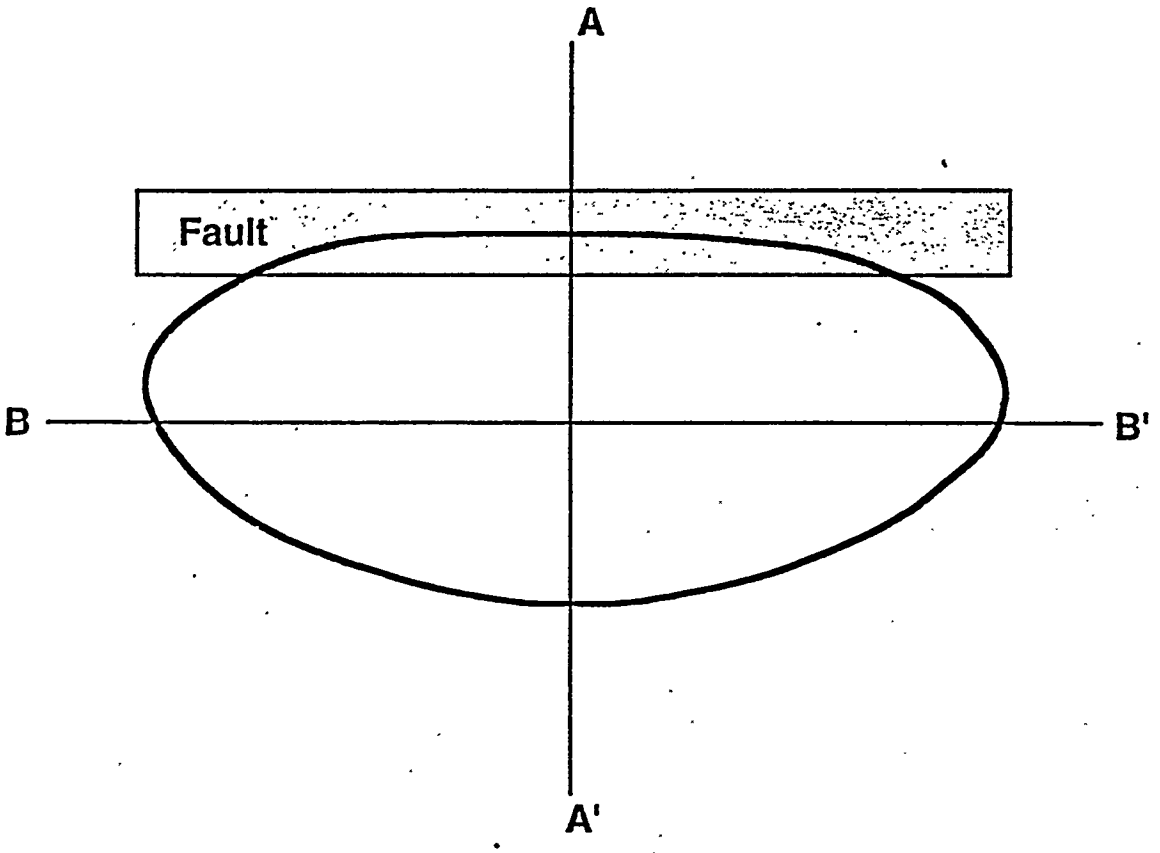

Fig. 2 Map view of a simulator test model showing transects AA' and BB'. Fig. II-2 shows cross-section corresponding to AA'.

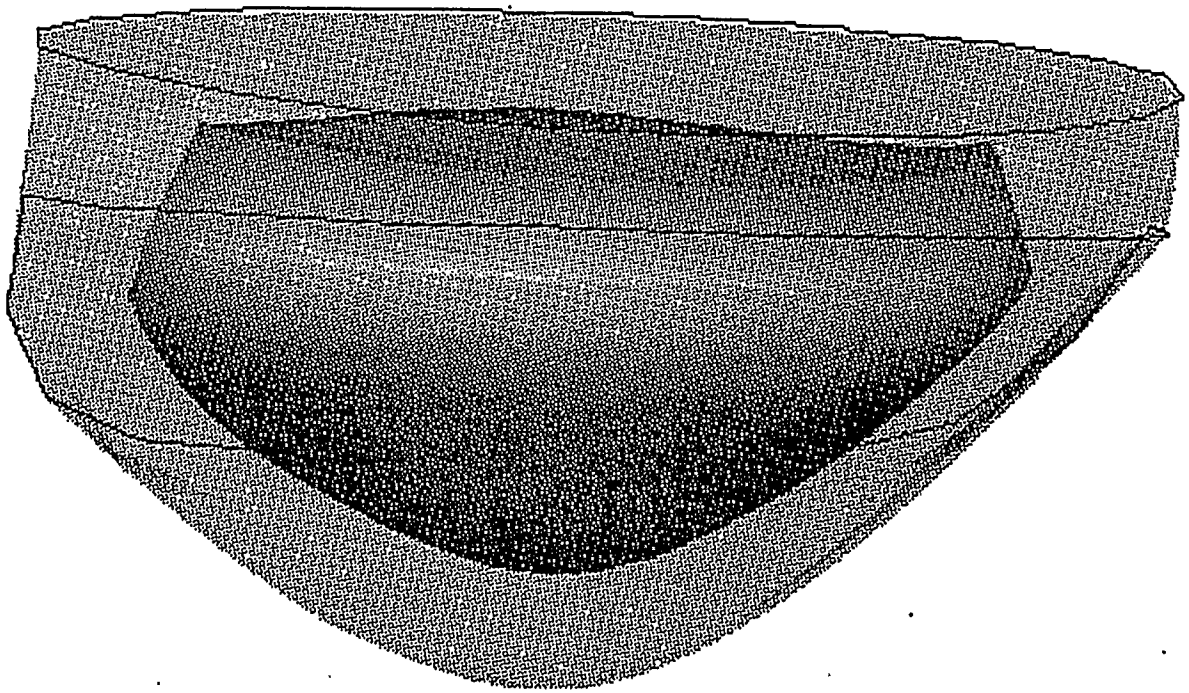

Fig. 3 Results of a simulation of a demonstration model. In plan view the domain is elliptical of dimension 200 x 100 km for a sea level of about .25 km and a maximum thickness of the sediment pile at about 7.2 km at the time shown. Shown are pressure isosurfaces for 200 (a) and 500 (b) bars.

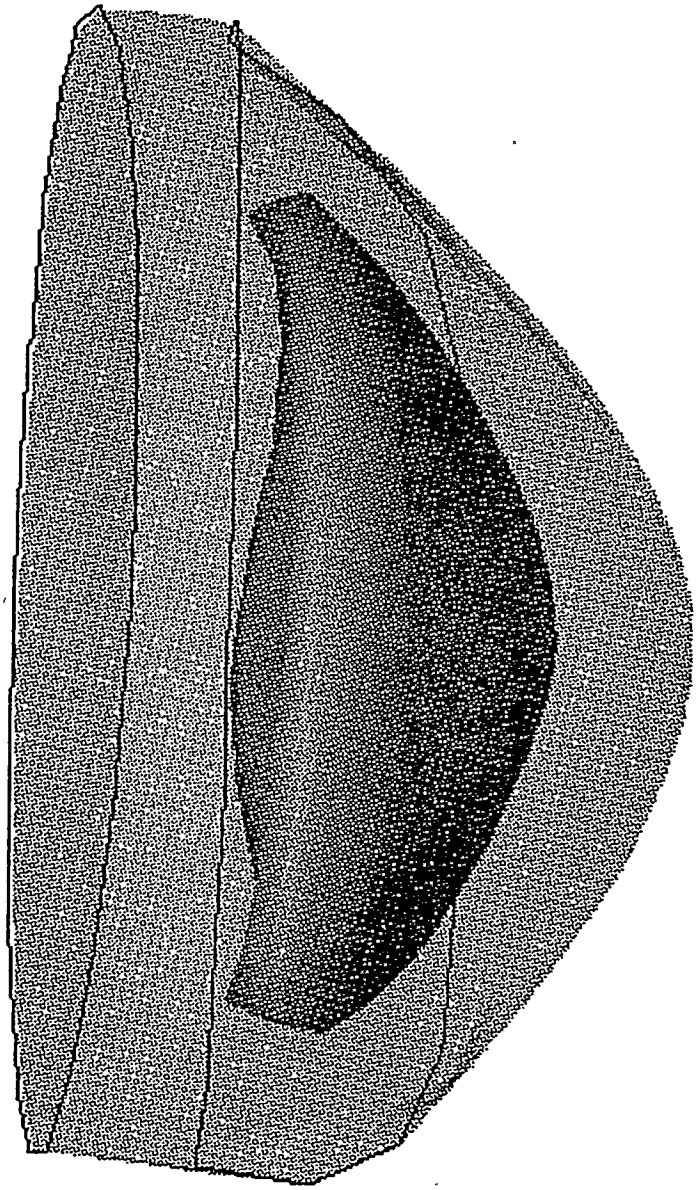

Fig. 3b

Appendix E2

Chemically Different Basin Diagenesis Modeling: The CIRF.B3 Simulator

C. Qin and P. Ortoleva

Laboratory for Computational Geochemistry
Indiana University
Bloomington IN 47405

A basin, with its sedimentary complexity, is certainly a three-dimensional system. However, a numerical simulation of the reaction-transport-mechanical processes within it have heretofore been considered unfeasible. We have now developed and implemented numerical schemes that make this possible. As a result, we have made great progress in developing the capability to predict the location and character of seals and reservoirs within a basin for use in E and P applications.

The simulator is named CIRF.B3 (chemical interaction of rocks and fluids in a basin (three-dimensional)) is now at a stage of testing and module integration. We believe that all major computational difficulties have been met and we are thus able to simulate the genesis of abnormally pressured compartments and the seals defining them. A key goal is to develop the capability to predict the location, characteristics and producibility of fractured reservoirs in tight formations.

The CIRF.B3 simulator serves as the platform for the integration of a number computational modules as follows. Central to CIRF.B3 is the implementation of the general chemistry, multi-mineralic reaction-transport and textural model as outlined in Park and Ortoleva (1994). CIRF.B3 houses a sediment history module that uses detailed petrologic data from selected well sites with data on the detailed geometry of formations as well as the timing of deposition of the latter. This sediment input module uses the adaptive gridding technology developed by Sibo and Ortoleva (1994). The CIRF.B3 also integrates fluid flow/pressure as well as temperature modules developed by Maxwell and Ortoleva (1994) and for basin deformation and compaction and fracturing made self-consistent via incremental stress theory (Tounsi and Ortoleva, 1994; Sakrani and Ortoleva, 1994). CIRF.B3 supplies heat flux as well as tectonic, sedimentation, subsidence and climatic history to the various models. Finally, all modules solve their respective problems self-consistently with respect to the solutions generated by the other modules. In this way, the fully coupled basin reaction, transport mechanical problem is solved.

Sample results are briefly as follows.

1. Overpressuring and Sealing in a Quiescent Basin

The development of seals and the preservation of porosity and permeability is strongly influenced by detrital and authigenic mineral content. Ten or more minerals and many more aqueous species are commonly present and couple strongly via fast (equilibrated) and finite rate reactions. Mineral reactions can occur on free faces and at grain-grain contacts (under stress mediation) and can be strongly influenced by clay coatings and the mineral identity of the grain with which a given grain is in contact.

CIRF.B3 has now been upgraded to have great chemical generality and to have extensive built-in kinetic and thermodynamic data banks. A preliminary result of a basin with relatively simple sedimentary and subsidence history is seen in Fig. 1. The simulation domain was 334 x 178 x 3 km. The maximum depth of the bottom of the domain was 3.5 km. Lithologic units present were a siltstone, two very fine sandstones, a fine sandstone, and a coarse sandstone. Minerals present were quartz, K-feldspar, and muscovite. The boundary condition for fluid pressure was chosen such that the bottom and sides are lossless while the top is maintained at hydrostatic pressure. The subsidence velocity was 22.28 m/MY for $t <= 22.5$ MY, 12.19 m/MY for $22.5 < t <= 43$MY, and 17.88 m/MY for $t > 43$ MY. The simulation was done on an IBM RS6000.

Fig. 1a shows isosurfaces of overpressure of 40 bars and 15 bars at 10 MY of simulation. Overpressure developed due to compaction and thermal expansion. The overpressure is contained due to the formation of diagenetic seals arising through pressure solution-mediated compaction. The configuration of the seals is associated with the interplay of sedimentology and pressure, temperature dependent and texture dependent compaction and overgrowth. Fig. 1b is a cross section of the three dimensional domain showing the interrelations among porosity, permeability and overpressure.

2. Effects of Sediment Input History

The sediment input module has now been completed in preliminary form. An example in Fig. 2 shows the early stage of a simulation. The basin is 178x334 m^2 in the horizontal directions. The sedimentation rate is approximately 180m/MY. It reaches maximum at the center of the basin and decreases towards and edge of the basin. The sediments are composed of three minerals: quartz, feldspar and muscovite. Initial sediments have the same porosity of 25%. The mineralogy and grain sizes, however, change with space and time. The boundary condition for the pressure equation is hydrostatic on top and no-flux on all sides and the bottom of the domain. At 5 MY the depth of the basin is about 700 m and maximum thickness of the sediments is 644 m and pressure is hydrostatic everywhere. At 8 MY the depth of the basin is about 720 m and maximum thickness of the sediments is 657 m and small overpressure was developed in the finer grain material due to chemical compaction and thermal expansion. At 10 MY, the depth of the basin is about 830 m and the maximum sediment thickness is 765 m. Overpressure is slightly higher than that at 8 MY. Because of the slow rate of sedimentation and small thickness of the sediments, no significant overpressure was developed.

References

Maxwell, J.M. and P. Ortoleva (1994) Basin Hydrologic, Compaction and Thermal Model (Appendix D1 of this report)

Park, A. and P. Ortoleva (1994) A Multimineralic Model of Pressure Solution Mediated Compaction (Appendix A of this report)

Sakrani, K. and P. Ortoleva (1994) Basin Incremental Stress Model and Finite Difference Simulator (Appendix D2 of this report)

Sibo, W. and P. Ortoleva (1994) Adaptive Gridding for Reaction-Transport Problems (Appendix I of this report)

Tounsi, F. and P. Ortoleva (1994) Moving, Second Order Finite Element Basin Incremental Stress Simulator (see Appendix D3)

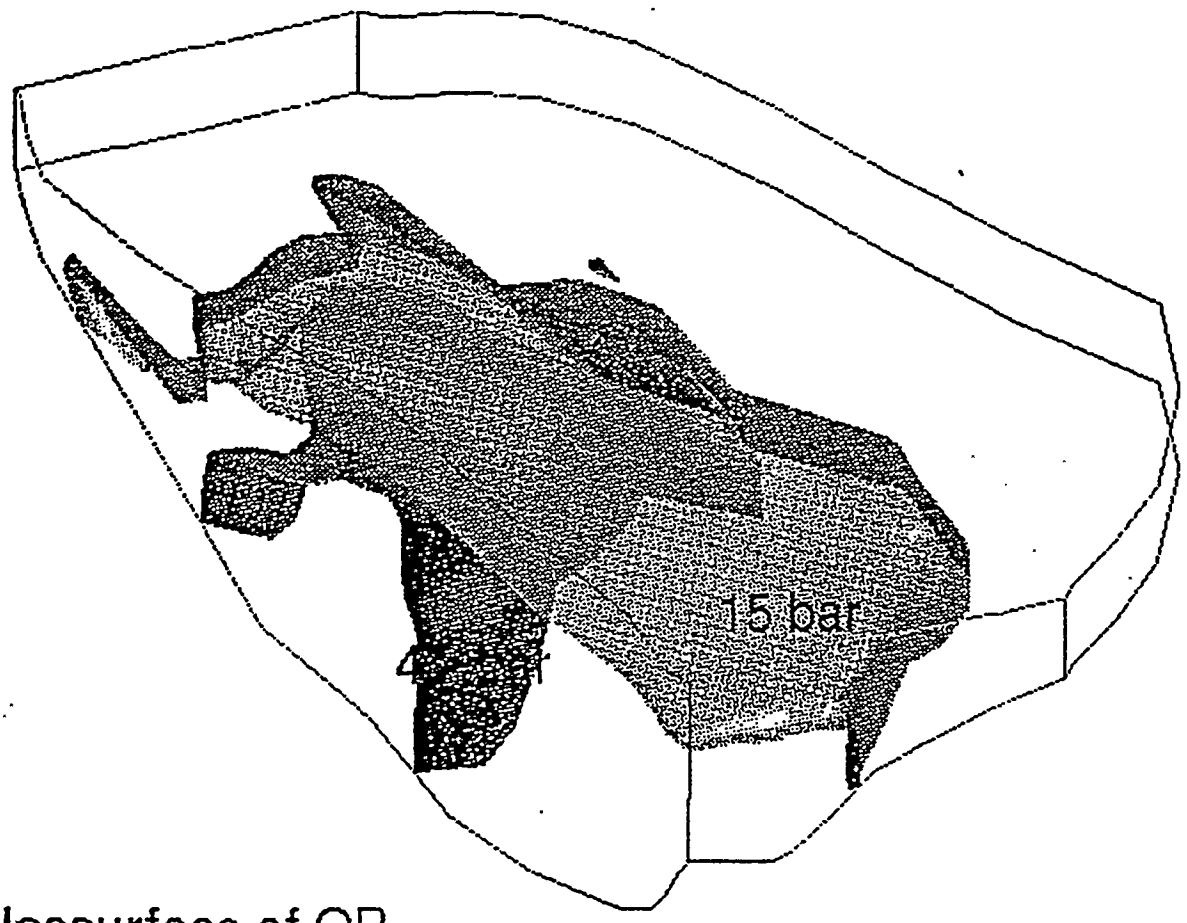

Fig. 1 (a) Isosurfaces of overpressure of 40 bars and 15 bars at 10 MY.

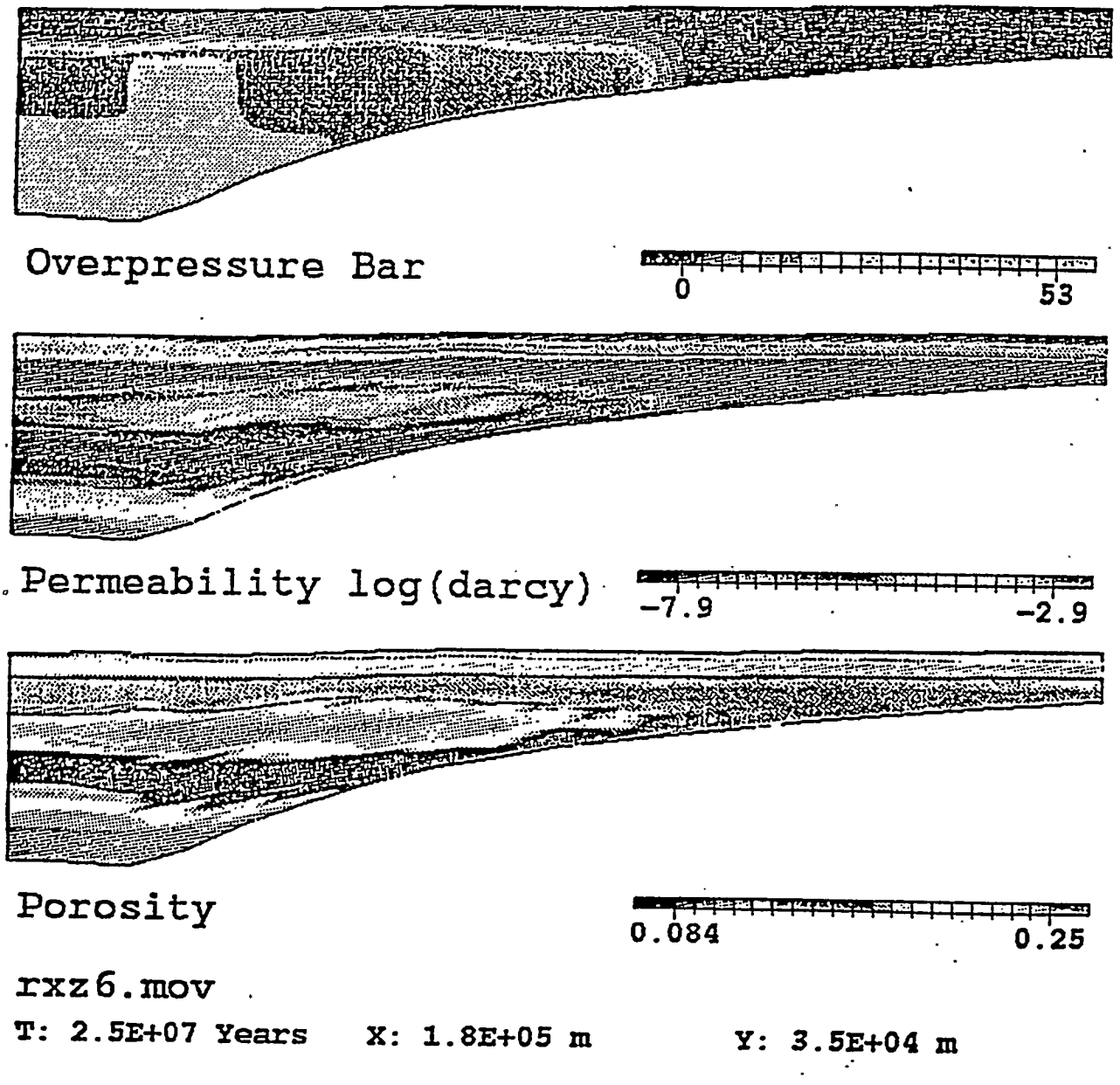

Fig. 1 (b) Cross-section of the 3D domain showing the interrelations among porosity, permeability and overpressure.

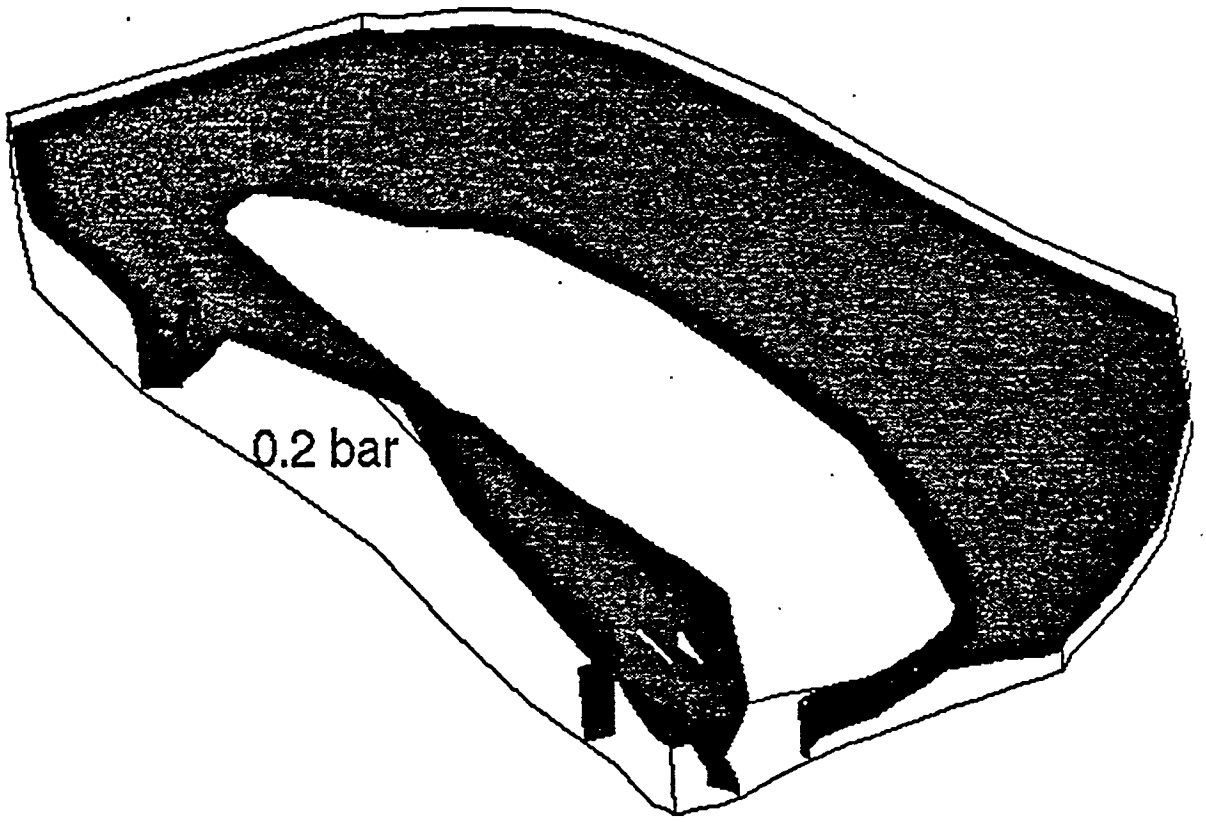

Overpressure isosurface, t=8 MY

Fig. 2 (a) Isosurface of and OP = 0.2 bar at t = 8 MY.

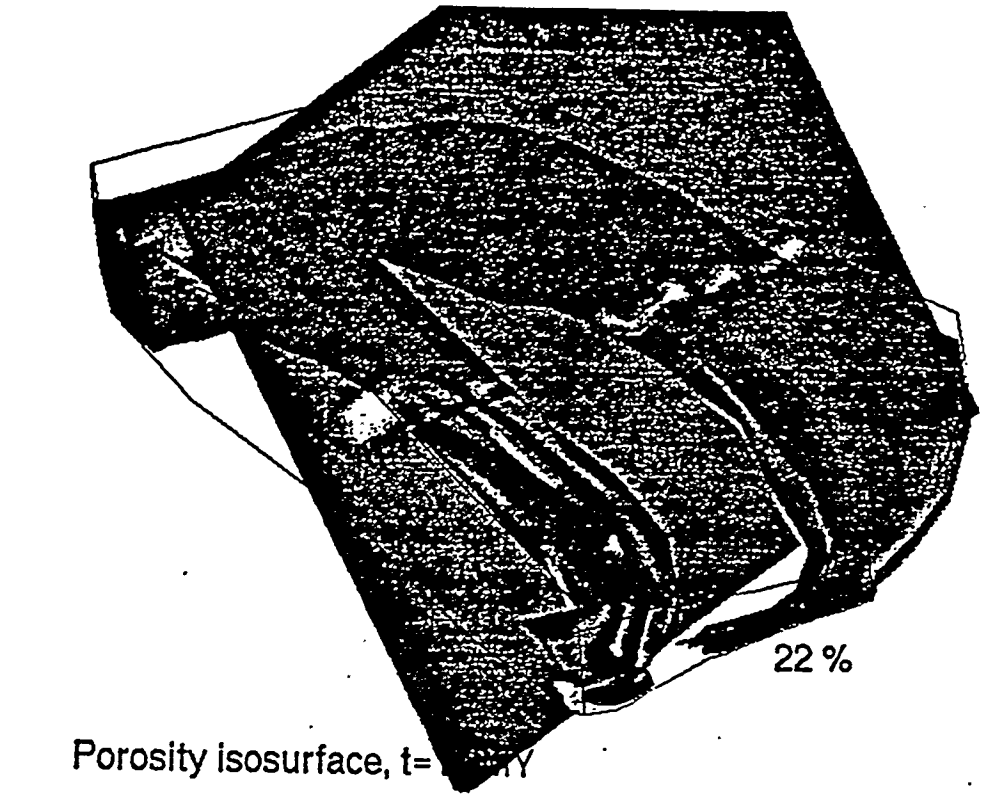

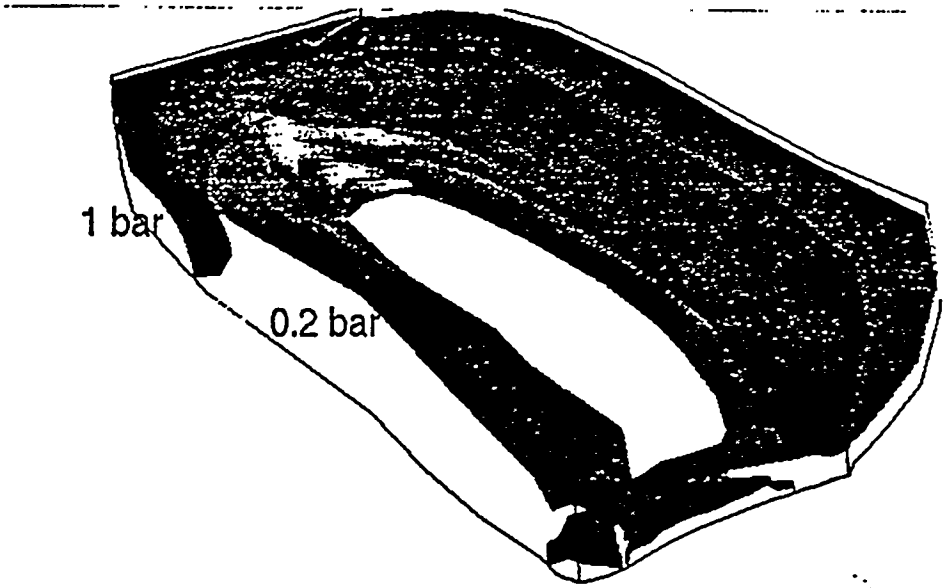

Overpressure isosurfaces, t=10 MY

Fig. 2 (b) Isosurfaces of porosity = 22% and OP = 0.2 and 1 bar at t = 8 MY. The lower porosity area corresponding to finer grain sediments.

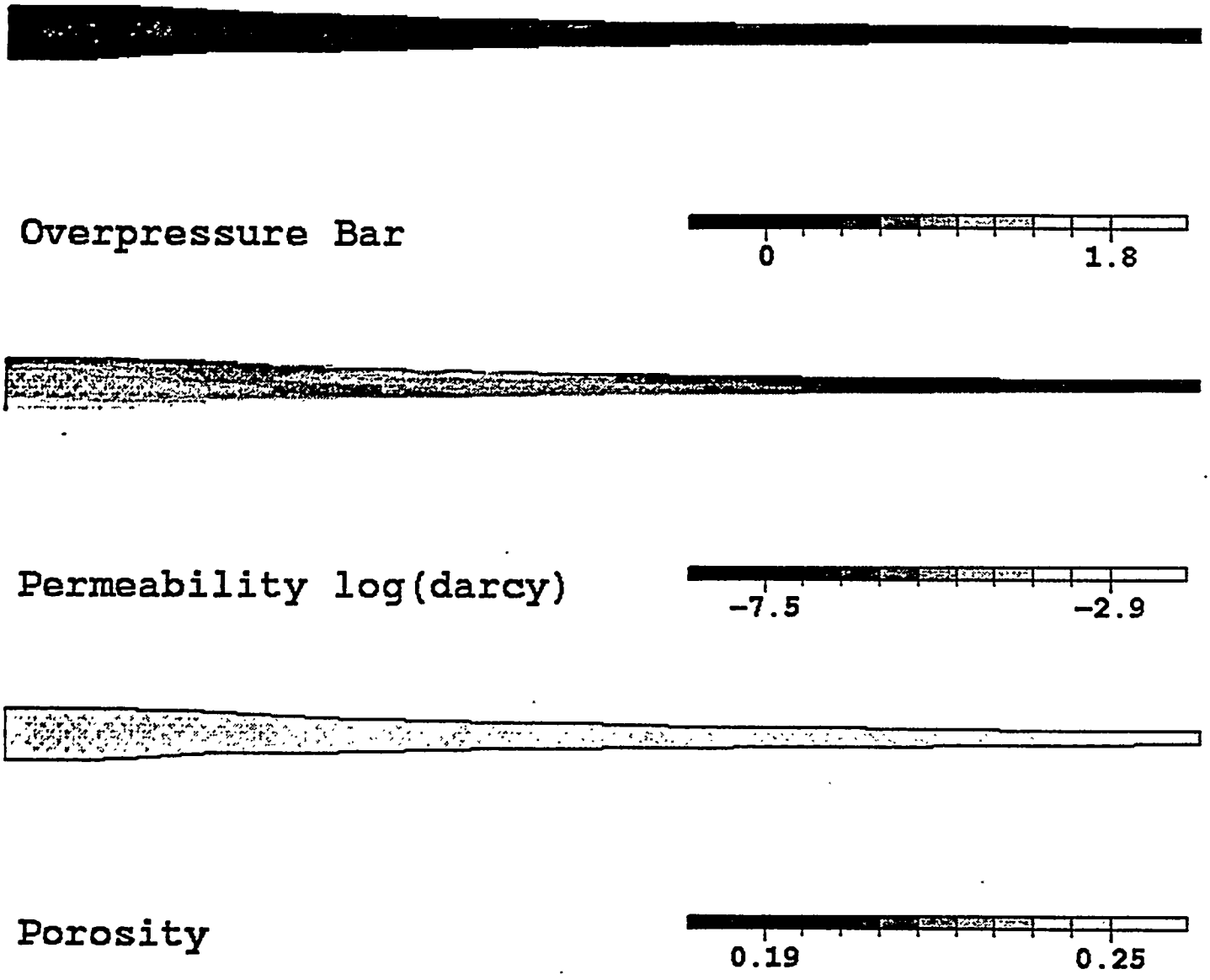

Fig. 2 (c-e) A cross section of the basin at t = 5, 8, 10 MY, respectively showing overpressure, permeability and porosity. Note: there is no overpressure and porosity is 25% everywhere in the basin initially.

Overpressure Bar

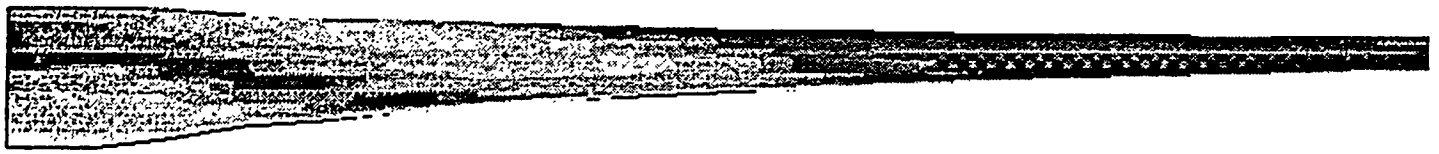

Permeability log(darcy)

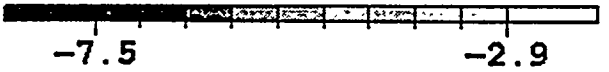

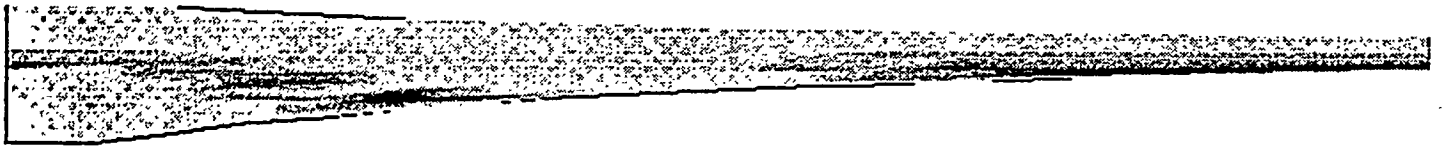

Porosity

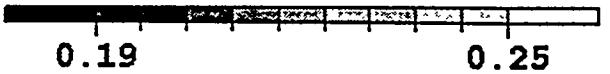

it2-2xz.mov

T: 1E+07 Years X: 1.7E+05 m Y: 1.7E+04 m

Overpressure Bar

Permeability log(darcy)

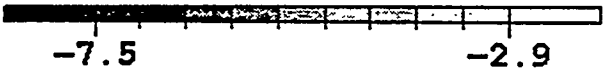

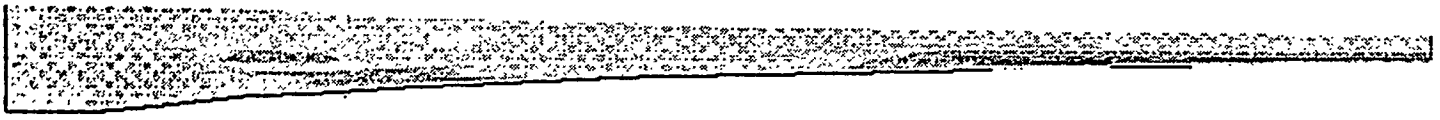

Porosity

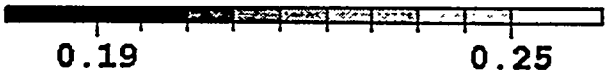

it2-2xz.mov

T: 8E+06 Years X: 1.7E+05 m Y: 1.3E+04 m

Appendix F

Bibliography

J. Comer[a] and D. Payne[b]

[a]Indiana Geological Survey
611 North Walnut Grove
Bloomington IN 47405

[b]Laboratory for Computational Geochemistry
Indiana University
Bloomington IN 47405

BIBLIOGRAPHY
PICEANCE BASIN, COLORADO

Armstrong, R. L., 1974, Magmatism, orogenic timing, and orogenic diachronism in the Cordillera from Mexico to Canada: Nature, v. 274, p. 348-351.

Bostick, N. H., 1983, Vitrinite reflectance and temperature gradient models applied at a site in Piceance Basin, Colorado (abs): AAPG Bulletin, v. 67, no. 3, p. 427-428.

Bredehoeft, J. D., Wolff, R. G., Keys, W. D., and Shuter, E., 1976, Hydraulic fracturing to determine the regional in situ stress field, Piceance Basin, Colorado: GSA Bulletin, v. 87, p. 250-258.

Brown, C. A., Smagala, T. M., and Haefele, G. R., 1986, Southern Piceance Basin model-Cozzette, Corcoran and Rollins Sandstones, *in* C. W. Spencer and R. F. Mast, eds., Geology of tight gas reservoirs: AAPG Studies in Geology 24, p. 207-219.

Chancellor, R. E., and Johnson, R. C., 1986, Geologic and engineering implications of production history from five Mesaverde wells in central Piceance Creek Basin, northwest Colorado: Society of Petroleum Engineers Symposium on Unconventional Gas Technology, Louisville, Kentucky, 1986, Proceedings 15237, p. 351-364.

Chancellor, R. E., and Johnson, R. C., 1988, Geologic and engineering implications of production history from five Mesaverde wells in central Piceance Creek Basin, northwest Colorado: Society of Petroleum Engineers Formation Evaluation, p. 307-314.

Dula, W. F., 1981, Correlation between deformation lamellae, microfractures, macrofractures, and in situ stress measurements, White River Uplift, Colorado: GSA Bulletin, v. 92, p. 37-46.

Dyni, J. R., 1969, Structure of the Green River Formation, northern part of the Piceance Creek Basin, Colorado: The Mountain Geologist, v. 6, p. 57-66.

Eckert, A. D., 1982, The geology and seismology of the Dudley Gulch graben and related faults, Piceance Creek Basin northwestern Colorado: Unpublished Master's Thesis, University of Colorado.

Garrett, C. H., and Lorenz, J. C., 1989, Fracturing along the Grand Hogback, Garfield County, Colorado: Sandia Report No. SAND88-3298, Published by Sandia National Laboratories for the U.S. Department of Energy, Available from National Technical Information Service, U.S. Department of Commerce, Springfield, Virginia, 35 p.

Gries, Robbie, 1983, North-south compression of Rocky Mountain foreland structures, *in* J. D. Lowell, ed. Rocky Mountain Foreland Basins and Uplifts: Rocky Mountain Association of Geologists, p. 9-32.

Gries, Robbie, 1983, Oil and gas prospecting beneath Precambrian of foreland thrust plates in Rocky Mountains: AAPG Bulletin, v. 67, p. 1-28.

Grout, M. A., Abrams, G. A., Tang, R. L., Hainsworth, T. J., and Verbeek, E. R., 1991, Late Laramide thrust-related and evaporite-domed anticlines in the southern Piceance Basin, northeastern Colorado Plateau: AAPG Bulletin, v. 75, no. 2, p. 205-218.

Hansley, P. L., and Johnson, R. C., 1980, Mineralogy and diagenesis of low permeability sandstones of Late Cretaceous age, Piceance Creek Basin, northwestern Colorado: The Mountain Geologist, v. 17, p. 88-129.

Hensen, W. R., 1984, Post-Laramide tectonic history of the eastern Uinta Mountains, Utah, Colorado, and Wyoming: The Mountain Geologist, v. 21, p. 5-29.

Ingersoll, R. V., 1982, Triple-junction instability as cause for late Cenozoic extension and fragmentation of the western United States: Geology, v. 10, p. 621-624.

Johnson, R. C., 1989, Geologic history and hydrocarbon potential of late Cretaceous-age, low-permeability reservoirs, Piceance Basin, western Colorado: U.S. Geological Survey Bulletin 1787-E, 51 p.

Johnson R. C., Crovelli, R. A., Spencer, C. W., and Mast, R. F., 1987, An assessment of gas resources in low-permeability sandstones of the Upper Cretaceous Mesaverde Group, Piceance Basin, Colorado: U.S. Geological Survey Open-File Report 87-357, 165 p.

Johnson, R. C., and Finn, T. M., 1986, Cretaceous through Holocene history of the Douglas Creek arch, Colorado, and Utah, *in* D. S. Stone, ed., New Interpretations of northwest Colorado Geology: Rocky Mountain Association of Geologists p. 77-95.

Johnson, R. C., and May, F., 1980, A study of the Cretaceous-Tertiary unconformity in the Piceance Creek Basin, Colorado: The underlying Ohio Creek Formation (Upper Cretaceous) redefined as a member of the Hunter Canyon or Mesaverde Formation: U.S. Geological Survey Bulletin 1482-B, 27 p.

Johnson, R. C., and Nuccio, V. F., 1986, Structural and thermal history of the Piceance Creek Basin, western Colorado, in relation to hydrocarbon occurrence in the Mesaverde Group, *in* C. W. Spencer and R. F. Mast, eds., Geology of Tight Gas Reservoirs: AAPG Studies in Geology 24, p. 165-205.

Johnson, R. C., and Nuccio, V. F., 1993, Surface vitrinite reflectance study of the Uinta and Piceance Basins and adjacent areas, eastern Utah and western Colorado - Implications for the development of Laramide basins and uplifts: U.S. Geological Survey Bulletin 1787-DD, 38 p.

Johnson, R. C., and Rice, D. D., 1990, Occurrence and geochemistry of natural gas, Piceance Basin, northwest Colorado: AAPG Bulletin, v. 74, no. 6, p. 805-829.

Larsen, E. E., Ozima, M., and Bradley, W. D., 1975, Late Cenozoic basic volcanism in northwestern Colorado and its implications concerning tectonism and the origin of the Colorado River system: GSA Memoir 144, p. 155-178.

Law, B. E., Nuccio, V. F., and Barker, C. E., 1989, Kinky vitrinite reflectance profiles - Evidence of paleopore pressure in low-permeability gas-bearing sequences in Rocky Mountain foreland basins: AAPG Bulletin, v. 73, no. 8, p. 999-1010.

Lorenz, J. C., 1985, Tectonic and stress histories of the Piceance Creek Basin and the MWX site, from 75 million years ago to the present: Preliminary report: Published by Sandia National Laboratories for the U.S. Department of Energy, Sandia Report No. SAND-84-2603, Available from National Technical Information Service, U.S. Department of Commerce, Springfield, Virginia, 50 p.

Lorenz, J. C., and Finley, S. J., 1991, Regional fractures II: Fracturing of Mesaverde reservoirs in the Piceance Basin, Colorado: AAPG Bulletin, v. 75, no. 11, p. 1738-1757.

Lorenz, J. C., and Hill, R. E., 1991, Subsurface fracture spacing: Comparison of interferences from slant/horizontal core and vertical core in Mesaverde reservoirs: Society of Petroleum Engineers Symposium on Low-Permeability Reservoirs, Denver, Colorado, 1991, Proceedings 21877, p. 705-716.

Lorenz, J. C., Teufel, L. W., and Warpinski, N. R., 1991, Regional fractures I: A mechanism for the formation of regional fractures at depth in flat-lying reservoirs: AAPG Bulletin, v. 75, no. 11, p. 1714-1737.

Martinsen, O. J., Martinsen, R. S., and Steidtmann, J. R., 1993, Mesaverde Group (Upper Cretaceous), southeastern Wyoming: Allostratigraphy versus sequence stratigraphy in a tectonically active area: AAPG Bulletin, v. 77, no. 8, p. 1351-1373.

Morrow, D.W., and Issler, D.R., 1993, Calculation of vitrinite reflectance from thermal histories: A comparison of some methods: AAPG Bulletin, v. 77, p. 610-624.

Multiwell Experiment Project Groups, 1987, Multiwell Experiment Final Report: I. The Marine interval of the Mesaverde Formation: Published by Sandia National Laboratories for the U.S. Department of Energy, Sandia Report No. SAND87-0327, Available from National Technical Information Service, U.S. Department of Commerce, Springfield, Virginia,.

Multiwell Experiment Project Groups, 1988, Multiwell Experiment Final Report: II. The Paludal interval of the Mesaverde Formation: Published by Sandia National Laboratories for the U.S. Department of Energy, Sandia Report No. SAND88-1008, Available from National Technical Information Service, U.S. Department of Commerce, Springfield, Virginia, 545 p.

Multiwell Experiment Project Groups, 1989, Multiwell Experiment Final Report: III. The Coastal interval of the Mesaverde Formation: Published by Sandia National Laboratories for the U.S. Department of Energy, Sandia Report No. SAND88-3284, Available from National Technical Information Service, U.S. Department of Commerce, Springfield, Virginia.

Multiwell Experiment Project Groups, 1990, Multiwell Experiment Final Report: IV. The Fluvial interval of the Mesaverde Formation: Published by Sandia National Laboratories for the U.S. Department of Energy, Sandia Report No. SAND89-2612, Available from National Technical Information Service, U.S. Department of Commerce, Springfield, Virginia,.

Nuccio, V. F., and Johnson, R. C., 1989, Variations in vitrinite reflectance values for the Upper Cretaceous Mesaverde Formation, southeastern Piceance Basin, northwestern Colorado -Implications for burial history and potential hydrocarbon generation: U.S. Geological Survey Bulletin 1787-H, 10 p.

Obradovich, J. D., Mutschler, F. E., and Bryant, B., 1969, Potassium-argon ages bearing on igneous and tectonic history of the Elk Mountains and vicinity, Colorado--A preliminary report: GSA Bulletin, v. 80, p. 1749-1756.

Peterson, V. E., 1955, Fracture production from Mancos Shale, Rangely Field, Colorado: Intermountain Association of Petroleum Geologists - Rocky Mountain Association of Geologists, Guidebook to the Geology of Northwest Colorado, p. 101-105.

Pitman, J. K., and Sprunt, E. S., 1986, Origin and distribution of fractures in lower Tertiary and Upper Cretaceous rocks, Piceance Basin, Colorado, and their relation to the occurrence of hydrocarbons, *in* C. W. Spencer and R. F. Mast, eds., Geology of Tight Gas Reservoirs: AAPG Studies in Geology 24, p. 221-233.

Price, J. G., and Henry, C. D., 1984, Stress orientations during Oligocene volcanism in trans-Pecos Texas: Timing the transition from Laramide compression to Basin and Range tension: Geology, v. 12, p. 238-241.

Quigley, M. D., 1965, Geologic history of Piceance Creek-Eagle Basins: AAPG Bulletin, v. 49, p. 1974-1996.

Spencer, C. W., 1989, Review of characteristics of low-permeability gas reservoirs in western United States: AAPG Bulletin, v. 73, no. 5, p. 613-629.

Stone, D. S., 1991, Wilson Creek Field-U.S.A., Piceance Basin, northern Colorado: AAPG Bulletin, v. 75, no. 1, p. 1-45.

Suzuki, N., Matsubayashi, H. and Waples, D.W., 1993, A simpler kinetic model of vitrinite reflectance: AAPG Bulletin, v. 77, p. 1502-1508.

Sweeney, J.J. and Burnham, A.K., 1990, Evaluation of a simple model of vitrinite reflectance based on chemical kinetics: AAPG Bulletin, v. 74, p. 1559-1570.

Tweto, O., 1975, Laramide (Late Cretaceous-early Tertiary) orogeny in the Southern Rocky Mountains, *in* B. G. Curtis, ed., Cenozoic History of the Southern Rocky Mountains: GSA Memoir 144, p. 1-44.

Appendix G

Burial and Thermal History Data

J. Comer

Indiana Geological Survey
611 North Walnut Grove
Bloomington IN 47405

INTRODUCTION

Appendix G contains the raw data and a series of graphs for the burial and thermal histories at each of 18 locations in the Piceance Basin. This information is presented in the following order for each location.

PAGE 1

The first page contains two graphs, one titled "Burial History" and the other titled "Temperature History." The subtitle of each graph is the well name and location. The name in the extreme upper right corner of the page is the name of the computer file from which the graphs were printed.

BURIAL HISTORY

The "Burial History" graph consists of the burial depths in feet plotted along the y axis and the age in millions of years (MA) plotted along the x axis. The zero depth datum at the top of the graph is the land surface or sediment-water interface at any given time. The oldest age is plotted at the right end of the x axis and the youngest age (present-day or 0 MA) at the origin. Most of the "Burial History" graphs show curves for three horizons, the top and base of the Mesaverde and the top of the Rollins. These horizons were chosen because they represent the stratigraphic subdivisions that are most easily recognized in geophysical logs, hence they are the boundaries for the Mesaverde interval that are most easily mappable in the subsurface. Also, the top of the Rollins is the boundary between the Iles Formation below and the Williams Fork Formation above, which are the two lithostratigraphic units of the Mesaverde Group formally recognized and mapped in most of the Piceance Basin by the U.S. Geological Survey (Johnson and Nuccio, 1993). Some of the "Burial History" graphs show curves for thin zones within the Mesaverde Group from which samples were obtained for vitrinite reflectance analysis. Such horizons are labelled "R_o MARKER" with the present-day depth of burial 1shown in parentheses. A few graphs contain burial curves for the top of the Fort Union Formation and the top of the Wasatch Formation.

Present-day depths for these horizons were obtained from scout tickets; their accuracy will be critically reviewed in the future using geophysical logs and the isopach maps prepared by ARI.

TEMPERATURE HISTORY

The "Temperature History" graph consists of the age (MA) plotted along the y axis and the temperature in degrees celsius (°C) plotted along the x axis. (This graph may be easier to read if one rotates the page 90° clockwise.) The graph shows a single temperature curve that in most cases represents the temperature history of the top of the Rollins. Occasionally, the curve represents the temperature history at a specified R_O marker. The R_O marker is used when its temperature curve is significantly offset along the temperature axis from that of the top of the Rollins.

PAGE 2

The second page contains a graph titled "Vitrinite Maturation," which represents a simulation of the maturation of vitrinite through time. Included on this page are the calculated and measured vitrinite reflectance values and the thermal gradient(s) used in the simulation. The name in the extreme upper right corner of the page is the name of the computer file from which the graph was printed.

The "Vitrinite Maturation" graph consists of the age (MA) plotted along the y axis and the mean random vitrinite reflectance value (R_O) plotted along the x axis. (This graph may be easier to read if one rotates the page 90° clockwise). The single curve shown in the graph is for the same horizon as that shown in the "Temperature History" graph on the previous page.

The vitrinite maturation simulator was used as a means of independently checking the burial and thermal histories and the paleogeothermal gradients at each site. The simulator used in this exercise is the spreadsheet EASY%R_O, a model based on chemical kinetics that treats the maturation of vitrinite as a series of 21 parallel, first-order reactions (Sweeney and Burnham, 1990). The input parameters are age (MA) and temperature (°C) and the output is the present-day reflectance value for vitrinite (%R_O). This particular vitrinite maturation model was selected from a number of other choices because all of the algorithms, the optimum spreadsheet layout, and the

specific parameters for the kinetics database are published and can easily be keyed directly into any vendor's recent spreadsheet release. Furthermore, EASY%R_o has become a standard against which other vitrinite maturation models are currently being compared (Morrow and Issler, 1993; Suzuki and others, 1993).

Input into the EASY%R_o simulator was changed when necessary to bring the calculated %R_o into agreement with the %R_o actually measured using samples from well cuttings or cores. Agreement was accomplished in most cases by changing the geothermal gradient from that published for the well (Johnson and Nuccio, 1986; 1993) or from that interpolated for the well location using published thermal gradient maps of the basin (Johnson and Nuccio 1986; Nuccio and Johnson, 1989). All of the "Vitrinite Maturation" graphs and data in Appendix G are the result of the final iteration from fitting the calculated values for %R_o to the observed values at each given site. The temperature history and thermal gradient data will be refined in the future if necessary as more data become available.

PAGE 3

The third page contains the table of numerical data (depth, age, and temperature) that were used to produce the "Burial History," "Temperature History," and "Vitrinite Maturation" graphs. The name in the extreme upper right corner is the name of the spreadsheet file from which this table was printed. Header information at the top of the page includes the source reference(s) that contained the data, the name and location (section-township-range) of the well, the name of the spreadsheet file containing the vitrinite maturation simulation (EASYRO--or SIMRO--), the datum for the elevations listed in the body of the table, the final thermal gradients from the vitrinite maturation simulator (T Gradient=), the source of data for the present-day depths (LOG TOPS indicates tops picked from geophysical logs; no listing means the depths are from the publication(s) listed at the top of the header), and the surface elevation at the well site (ELEVATION KB=).

The body of the table consists, from left to right, of a column for the age (MA), several columns starting with the number 1000 representing elevations in feet relative to present-day mean sea level (ELEVATIONS), several columns starting with the number zero representing depths of

burial in feet (DEPTHS), and a final column giving the temperature of the specified horizon (TEMPERATURE). The starting elevation of 1000 feet was taken from Lorenz (1985), who argued that this was a reasonable elevation for the depositional surface of Mesaverde sediments given that sea level was considerably higher during the Late Cretaceous than it is today and given that the Mesaverde was deposited near sea level as marginal marine, shoreline, and distal fluvial facies. Because of the generally consistent distribution of Mesaverde facies across the Piceance Basin, we have assumed a starting elevation of 1000 feet for all sites. Even though stratigraphic analysis has revealed onlap and offlap of facies, which attests to the relative rise and fall of sea level during Mesaverde deposition, change in the elevation of Cretaceous sea level by itself should not significantly affect the thermal history. This assumption and the choice of starting elevation will be further evaluated during the course of this study.

The bottom row of the table (0 MA) contains the present-day elevations and depths taken from the geophysical log, scout ticket, or reference followed by the current subsurface temperature of the specified horizon as calculated using the present-day geothermal gradient. The column containing the burial depths for either the R_O marker or the top of the Rollins were constructed by picking depths from published burial history curves (Lorenz, 1985; Johnson and Nuccio, 1986; 1993) and entering these values directly into the table. The values for MA in the first column were also picked from the published curves. All other depths and elevations in the table were then calculated assuming that the vertical distance between the given horizons remained constant through time. For example, the vertical distance between the Rollins top and the Mesaverde base is 900 feet at the MWX site based on the evaluation of geophysical logs; hence at each specified time in the geologic past the Mesaverde base is 900 feet deeper than the Rollins top. The temperature in the last column was calculated by first converting the depth in feet to meters, multiplying by the geothermal gradient (°C/m), and adding the ambient surface temperature (10°C). The choice of 10°C for the ambient surface temperature is from Johnson and Nuccio (1986). All of these assumptions and choices will be further evaluated during the course of this study.

BURIAL HISTORY

MWX SITE

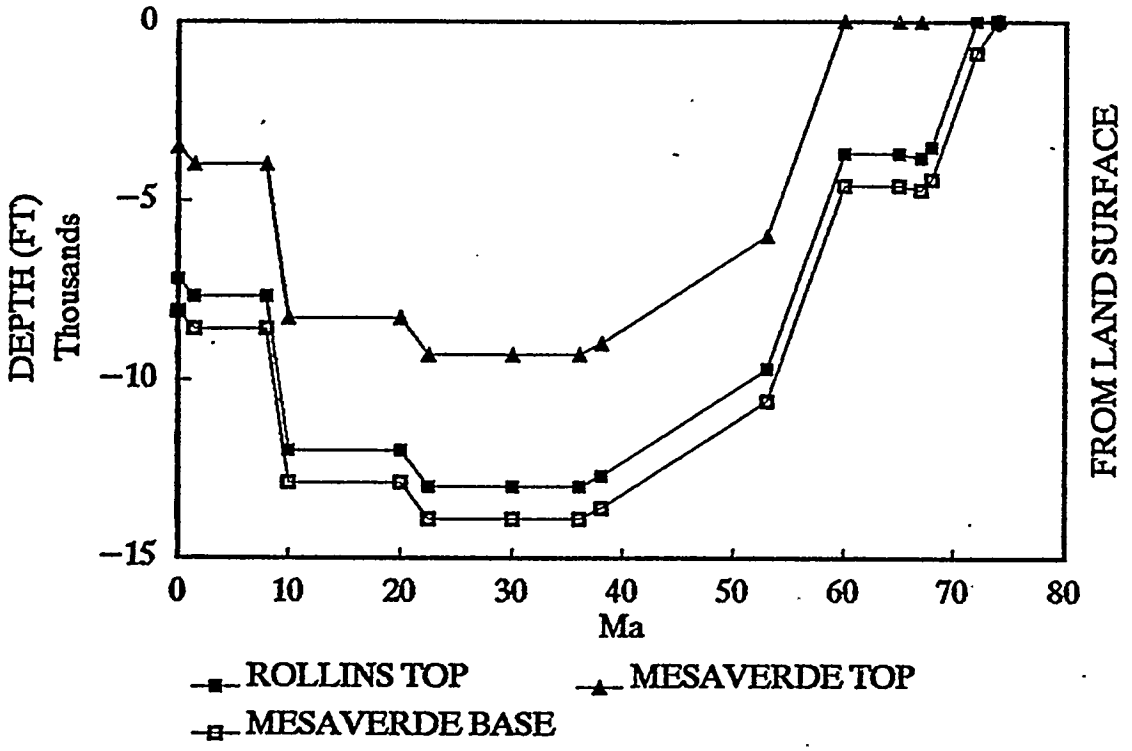

TEMPERATURE HISTORY

MWX SITE

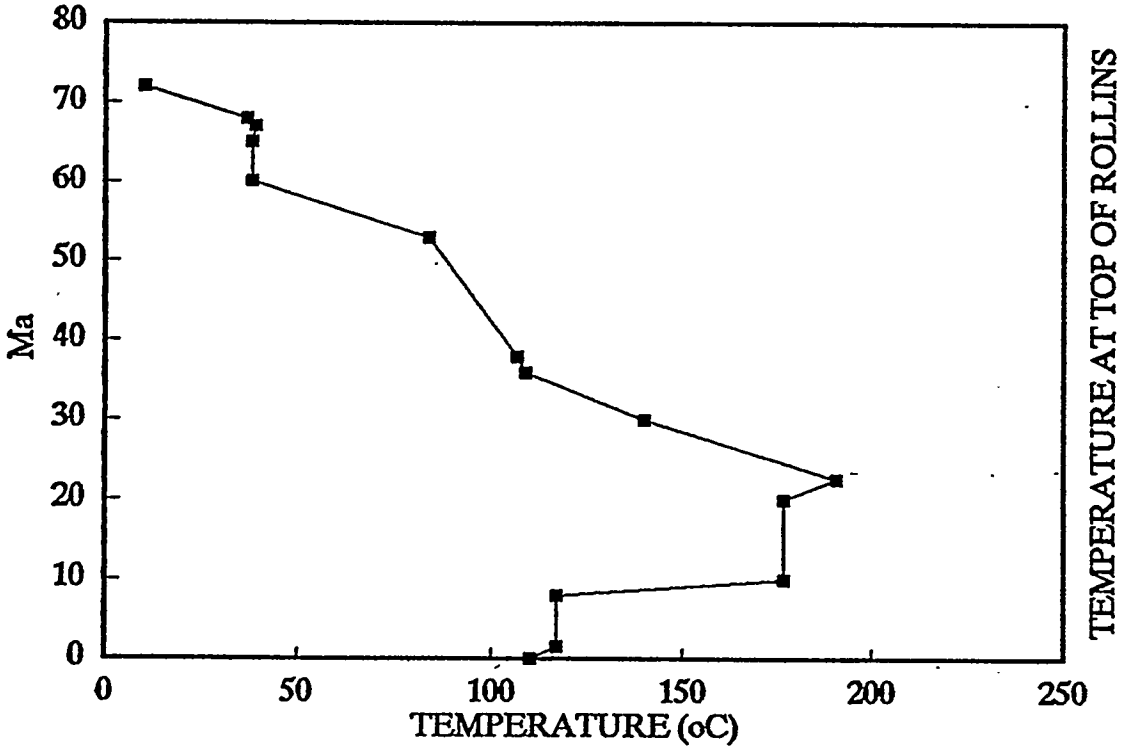

VITRINITE MATURATION

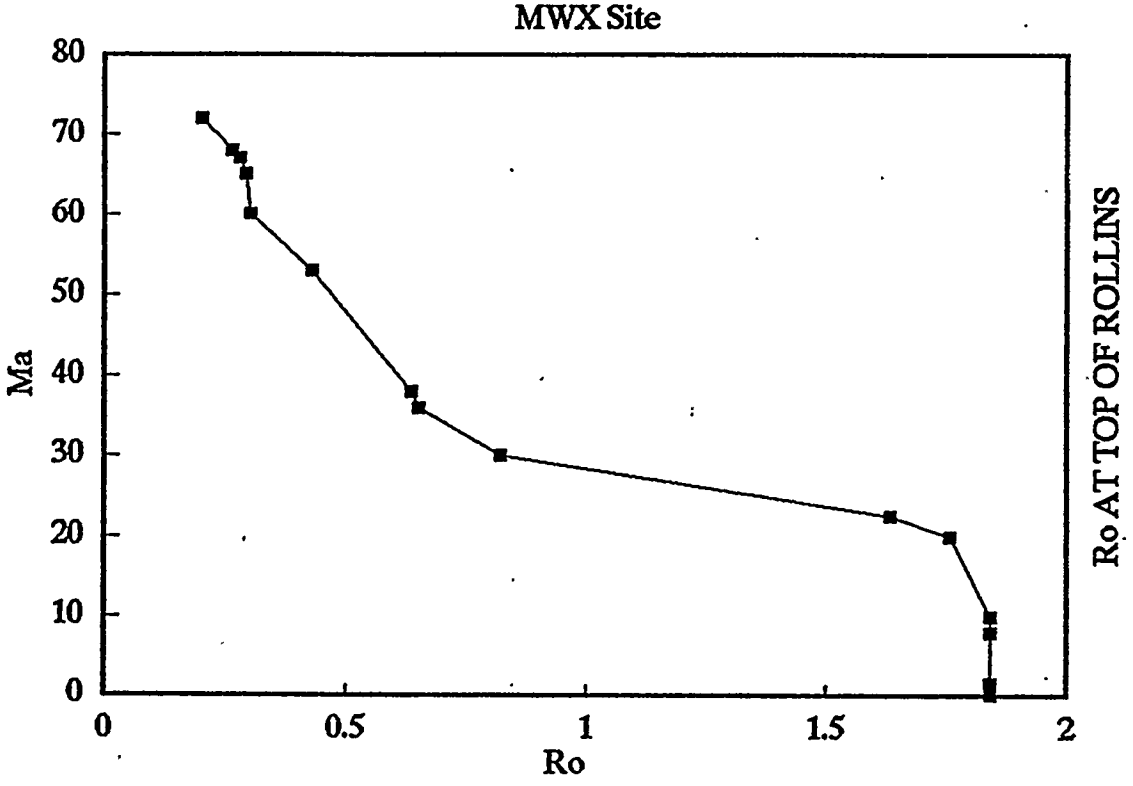

SUBSIDENCE HISTORY
MWX Site
34-6S-94W SE,SW,NW

EASYROMV
LOG TOPS

J.C. LORENZ, 1985, Tectonic and s
LORENZ and FINLEY, 1991, Region
DATUM = PRESENT MEAN SEA LEV
T GRADIENT (corr.)= 0.0250 1.4 oF/100
0.0328 1.8 oF/100
0.0456 2.5 oF/100
ELEVATION KB= 5374 ft

		ELEVATIONS			
		MESAVERDE	ROLLINS	OHIO CREE	MESAVERDE
Ma	Ma	BASE	TOP	BASE	TO
72	74	1000			
71	72	100	1000		
68	68	-3400	-2500	1000	
67	67	-3700	-2800	700	1000
66	65	-3200	-2300	1200	1500
60	60	-3200	-2300	1200	1500
52	53	-8200	-7300	-3800	-3500
40	38	-12200	-11300	-7800	-7500
36	36	-12300	-11400	-7900	-7600
30	30	-9900	-9000	-5500	-5200
22.5	22.5	-9900	-9000	-5500	-5200
20	20	-7700	-6800	-3300	-3000
10	10	-7700	-6800	-3300	-3000
8	8	-3400	-2500	1000	1300
1.5	1.5	-3400	-2500	1000	1300
0	0	-2900	-2000	1500	1800

			DEPTHS			TEMPERAT
SEDIMENT	MESAVERDE	OHIO CREE	ROLLINS		MESAVERDE	ROLLINS
SURFACE	TOP	BASE	TOP		BASE	
1000					0	
1000				0	-900	10
1000			0	-3500	-4400	37
1000		0	-300	-3800	-4700	39
1400		0	-200	-3700	-4600	38
1400		0	-200	-3700	-4600	38
2400		-6000	-6200	-9700	-10600	84
1400		-9000	-9200	-12700	-13600	107
1600		-9300	-9500	-13000	-13900	109
4000		-9300	-9500	-13000	-13900	140
4000		-9300	-9500	-13000	-13900	191
5200		-8300	-8500	-12000	-12900	177
5200		-8300	-8500	-12000	-12900	177
5200		-4000	-4200	-7700	-8600	117
5200		-4000	-4200	-7700	-8600	117
5200		-3500	-3700	-7200	-8100	110

BURIAL HISTORY

Cities Service No. 4A Federal 26–2N–97W

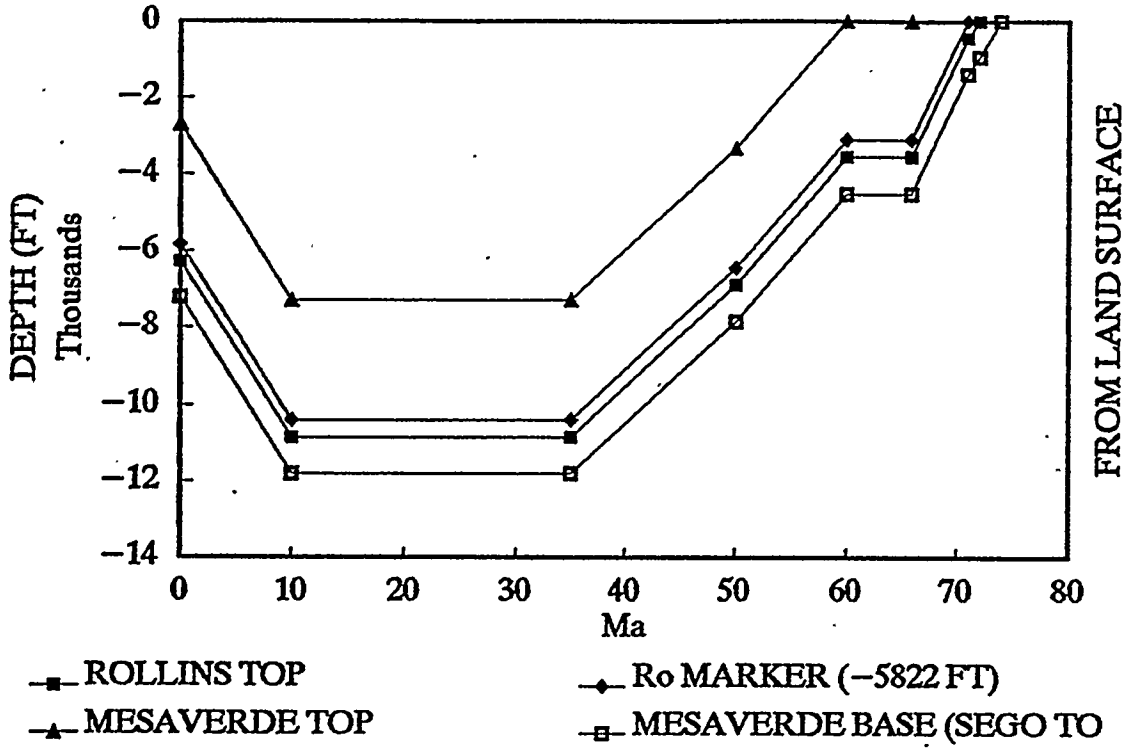

TEMPERATURE HISTORY

Cities Service No. 4A Federal 26–2N–97W

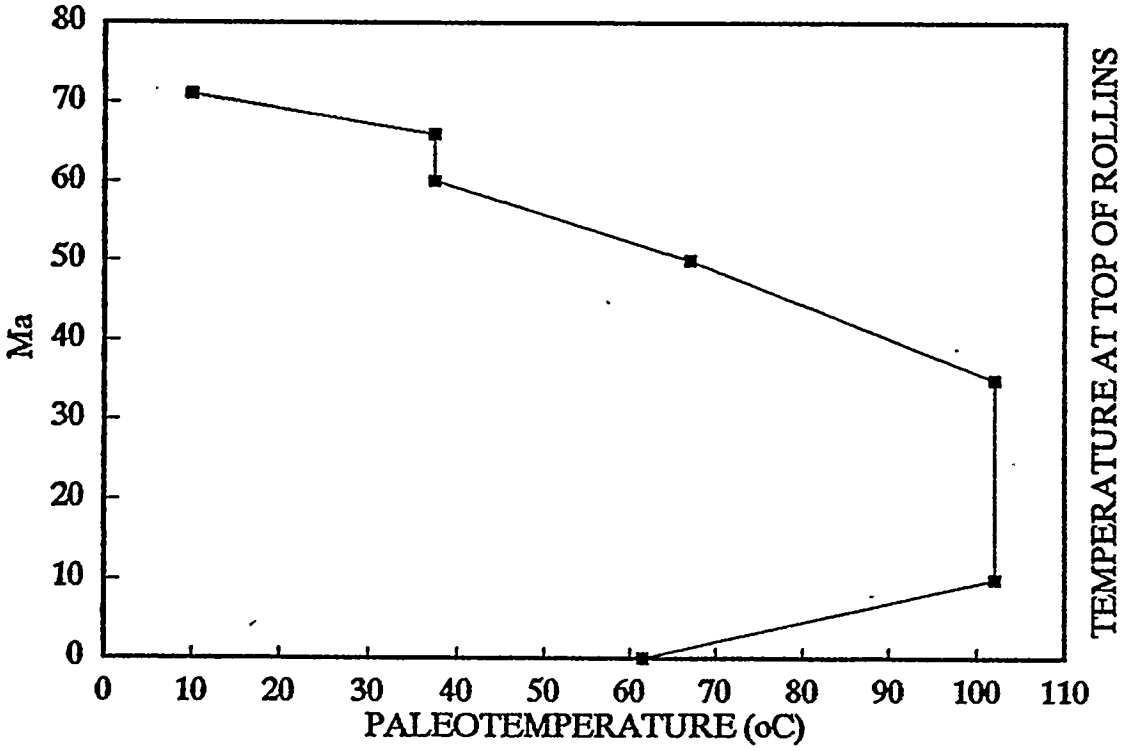

VITRINITE MATURATION

Cities Service No. 4A Federal 26–2N–97W

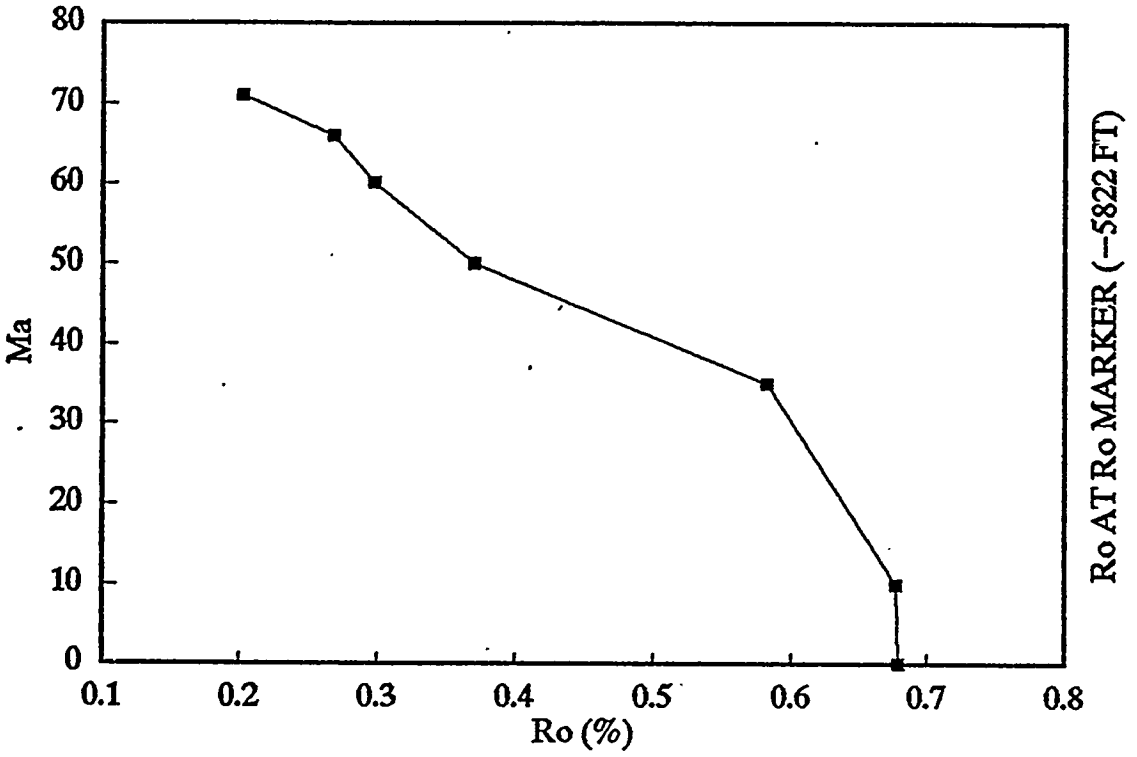

SUBSIDENCE HISTORY Johnson and Nuccio, 1986, Structural and Th
26-2N-97W NE,SE,NW Cities Service No. 4A Federal

T GRADIENT (corr.)=	1.6	DEG F/1
DEG	0.0290	Before 30
	0.0290	After 30 M
KB (elev. in ft.)=	5973	

	ELEVATIONS				
Ma	MESAVERDE BASE	ROLLINRo TOP	MARKER	MESAVERDE TOP	SEDIME SURFAC
74	1000				1000
72	62	1000			1000
71	-390	548	1000		1000
66	-3100	-2162	-1710	1400	1400
60	-3100	-2162	-1710	1400	1400
50	-5440	-4502	-4050	-940	2400
35	-7800	-6862	-6410	-3300	4000
10	-7100	-6162	-5710	-2600	4700
0	-1239	-301	151	3261	5973

DEPTHS				TEMPERATURE	
MESAVERDE BASE	ROLLINSRo TOP	MARKER	MESAVERDE TOP	Ro	MARKER
0					
-938	0				
-1390	-452	0		10	
-4500	-3562	-3110	0	37	
-4500	-3562	-3110	0	37	
-7840	-6902	-6450	-3340	67	
-11800	-10862	-10410	-7300	102	
-11800	-10862	-10410	-7300	102	
-7212	-6274	-5822	-2712	61	

BURIAL HISTORY

Cities Service No. B–1 Federal Preece 19–3N–96W

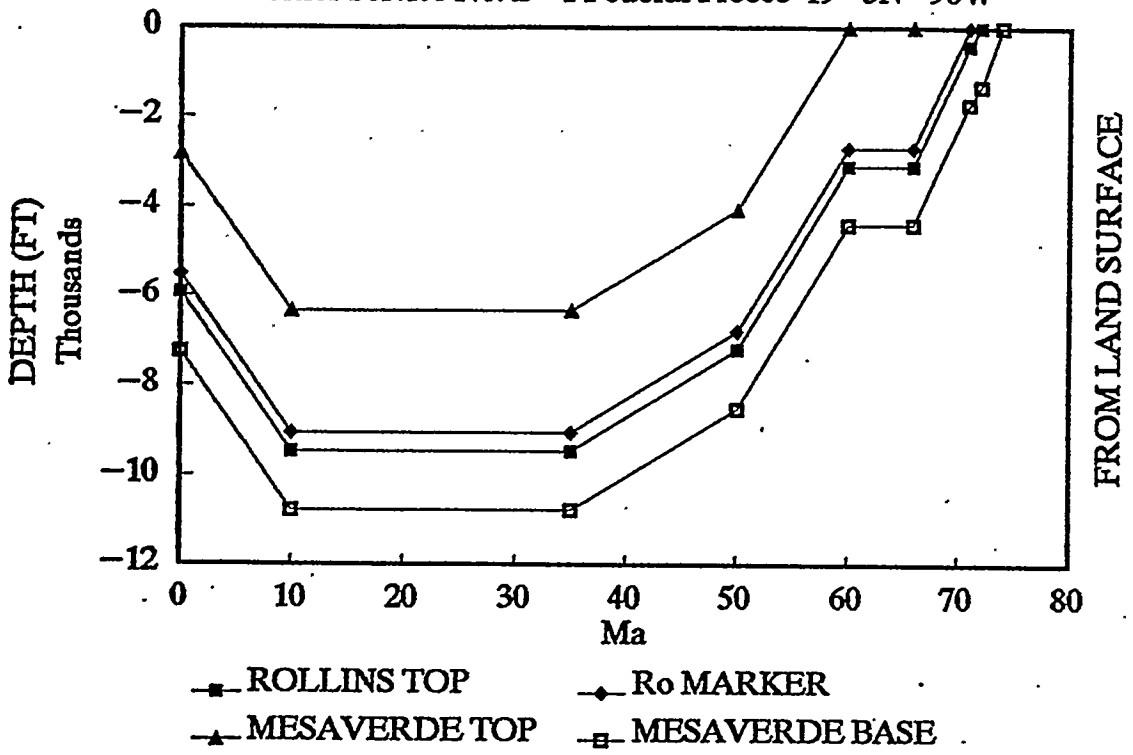

TEMPERATURE HISTORY

Cities Service No. B–1 Federal Preece 19–3N–96W

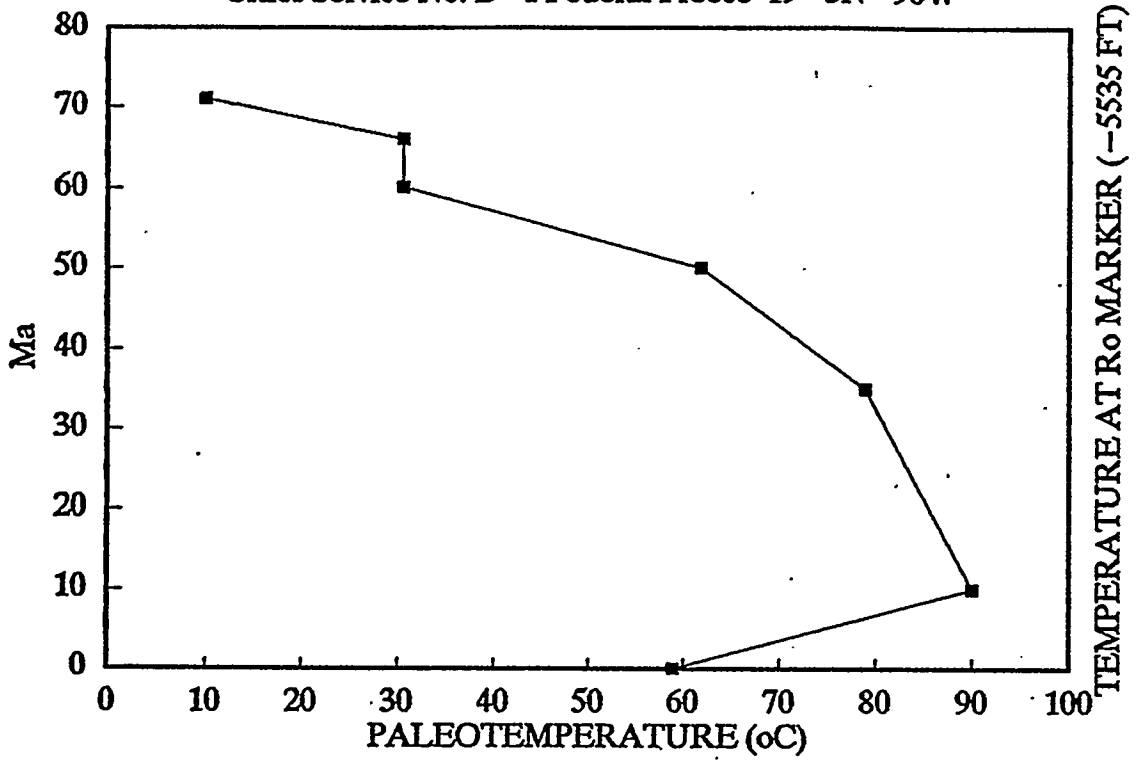

TEMPERATURE HISTORY

Cities Service No. B–1 Federal Preece 19–3N–96W

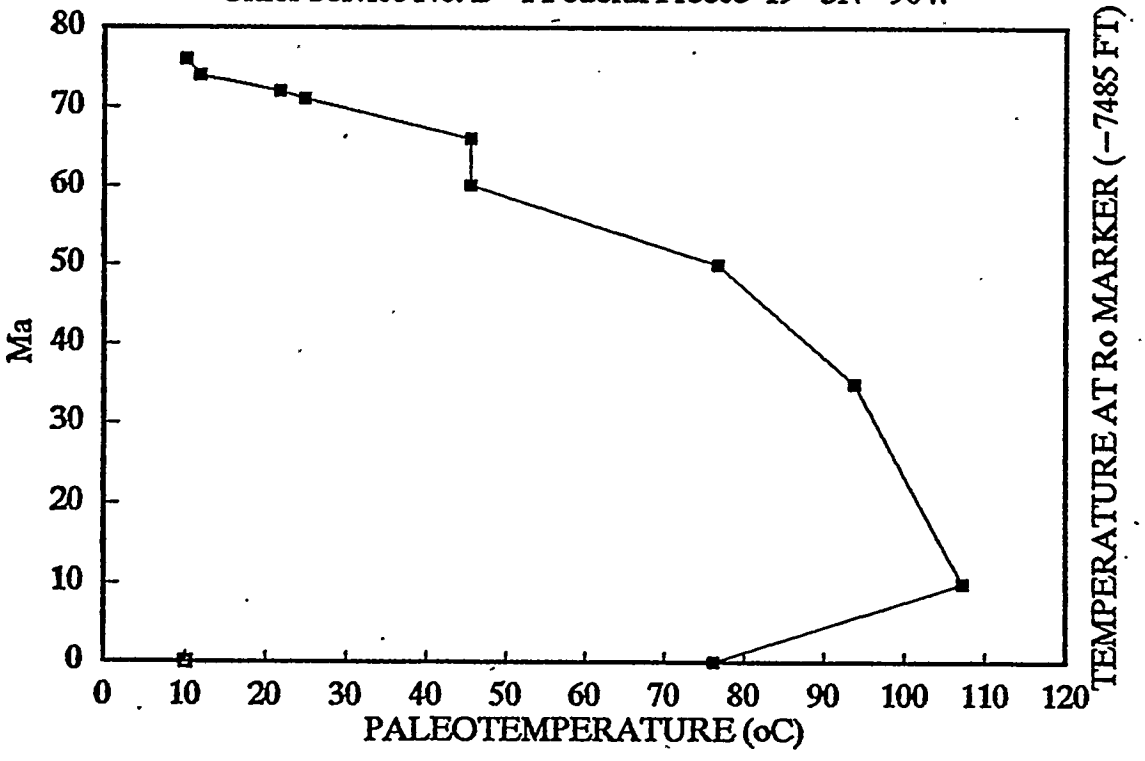

VITRINITE MATURATION

Cities Service No. B–1 Federal Preece 19–3N–96W

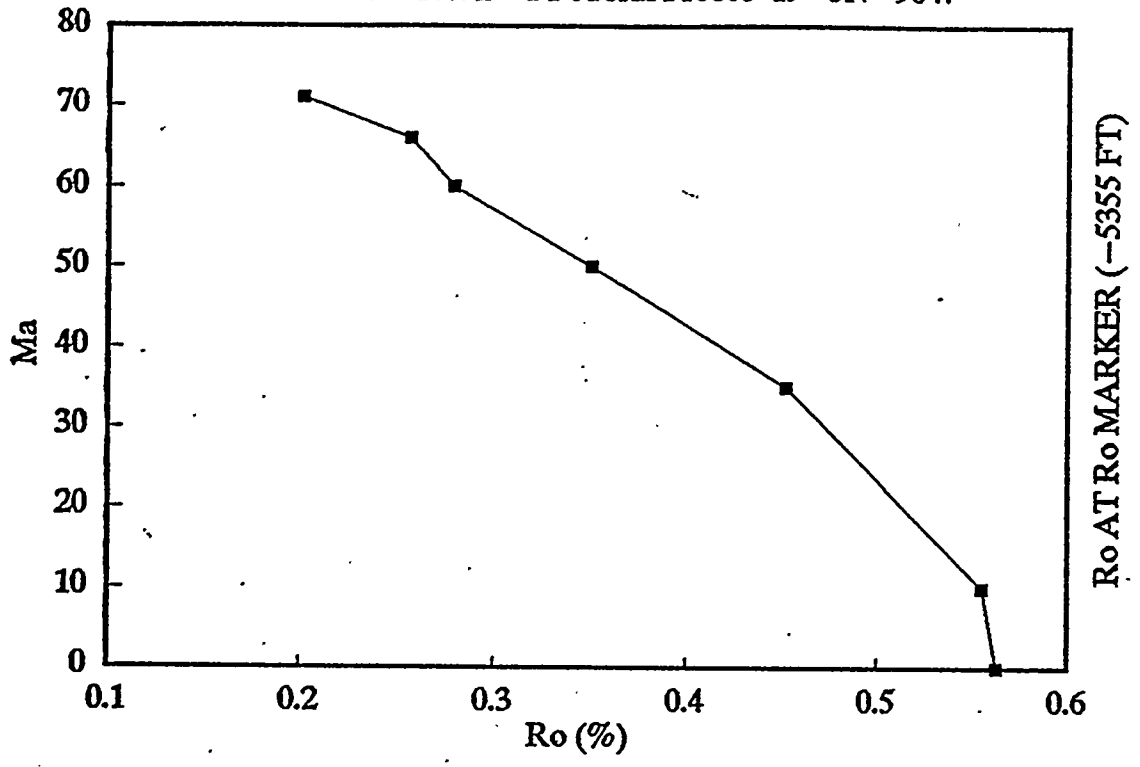

VITRINITE MATURATION

Cities Service No. B–1 Federal Preece 19–3N–96W

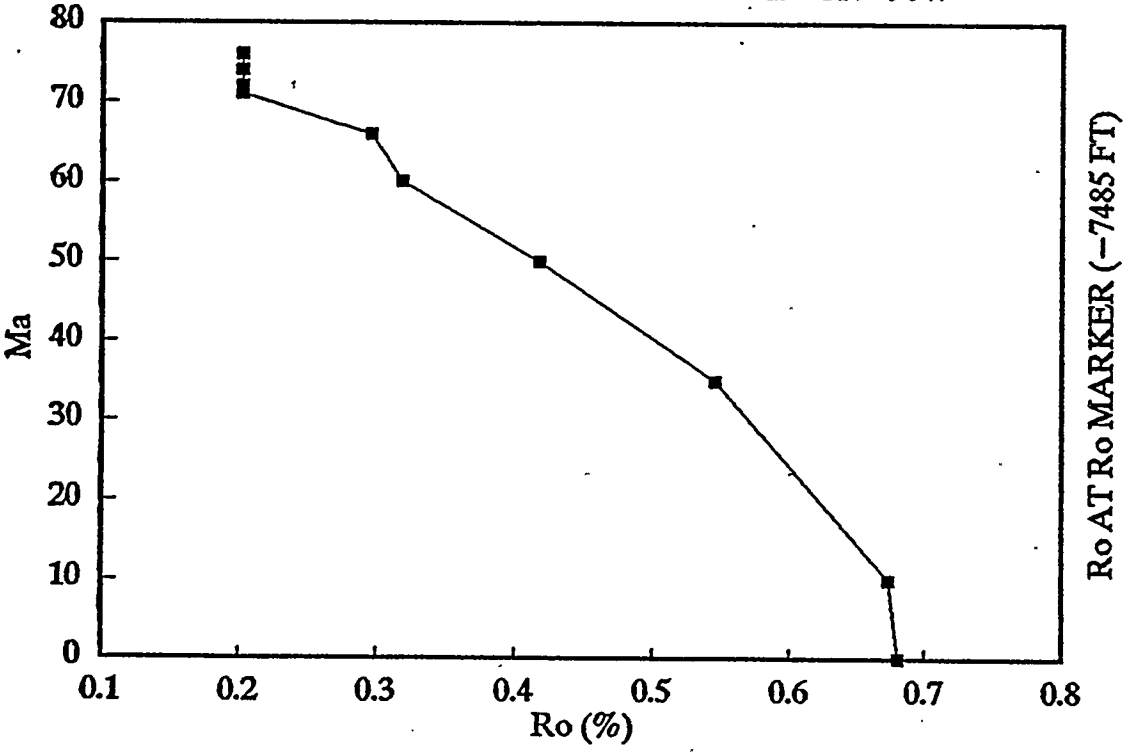

SUBSIDENCE HISTORY
19-3N-96W C,NW,SE

Johnson and Nuccio, 1986, Struct
Cities Service No. B-1 Federal Pr
T GRADIENT (corr.)= 1
DEG 0.0250
0.0290
KB (elev. in ft.)= 6089

Ma	Ro MARKER	MESAVERDE BASE	ROLLIN TOP	Ro MARKER	ELEVATION MESAVERDE TOP
76	1000				
74	773	1000			
72	-540	-313	1000		
71	-950	-723	590	1000	
66	-3258	-3031	-1718	-1308	1400
60	-3258	-3031	-1718	-1308	1400
50	-6350	-6123	-4810	-4400	-1692
35	-7000	-6773	-5460	-5050	-2342
10	-5800	-5573	-4260	-3850	-1142
0	-1396	-1169	144	554	3262

S SEDIME SURFACE	DEPTHS Ro MARKER	MESAVERDE BASE	ROLLINS TOP	Ro MARKER	MESAVERDE TOP
1000	0				
1000	-227	0			
1000	-1540	-1313	0		
1000	-1950	-1723	-410	0	
1400	-4658	-4431	-3118	-2708	0
1400	-4658	-4431	-3118	-2708	0
2400	-8750	-8523	-7210	-6800	-4092
4000	-11000	-10773	-9460	-9050	-6342
5200	-11000	-10773	-9460	-9050	-6342
6089	-7485	-7258	-5945	-5535	-2827

TEMPERAT Ro MARKER (-7485 FT)	TEMPERAT Ro MARKER (-5535 FT)
10	
12	
22	
25	10
45	31
45	31
77	62
94	79
107	90
76	59

BURIAL HISTORY

Forest Sinclair No. 15–1 Krause 15–4N–97W

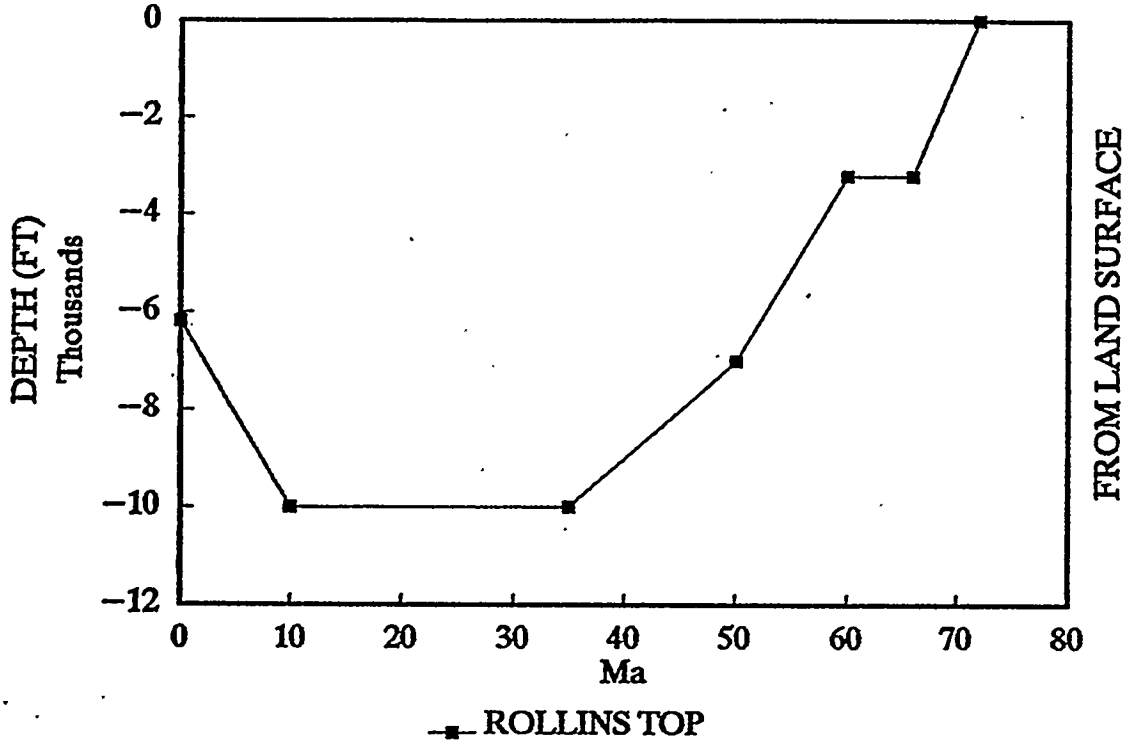

TEMPERATURE HISTORY

Forest Sinclair No. 15–1 Krause 15–4N–97W

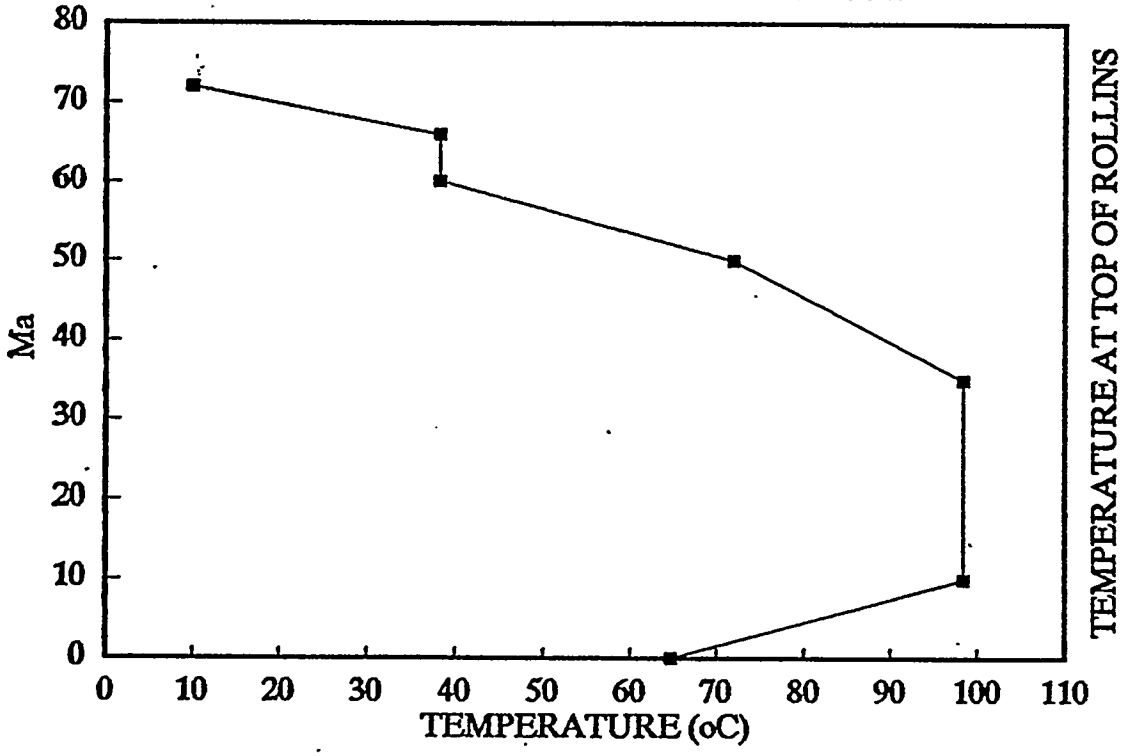

VITRINITE MATURATION

Forest Sinclair No. 15–1 Krause 15–4N–97W

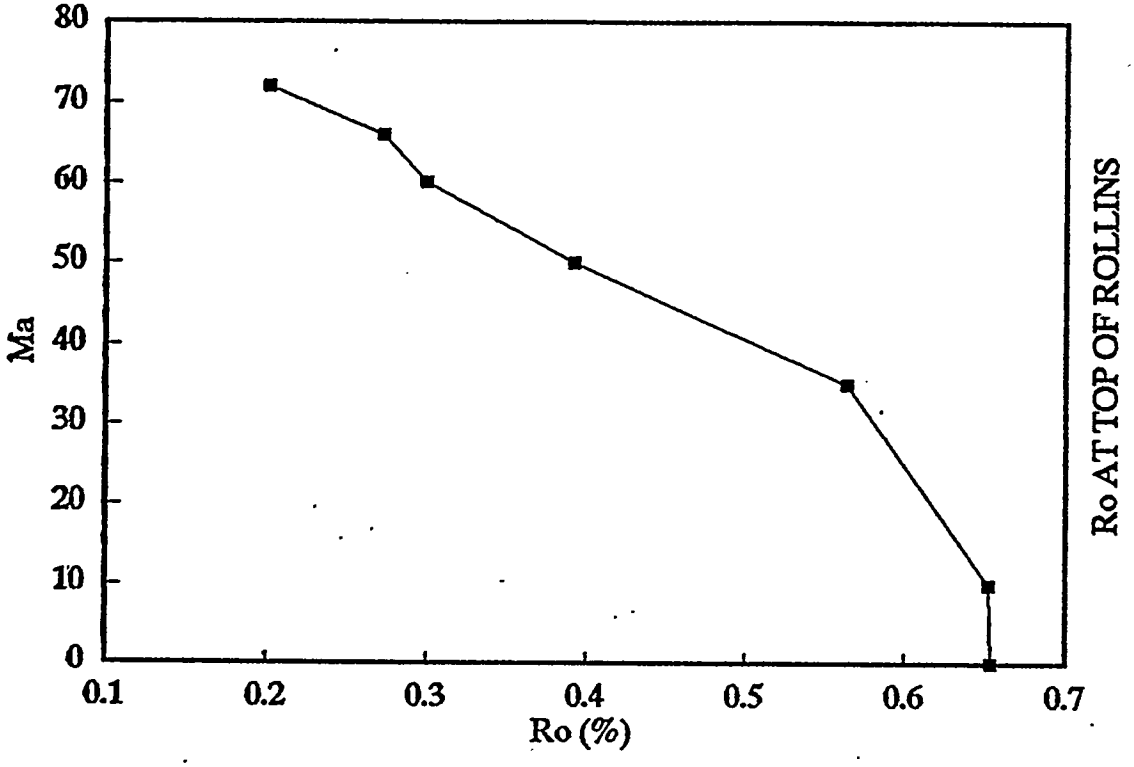

SUBSIDENCE HISTORY Johnson and Nuccio, 1986, Structural and Th
15-4N-97W SE,SE Forest Exploration Sinclair No. 15-1 Krause

T GRADIENT (corr.)=	1.6	DEG F/1
	0.0290	DEG C/
KB (elev. in ft.)=	6087	

ELEVATIONS

Ma	MESAVERDE BASE	ROLLINOHIO TO	CREE BAS	MESAVERDE TOP	SEDIME SURFAC
74	1000				1000
72		1000			1000
66		-1800	1000		1400
60		-1800		1000	1400
50		-4600			2400
35		-6000			4000
10		-4800			5200
0		-100			6087

DEPTHS				TEMPERATURE
MESAVERDE BASE	ROLLINSOHIO TOP	CREE BASE	MESAVERDE TOP	ROLLINS TOP
	0			10
	-3200			38
	-3200			38
	-7000			72
	-10000			98
	-10000			98
	-6187			65

BURIAL HISTORY

Fuelco No. 1 Federal 31–2N–96W

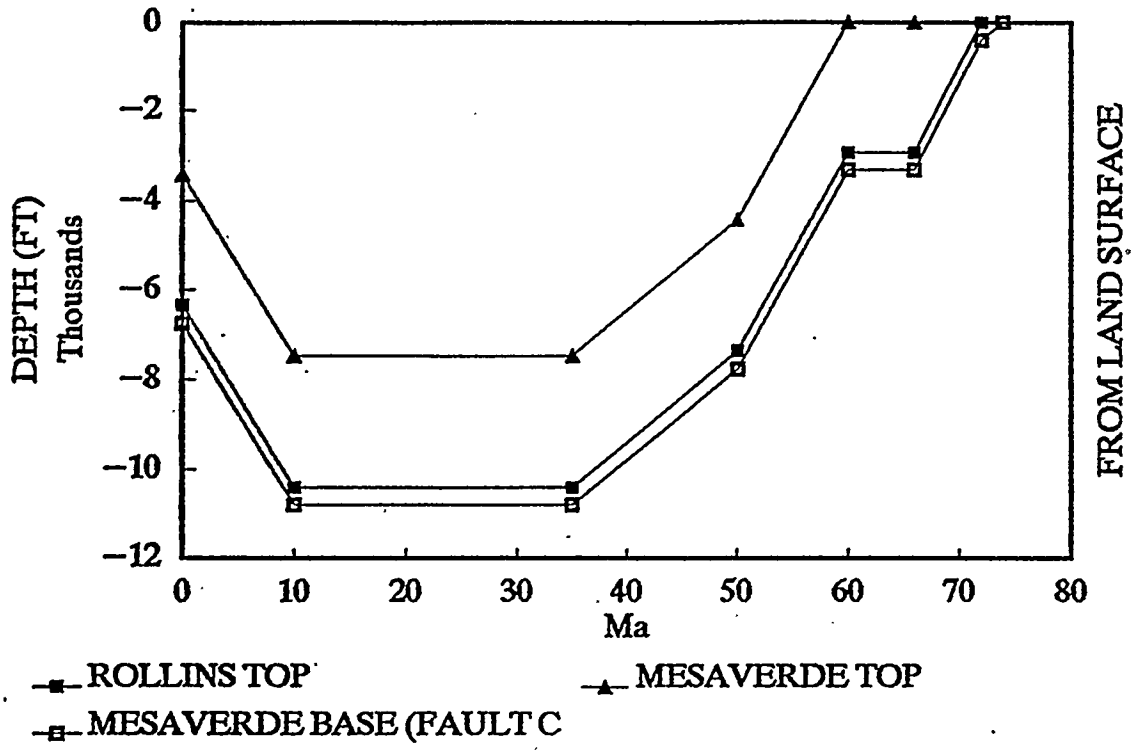

TEMPERATURE HISTORY

Fuelco No. 1 Federal 31–2N–96W

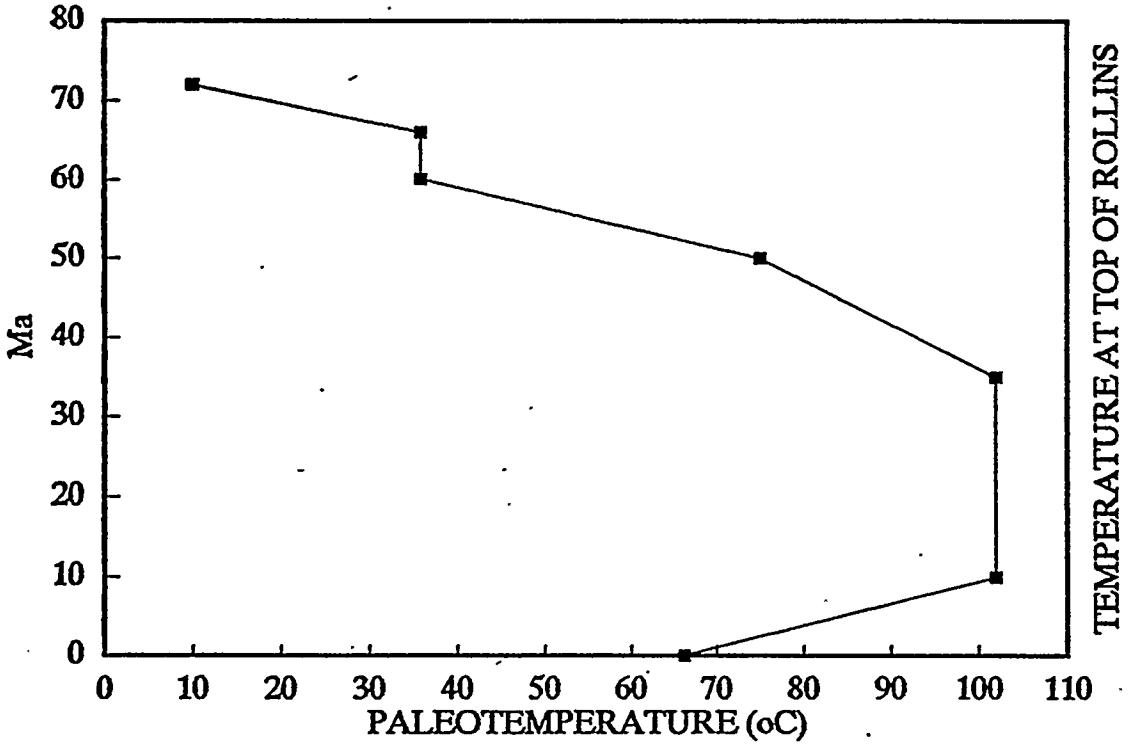

VITRINITE MATURATION

Fuelco No. 1 Federal 31–2N–96W

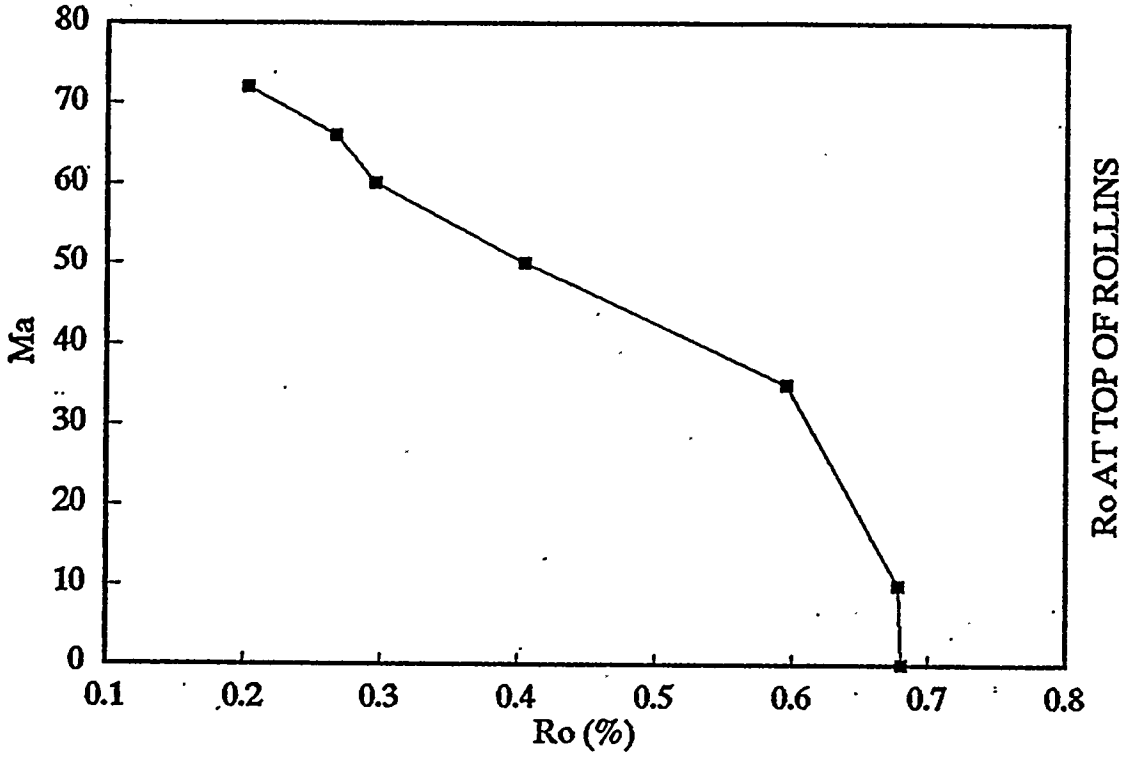

SUBSIDENCE HISTORY Johnson and Nuccio, 1986, Structural and Th
31-2N-96W SW,NE Fuelco No. 1 Federal

T GRADIENT (corr.)=	1.6	DEG F/1
DEG	0.0290	Before 30
	0.0290	After 30 M
KB (elev. in ft.)=	5858	

	ELEVATIONS			
Ma	MESAVERDE BASE	ROLLIN TO	MESAVERDE TOP	SEDIME SURFAC
74	1000			1000
72	600	1000		1000
66	-1920	-1520	1400	1400
60	-1920	-1520	1400	1400
50	-5350	-4950	-2030	2400
35	-6800	-6400	-3480	4000
10	-5600	-5200	-2280	5200
0	-892	-492	2428	5858

DEPTHS		TEMPERATURE	
MESAVERDE BASE	ROLLINS TOP	MESAVERDE TOP	ROLLINS TOP
0			
-400	0		10
-3320	-2920	0	36
-3320	-2920	0	36
-7750	-7350	-4430	75
-10800	-10400	-7480	102
-10800	-10400	-7480	102
-6750	-6350	-3430	66

BURIAL HISTORY

Chancellor No. 397–3–1 Government 3–3S–97W

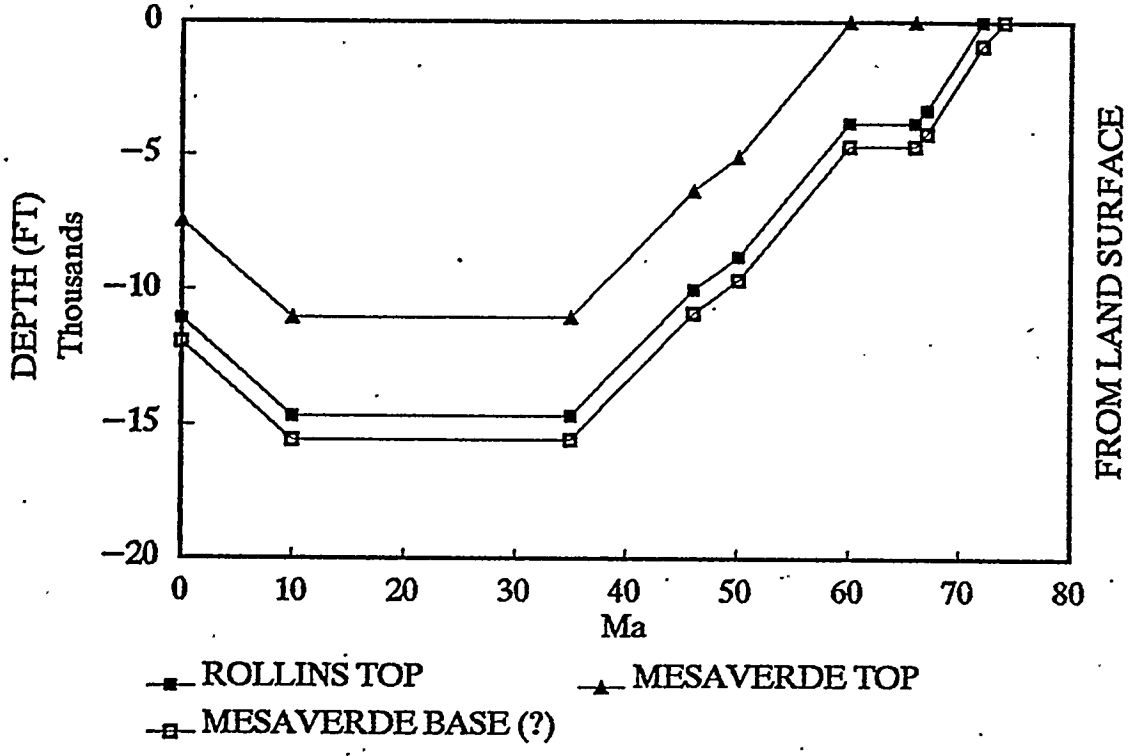

TEMPERATURE HISTORY

Chancellor No. 397–3–1 Government 3–3S–97W

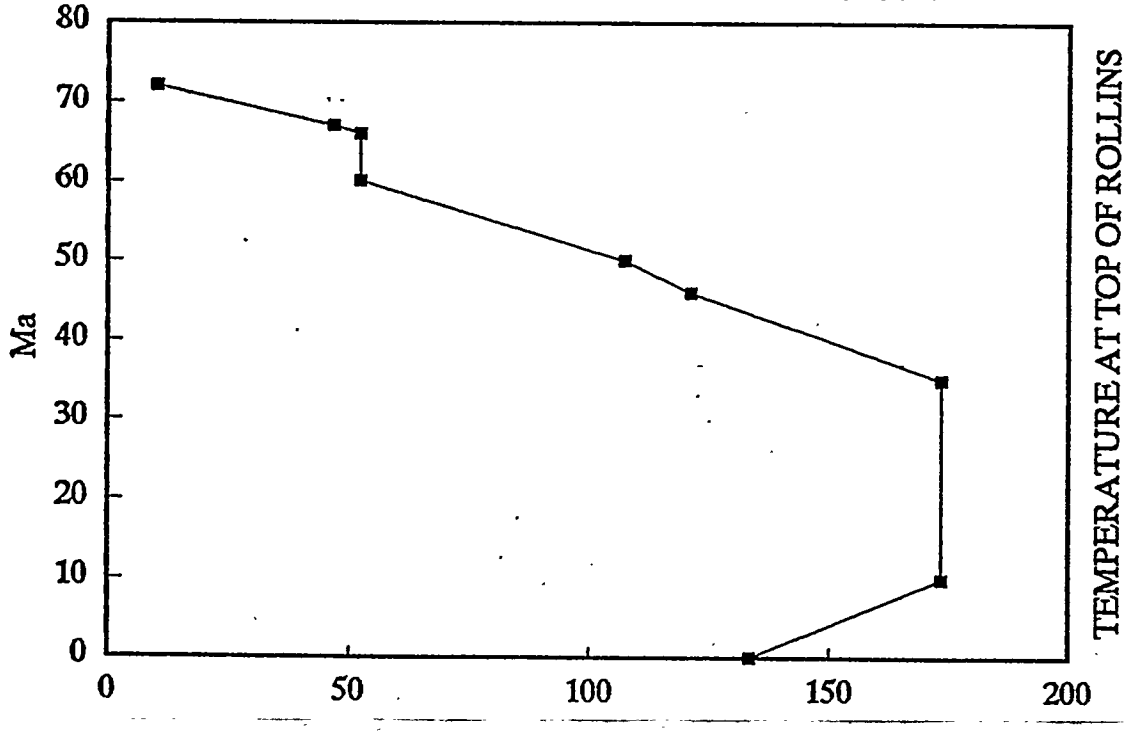

VITRINITE MATURATION

Chancellor No. 397–3–1 Government 3–3S–97W

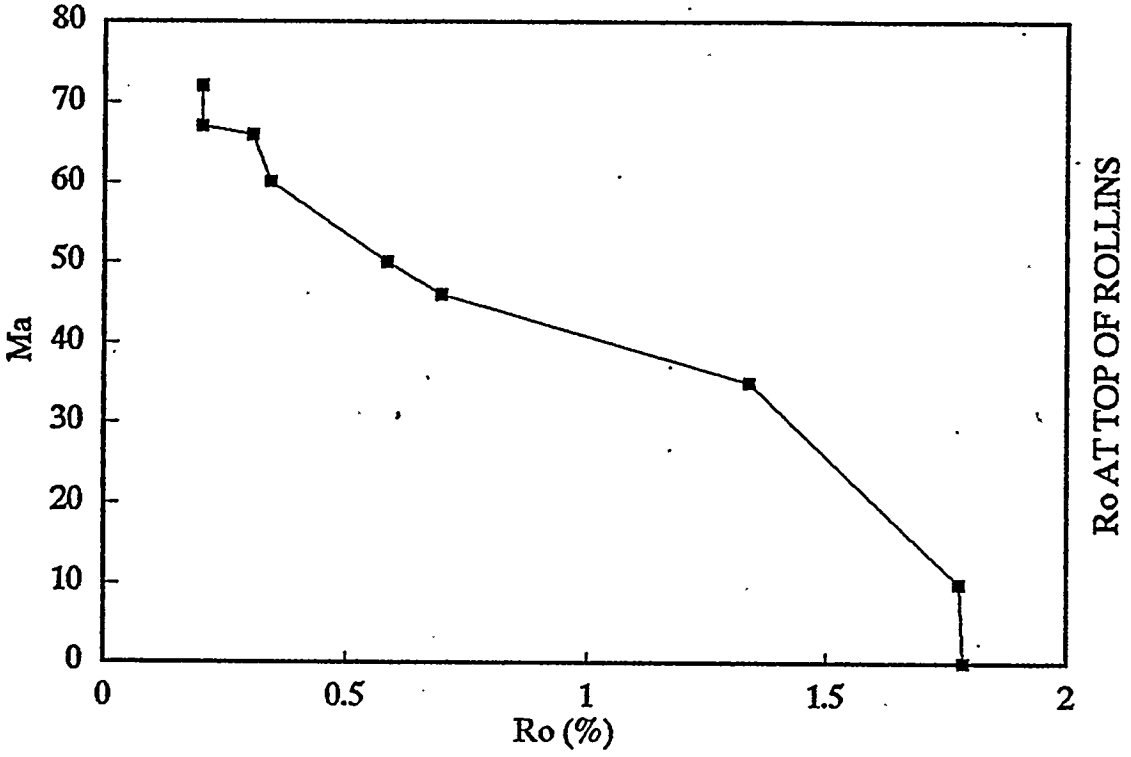

SUBSIDENCE HISTORY Johnson and Nuccio, 1986, Structural and Th
3-3S-97W SE,NW C. E. Chancellor No. 397-3-1
T GRADIENT (corr.)= 2 DEG F/1
0.0365 DEG C/
LOG TOPS KB (elev. in ft.)= 6696

ELEVATIONS

Ma	MESAVERDE BASE	ROLLINTO	OHIO CREE BAS	MESAVERDE TOP	SEDIME SURFAC
74	1000				1000
72	114	1000			1000
67	-3186	-2300	1000		1000
66	-3286	-2400	1115	1400	1400
60	-3286	-2400	1115	1400	1400
50	-7236	-6350	-2835	-2690	2400
46	-8286	-7400	-3885	-3740	2600
35	-11586	-10700	-7185	-7040	4000
10	-10386	-9500	-5985	-5840	5200
0	-5285	-4399	-884	-739	6696

DEPTHS

MESAVERDE BASE	ROLLINSOHIO CREE TOP	BASE	MESAVERDE TOP	TEMPERAT ROLLINOHIO CREE TOP	TEMPERAT BASE
0					
-886	0			10	
-4186	-3300	0		47	10
-4686	-3800	-285	0	52	13
-4686	-3800	-285	0	52	13
-9636	-8750	-5235	-5090	107	68
-10886	-10000	-6485	-6340	121	82
-15586	-14700	-11185	-11040	174	134
-15586	-14700	-11185	-11040	174	134
-11981	-11095	-7580	-7435	133	94

BURIAL HISTORY

CSG No. 397–8–4 Government 8–3S–97W

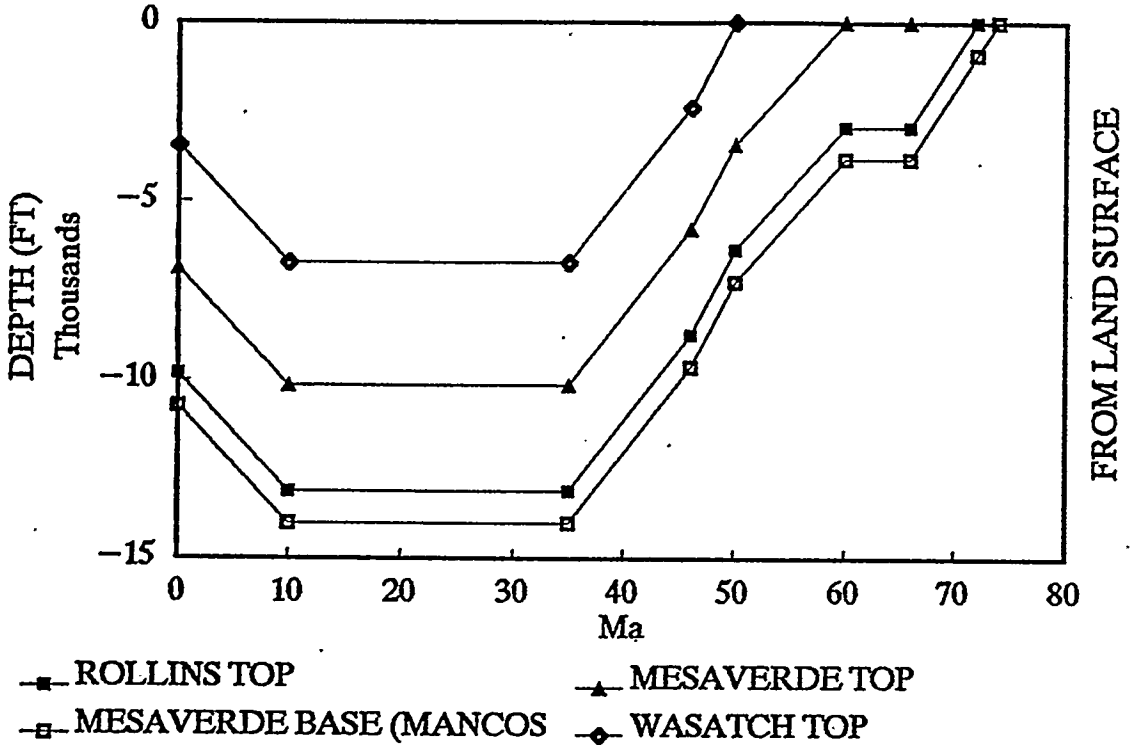

TEMPERATURE HISTORY

CSG No. 397–8–4 Government 8–3S–97W

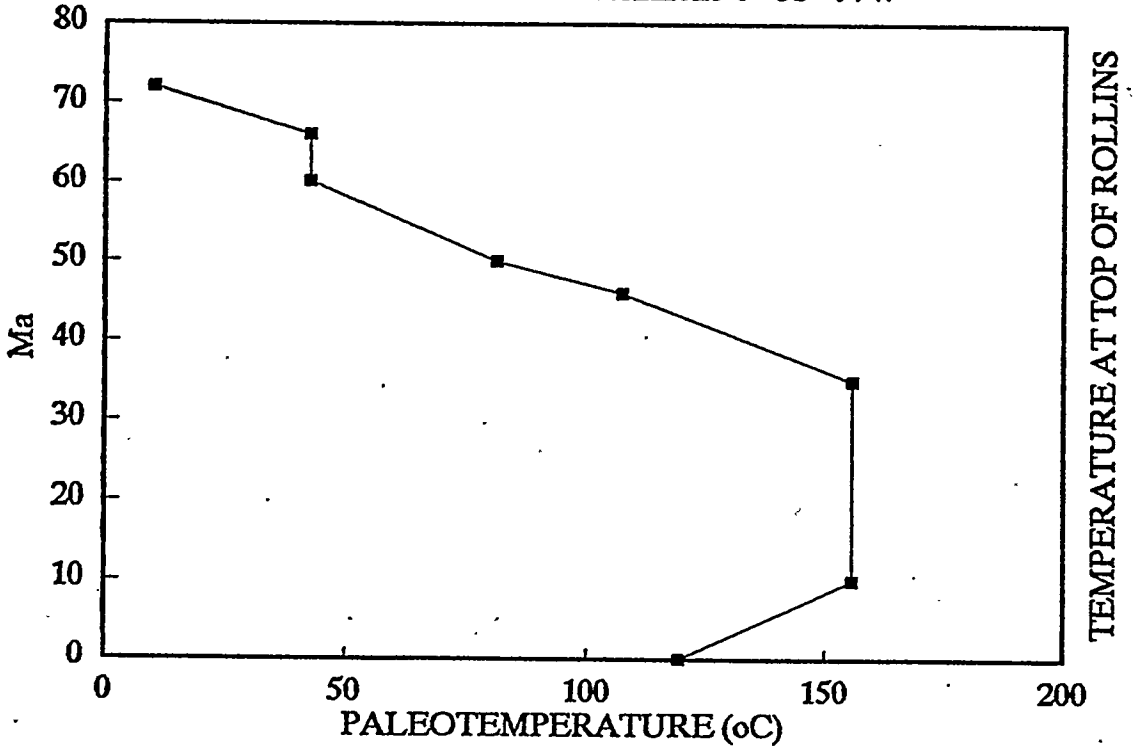

VITRINITE MATURATION

CSG No. 397–8–4 Government 8–3S–97W

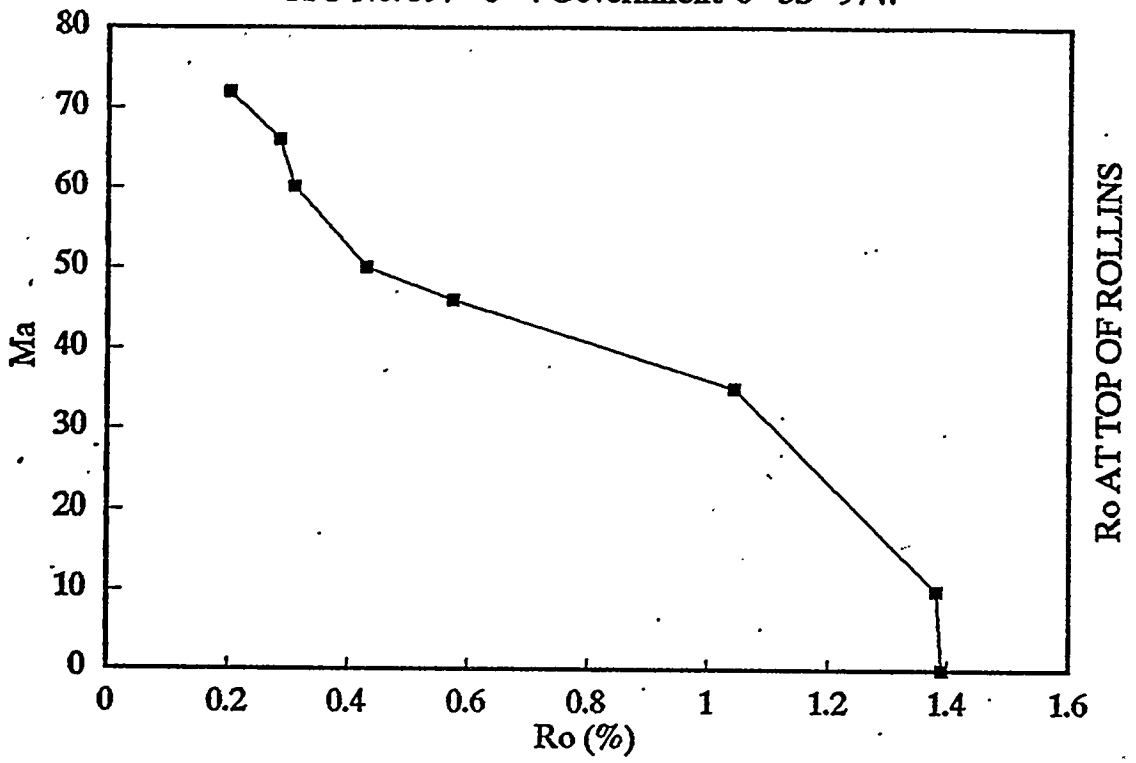

SUBSIDENCE HISTORY Johnson and Nuccio, 1986, Structural and Th
8-3S-97W NE,SW CSG No. 397-8-4 Government
T GRADIENT (corr.)= 2.0
DEG C/m= 0.0365
0.0365
LOG TOPS KB (elev. in ft.)= 6815

	ELEVATIONS				
	MESAVERDE	ROLLIN	MESAVERDE	WASATCH	SEDIME
Ma	BASE	TO	TOP	TOP	SURFAC
74	1000				1000
72	115	1000			1000
66	-2428	-1543	1400		1400
60	-2428	-1543	1400		1400
50	-4855	-3970	-1027	2400	2400
46	-6635	-5750	-2807	620	3000
35	-9985	-9100	-6157	-2730	4000
10	-8785	-7900	-4957	-1530	5200
0	-3900	-3015	-72	3355	6815

DEPTHS				TEMPERATURE
MESAVERDE	ROLLINS	MESAVERDE	WASATCH	ROLLINS
BASE	TOP	TOP	TOP	TOP
0				
-885	0			10
-3828	-2943	0		43
-3828	-2943	0		43
-7255	-6370	-3427	0	81
-9635	-8750	-5807	-2380	107
-13985	-13100	-10157	-6730	156
-13985	-13100	-10157	-6730	156
-10715	-9830	-6887	-3460	119

BURIAL HISTORY

Mobil No. T–52–19G Mobil 19–2S–96W

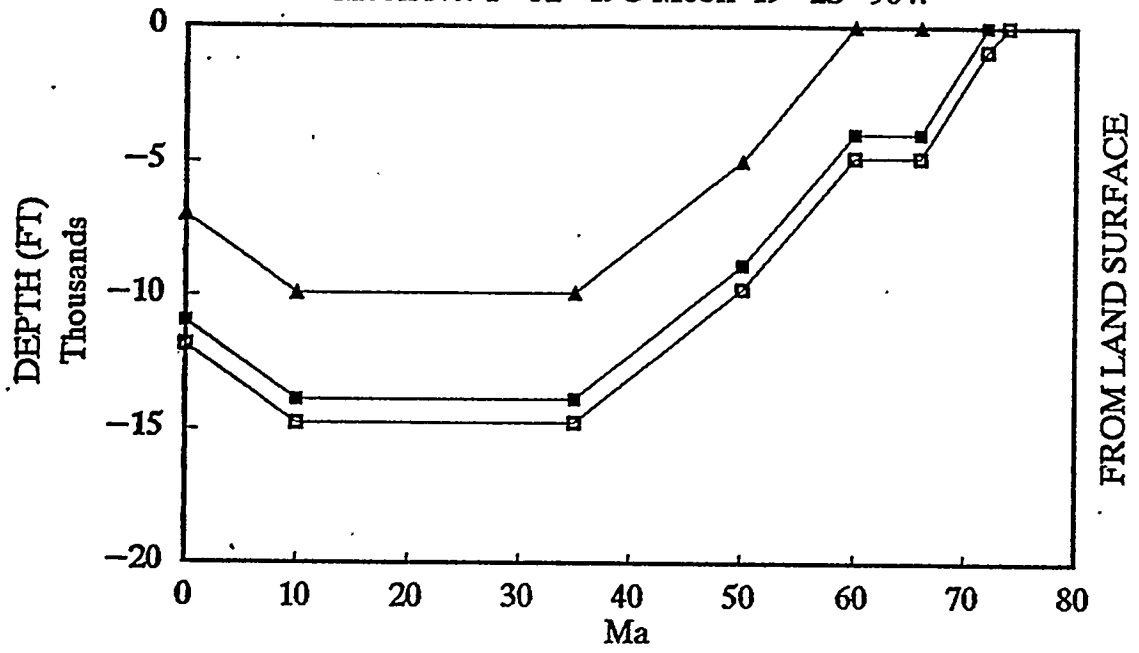

ROLLINS TOP

MESAVERDE TOP (?)

MESAVERDE BASE (MANCOS

TEMPERATURE HISTORY

Mobil No. T–52–19G Mobil 19–2S–96W

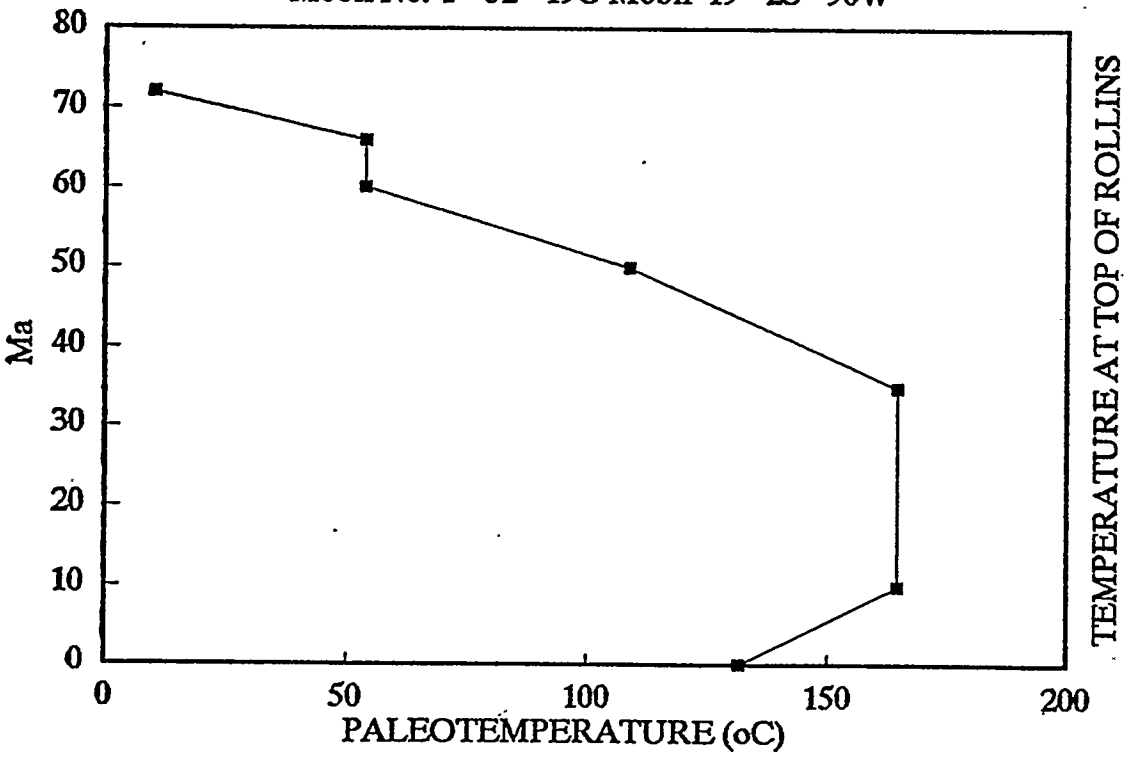

VITRINITE MATURATION

Mobil No. T–52–19G Mobil 19–2S–96W

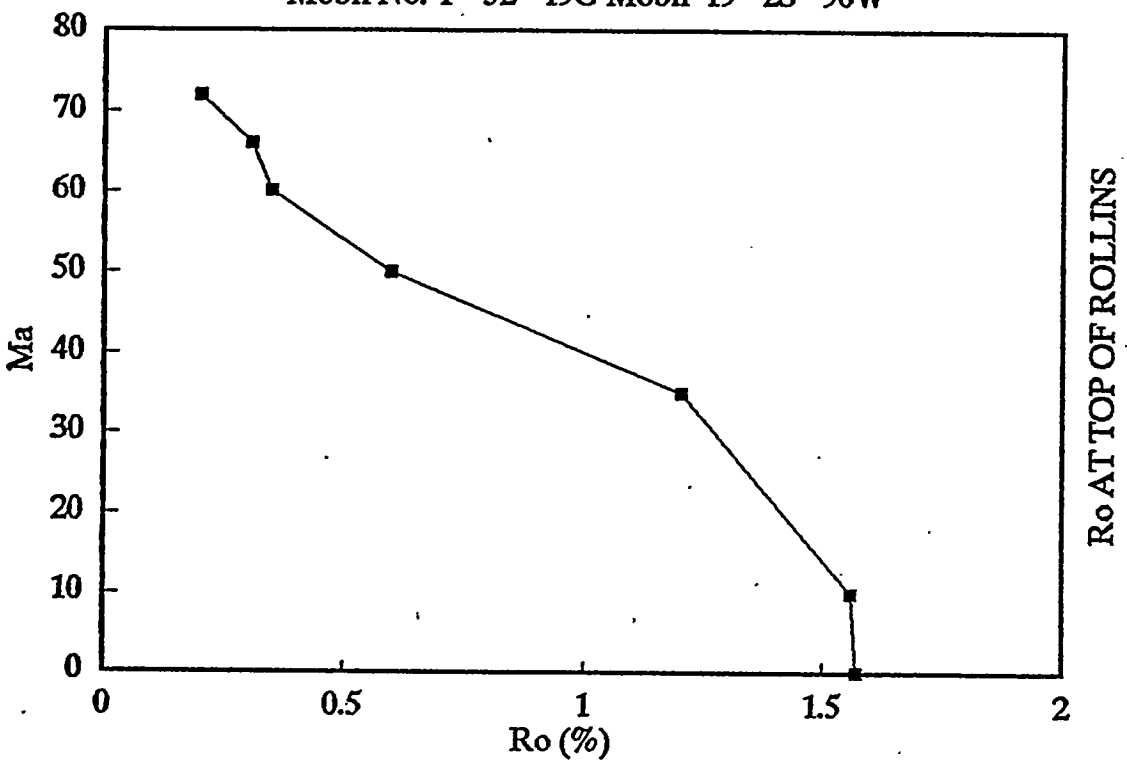

SUBSIDENCE HISTORY Johnson and Nuccio, 1986, Structural and Th
19-2S-96W SW,NW,NE Mobil No. T-52-19G Mobil

T GRADIENT (corr.)= 2.0 DEG F/1
DEG 0.0365 Before 30
0.0365 After 30 M

KB (elev. in ft.)= 6885

	ELEVATIONS			
Ma	MESAVERDE BASE	ROLLIN TO	MESAVERDE TOP	SEDIME SURFAC
74	1000			1000
72	115	1000		1000
66	-3435	-2550	1400	1400
60	-3435	-2550	1400	1400
50	-7385	-6500	-2550	2400
35	-10785	-9900	-5950	4000
10	-9585	-8700	-4750	5200
0	-4955	-4070	-120	6885

DEPTHS		TEMPERATURE	
MESAVERDE BASE	ROLLINS TOP	MESAVERDE TOP	ROLLINS TOP
0			
-885	0		10
-4835	-3950	0	54
-4835	-3950	0	54
-9785	-8900	-4950	109
-14785	-13900	-9950	165
-14785	-13900	-9950	165
-11840	-10955	-7005	132

BURIAL HISTORY

Ralston No. 31 Federal 31–10S–90W

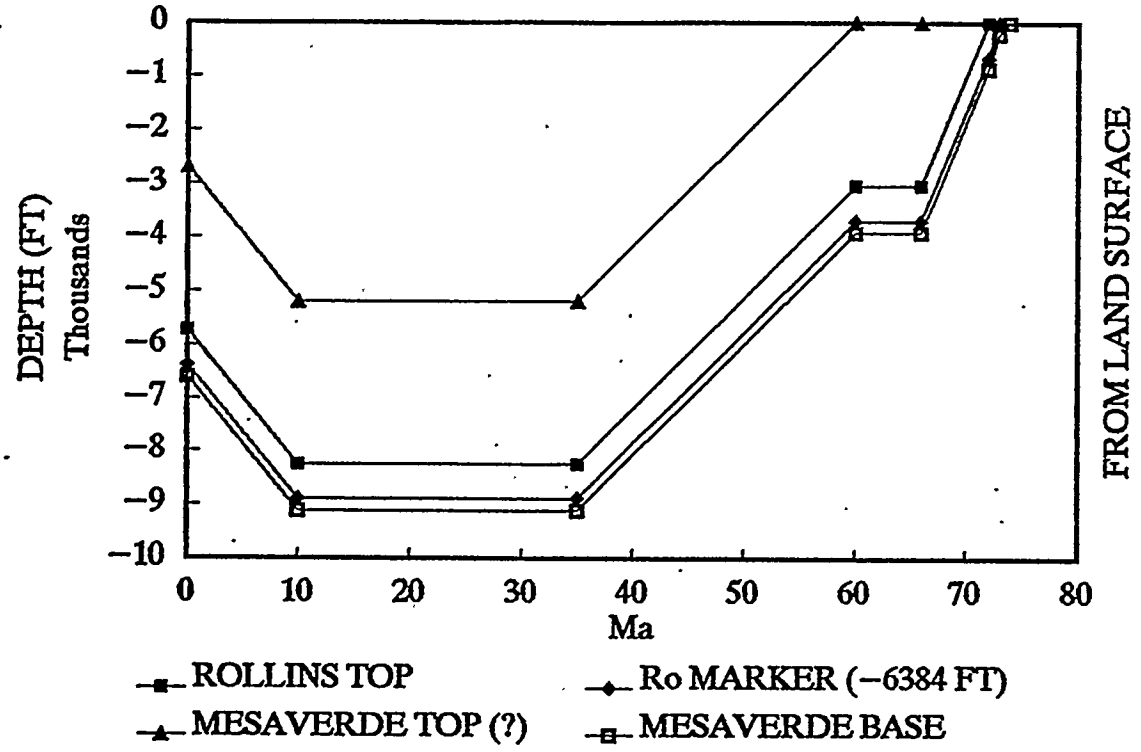

TEMPERATURE HISTORY

Ralston No. 31 Federal 31–10S–90W

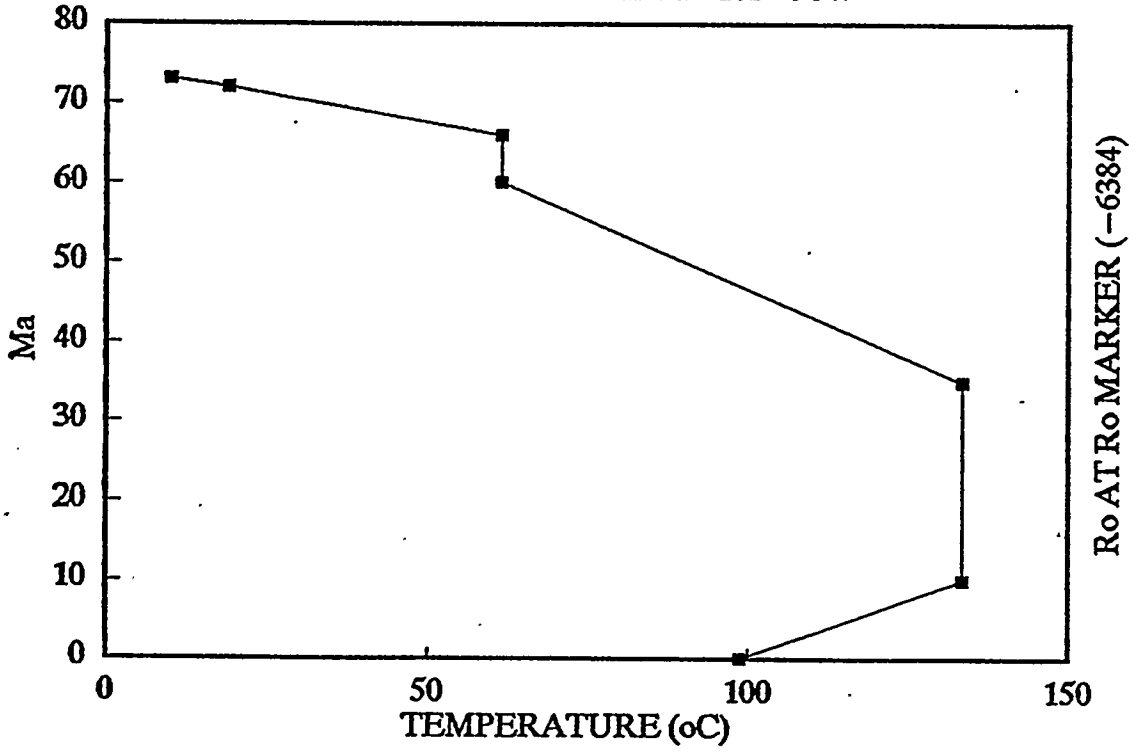

VITRINITE MATURATION

Ralston No. 31 Federal 31–10S–90W

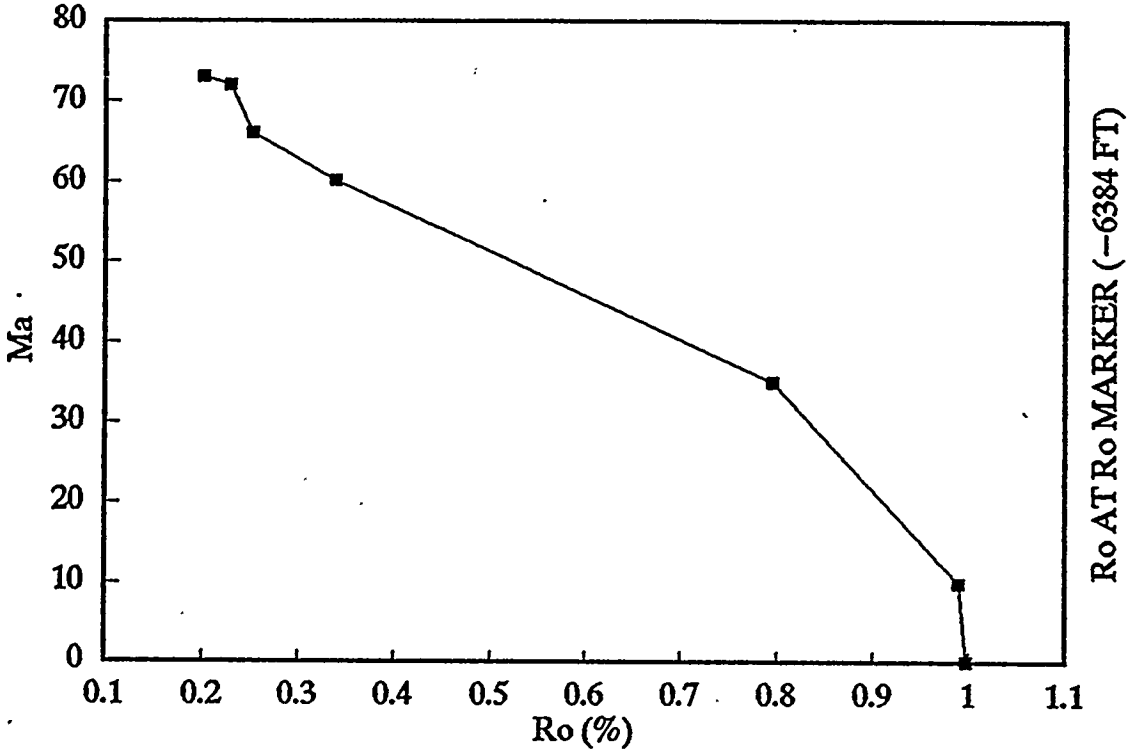

SUBSIDENCE HISTORY Johnson and Nuccio, 1986, Structural and Th
31-10S-90W Ralston Production Co. No. 31 Federal
T GRADIENT (corr.)= 2.5 DEG F/1
SIMRO8 0.0456 DEG C/
LOG TOPS KB (elev. in ft.)= 7901

	ELEVATIONS				
Ma	MESAVERDERo MARKER BASE		ROLLIN TO	MESAVERDE TOP	SEDIME SURFAC
74	1000				1000
73	784	1000			1000
72	134	350	1000		1000
66	-2516	-2300	-1651	1400	1400
60	-2516	-2300	-1651	1400	1400
35	-5116	-4900	-4251	-1200	4000
10	-3216	-3000	-2351	700	5900
0	1301	1517	2166	5217	7901

DEPTHS			TEMPERATURE	
MESAVERDERo MARKER BASE		ROLLINS TOP	MESAVERDERo TOP	MARKER
0				
-216	0			10
-866	-650	0		19
-3916	-3700	-3051	0	61
-3916	-3700	-3051	0	61
-9116	-8900	-8251	-5200	134
-9116	-8900	-8251	-5200	134
-6600	-6384	-5735	-2684	99

BURIAL HISTORY

Apache No. 1 Rushmore 5–9S–92W

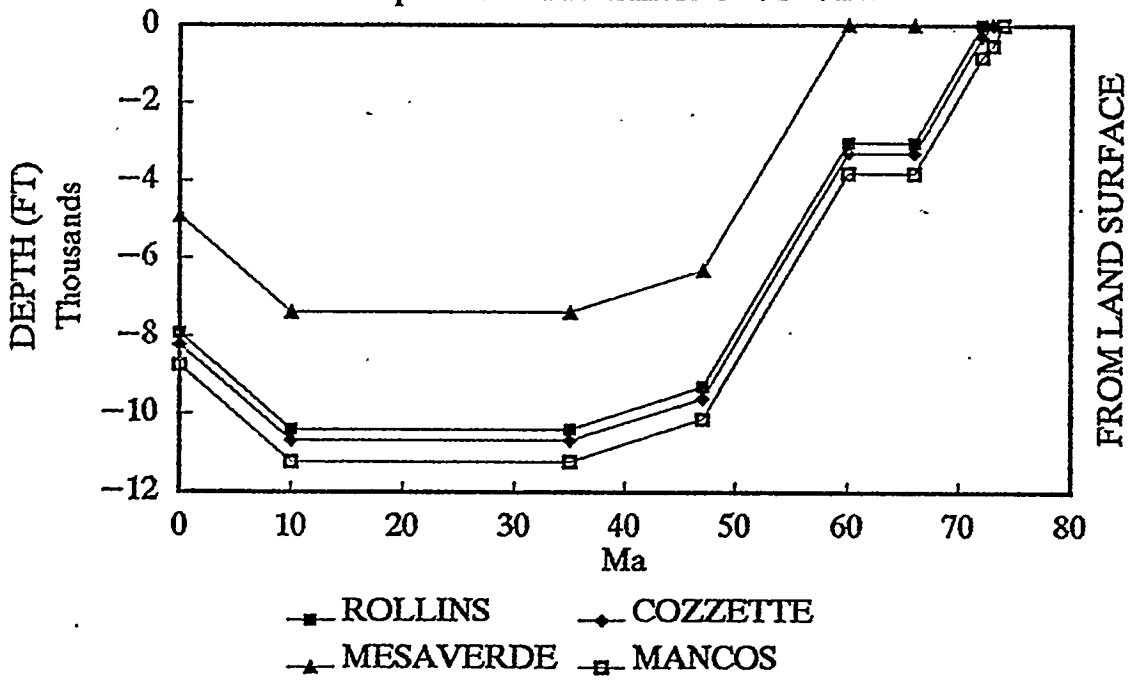

OPTION 2: HIGH PALEOGRADIENT, MODERATE BURIAL TOPS

TEMPERATURE HISTORY

Apache No. 1 Rushmore 5–9S–92W

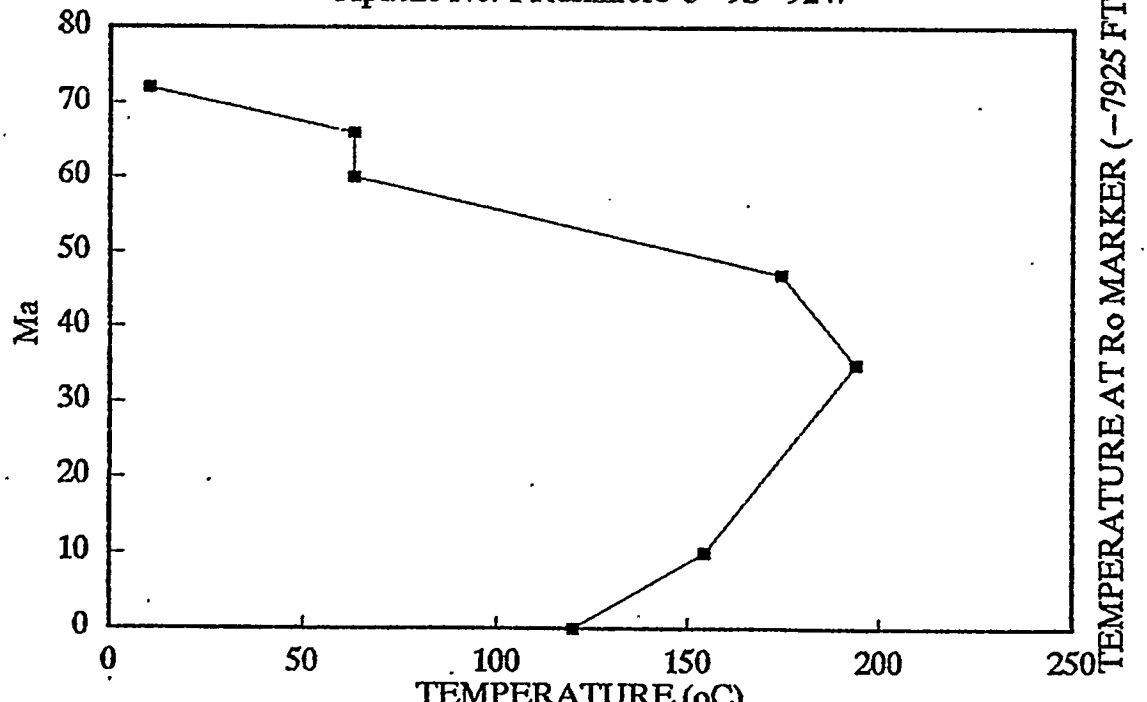

OPTION 2: HIGH PALEOGRADIENT (3.2 oF/100 FT)

VITRINITE MATURATION

Ralston No. 31 Federal 31–10S–90W

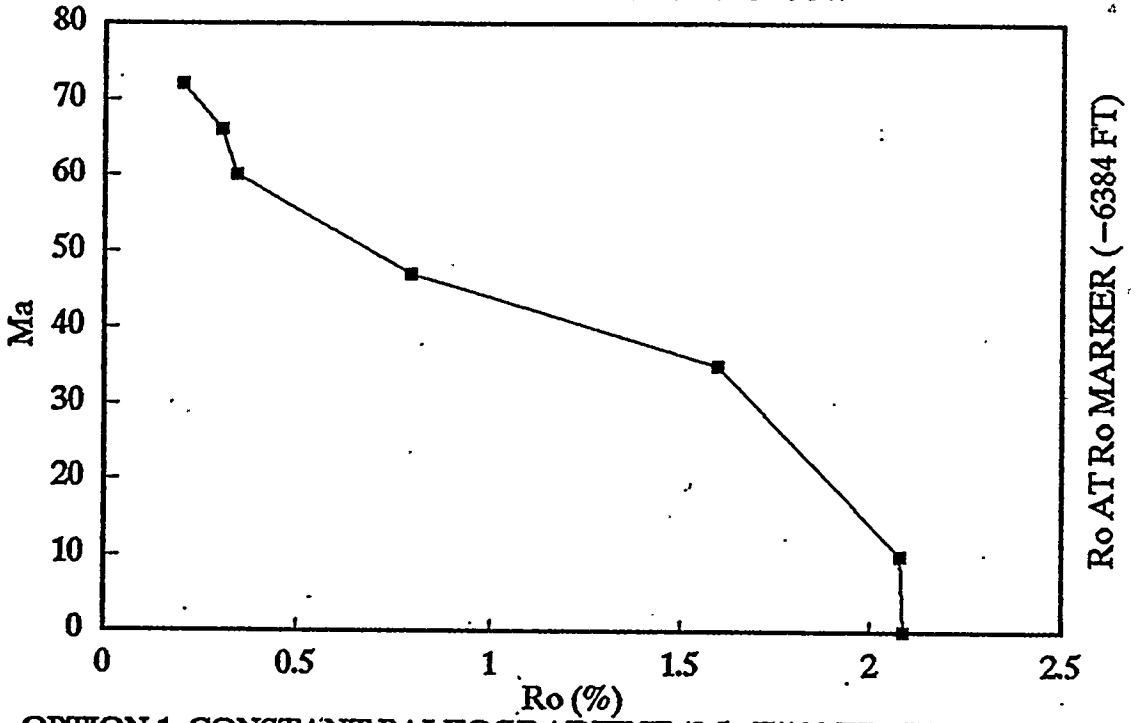

OPTION 1: CONSTANT PALEOGRADIENT (2.5 oF/100 FT), DEEP BURIAL

VITRINITE MATURATION

Ralston No. 31 Federal 31–10S–90W

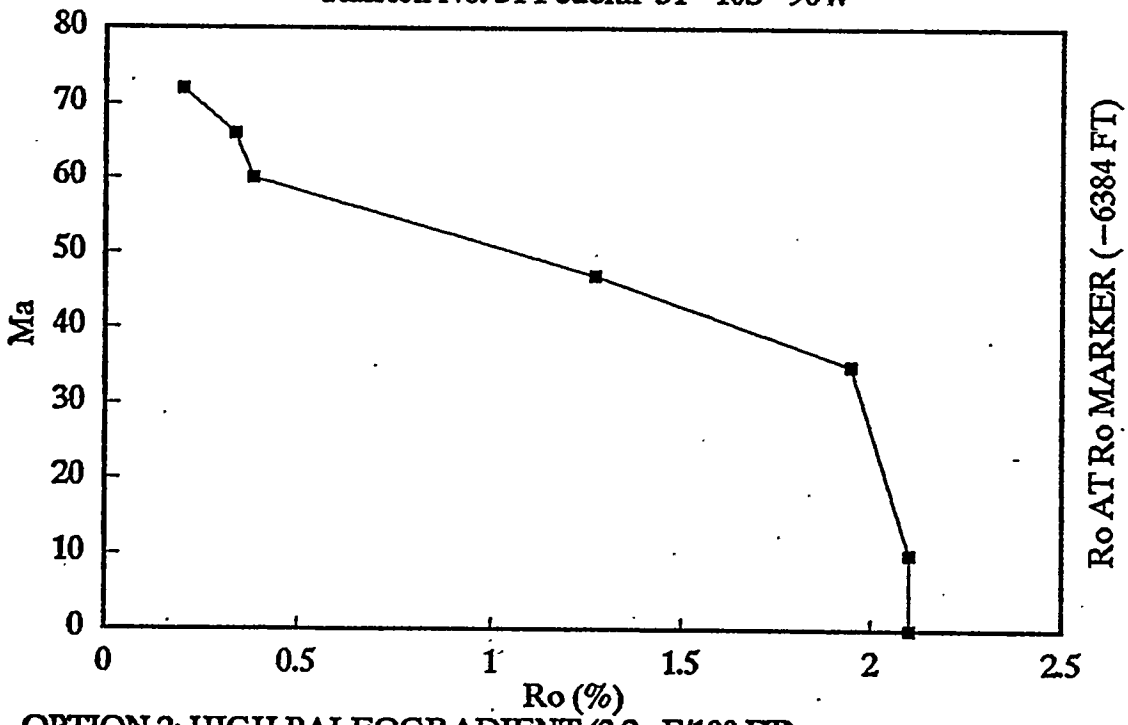

OPTION 2: HIGH PALEOGRADIENT (3.2 oF/100 FT)

SUBSIDENCE HISTORY Johnson and Nuccio, 1986, Structural and Th
5-9S-92W Apache Corp. No. 1-C U.S. Rushmore

	T GRADIENT (corr.)=	2.5
SIMRO9		0.0456
	KB (elev. in ft.)= ?	7745

ELEVATIONS

Ma	MESAVERDE BASE	COZZETTE TO	ROLLINS OPTION 1	ROLLINS OPTION 2	MESAVERDE TOP
74	1000				
73	465	1000			
72	175	710	1000	1000	
66	-2425	-1890	-1600	-1600	1400
60	-2425	-1890	-1600	-1600	1400
47	-7525	-6990	-6700	-6700	-3700
35	-7225	-6690	-8600	-6400	-3400
10	-5225	-4690	-6600	-4400	-1400
0	-1005	-470	-180	-180	2820

DEPTHS

SEDIME SURFAC	MESAVERDE BASE	COZZETTE TOP	ROLLINS OPTION 1	ROLLINS OPTION 2	MESAVERDE TOP
1000	0				
1000	-535	0			
1000	-825	-290	0	0	
1400	-3825	-3290	-3000	-3000	0
1400	-3825	-3290	-3000	-3000	0
2600	-10125	-9590	-9300	-9300	-6300
4000	-11225	-10690	-12600	-10400	-7400
6000	-11225	-10690	-12600	-10400	-7400
7745	-8750	-8215	-7925	-7925	-4925

TEMPERAT ROLLINS OPTION 1	TEMPERATURE ROLLINS OPTION 2
10	10
52	63
52	63
139	174
185	194
185	155
120	120

BURIAL HISTORY

Chorney No. 1–14 East Rangely 14–1N–100W

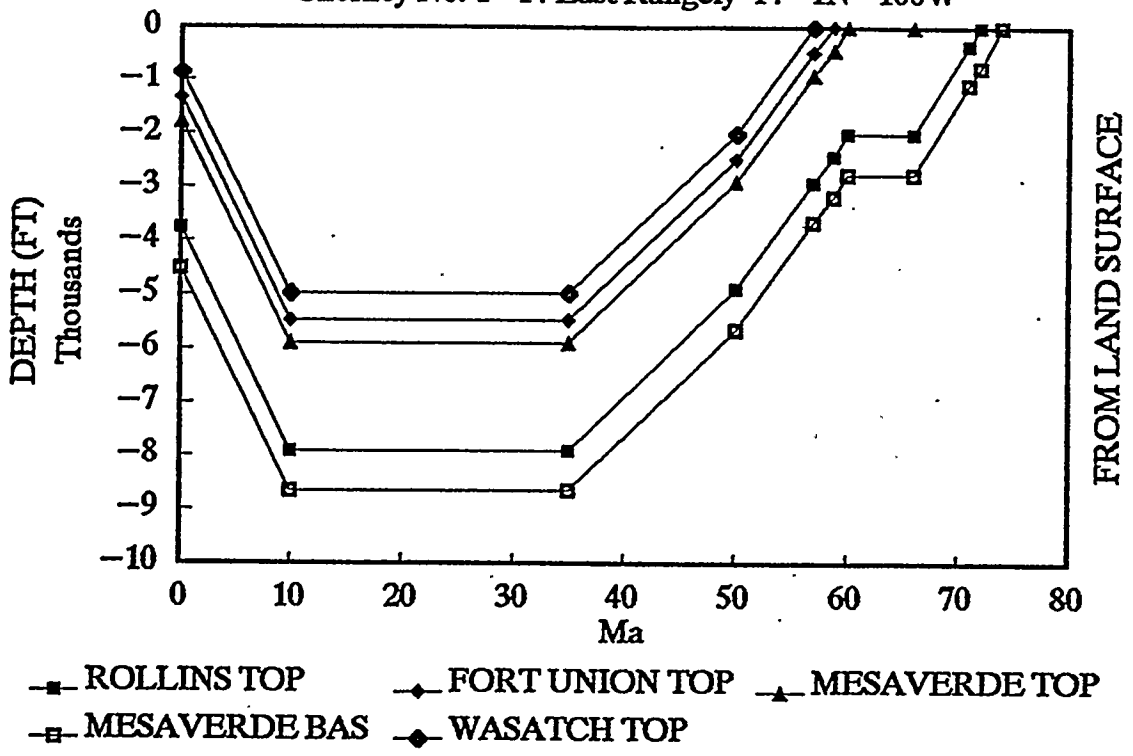

TEMPERATURE HISTORY

Chorney No. 1–14 East Rangely 14–1N–100W

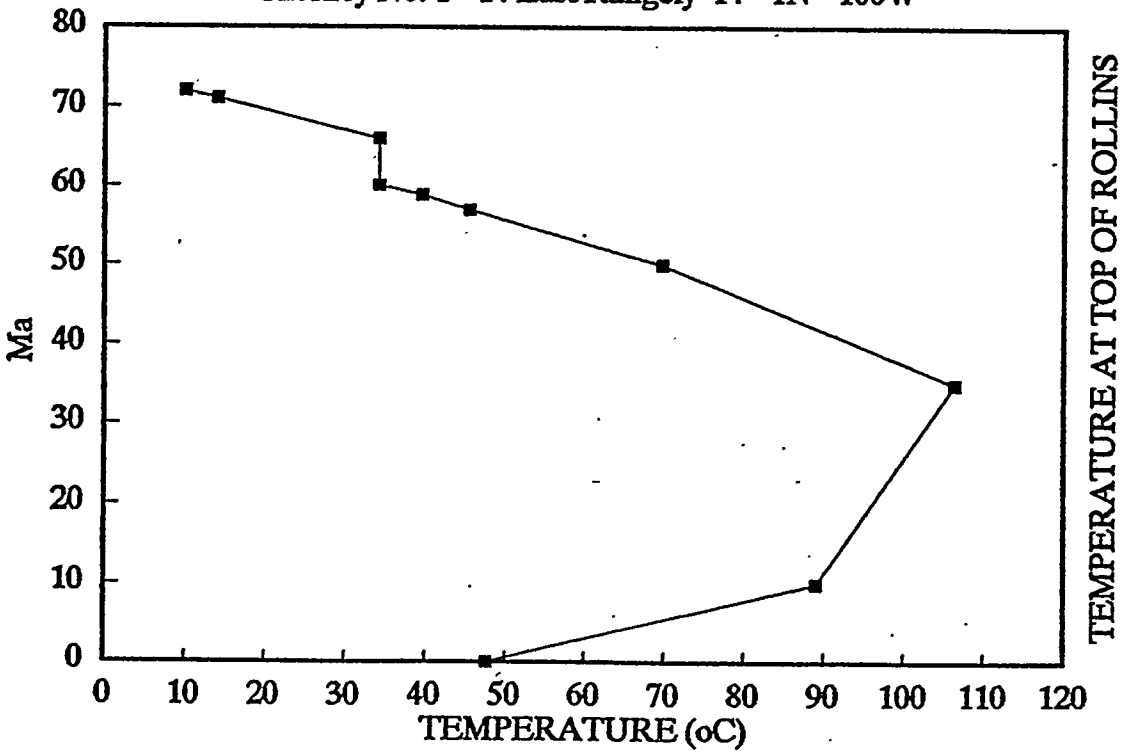

VITRINITE MATURATION

Chorney No. 1–14 East Rangely 14–1N–100W

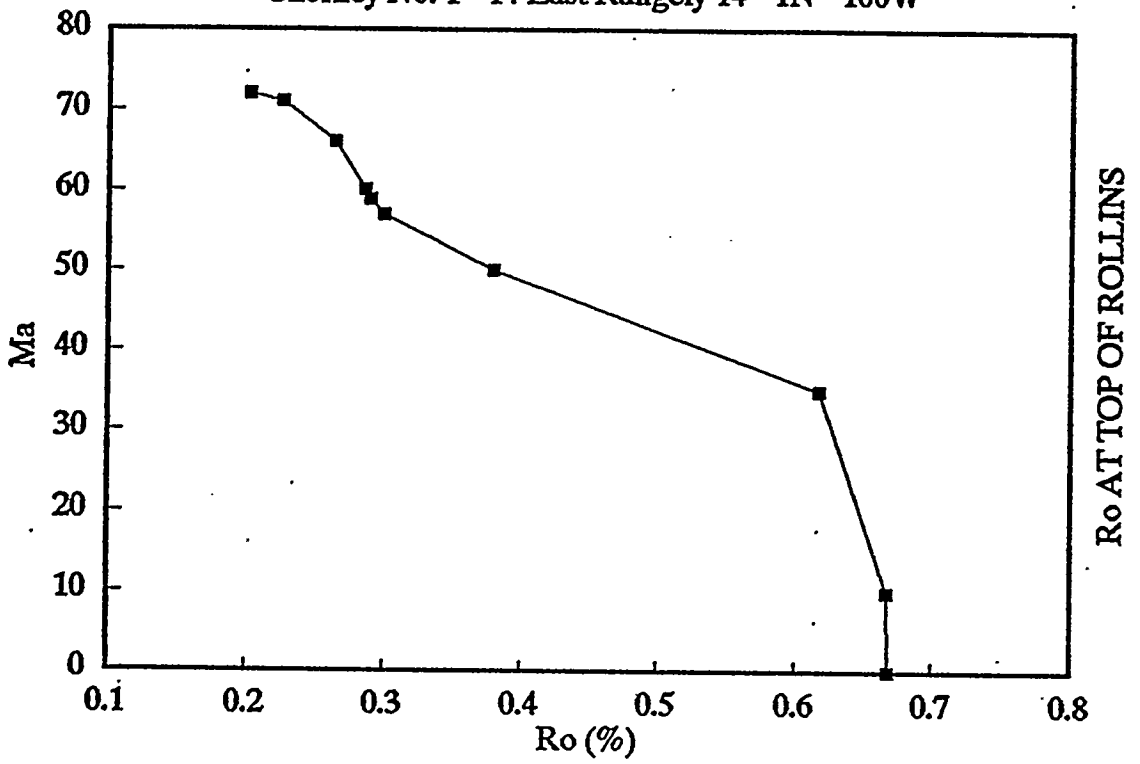

SUBSIDENCE HISTORY Johnson and Nuccio, 1986, Struct
14-1N-100W C,SE,SW Chorney No. 1-14 East Rangely
T GRADIENT (corr.)= 0.0400
oC/m 0.0328
LOG TOPS KB (elev. in ft.)= 6919

ELEVATIONS

Ma	MESAVERDE BASE	ROLLINR) TOP	MARKER	MESAVERDE TOP	FORT UNIO TOP
74	1000				
72	245	1000			
71	-88	667	1000		
66	-1355	-600	-595	1400	
60	-1355	-600	-595	1400	
58.8	-1583	-828	-823	1172	1600
57	-1870	-1115	-1110	885	1313
50	-3262	-2507	-2502	-507	-79
35	-4661	-3906	-3901	-1906	-1478
10	-3161	-2406	-2401	-406	22
0	2394	3149	3154	5149	5577

DEPTHS

WASATCH TOP	SEDIME SURFAC	MESAVERDE BASE	ROLLINSRo TOP	MARKER	MESAVERDE TOP
	1000	0			
	1000	-755	0		
	1000	-1088	-333	0	
	1400	-2755	-2000	-1995	0
	1400	-2755	-2000	-1995	0
	1600	-3183	-2428	-2423	-428
1800	1800	-3670	-2915	-2910	-915
408	2400	-5662	-4907	-4902	-2907
-991	4000	-8661	-7906	-7901	-5906
509	5500	-8661	-7906	-7901	-5906
6064	6919	-4525	-3770	-3765	-1770

TEMPERAT TEMPERATURE

FORT UNIO TOP	WASATCH TOP	ROLLINRo TOP	MARKER	
		10		
		14	20	
		34	40	
		34	40	
0		40	44	
-487	0	46	49	
-2479	-1992	70	69	
-5478	-4991	106	99	262
-5478	-4991	89	99	
-1342	-855	48	58	

BURIAL HISTORY

Snyder No. 1–16 Barton Porter 16–6S–90W

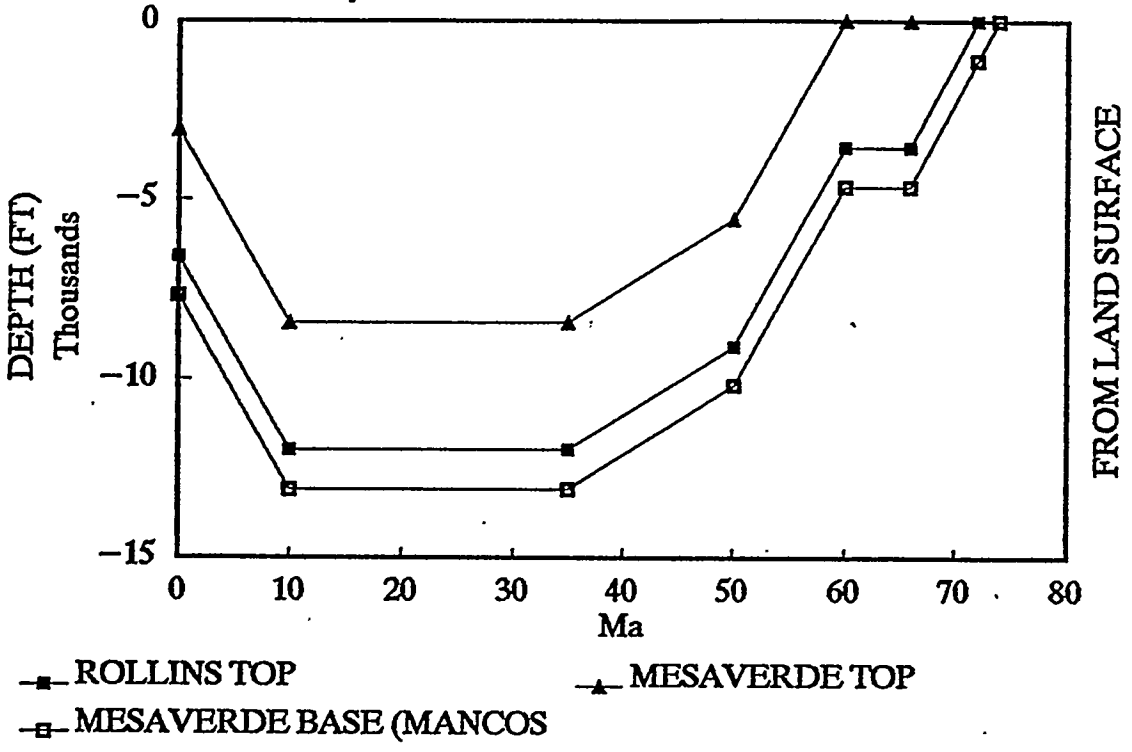

TEMPERATURE HISTORY

Snyder No. 1–16 Barton Porter 16–6S–90W

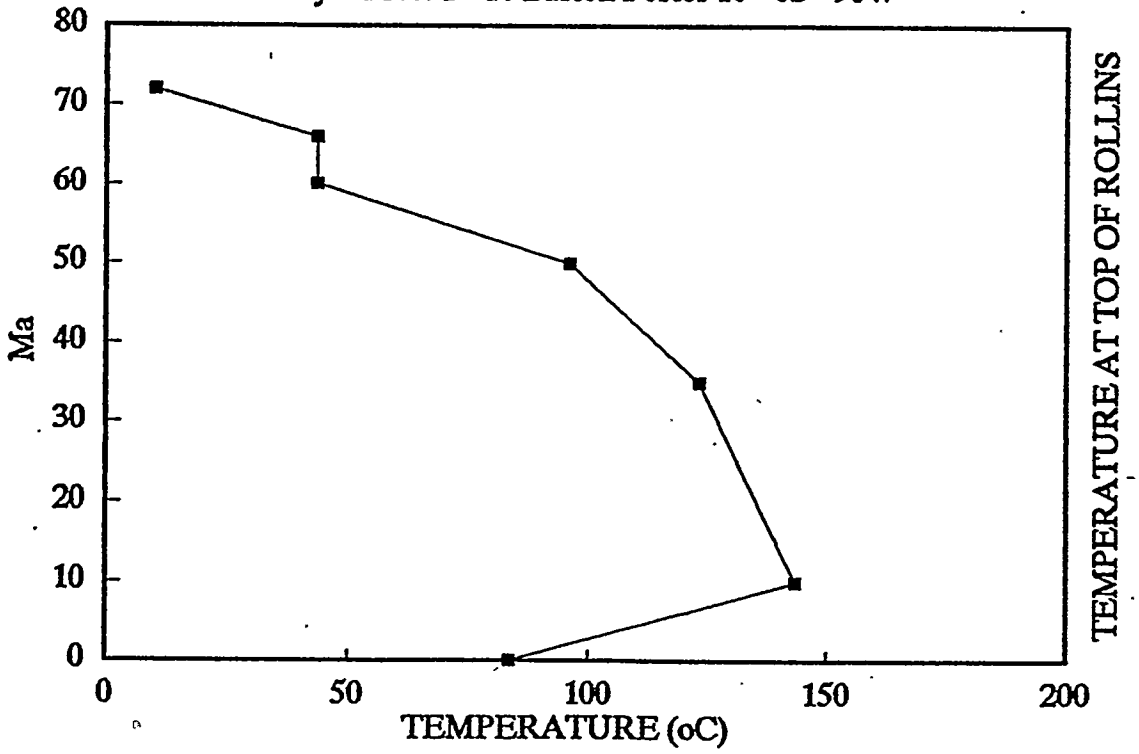

VITRINITE MATURATION

Snyder No.1–16 Barton Porter 16–6S–90W

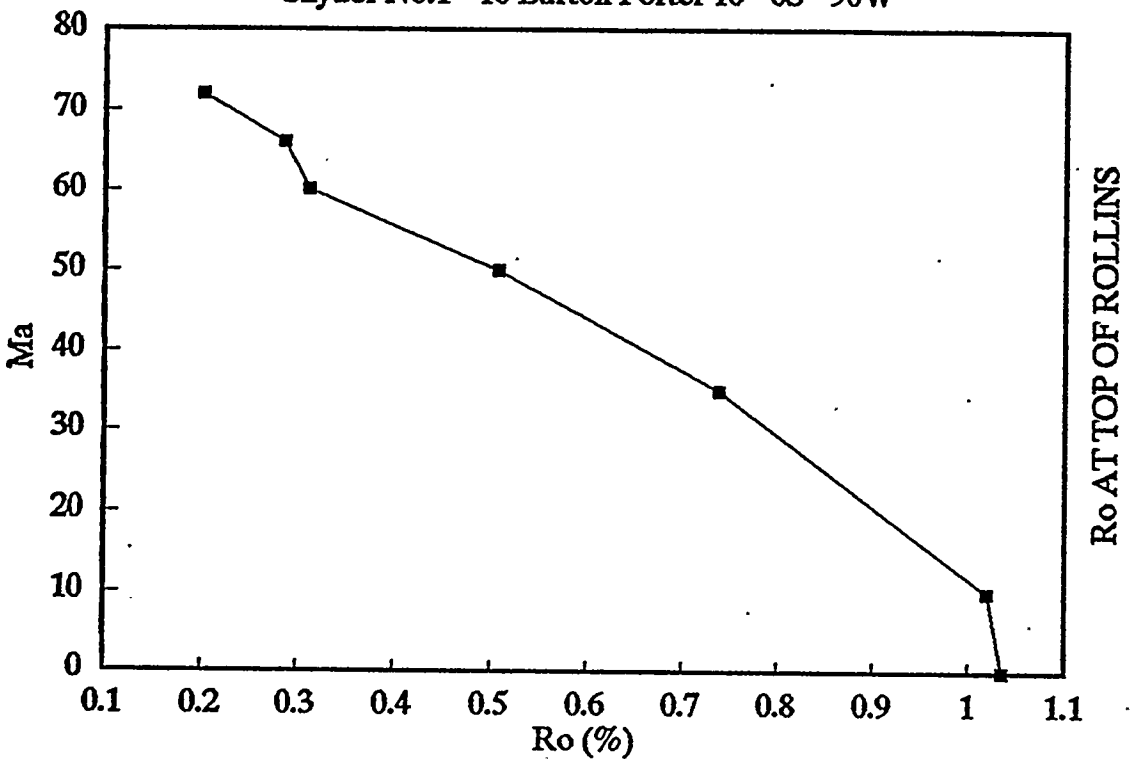

SUBSIDENCE HISTORY Johnson and Nuccio, 1986, Structural and Th
16-6S-90W C,SE,SW Snyder No. 1-16 Barton Porter
T GRADIENT (corr.)= 1 DEG F/1
DEG 0.0310 Before 30
0.0365 After 30 M
LOG TOPS KB (elev. in ft.)= 6935

	ELEVATIONS			
Ma	MESAVERDE BASE	ROLLIN TO	MESAVERDE TOP	SEDIME SURFAC
74	1000			1000
72	-96	1000		1000
66	-3246	-2150	1400	1400
60	-3246	-2150	1400	1400
50	-7796	-6700	-3150	2400
35	-9096	-8000	-4450	4000
10	-7596	-6500	-2950	5500
0	-761	335	3885	6935

DEPTHS		TEMPERATURE	
MESAVERDE BASE	ROLLINS TOP	MESAVERDE TOP	ROLLINS TOP
0			
-1096	0		10
-4646	-3550	0	44
-4646	-3550	0	44
-10196	-9100	-5550	96
-13096	-12000	-8450	123
-13096	-12000	-8450	144
-7696	-6600	-3050	83

BURIAL HISTORY

Tipperary No. 1–30 F Bear Gultch Unit

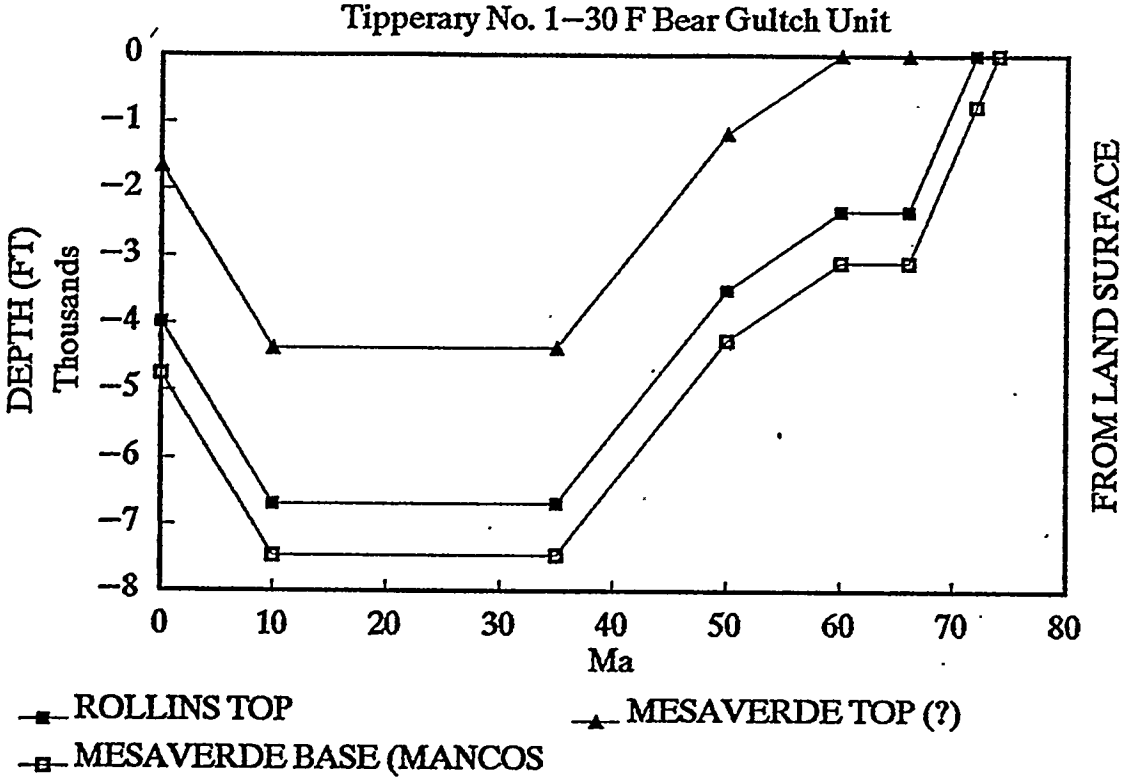

TEMPERATURE HISTORY

Tipperary No. 1–30 F Bear Gultch Unit

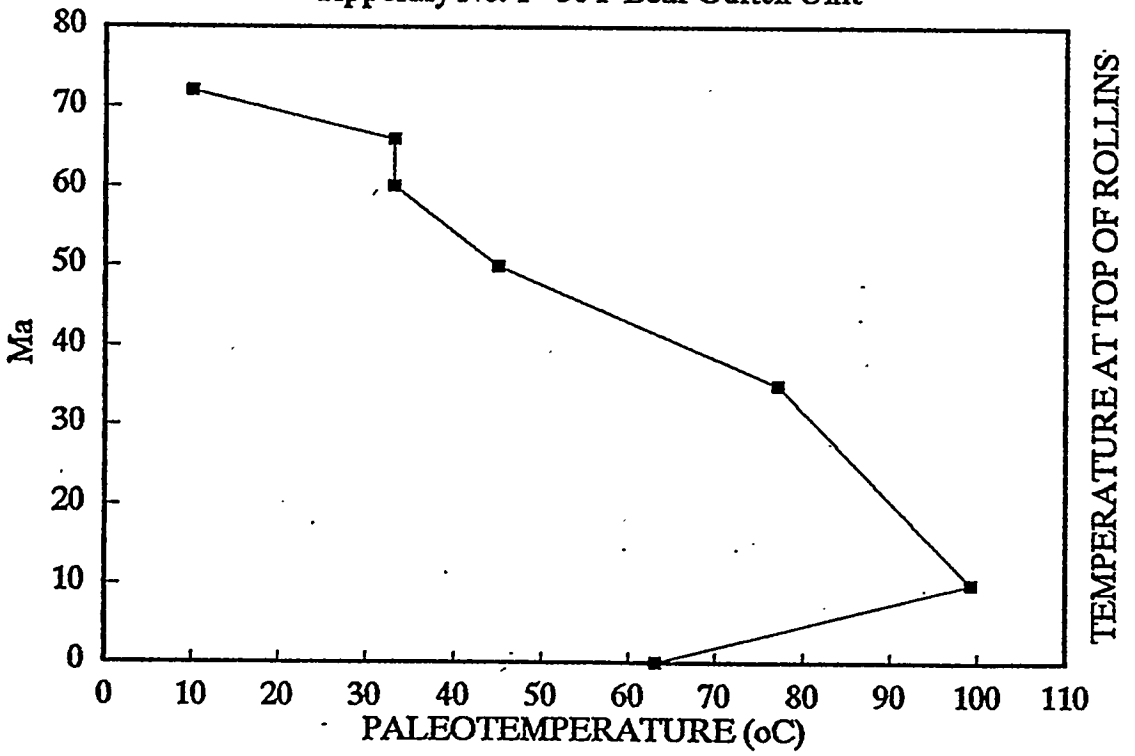

VITRINITE MATURATION

Tipperary No. 1–30 F Bear Gultch Unit

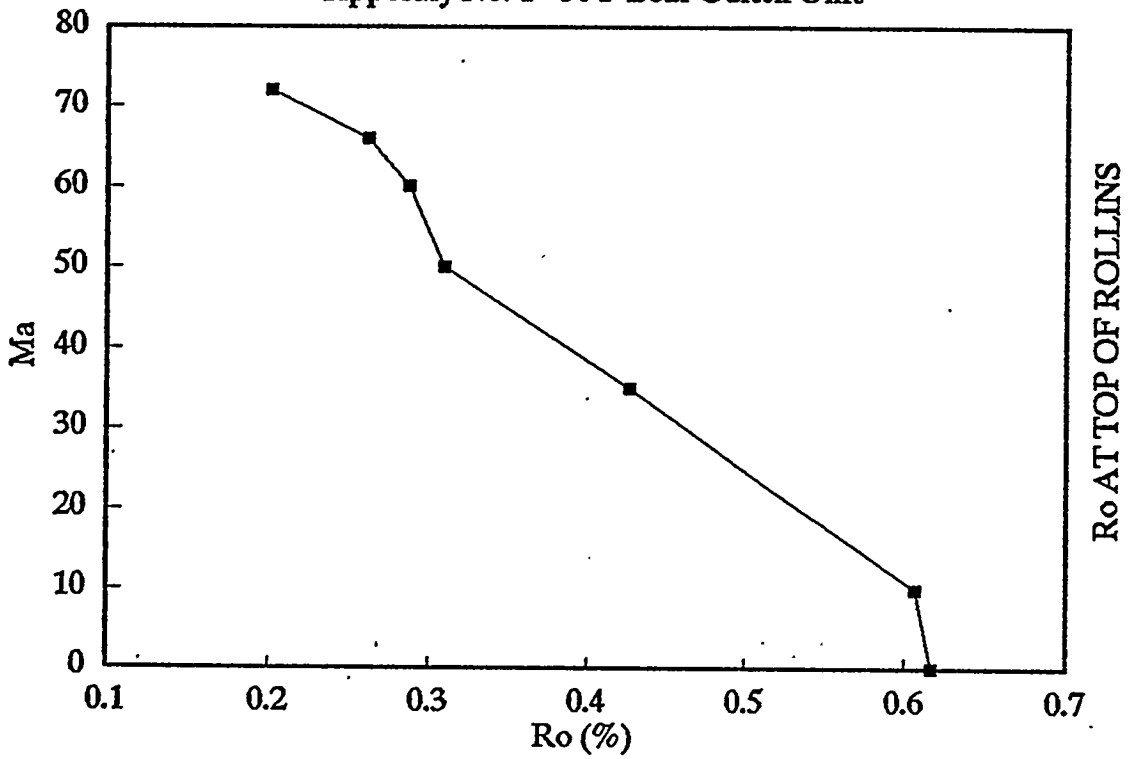

SUBSIDENCE HISTORY Johnson and Nuccio, 1986, Structural and Th
30-5S-100W NE,NW,SW Tipperary No. 1-30 Bear Gulch Unit (now Am
T GRADIENT (corr.)= 1.8 DEG F/1
DEG 0.0328 Before 30
0.0437 After 30 M

SCOUT TICKET TOPS KB (elev. in ft.)= 8884

	ELEVATIONS			
Ma	MESAVERDE BASE	ROLLIN TO	MESAVERDE TOP	SEDIME SURFAC
74	1000			1000
72	238	1000		1000
66	-1683	-921	1400	1400
60	-1683	-921	1400	1400
50	-1862	-1100	1221	2400
35	-3462	-2700	-379	4000
10	-1462	-700	1621	6000
0	4124	4886	7207	8874

DEPTHS		TEMPERATURE	
MESAVERDE BASE	ROLLINS TOP	MESAVERDE TOP	ROLLINS TOP
0			
-762	0		10
-3083	-2321	0	33
-3083	-2321	0	33
-4262	-3500	-1179	45
-7462	-6700	-4379	77
-7462	-6700	-4379	99
-4750	-3988	-1667	63

BURIAL HISTORY

Munson No. 36–1–100 36–1S–100W

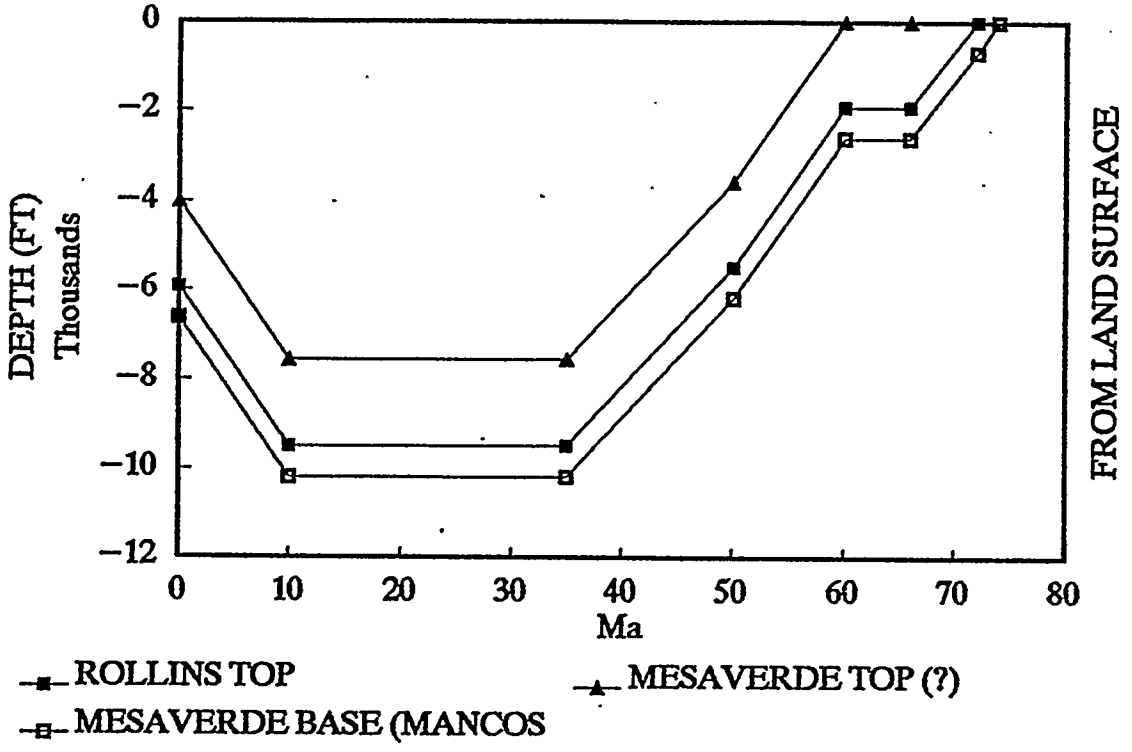

TEMPERATURE HISTORY

Munson No. 36–1–100 36–1S–100W

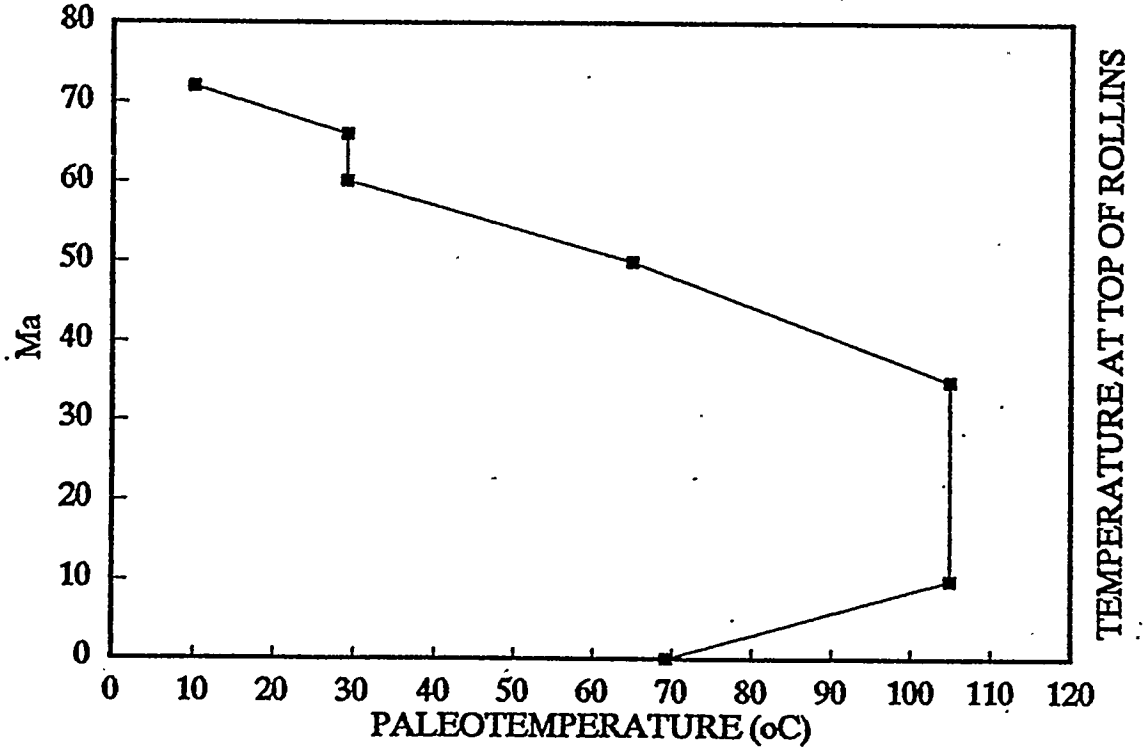

VITRINITE MATURATION

Munson No. 36–1–100 36–1S–100W

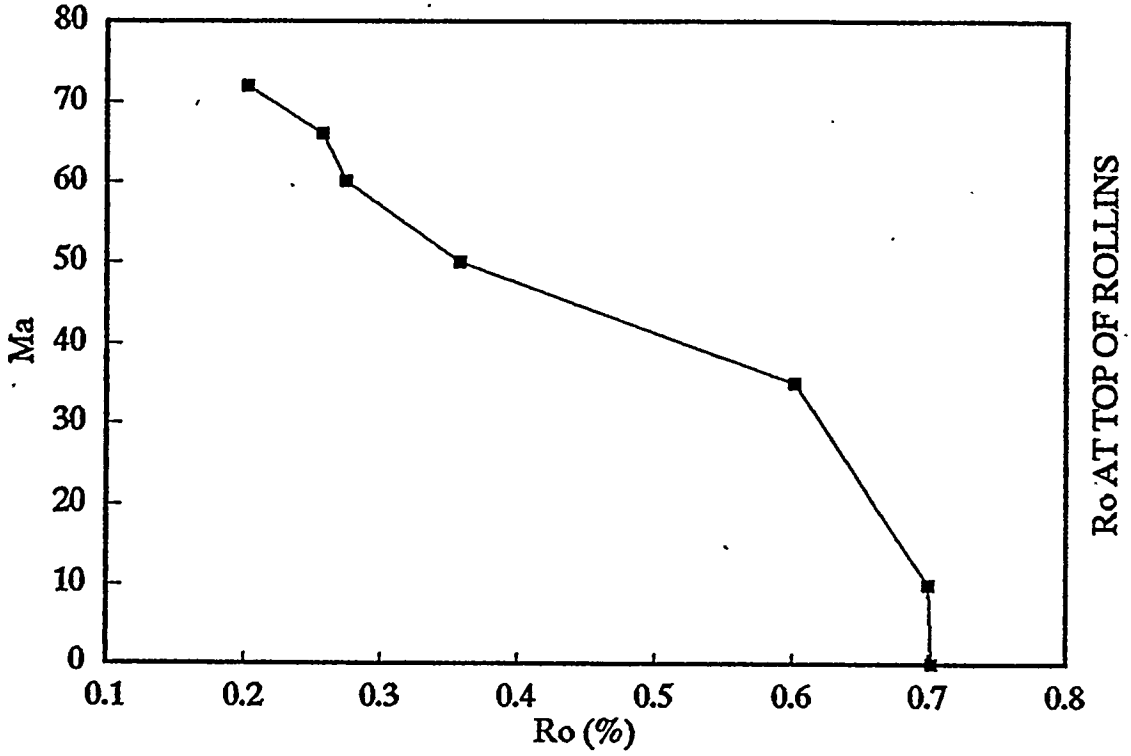

SUBSIDENCE HISTORY Johnson and Nuccio, 1986, Structural and Th
36-1S-100W NE,NE Munson No. 36-1-100
T GRADIENT (corr.)= 1.8 DEG F/1
DEG 0.0328 Before 30
0.0328 After 30 M
LOG TOPS KB (elev. in ft.)= 7853

	ELEVATIONS			
Ma	MESAVERDE BASE	ROLLIN TO	MESAVERDE TOP	SEDIME SURFAC
74	1000			1000
72	306	1000		1000
66	-1220	-526	1400	1400
60	-1220	-526	1400	1400
50	-3794	-3100	-1174	2400
35	-6194	-5500	-3574	4000
10	-4194	-3500	-1574	6000
0	1233	1927	3853	7853

DEPTHS		TEMPERATURE	
MESAVERDE BASE	ROLLINS TOP	MESAVERDE TOP	ROLLINS TOP
0			
-694	0		10
-2620	-1926	0	29
-2620	-1926	0	29
-6194	-5500	-3574	65
-10194	-9500	-7574	105
-10194	-9500	-7574	105
-6620	-5926	-4000	69

BURIAL HISTORY

El Paso No. 1 Standard Shale 6–7S–99W

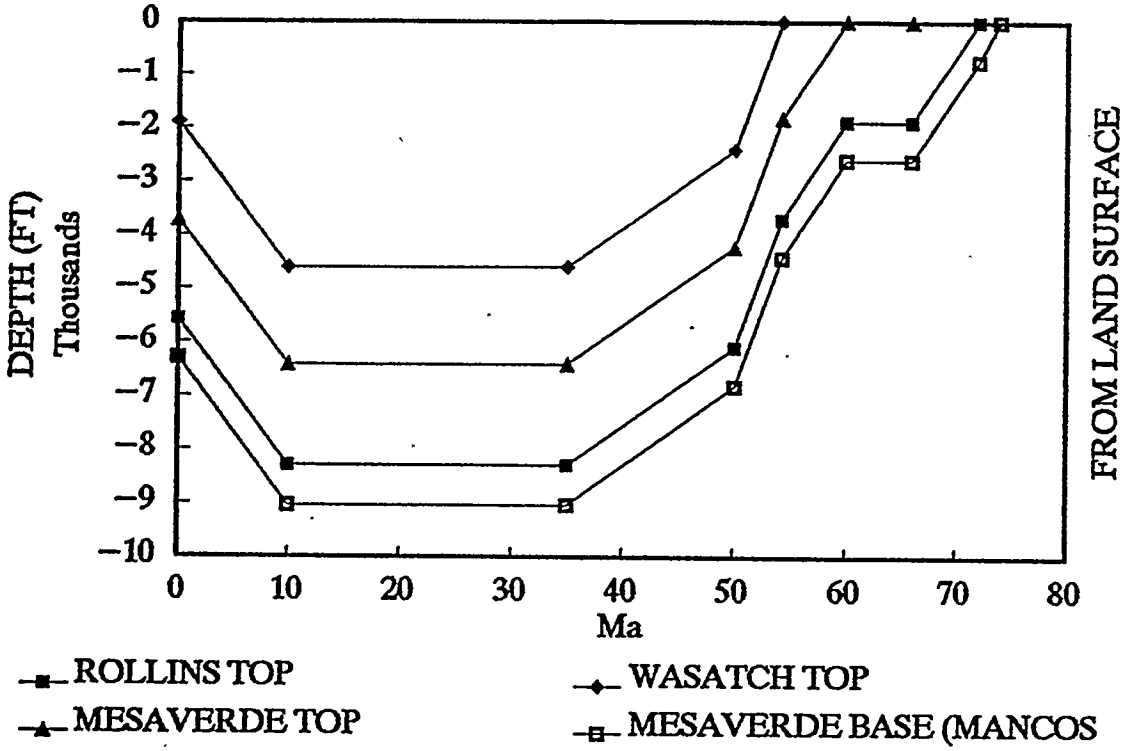

TEMPERATURE HISTORY

El Paso No. 1 Standard Shale 6–7S–99W

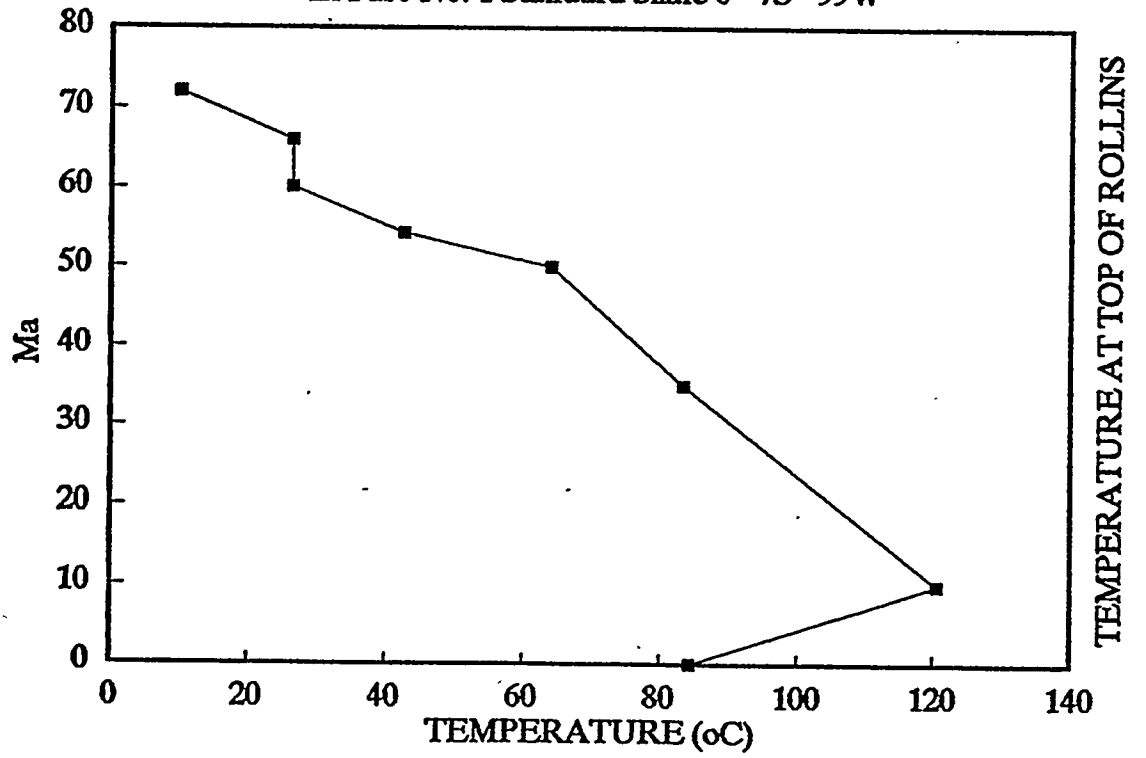

VITRINITE MATURATION

Snyder No.1–16 Barton Porter 16–6S–90W

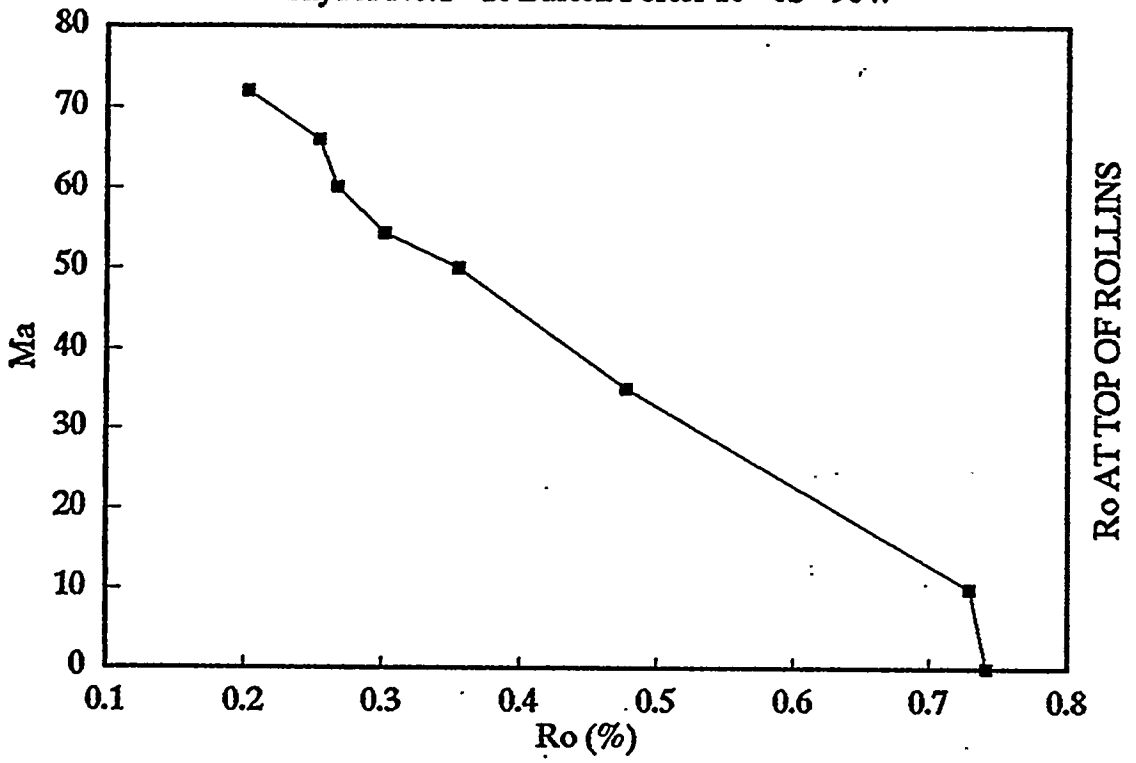

SUBSIDENCE HISTORY Johnson and Nuccio, 1986, Structural and Th
6-7S-99W NE,NE El Paso No. 1 Standard Shale
T GRADIENT (corr.)= 1
DEG C/m= 0.0290
0.0437
LOG TOPS KB (elev. in ft.)= 8256

ELEVATIONS

Ma	MESAVERDE BASE	ROLLIN TO	MESAVERDE TOP	WASATCH TOP	SEDIME SURFAC
74	1000				1000
72	268	1000			1000
66	-1202	-470	1400		1400
60	-1202	-470	1400		1400
54.3	-2427	-1695	175	2000	2000
50	-4432	-3700	-1830	-5	2400
35	-5032	-4300	-2430	-605	4000
10	-2832	-2100	-230	1595	6200
0	1939	2671	4541	6366	8256

DEPTHS

MESAVERDE BASE	ROLLINS TOP	MESAVERDE TOP	WASATCH TOP
0			
-732	0		
-2602	-1870	0	
-2602	-1870	0	
-4427	-3695	-1825	0
-6832	-6100	-4230	-2405
-9032	-8300	-6430	-4605
-9032	-8300	-6430	-4605
-6317	-5585	-3715	-1890

TEMPERATURE

ROLLINS TOP
10
27
27
43
64
83
121
84

BURIAL HISTORY

CSG No. 298–29–2 Rio Blanco 29–2S–98W

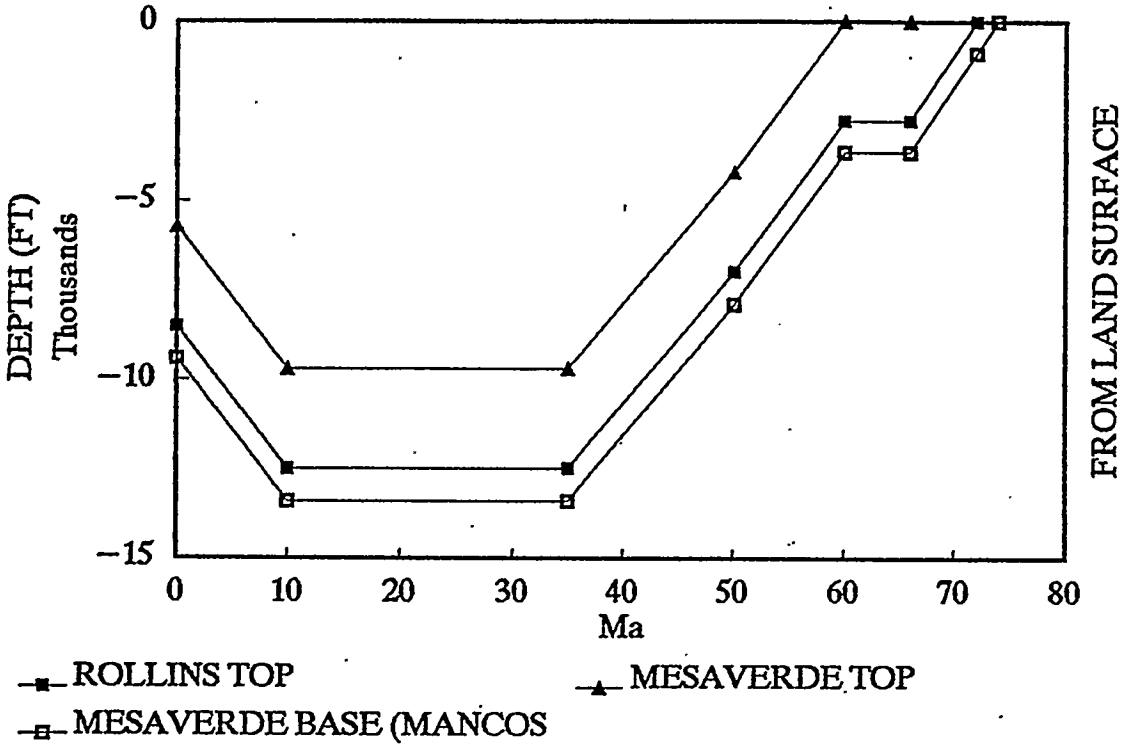

TEMPERATURE HISTORY

CSG No. 298–29–2 29–2S–98W

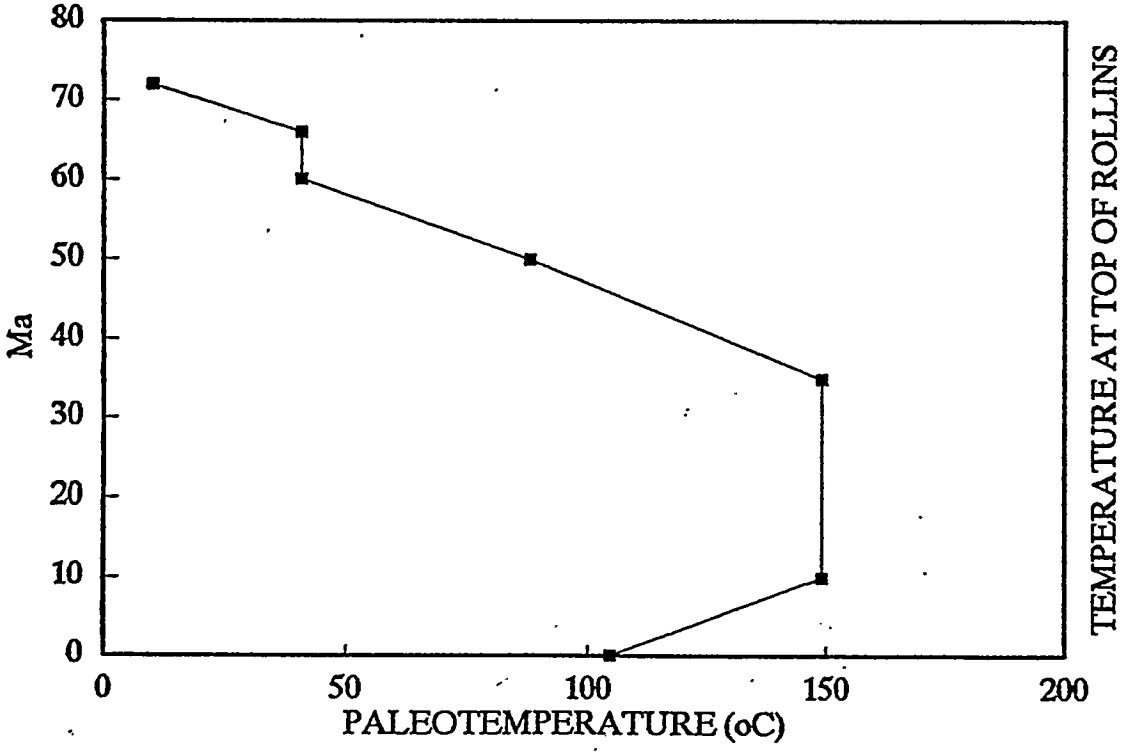

VITRINITE MATURATION

CSG No. 298–29–2 29–2S–98W

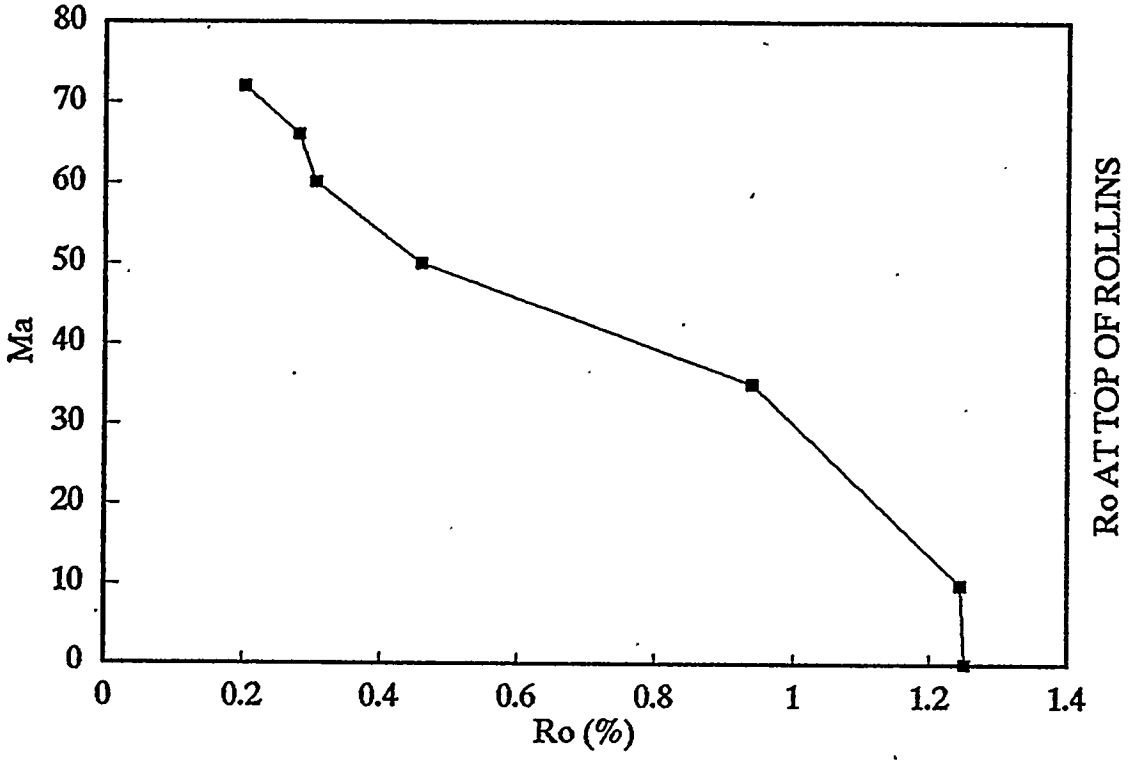

SUBSIDENCE HISTORY Johnson and Nuccio, 1986, Structural and Th
29-2S-98W SE,NW CSG No. 298-29-2
T GRADIENT (corr.)= 2.0 DEG F/1
DEG 0.0365 Before 30
0.0365 After 30 M
LOG TOPS KB (elev. in ft.)= 7055.46

Ma	MESAVERDE BASE	ROLLIN TO	MESAVERDE TOP	SEDIME SURFAC
		ELEVATIONS		
74	1000			1000
72	115	1000		1000
66	-2271	-1386	1400	1400
60	-2271	-1386	1400	1400
50	-5485	-4600	-1814	2400
35	-9385	-8500	-5714	4000
10	-7885	-7000	-4214	5500
0	-2341	-1456	1330	7055

MESAVERDE BASE	ROLLINS TOP	MESAVERDE TOP	ROLLINS TOP
DEPTHS		TEMPERATURE	
0			
-885	0		10
-3671	-2786	0	41
-3671	-2786	0	41
-7885	-7000	-4214	88
-13385	-12500	-9714	149
-13385	-12500	-9714	149
-9396	-8511	-5725	105

BURIAL HISTORY

Exxon No. C–1 Kenny Creek 9–11S–93W

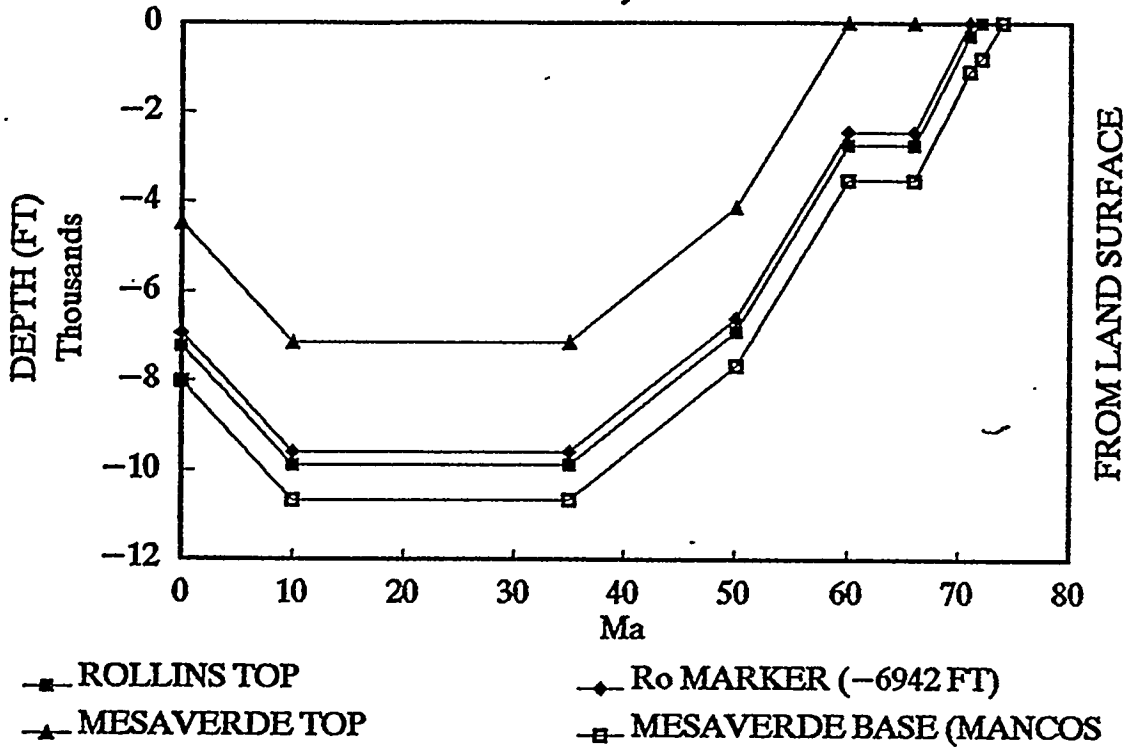

TEMPERATURE HISTORY

Exxon No. C–1 Kenny Creek 9–11S–93W

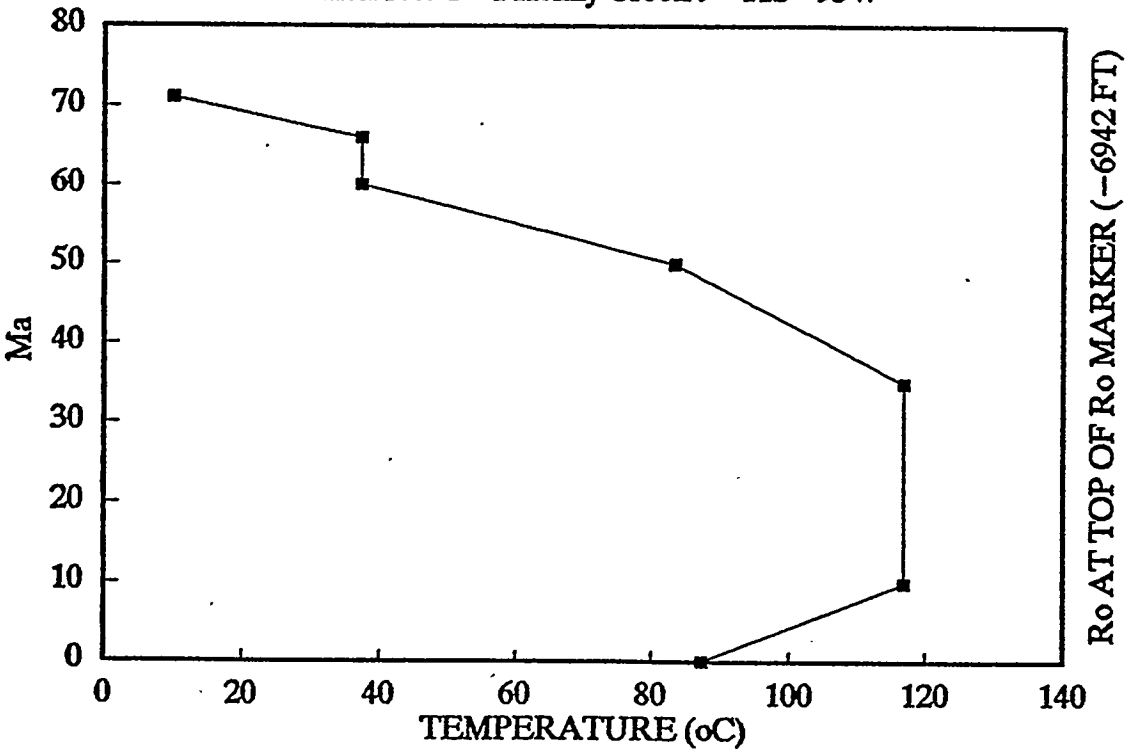

VITRINITE MATURATION

Exxon No. C–1 Kenny Creek 9–11S–93W

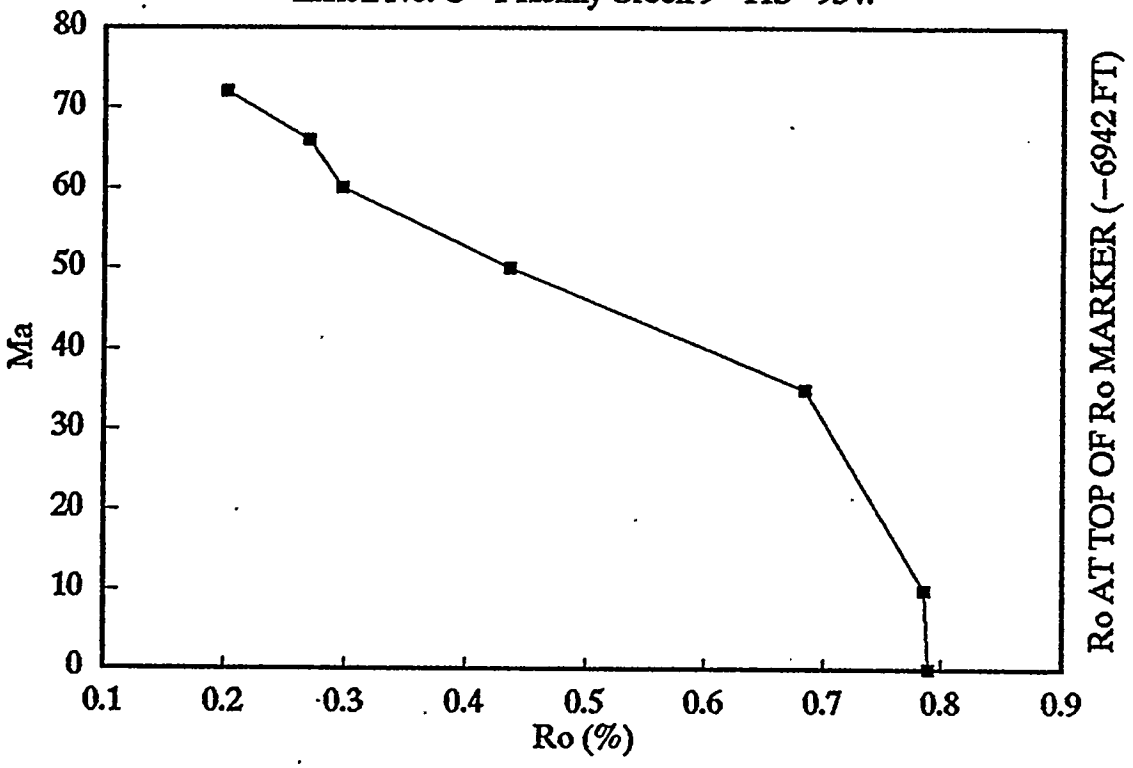

SUBSIDENCE HISTORY Johnson and Nuccio, 1986, Structural and Th
9-11S-93W NW,NE Exxon No. C-1 Kenny Creek

T GRADIENT (corr.)=		2.0
	DEG C/m=	0.0365
		0.0365
LOG TOPS	KB (elev. in ft.)=	9578

	ELEVATIONS				
Ma	MESAVERDE BASE	ROLLINRo TOP	MARKER	MESAVERDE TOP	SEDIME SURFAC
74	1000				1000
72	215	1000			1000
71	-73	712	1000		1000
66	-2133	-1348	-1060	1400	1400
60	-2133	-1348	-1060	1400	1400
50	-5273	-4488	-4200	-1740	2400
35	-6673	-5888	-5600	-3140	4000
10	-4173	-3388	-3100	-640	6500
0	1563	2348	2636	5096	9578

	DEPTHS			TEMPERATURE	
MESAVERDE BASE	ROLLINSRo TOP	MARKER	MESAVERDE TOP	ROLLINS TOP	
0					
-785	0				
-1073	-288	0		10	
-3533	-2748	-2460	0	37	
-3533	-2748	-2460	0	37	
-7673	-6888	-6600	-4140	83	
-10673	-9888	-9600	-7140	117	
-10673	-9888	-9600	-7140	117	
-8015	-7230	-6942	-4482	87	

BURIAL HISTORY

Exxon No. 1 Kenney Estate 11–9S–95W

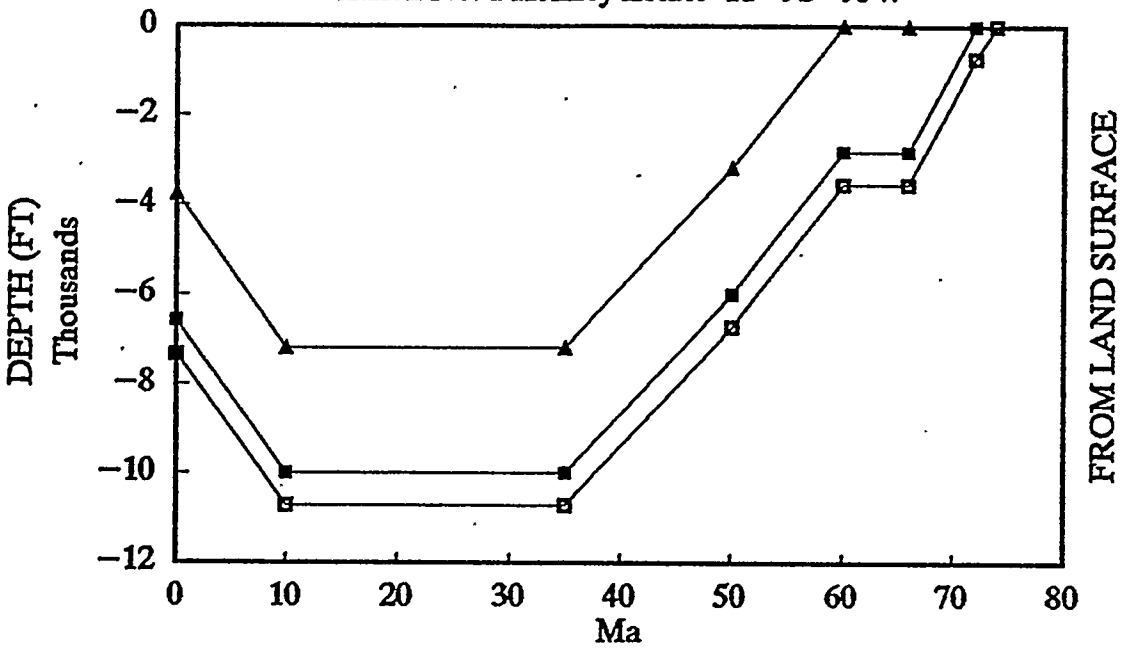

ROLLINS TOP

MESAVERDE TOP

MESAVERDE BASE (MANCOS

TEMPERATURE HISTORY

Exxon No. 1 Kenney Estate 11–9S–95W

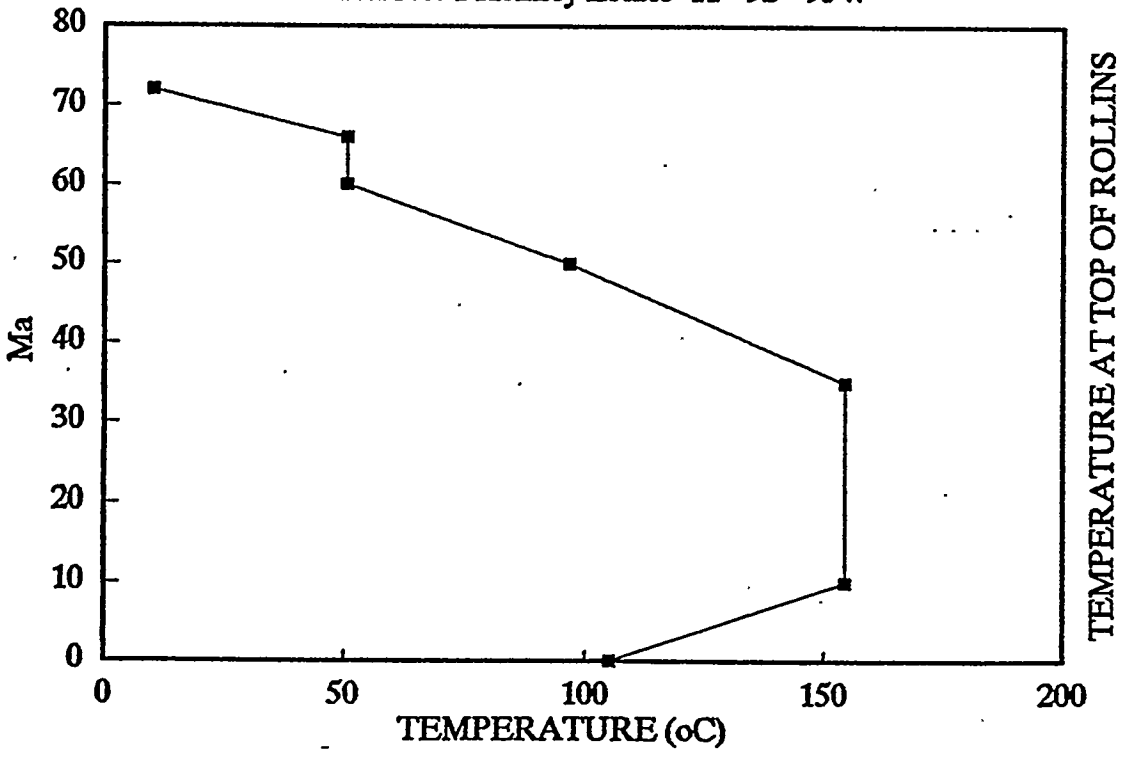

VITRINITE MATURATION

Exxon No. 1 Kenney Estate 11–9S–95W

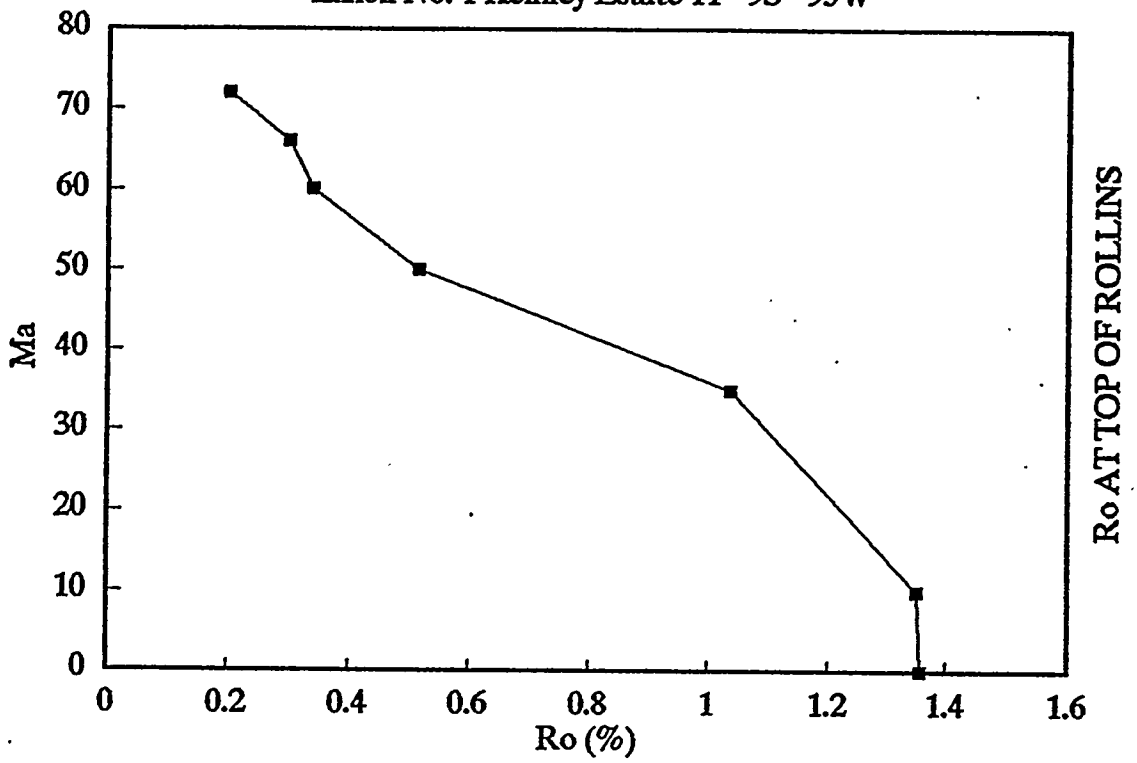

SUBSIDENCE HISTORY Johnson and Nuccio, 1986, Structural and Th
11-9S-95W SE,SE Exxon No. 1 Kenney Estate
T GRADIENT (corr.)= 2.6 DEG F/1
DEG 0.0474 Before 30
0.0474 After 30 M
LOG TOPS KB (elev. in ft.)= 7029.5

	ELEVATIONS			
Ma	MESAVERDE BASE	ROLLIN TO	MESAVERDE TOP	SEDIME SURFAC
74	1000			1000
72	272	1000		1000
66	-2148	-1420	1400	1400
60	-2148	-1420	1400	1400
50	-4328	-3600	-780	2400
35	-6728	-6000	-3180	4000
10	-4828	-4100	-1280	5900
0	-291	437	3257	7029

DEPTHS		TEMPERATURE	
MESAVERDE BASE	ROLLINS TOP	MESAVERDE TOP	ROLLINS TOP
0			
-728	0		10
-3548	-2820	0	51
-3548	-2820	0	51
-6728	-6000	-3180	97
-10728	-10000	-7180	154
-10728	-10000	-7180	154
-7320	-6592	-3772	105

Appendix H

Summary of Petrographic Database

D. Payne[a] and J. Comer[b]

[a]Laboratory for Computational Geochemistry
Indiana University
Bloomington IN 47405

[b]Indiana Geological Survey
611 North Walnut Grove
Bloomington IN 47405

This table shows a summary of the petrographic database on Excel spreadsheets. Data for each of the parameters was averaged over the interval, and in some cases over distinguishable units. The clay minerals illite, chlorite, and kaolinite were only semi-quantified in the original petrographic data sheets in the Sandia Laboratory reports for the MWX site. The semi-quantitative categories used were dominant, subdominant, moderate, minor, trace, and combinations of these terms. To quantify these paramters, values of 1.0, 0.8, 0.5, 0.25, and 0.05 were used respectively. These values were then normalized on the value for the mode of clay minerals, assuming that illite + chlorite + kaolinite comprised the total quantity of clays. Other unquanitified parameters, such as sorting and angularity were left unquantified because they are not imminently useful.

							PETROLOGY AVERAGES						
INTERVA	UNIT	WELL	DEPTH RANGE			MEAN	RANGE		POROSIT	SORTIN	QUARTZ	K-FELDS	PLAG
						(mm)	(mm)		(%)		(%)	(%)	(%)
fluvial	HF II	MWX1	4490.40	4793.40		0.14	0.06	0.25	4.11		45.59	3.94	9.41
	HF I	MWX1	4795.30	4949.80		0.17	0.04	0.55	9.85		48.15	2.35	9.38
	MF I	MWX1	4969.60	5294.50		0.22	0.07	0.46	1.02		35.11	11.18	15.73
	MF II	MWX1	5302.50	5668.50		0.20	0.07	0.41	2.70		43.31	4.70	10.05
	fraczone	MWX1	5706.50	5870.40		0.14	0.03	0.39	11.55		48.90	0.28	7.28
	LF	MWX1	5872.50	6331.20		0.15	0.06	0.30	2.87		44.00	1.35	4.76
	fraczone	MWX2	5704.00	5849.90		0.16	0.05	0.39	6.35		43.31	0.27	9.00
	all					0.17	0.06	0.37	4.80		43.85	3.75	9.31
coastal		MWX1	6345.60	6582.50									
		MWX2	6425.80	6556.90									
	all					0.12	0.03	0.27	8.41		44.80	0.84	5.38
paludal	coastal	MWX1	6625.50	6895.80		0.11	0.03	0.25	0.93		39.93	1.37	4.63
	paludal	MWX3	7081.55	7152.60		0.10	0.04	0.20	9.51		43.66	0.49	5.94
	all					0.11	0.04	0.22	5.55		41.94	0.89	5.34
marine	cozzette	MWX1	7883.30	7957.30									
		MWX2	7832.20	7898.10									
		both				0.08	0.03	0.17	10.65		59.82	1.25	6.68
	corcoran	MWX2	8105.90	8122.20		0.11	0.03	0.25	14.54		47.07	0.05	5.07
	rollins	MWX3	7536.80	7563.20		0.13	0.05	0.26	5.08		43.21	2.50	7.07
	all					0.10	0.03	0.21	10.28		53.19	1.76	6.40

CHERT	LITHICS	CLAY MI	CALCITE	DOLOMI	SILICA O.	MUSCOV	BIOTITE	ORG C	ILLITE ra	CHLORIT	KAOLINI	SUM	UNIT
(%)	(%)	(%)	(%)	(%)	(%)	(%)	(%)	(%)				(%)	
1.92	18.89	7.78	2.73	0.00	2.71	0.06	0.19	0.00	3.20	3.95	0.63	97.33	HF II
3.19	12.15	7.23	2.92	0.00	2.46	0.19	0.04	0.00	3.81	0.68	2.74	97.92	HF I
1.66	13.14	12.02	6.58	0.02	0.57	0.61	1.80	0.16	5.09	6.93	0.00	99.45	MF I
4.82	9.74	12.54	6.64	2.00	0.52	0.28	1.30	0.54	6.43	6.12	0.00	99.11	MF II
7.10	6.70	4.03	8.80	2.50	2.45	0.05	0.08	0.00	1.41	0.29	2.33	99.70	fraczone
6.17	11.52	10.17	5.13	11.24	0.78	0.09	0.17	1.17	5.70	3.67	0.80	99.41	LF
4.15	14.88	7.04	6.69	2.04	4.85	0.00	0.00	0.00	3.18	0.10	3.76	98.58	fraczone
4.13	12.60	9.12	5.56	2.81	1.78	0.19	0.58	0.33	4.34	3.68	1.10	98.79	all
4.47	11.52	7.70	6.94	6.09	3.53	1.00	0.05	2.50	7.51	0.18	0.02	96.50	all(coastal
4.87	8.43	11.57	4.40	19.93	1.20	0.07	0.00	2.00	9.35	1.36	0.85	98.40	
2.83	10.34	7.43	2.46	13.57	0.43	0.20	0.11	1.56	7.43	0.00	0.00	88.97	
3.77	9.46	9.34	3.35	16.51	0.78	0.14	0.06	1.77	8.32	0.63	0.39	93.32	all(paludal
1.76	3.59	2.59	7.80	7.84	4.32	0.16	0.05	0.03	1.67	0.09	0.83	98.35	cozzette
1.85	5.36	8.22	1.00	5.23	4.00	0.04	0.04	0.00	6.09	0.30	1.83	89.64	corcoran
4.14	9.86	6.36	12.45	9.27	1.22	0.66	0.19	0.01	6.09	0.11	0.16	96.50	rollins
2.42	5.40	4.71	9.89	7.52	3.75	0.25	0.08	0.02	3.67	0.14	0.91	95.97	all(marine)

Appendix I

Adaptive Gridding for Reaction-Transport Problems

W. Sibo and P. Ortoleva

Laboratory for Computational Geochemistry

Department of Chemistry
Indiana University
Bloomington IN 47405

ABSTRACT

A completely automatic computational technique is introduced to obtain grids needed for simulating reaction-transport-mechanical problems. The resulting grids make simulation of the great geometric internal and external complexity of a sedimentary basin feasible. The method is implemented in two spatial dimensions for the case of irregular quadrilateral elements. The computational technique used to establish the grid is based on notions from optimal control theory and accelerated by a multi-splitting technique that has some roots in the multi-gridding approach to the solution of partial differential equations.

I. INTRODUCTION

Adaptive gridding is an efficient tool for the numerical simulation of many complicated systems. Applications include the simulation of fluid motion interfaces such as flames reaction or stress analysis in equipment design. In the present an emerging important area for the application of adaptive gridding is in the analysis of geochemical systems wherein the variation of material properties between sedimentary features (such as layers) can change dramatically.

Two types of meshes are used - structured and unstructured. The structured meshes are those with simplified geometric elements such as quadrilaterals (in 2D) or hexahedral elements (in 3D). While the unstructured meshes often consist of triangles (2D) or tetrahedral shapes (3D) with irregular connections of edges [1].

The grid generation of an unstructured mesh consists of either (a) modifying an existing grid, or (b) filling an empty space not yet gridded by elements. The most commonly used technique for filling an empty space is by advancing-front algorithm [2,3]. Modifying an existing grid is performed by introducing new points within some primitive or typically structured grid. This method is called the Voronoi algorithm [4,5].

The optimization of grids may be carried out either by adaptive gridding moving existing grid nodes or by adding more degrees of freedom by subdividing existing cells so as to refine the grid. This latter method is called the h-method while [6], using higher degree interpolation polynomials, is called the p-method [7]. For more complete references about grid optimization and refinement see [8,9].

Here we introduce and implement a method of grid adaptation to focus grid nodes where needed by the numerical computations. The gridding satisfies the following rather severe demands:

i) the grid must be obtained completely automatically by a computation algorithm;

ii) the algorithm may have to readjust every time-step of a calculation as the system evolves;

iii) the grid must have certain smoothness and orthogonality properties needed by numerical algorithms used to solve elliptic and other equations on them;

iv) the method must be applicable in systems of complex and changing geometry in two and three dimensions.

The algorithm developed here meets all these criteria.

Our method is modifying an existing grid by repositioning the grid nodes according to an optimization criterion. The procedure starts with a grid of small number of nodes at the first step of optimization, the grid is then split (subdivided). This is continued until the final number of nodes is obtained and the optimatization criterion is satisfied.

The optimization criterion is based on an objective function that consists of several contributions to force the grid to meet desired objectives (focusing nodes to appropriate regions of space, maintaining good aspect ratios for elements, etc.). The main contribution is a spring-like term that forces the nodes to focus on appropriate regions of space while the remaining appropriate contributions insure certain smoothness and other grid criteria.

Therefore this aspect of our procedure is somewhat like that of [9] wherein suggests mass is assigned to each element center and the surrounding nodes can be attracted to that mass. However, our procedure dramatically differs from that of [9] in that in obtaining the ideal grid we combine optimization grid with refinement through our splitting approach.

II. GRID OPTIMIZATION

The adaptation of the grid is carried out by constructing a functional of the set of all grid coordinates X and the spatial distribution of concentrations and other variables ψ.

When this functional $\mathcal{F}$ is a minimum with respect to X then the grid is, by definition, adapted.

Let an index i label the grid coordinates. Thus if there are N/3 grid nodes in 3 dimensions then $X = \{X_1, X_2, \cdots, X_N\}$. The minimum in $\mathcal{F}$ is then obtained when the X-gradient of $\mathcal{F}$ vanishes:

$$\Gamma_i = \frac{\partial \mathcal{F}}{\partial X_i} \tag{II.1}$$

$$\Gamma_i = 0,\ i = 1,2,\cdots,N \text{ at adaptation} \tag{II.2}$$

A simple procedure suggests itself based on a steepest descent method. The gradient Γ provides, in some sense, an optimal direction in X space for a small grid rearrangement that would reduce $\mathcal{F}$. This if X^{old} is a grid of less than acceptable adaptation, then a better grid would be

$$X_i^{new} = X_i^{old} + \frac{\Gamma_i}{|\Gamma|}\lambda \tag{II.3}$$

$$|\Gamma|^2 = \sum_{i=1}^{N} \Gamma_i^2 \tag{II.4}$$

where λ measures the amount of the move. As λ is to be small (or the grid may lose its logic through overshooting) we can determine the best λ by fitting numerically $\mathcal{F}\left(x^{old} + |\Gamma|^{-1}\Gamma\lambda\right)$ to a quadratic

$$f = a + b\lambda + c\lambda^2 \tag{II.5}$$

and taking the best λ, λ_c, to be

$$\lambda_c = -b/2c. \tag{II.6}$$

This procedure could then be done iteratively until $\mathcal{F}$ is reduced to an acceptable level and hence a degree of adaptation required is obtained.

The problem with this method is that the amount of the move, λ_c, so obtained reflects the minimum grid spacing in the domain and hence the relatively large moves needed to adapt in the coarser regions do not take place in an acceptable number of

iterations. Consider, however, a reformulation which loses some of the advantage of the gradient direction to take the much greater advantage of a scaling of the move by a local measure of the grid spacing. We introduce a quantity a_i that measures the order of magnitude of the grid spacing near the i-th point. Then we put

$$X_i^{new} = X_i^{old} + |\Gamma|^{-1}\Gamma_i a_i \lambda_c. \qquad (II.7)$$

This turns out to yield a much faster convergence to a well adapted grid.

III. ADAPTATION ACCELERATION

A key problem with this adaptation method is that it takes many iterations and furthermore has difficulty in placing many grid points in a shock front because such a narrow structure only manifests itself on a change between two neighboring grid points of the coarser grid on either side of the shock on its way to final adaptation and resolution of the shock. The following strategy surmounts this by going through a sequence of grid meshes with greater and greater numbers of grid nodes.

Let the final grid of interest be quadrilateral with $(N_x + 1) \times (N_y + 1)$ nodes. Then we introduce a coarser grid of $(M_x + 1) \times (M_y + 1)$ such that

$$N_x = M_x 2^q, \; N_y = My2^q$$

for integers M_x, M_y and q. Thus if we divide the coarse grid $((M_x + 1) \times (M_y + 1))$ into 2^q subdivisions in each direction we get the $(N_x + 1) \times (N_y + 1)$ grid.

Our multi-step procedure is as follows:

1) Adapt the M_x+1, M_y+1 grid to the function of interest.
2) From the grid of 1) make a new $(2M_x+1)$, $(2M_y+1)$ grid by subdividing as shown in Fig. 1. The new grid points are halfway between the old points while the center point is the average position of the new four side points.
3) Starting with the bisection grid constructed in 2) (of size $(2M_x+1, 2M_y+1)$) go through the adaptation procedure to get a refined $(2M_x+1, 2M_y+1)$ grid.

4) Repeat steps 2) and 3) q times until the full adapted (N_x+1, N_y+1) grid is obtained.

a) In the sequence of splitting/adaption cycles, for the optimization should reflect the intermediate number of grids.

b) Each cycle should only take a few iterations because only a few points need to be adjusted--i.e., those in or near the region where the descriptive variable to be adapted to is changing much.

c) One may optimize the degree to which the intermediate grids need to be adapted so as to get the final adapted grid in the shortest CPU time.

d) In the final grid there should be some 2^q or more grid points in the transition region.

IV. IRREGULAR DOMAINS

Many applications involve domains with curved boundaries. This situation can be handled via an adaptation of the boundary grid nodes using a parameter fixing distance along an arc defining the boundary as follows.

Again we consider a quadrilated grid as suggested in Fig. 1. For each of the four sides, it is assumed that a set of points $\vec{r}_0, \vec{r}_1, \vec{r}_2, \cdots \vec{r}_P$ are known that lie within it. We introduce a parameter τ ($0 \le \tau \le 1$) fixed so that the polynomial

$$\vec{r}(\tau) = \sum_{n=0}^{N_b} \vec{a}_n \tau^h \qquad \text{(IV.1)}$$

describes the bounding curve -- i.e., passes through the P+1 arc-defining points either exactly (N_b=P) or in a least squares sense (N_b<P). In either case the vector coefficients $\vec{a}_n$ ($0 \le n \le N_b$) are known and the challenge is to move the boundary grid nodes along the arc in order to achieve adaptation.

For the least square case we choose to constrain the boundary arc to pass through the endpoints $\vec{r}_0, \vec{r}_P$. Thus

$$\vec{a}_0 = \vec{r}_0 \qquad \text{(IV.2)}$$

$$\sum_{n=0}^{N_b} \vec{a}_n = \vec{r}_P . \tag{IV.3}$$

Eliminating $\vec{a}_0$ and $\vec{a}_{N_b}$ we get

$$\vec{r}(\tau) = \vec{r}_0 + \sum_{n=1}^{N_b-1} \vec{a}_n \tau^n + \left(\vec{r}_P - \sum_{n=1}^{N_b-1} \vec{a}_n - \vec{r}_0 \right) \tau^{N_b} . \tag{IV.4}$$

Finally the points $\vec{r}_0, \vec{r}_1, \cdots \vec{r}_{N_b}$ are assumed arranged in an orderly way so that $\vec{r}_{i+1}$ is further along the arc than $\vec{r}_i$. Thus we make the specific assumption that $\vec{r}_i$ lies along $\vec{r}(\tau)$ at a value τ_i^0 given by

$$\tau_i^0 = \frac{i}{P}, 0 \le i \le P . \tag{IV.5}$$

Thus the least square fit minimizes $\left| \vec{r}_i - \vec{r}\left(\tau_i^0\right) \right|$ over all the i. Finally if N_b should be kept below about P/2 to avoid artifactual bumps or looping in the fitted linear system boundary curve $\vec{r}(\tau)$.

The task of adapting the grid is accomplished as follows. The interior grid adaptation is exactly the same as that for the rectangular domain. The difference comes in computing Γ of (II.1) the boundary grid points. However, adaptation simply means changing the τ values corresponding to the boundary grid points. Assume an unadapted grid is known. For one of the boundary arcs $\vec{r}(\tau)$ the related boundary grid nodes are at τ values $0 = \sigma_0, \sigma_1, \sigma_2, \cdots \sigma_{M-1}, \sigma_M = 1$. There are four such sets of σ's (from the 2 side, the top and the bottom arcs) that we denote collectively as $\underline{\sigma}$ and the corresponding set of values after adaptation is denoted $\underline{\tau}$. Then if $\underline{x}$ and $\underline{y}$ denote the coordinates of all the interim grid nodes and $\underline{x}^b$, $\underline{y}^b$ are the set of all x,y-coordinates of the boundary nodes, the objective function has the form

$$\mathcal{F}\left(\underline{x}, \underline{y}, \underline{x}^b(\underline{\tau}), \underline{y}^b(\tau)\right). \tag{IV.6}$$

Then we proceed by minimizing $\mathcal{F}$ with respect to $\underline{x}$, $\underline{y}$ and $\underline{\tau}$ in a manner much like that outlined in Sects. II, III.

V. SPECIFIC IMPLEMENTATION

The above approach was implemented on distorted quadrilateral grids as in Fig. 2. Such grids are of great programming advantage since the mesh maps logically (in grid index space) onto a square grid.

An example is seen in Fig. 3 showing three circular regions wherein the descriptive variable Ψ changes sharply. The sequence of grid splittings and adaptions leading to the final adaptation is illustrated in Fig. 4 for a single circular nonuniformity. In both cases of Figs. 3 and 4 the descriptive variable Ψ is essentially constant within the circle and changes rapidly at its periphery. Figs. 5 and 6 show examples of adaptation on irregular domains.

REFERENCES

[1] Timothy, J.B. (May, 1992) Aspects of unstructured grids and finite-volume solvers for Euler and Navier-Stokes equations, Special Course on Unstructured Grid Methods, AGARD-R-787.

[2] Lôhner, R. and P. Parikh, (1988) Int. J. Numer. Meth. Fluids, 8, 1135.

[3] Huet, F. (1988) AGARD-CP-484, 17-1.

[4] Bowger, A. (1981) Computing Dirichlet tessellation, The Computer Journal 24-2, 162-167.

[5] Yerry, M. and M. Shephard (1984) Automatic Three-dimensional mesh generation by the modified-octree techniques, Int. J. Num. Meth. Engrg. 20, 1965-1990.

[6] Baum, J.D. and R. Lôhner (1989) AIAA 89-0653.

[7] Lôhner, R. (1988) Comp. Struct. 30, 303.

[8] Lôhner, R. and J.D. Baum (1990) Numerical simulation of time dependent 3D flow using adaptive unstructured grids, in H.E. Trease et al., Advances in Free Lagrange Method, Springer-Verlag.

[9] Diaz, A.R., N. Kikuchi and J.E. Taylor (1983) A method of grid optimization for finite element methods, Comp. Meths. Appl. Mech. Engrg,. 41, 29-45.

[10] Chen, Y., A. Chen, A. Park, J. Mu and P. Ortoleva (1994) CIRF.A: A General Coupled Reaction Transport Model and Simulator, Applied Geochemistry (submitted for publication).

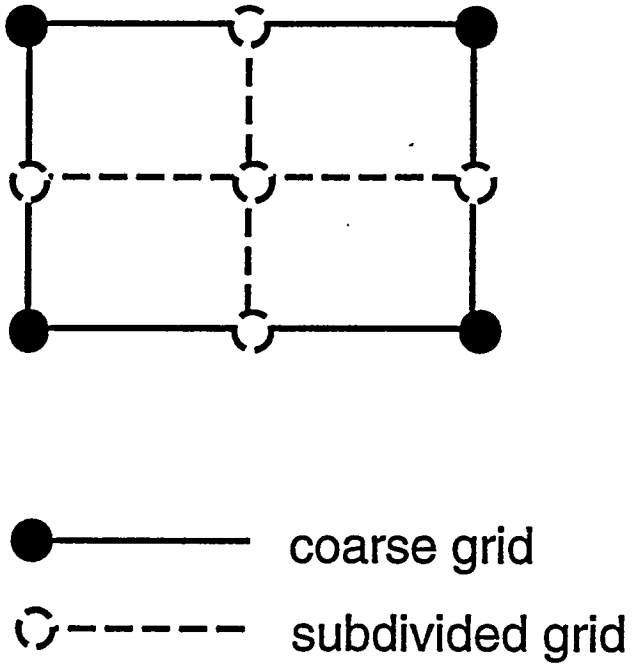

Fig. 1 Distorted quadrilateral grid

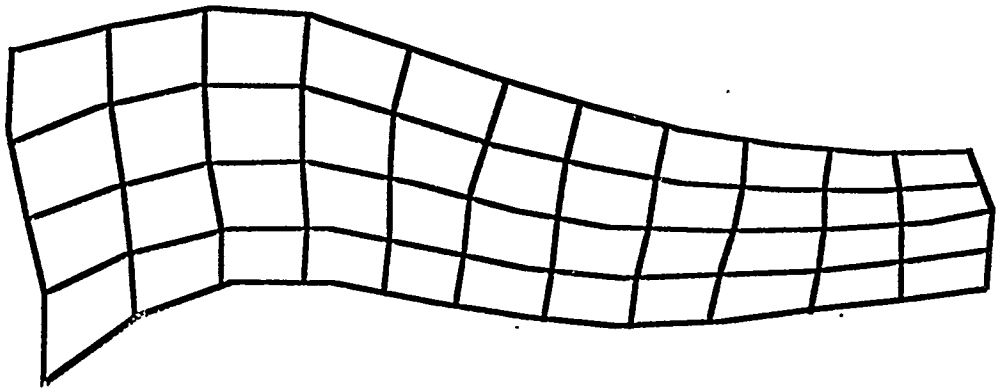

Fig. 2 Distorted quadrilateral grid

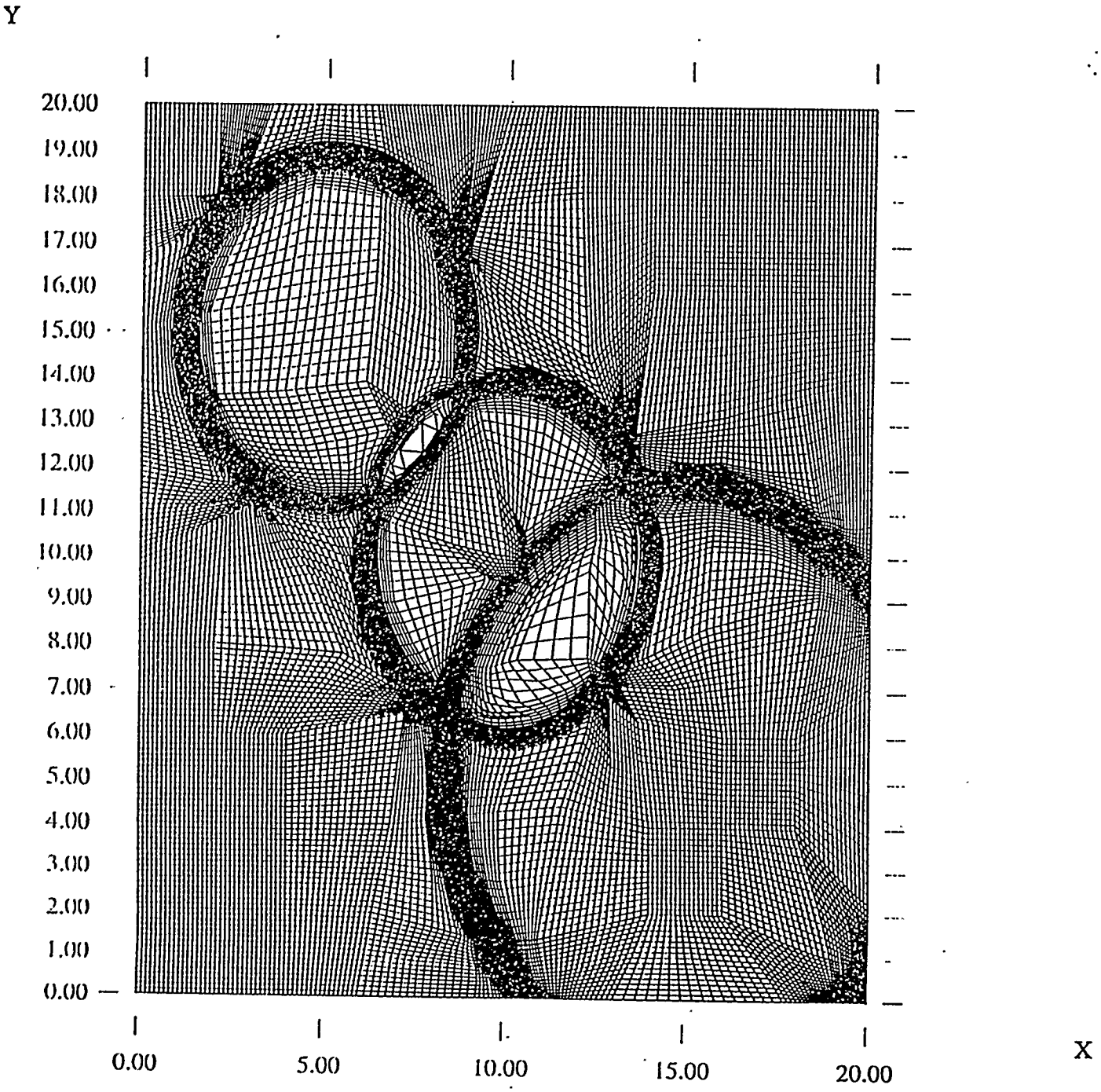

Fig. 3 Computationally adapted grid used to capture a set of three lenticular sediment bodies.

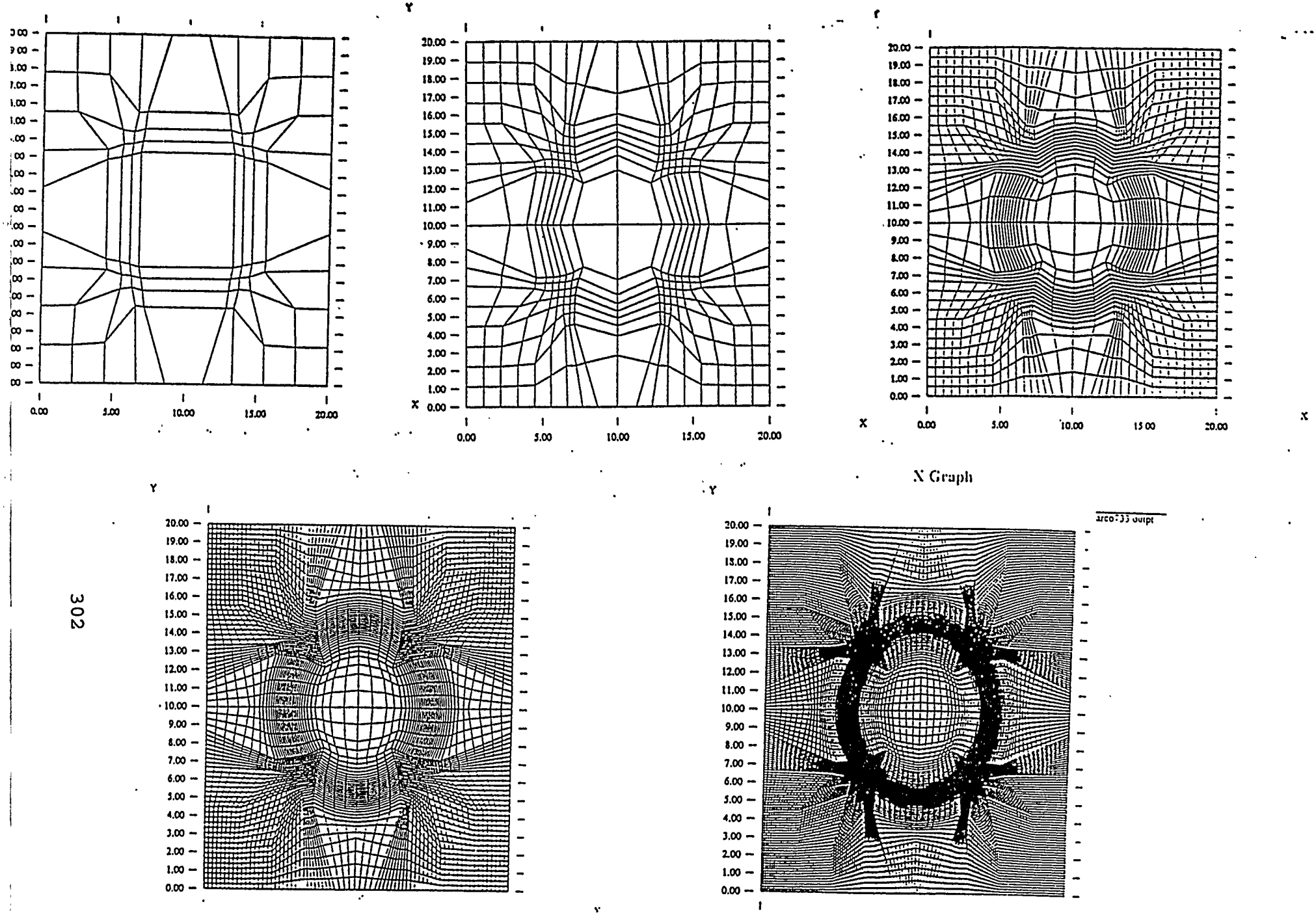

Fig. 4 Sequence of intermediate grids leading to the finely adapted grid using our multiple grid-splitting method.

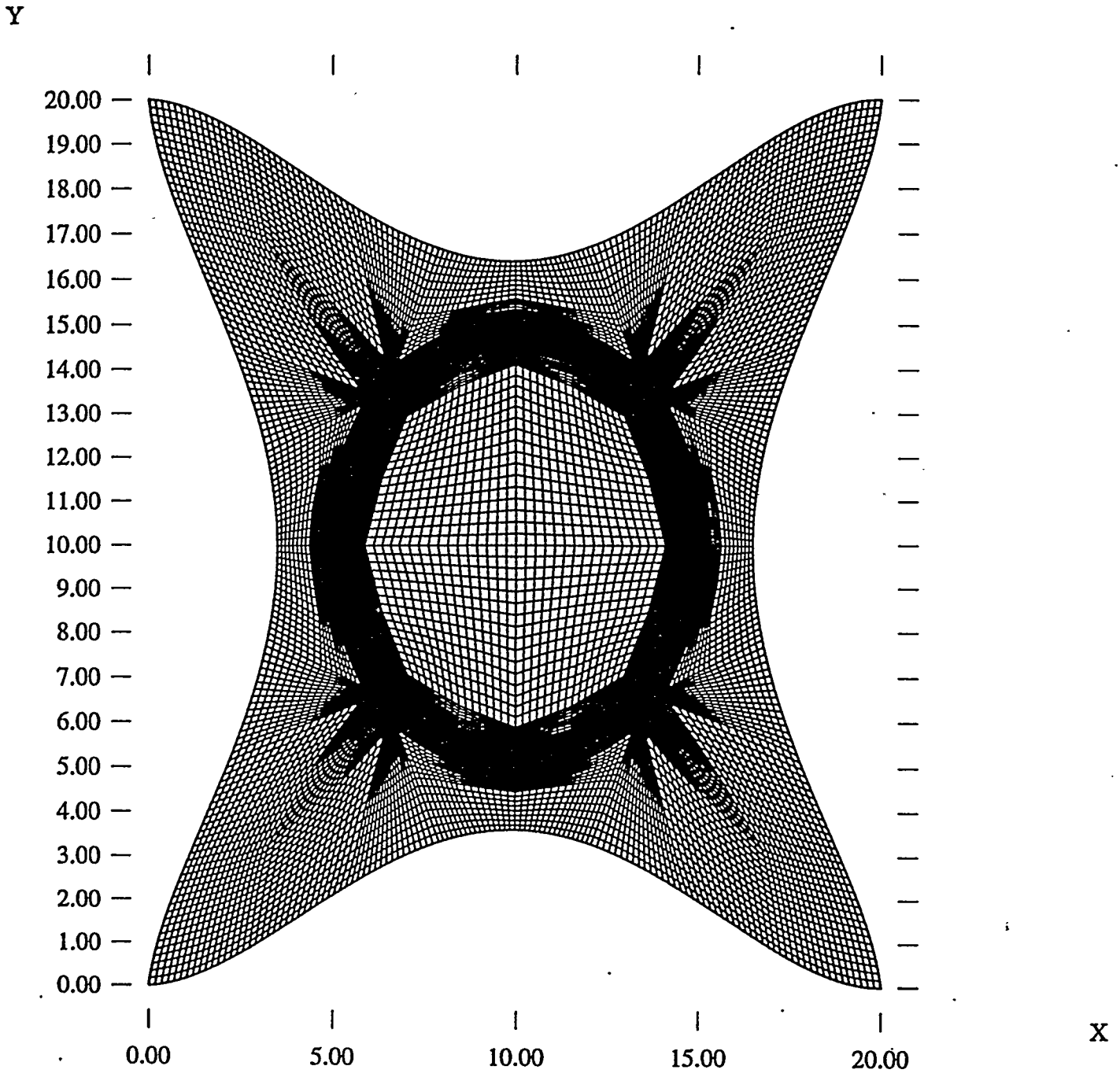

Fig. 5 The final adapted grid on an irregular domain.

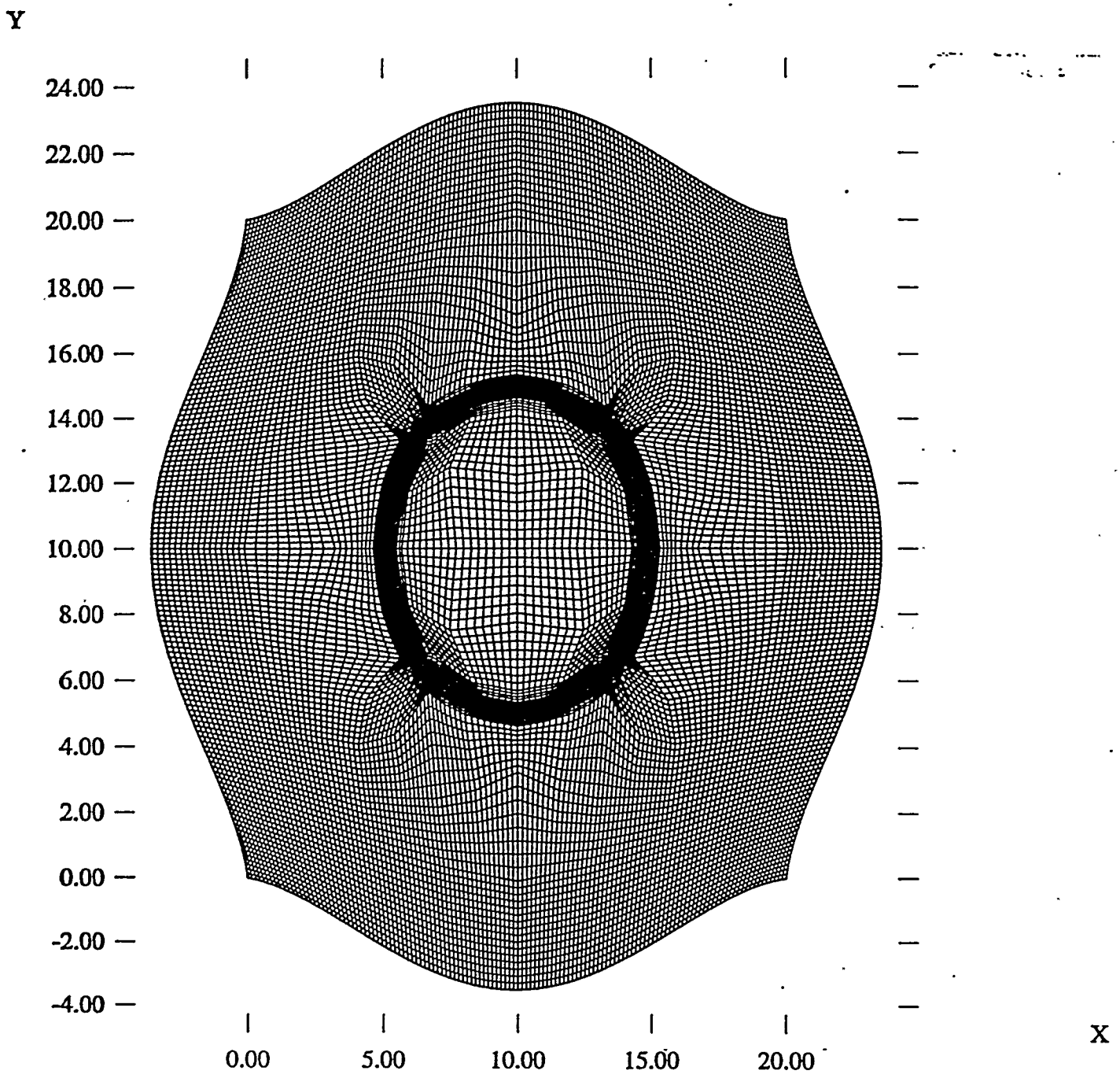

Fig. 6 Another adapted grid on an irregular domain.